A STUDY OF ATOMIC AND MOLECULAR HYDROGEN EMISSION FROM A MAGNETICALLY CONFINED PLASMA

by

THOMAS G.MORAN

B.S.SOUTHERN ILLINOIS UNIVERSITY
1979

Submitted to the Department of
Physics
in Partial Fulfillment of the
Requirements for the Degree of

DOCTOR OF PHILOSOPHY

at the

MASSACHUSETTS INSTITUTE OF TECHNOLOGY
OCTOBER 1988

Signature of Author _____
Department of Physics
October 7,1988

Certified by _____
Dr.John King
Thesis Supervisor

Accepted by _____
Dr.George Koster
Chairman, Departmental Graduate Committee

A STUDY OF ATOMIC AND MOLECULAR HYDROGEN EMISSION FROM A MAGNETICALLY CONFINED PLASMA

by

THOMAS GERARD MORAN

Submitted to the Department of Physics
on OCTOBER 7, 1988 in Partial Fulfillment of the
Requirements for the Degree of DOCTOR OF PHILOSOPHY

ABSTRACT

The atomic and molecular hydrogen emission from the Tara Tandem Mirror central cell plasma was investigated using several spectrometers and a Fabry-Perot interferometer. Hydrogen atoms and molecules in plasmas radiate light due to electron impact excitation. The spatial light distributions, along with a knowledge of the plasma electron density and electron temperature, determine the particle density distributions, ionization rates, and power expended in ionization, radiation, and charge-exchange. The atomic spectral line profiles give information about the kinetic energies of the emitting atoms.

Low wavelength resolution measurements in the visible and vacuum ultraviolet using several spectrometers showed the atomic and molecular densities concentrated axially at the gas port, and radially at the plasma edge. The estimated fueling rate determined from the measurements is 462 amps(208 amps of atomic ionization and 254 amps of molecular ionization).The estimated power loss due to neutral particle processes is 90 kilowatts, out of 300 kilowatts injected. High wavelength resolution measurements of the doppler-broadened atomic Hα line using the interferometer and a multichannel spectrometer showed the presence of two energy components at the measurement location farthest from the gas port(350 cm away), and one component at the other locations(0 cm, 30 cm and 110 cm away). The 'cold' component had an average energy of 1.5 ev, roughly consistent with molecular dissociation energies, and the 'hot' component had a average temperature of 65 ev, which is half the estimated ion temperature in the outer plasma at the axial location where the hot component was observed. The hot atoms probably originated in charge-exchange reactions and lost energy in wall reflections.

Molecular line, and continuum emission was measured in the visible and near ultraviolet. Line emission from the $G \rightarrow B$, $K \rightarrow B$, and $I \rightarrow B$ bands was measured and used to determine molecular densities and ionization rates. The wavelength distribution of the $X^1\Sigma_g^+ \rightarrow a^3\Sigma_g^+ \rightarrow b^3\Sigma_u^+$ continuum was measured and the total continuum intensity was estimated to obtain the ratio of continuum dissociation to molecular ionization, .025.

Thesis Supervisor: Dr. John King

Title: Professor of Physics, Massachusetts Institute of Technology

ACKNOWLEDGEMENTS

Now that I have finished my dissertation, there are several people I wish to thank for their help and support. I would like to thank Bob for machining help and Michelle for help with the figures. I would like to thank my thesis readers, Kate Kirby and George Bekefi, for their time and their helpful comments. I would like to thank John King for being my advisor, and believing in my project. I would like to thank my close friends, Mark, Bunny, Kevin, George, Kim, and Elisabeth. Finally, I would like to thank my family for their support and encouragement.

Contents

List of Figures

List of Tables

Chapter 1

Introduction

1.1 Introduction to Magnetic Mirrors

This work presents a study of the spectra of the atomic hydrogen and molecular hydrogen in the Tara Tandem Mirror central cell plasma. The Tara Tandem Mirror is one of several tandem mirrors constructed to study the feasibility of such devices in confining and heating a plasma of sufficiently high temperature and density for energy to be produced through nuclear fusion reactions. A tandem mirror device is an arrangement of several magnetic mirrors. The simplest type of magnetic mirror is called a 'simple mirror'. A simple mirror is a device which produces an approximately solenoidal magnetic field in the center with higher fields at both ends. The plasma is prevented from expanding radially by the Lorentz force, which causes the particles to have helical orbits. At the end of the device the field strength increases and the field lines have an inward radial component. This component causes a force on the gyrating charge particles in the direction towards the center of the mirror. If the ratio of a particle's parallel velocity to its perpendicular velocity is less than the square root of the ratio of the minimum to maximum field strength, the particle will be reflected back towards the center. Otherwise, the particle will escape from the mirror.

A simple mirror has several weaknesses. One is the loss of particles in the velocity space cone defined by the above-stated relation. Particles will constantly diffuse into this cone due to collisions causing a constant particle loss. Another problem is the lack of magneto-hydro-dynamic(mhd) stability due to the outward curvature of the field lines which allow fluid-like instabilities.

The 'tandem mirror' was designed to solve these problems. The tandem mirror

is composed of a solenoidal field region with mirror coils at each end and one or two mirror regions beyond the central cell mirror coils. The purpose of the end mirror plasmas is to confine plasma particles which are not confined by the central cell mirror fields and to keep the central cell plasma stable. There may be an azimuthally symmetric or a non-azimuthally symmetric mirror called the 'plug' adjacent to the central cell on each end. An attempt is made, by the injection of high energy neutral hydrogen beams, and injection of radio wave of microwave power into the plug plasma, to create electric fields in this plasma which will confine the non-magnetically-confined central cell plasma. Adjacent to the plugs on each end may be non-axisymmetric mirrors known as 'anchors'. These have a magnetic field configuration of a simple mirror with a quadrapole field superimposed. The purpose of the imposed quadrapole fields is to create a 'minimum B' configuration. In a minimum-B mirror, the field strength increases with the distance from the center of the mirror in any direction. A plasma in this type of mirror will be stable to mhd fluctuations. The stable anchor plasma then keeps the rest of the plasma stable. Stability can also be achieved through the use of coils added to the solenoidal region known as a 'divertor', which divert magnetic flux outward and cause a magnetic field null at the edge of the plasma. In some devices the plug and the anchor may be combined into one end mirror plasma. A thorough discussion of tandem mirrors is found in ref. [1,2,3,4].

1.2 The Tara Tandem Mirror

The Tara device is a tandem mirror. It has a 10 meter long solenoidal section with two additional mirror-confined plasmas on each ends. Figure 1.1 shows a scale drawing of the device. Adjacent to both ends of the central cell are axisymmetric mirrors, known as the plugs. Neutral beams of hydrogen atoms are injected into the plug plasma in order to heat the ions and create a 'sloshing-ion' distribution, which is needed to create the confining plug potentials [1,2]. On the outside of each plug is an anchor, which confines an mhd-stable plasma in a minimum-B configuration. Since the magnetic field lines in the anchor passed through the entire length of the device, the stable anchor held the central cell plasma and plug plasmas stable as well. In the operation of Tara, a divertor was also used to provide stability. In the center of the central cell magnetic flux from the outer region of

the column is diverted in a loop outside the plasma. This held the plasma stable independently of the anchors. Figure 1.2 shows an interior view of the device with the plasma and coils visible. The central cell plasma is created from hydrogen gas which is pumped into a baffled region in the middle of the central cell known as the gas box [5]. Figure 1.3 shows a cut-away view of the gas box. Gas is injected at two ports on the sides of the chamber. There are flat disks in front of the port to diffuse the gas before it encounters the plasma. The magnetic field is increased at the location of the gas box, so that ions created in the gas box will flow to a region of lower field and leave the gas box. This is done in order to minimize the interaction between the ion population and the neutral particle population, which can lead to energy loss through charge exchange reactions. More than ninety nine percent of the plasma particles are created in the gas box, or within .5 meters of the edges of the gas box. This will be discussed in chapter 6.

The central cell discharge was initiated by injection of microwave power at the electron cyclotron frequency which created pre-ionization. At the same time, gas was injected into the gas box. Ten milliseconds later radio wave power at the ion cyclotron frequency was injected through the slot antenna, which was located .5 meters south of the machine center. The ions were heated directly by the rf power and the electrons were heated by collisions with the ions. The discharge lasted as long as the ion cyclotron heating continued, or about 60 milliseconds.

1.3 Diagnostic Set

The Tara device operated with a set of diagnostic instruments which routinely measured plasma parameters. Some diagnostics operated for all of the discharges, while others were used for relatively few discharges. The parameters relevant to this work are electron density, electron temperature, ion temperature, plasma pressure and edge gas pressure.

Electron density was measured with an interferometer. The interferometer sent a microwave beam through the plasma column. It measured the phase shift of that beam due to interaction with the plasma by comparing its phase to the phase of a reference beam which traveled outside the plasma. That phase difference $\Delta\phi$ is proportional to the line integral of the electron density along the path of the

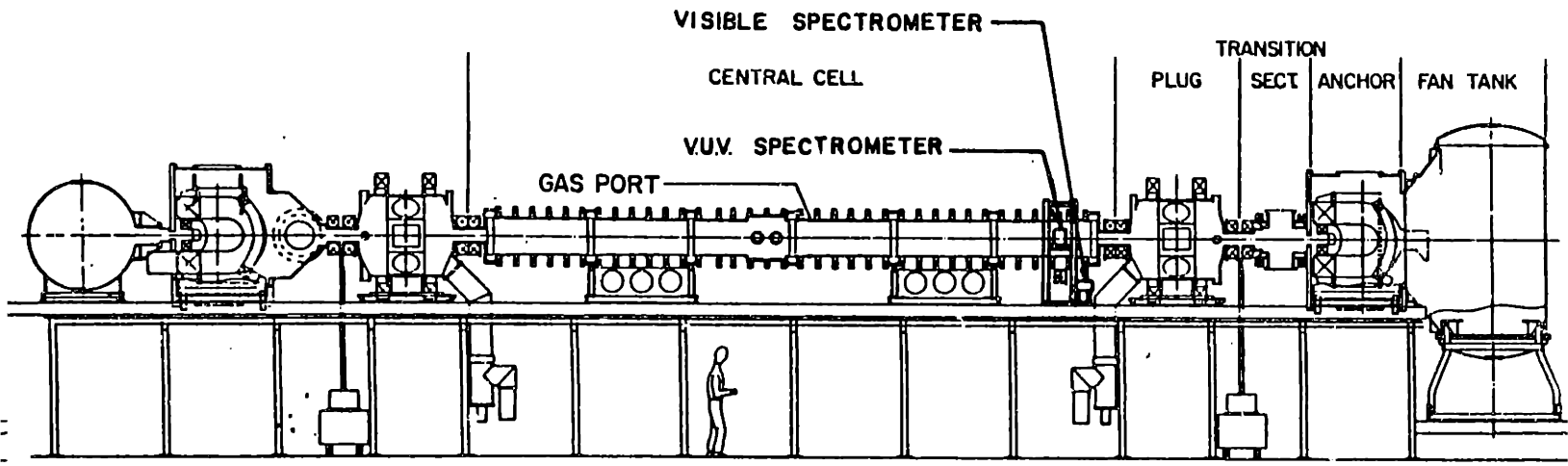

Figure 1.1: Schematic view of the Tara Tandem Mirror. The central cell, plugs, gas port, and anchors are labeled.

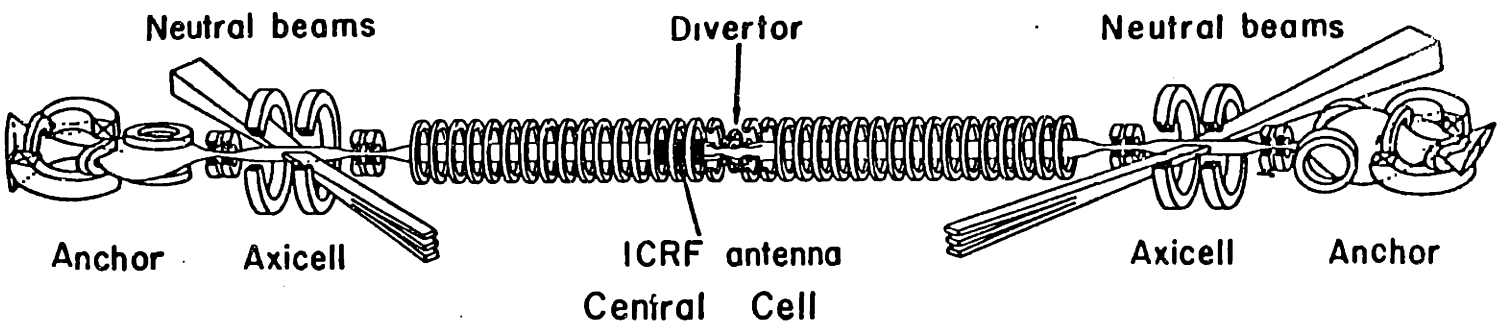

Figure 1.2: Schematic showing the magnetic coils and the plasma surface.

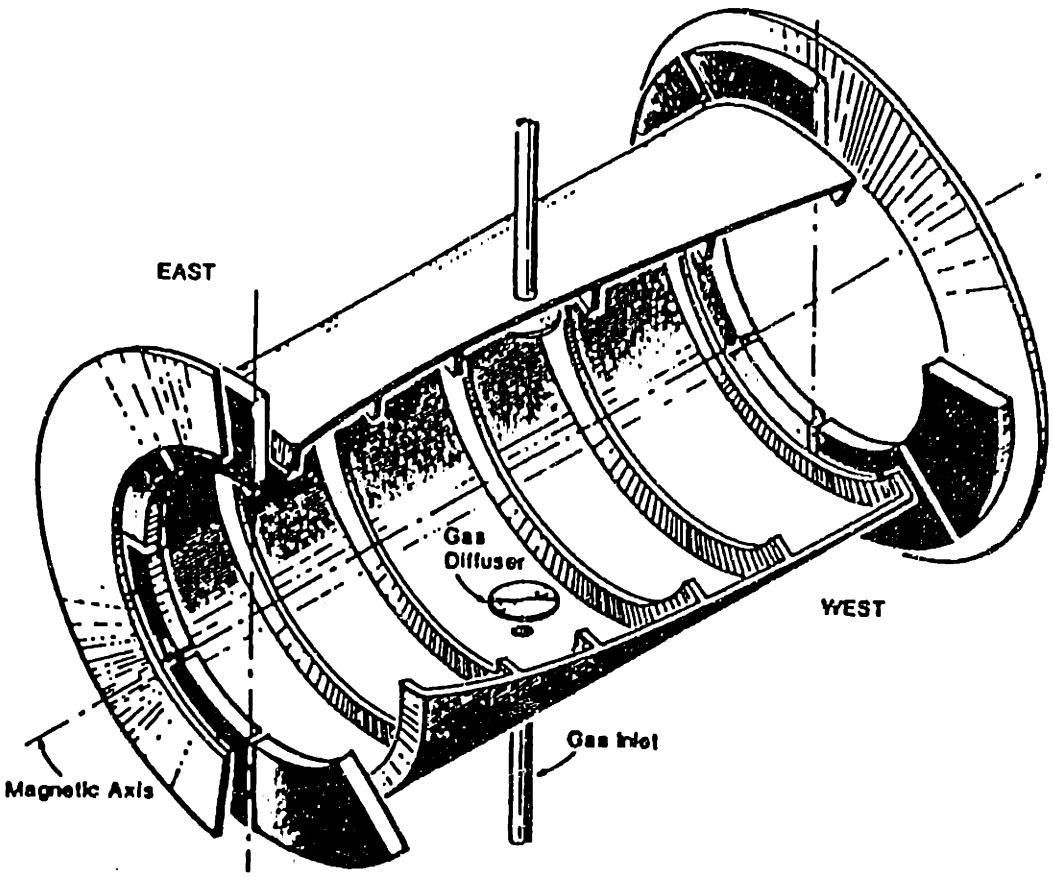

Figure 1.3: Cutaway view of the gas box showing the gas injection ports and diffusers. The diagram shows the gas box rotated 90 degrees from its orientation on the Tara device.

beam,

$$\Delta\phi \propto \int n_e(y)dy \tag{1.1}$$

where y is the distance along the beam path. Several of these interferometers were located along the length of the chamber and operated for all of the discharges. A 5-chord interferometer array was installed shortly before the end of the operating period of the device.

Electron temperature was measured by illuminating a region of the plasma with a ruby laser and measuring the wavelength distribution of the scattered light. The width of the scattered distribution is proportional to the square root of the electron temperature. This diagnostic was located in the north half of the chamber and operated for selected discharges.

Ion temperature was determined by measuring the energy distribution of en-

ergetic neutral atoms produced in charge-exchange reactions between plasma protons and cold atoms. The ion temperature is inferred from the energetic atom distribution. The charge-exchange diagnostic was located in the south half of the chamber and operated for selected discharges.

The plasma pressure was measured with diamagnetic loops, which are loops of wire encircling the plasma column. The time-integrated voltage induced in the loop is proportional to the plasma diamagnetism, β. The diamagnetism is proportional to the perpendicular plasma pressure $P_\perp$ integrated over the area enclosed by the loop:

$$\beta = \int_A \frac{P_\perp}{B^2/2} dA \tag{1.2}$$

The perpendicular plasma pressure is given by

$$P_\perp = \frac{3}{2}[n_e T_{e_\perp} + n_i T_{i_\perp}] \tag{1.3}$$

where n_e and n_i are the electron density and ion density, respectively, and $T_{e_\perp}$ and $T_{i_\perp}$ are the perpendicular electron temperature and perpendicular ion temperature, respectively. There were several loops located along the length of the machine and they operated for all of the discharges.

Several fast-ion gauges (FIG's) along the length of the chamber measured the gas pressure inside the gauges. The gauges have a filament which emits electrons. The electrons ionize neutral atoms or molecules. These particles are collected and the collected current is proportional to the pressure of neutral particles in the gauge. The gauge is thus sensitive to any neutral gas. However, measurements to be discussed in chapter 3 show that 99 % of the particles entering the plasma were hydrogen atoms. Therefore, virtually all of the pressure detected by the gauges must have been due to hydrogen molecules.

Figure 1.4 shows a schematic of the central cell and the locations of the above mentioned diagnostics. Included in the figure is the axial scale. All z-locations refer to this scale. Figure 1.5 shows a plot of the electron density and electron temperature versus radius for a typical discharge. Plots of several plasma parameters and of the injected rf power versus time are shown in figure 1.6. An ion temperature profile was inferred from impurity spectra measurements and is shown in chapter 3. The ion temperature measured with the charge exchange diagnostic varied between 300 ev and 700 ev. Owing to the magnetic bump in the center of the machine and the location of the slot antenna on the south edge of

that bump, the ion temperature was higher in the south than in the north and the charge exchange diagnostic measured only the south central cell ion temperature. The loops in the north measured the diamagnetism to be consistently lower then the diamagnetism in the south.

There were other diagnostics which were operated for a limited period of time or which measured quantities which did not give direct information about plasma parameters. Some of these diagnostics were relevant to this study and they will be discussed later.

1.4 Motivation for Atomic and Molecular Hydrogen Spectra Studies

Hydrogen atoms and hydrogen molecules play an important role in the operation of plasma confinement experiments. They provide the source of plasma ions and electrons as well as account for significant power loss from the plasma through ionization, radiation, and charge-exchange. The intent of this work is to study the plasma fueling in the Tara Tandem Mirror central cell, from the dissociation of the hydrogen molecules to the ionization of the hydrogen atoms, through an investigation of the atomic hydrogen emission and molecular hydrogen emission.

The hydrogen plasma is created by puffing molecular hydrogen gas into the central cell gas box where the molecules then become dissociated by electron collisions into neutral atoms and protons. [6]. Due to the low kinetic energies of the molecules, they do not penetrate the plasma and exist in a narrow shell outside the plasma column. The product atoms may penetrate the plasma, depending on their dissociation energies, or may encounter the chamber wall, where they may stick or reflect with a lower energy. Atoms in the plasma may be ionized through electron collisions and become plasma particles. The spatial distributions of molecules, atoms, and plasma electrons will thus determine the spatial distribution of fueling.

Plasma fueling has been studied in the Tara experiment and in several other plasma confinement experiments through an investigation of atomic hydrogen emission. If the electron temperature is above 10 ev, the ratio of atomic ionization to atomic excitation is only weakly dependent on electron temperature [7]. In the absence of any molecular contribution to the radiated light or ionization, the local emission measurement yields the local plasma fueling rate. Atomic

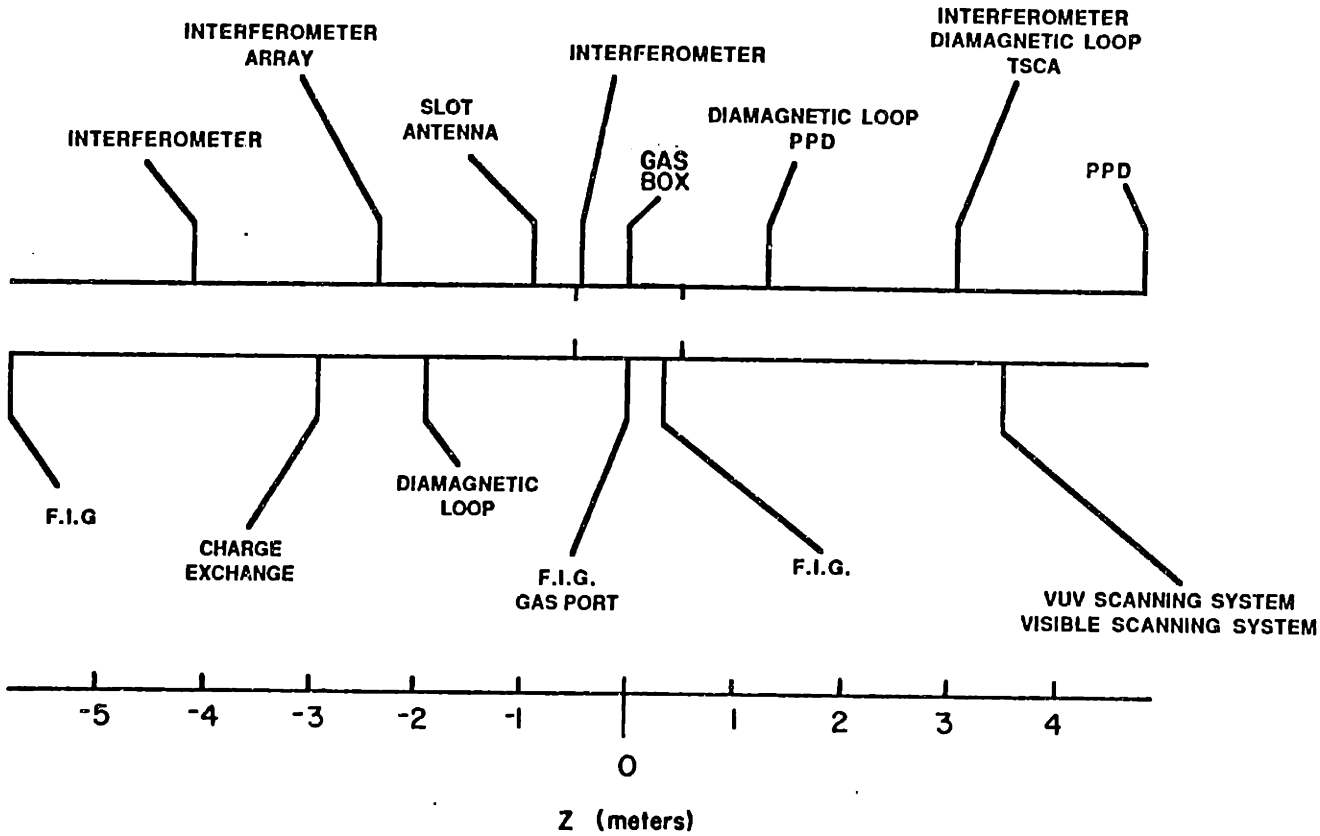

Figure 1.4: Diagram showing the locations of several diagnostics. All z-locations refer to the scale shown.

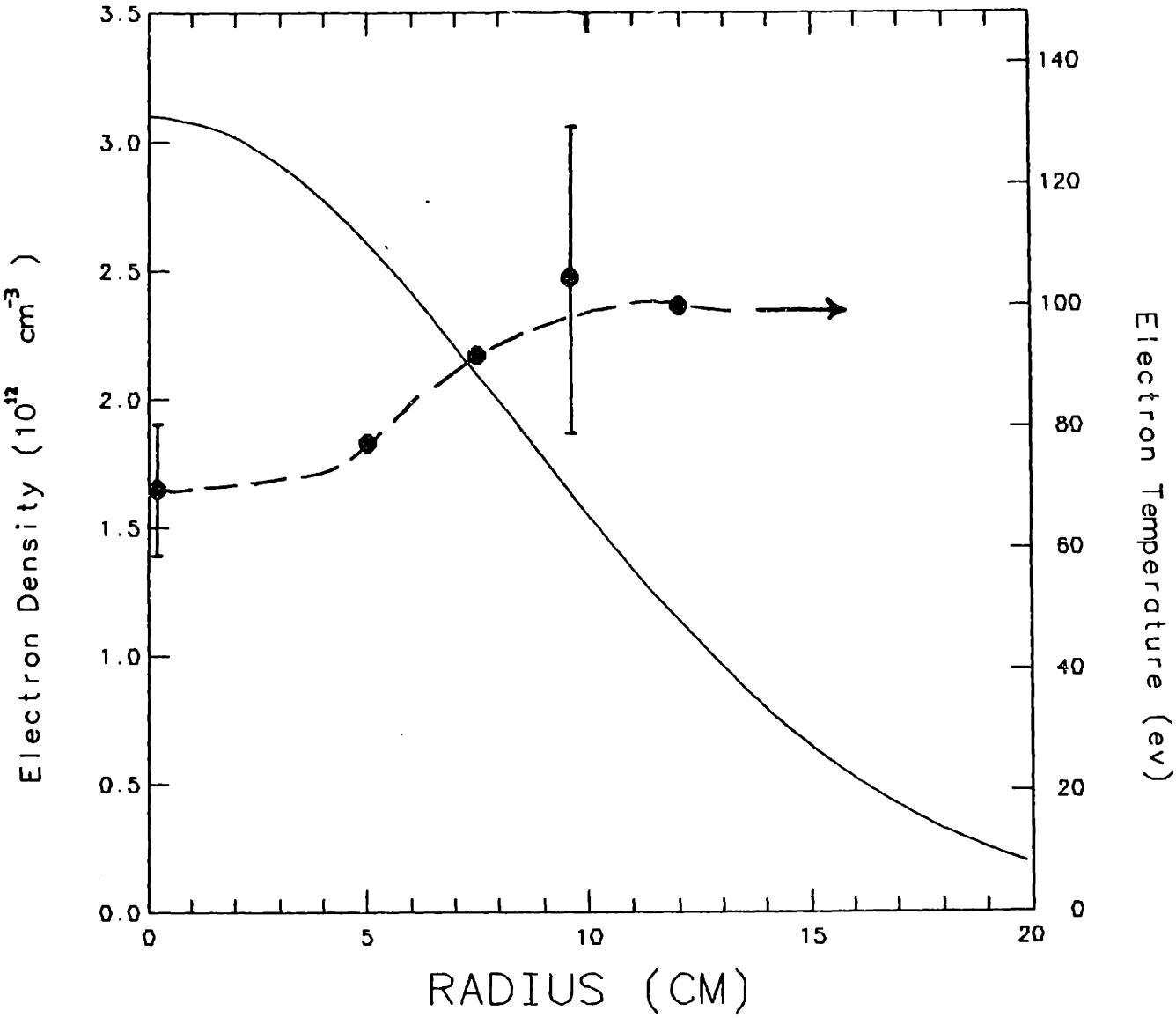

Figure 1.5: Typical electron density and electron temperature profiles.

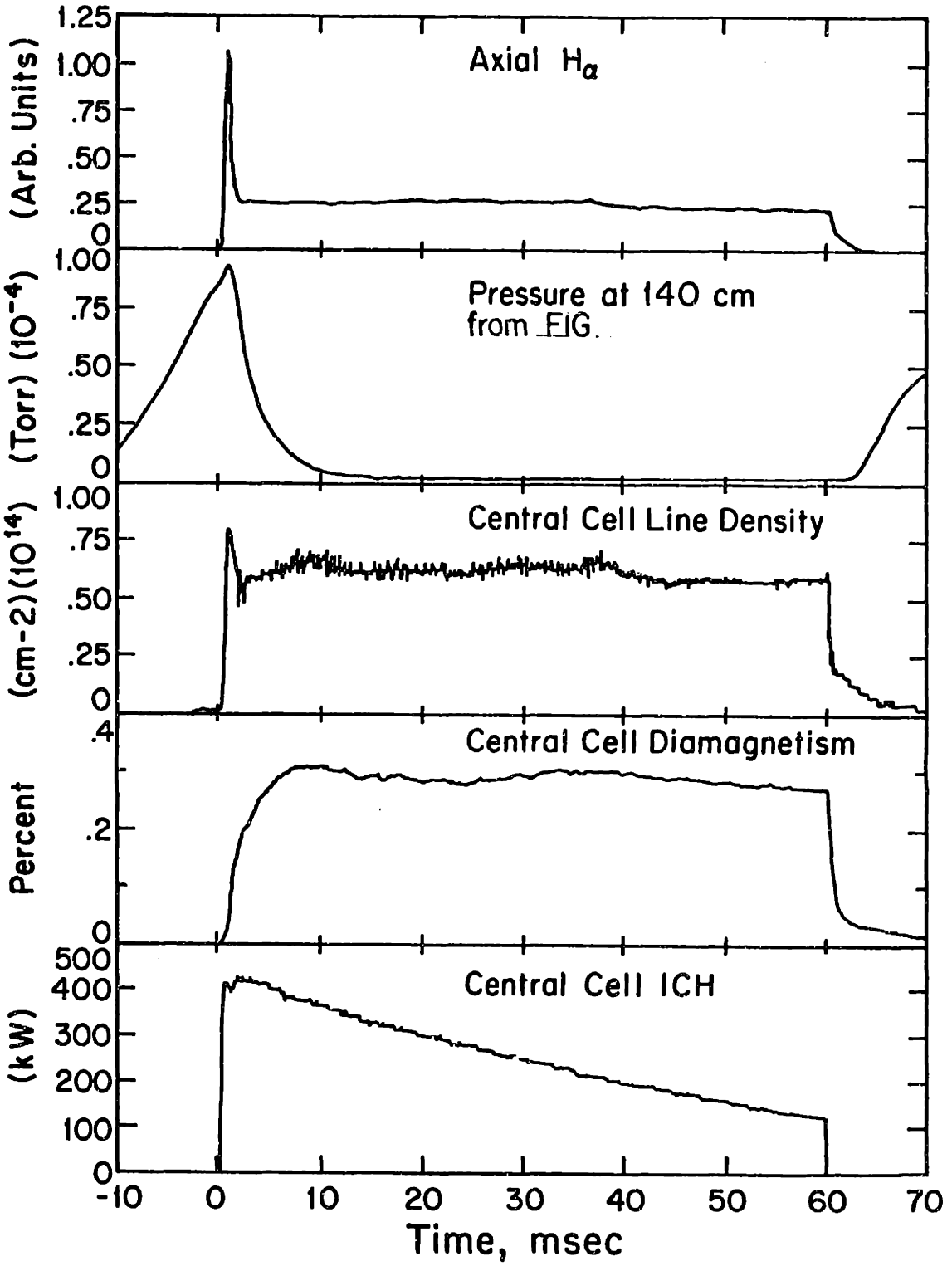

Figure 1.6: Plasma parameters versus time for a typical discharge

hydrogen emission has been used in this way to obtain fueling rates at several magnetic confinement experiments. [8,9,10]

While plasma fueling has been investigated at a few confinement experiments, there are several aspects of it which have not been well investigated. They are: 1) the dissociation processes which give rise to the product hydrogen atoms, 2) the atomic interaction with the chamber wall, 3) the molecular contribution to atomic emission, 4) the molecular contribution to ionization. This work presents a study of these aspects through an investigation of atomic hydrogen and molecular hydrogen emission from the plasma.

Since the atoms in the plasma arise from molecular dissociation, charge-exchange, and reflection from the walls, the atomic kinetic energy distribution will contain components from these different processes. Therefore, a knowledge of the atomic kinetic energy distribution is important in understanding the origins of the atoms and their interaction with the wall. The energy distribution is studied in this work through an investigation of atomic line shapes. Since the wavelengths of line radiation photons emitted by moving atoms are shifted with respect to the wavelengths of those photons emitted by atoms at rest (doppler-broadening), a high-resolution measurement of the atomic hydrogen line gives information about the atomic kinetic energy distribution, which in turn gives information about dissociation processes and wall interactions.

Molecular hydrogen emission measurements give information about the spatial distribution of molecules, their ionization/dissociation rates, and their contribution to the radiated atomic spectra through molecular dissociative excitation. Molecules may be dissociated into atoms or protons through electron collisions. As will be explained in chapter 5, the local molecular ionization rate is proportional to the local emission rate of specific molecular spectral lines. Molecules may also be dissociated into excited atoms which then radiate atomic hydrogen lines. This light may then contribute to the light collected for the atomic ionization measurement and cause an erroneous result. A measurement of specific molecular line intensities and atomic hydrogen line intensities yields the molecular contribution to the atomic light. The molecular ionization rate is proportional to the excitation rate for certain transitions. Thus, a measurement of molecular line intensities can be used to infer molecular ionization rates. The dissociation rate for break-up into ground state atoms is equivalent to the rate of emission of

'dissociative continuum' photons. Thus, a measurement of the ratio of the line to continuum intensities yields the ratio of dissociation mechanisms.

1.5 Nature of Measurements

The measurements made in this study were all spectroscopic in nature. There were six instruments assembled by the author to complete the study. They were installed at five axial locations. The instruments covered much of the vacuum ultraviolet range of the spectrum as well as the near-ultraviolet and visible range.

Atomic hydrogen line spectra in the visible were studied using instruments which ranged in resolution from .13$\mathring{A}$ to 30$\mathring{A}$. Atomic hydrogen line spectra in the vacuum ultraviolet were studied using an instrument which obtained a resolution of 6$\mathring{A}$. Radially-resolved measurements were made at two axial locations and central chord measurements were made at five axial locations.

Molecular line spectra and continuum spectra were measured at three axial locations. Radially-resolved measurements were made at one axially location and central chord measurements were made at the other locations. The measurements were made in the visible and near-ultraviolet.

Impurity ion spectra were investigated at five axial locations. The instruments used covered the visible, the near-ultraviolet, and much of the vacuum ultraviolet. Radially-resolved measurements were made at two axial locations.

1.6 Analysis

Absolute densities of atomic hydrogen and molecular hydrogen will be inferred from absolute emission measurements using the measured electron density and electron temperature profiles. In the same way, atomic and molecular ionization rates will be inferred. The atomic kinetic energy distribution will be obtained through analysis of a highly resolved atomic spectral line profile. The results will be compared with a model in order to gain information about the atom-wall interaction.

The absolute impurity emission measurements will be used to infer impurity concentrations as well as impurity temperatures and drifts.

1.7 Organization of Thesis

The body of the thesis is organised into five chapters. Chapter 2 contains a description of the instruments and their calibrations. Chapter 3 presents the impurity spectra measurements as well as the analysis of those data. Chapter 4 presents the atomic hydrogen spectra measurements. Chapter 5 presents the molecular hydrogen measurements, as well as the theory of molecular hydrogen spectra and dissociation. The analysis of the atomic and molecular results is contained in chapter 6, which also contains a comparison of those results with a model. Conclusions and suggestions for future work are contained in chapter 7.

Chapter 2

Experimental Apparatus

2.1 Introduction

Six instruments were assembled for this work in order to investigate the visible and ultraviolet light emitted by the Tara plasma. The purpose of this chapter is to describe these instruments and their calibrations. Other light detection methods not described here were also used to measure light emitted from the Tara plasma. They are single wavelength bandpass photodiodes and a video camera, and were not specifically installed for this study.

Section 2.2 will describe the vacuum ultraviolet (vuv) spectrometer system, including the photon counting channeltron detector. Section 2.3 will describe the visible grating systems, with which the medium resolution measurements were made, and section 2.4 will describe the Fabry- Perot Interferometer system, with which the high resolution measurements were made. Section 2.4 will describe the single chord Balmer-alpha detector which was operating for all of the experiments reported in this study.

2.2 Vacuum Ultraviolet Spectrometer System

The vuv spectrometer is used to measure emission above $400\mathring{A}$ below $2000\mathring{A}$ in wavelength. This wavelength region is important since many resonance lines (lines resulting from ground state excitation) of the plasma impurities as well as resonance lines of atomic and molecular hydrogen are in this range. Measurement of the intensities of these transitions gives a measure of the concentrations of the radiating species. These measurements are more difficult then measurements in

the visible since photons with wavelengths below 2000$\AA$ will not pass through air at atmospheric pressure and radiation below 1100$\AA$ and above 400$\AA$ will not pass through any solid material thick enough to support atmospheric pressure.

The instrument is a Minuteman Model 302-VM spectrometer. It has a 0.2 meter focal length and a Jobin-Yvon aberration-corrected concave holographic grating, which is the extent of the focussing optics. The optical system is known as 'quasi-normal incidence'. The angle between the entrance and exit beams is 62 degrees. A rotation of the grating changes the wavelength of the radiation at the exit slit. The instrument has a maximum aperture of f/4.5, however the aperture in practice was f/6, which was determined by a 1 cm by 4 cm mask welded to the end of 5 cm diameter pipe inside the vacuum connection bellows. It has a minimum resolution of 1$\AA$ with a slit width of 10 μm and slit height of 4 mm at a wavelength of 1000$\AA$. In practice the resolution was approximately 6.5$\AA$ at a slit width of 60 μm and slit height of 5 mm.

The detector used was a Galileo Model 4800 channeltron. This device consists of a tapered curved glass tube approximately 5 cm long, coated on the inside with a low-resistance semiconducting material and mounted to a ceramic holder. There are three electrical leads connected to the half- inch wide mouth, the electron collector, and the ground strap. A schematic diagram of the device and accompanying electronics is shown in figure 2.1. The mouth electrode is set at negative 3000 volts, the ground strap is connected to system ground and the collector is connected to the input of an Amtek PAD (pulse-amplifier-discriminator). Photons of sufficient energy entering the mouth will knock electrons from the coated surface. The voltage drop across the tube creates a field which pulls electrons toward the back. The electrons collide with the wall and secondary electrons are emitted. These electrons are pulled further down the tube where they knock off more electrons. Thus, one photo-electron at the front can produce a pulse of many electrons at the collector. For this model channeltron, the multiplication can be as high as 10^8.

This pulse of electrons, which has a temporal width of less than a nanosecond, is sent to the input of the PAD. If the charge content is greater than a set value, the PAD produces a TTL pulse out, with a rise-time of 50 nanoseconds, a width of about 300 nanoseconds at a fall-time of 50 nanoseconds. nanoseconds. The TTL pulse is sent to an emitter-follower transistor circuit which has an output

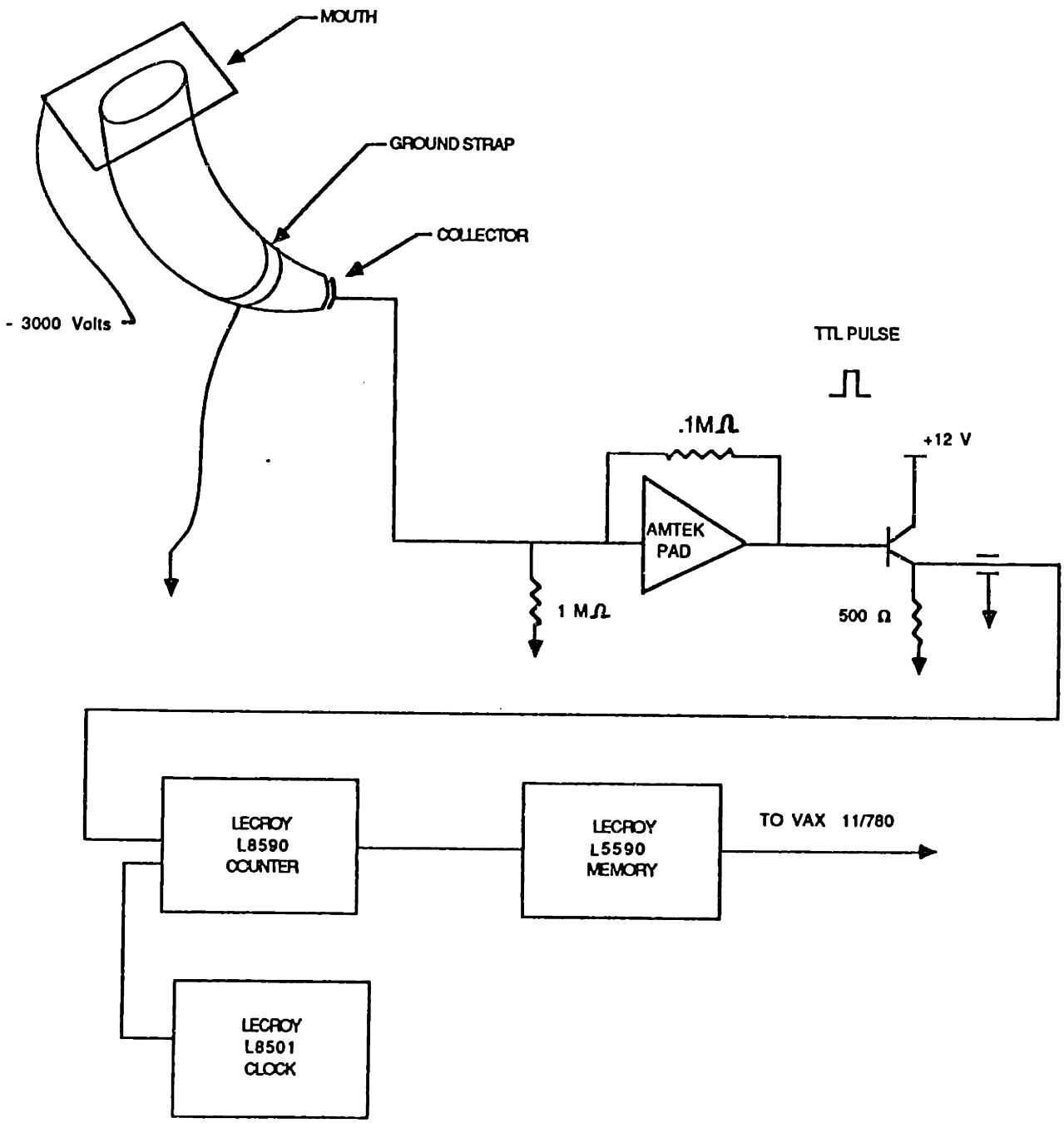

Figure 2.1: Schematic of the vuv channeltron detection system.

impedance of 50 ohms, in order to send the pulses along the 8 meter coaxial cable to the Lecroy Model L8590 counter located in the shielded equipment racks. The counter counts all the TTL pulses in a time interval set by a Lecroy L8501 clock. The counting times were typically one or two milliseconds. The output of the counter is taken into the VAX 11/780 computer via the Camac data acquisition system where it is stored in the common data base.

Since photons in the vuv range will not pass through air at atmospheric pressure, the entire instrument must be maintained at a low pressure, below 10^{-4} torr, and it must have vacuum connection to the Tara vacuum chamber. Figure 2.2 shows a schematic diagram of the vuv instrument and mounting hardware, as well as the visible spectrometer scanning system at the same axial location, which is 380 cm. north of the Tara center. The instrument is supported by a mount made of 1.3 cm by 2.54 cm stainless steel bars. The front of the instrument is vacuum connected to an adapter piece, which connects to a VAT vacuum valve, which is vacuum connected to a flange welded to the end of a 12 cm diameter flexible vacuum bellows. The mount is supported at the machine end by two 1.3 cm bearing bronze pins which allow the instrument to rotate about an axis parallel to the central cell vacuum chamber and located at the machine side of the vacuum bellows. The back end of the mount is supported by a .5 cm stainless steel cable which is connected by brass pulleys to a hand cranked ratchet winch. Cranking the winch changes the height of the back of the mount which allows the instrument to view different radial chords of the plasma column. An inclinometer attached to the mount shows the angle from horizontal to within .5 degrees, which corresponds to a .6 cm difference at the center of the plasma. The spatial resolution of the instrument was determined by the above mentioned aperture and was 1.5 cm. at the plasma center. A Varian Model 911-5005 eight liter per second ion pump was connected to the pump-out flange of the spectrometer in order to measure and maintain a low pressure, which was typically at 1.1×10^{-6} torr.

The instrument was taken to Johns Hopkin's University to be absolutely calibrated. This involved illuminating a grating with radiation from a hollow cathode lamp and selecting a spectral line with a wavelength in the range of the spectrometer, illuminating the spectrometer with that line radiation, and measuring the count rate. This was followed by illuminating a calibrated photodiode with the same line radiation and measuring the photon flux. The photodiode had been

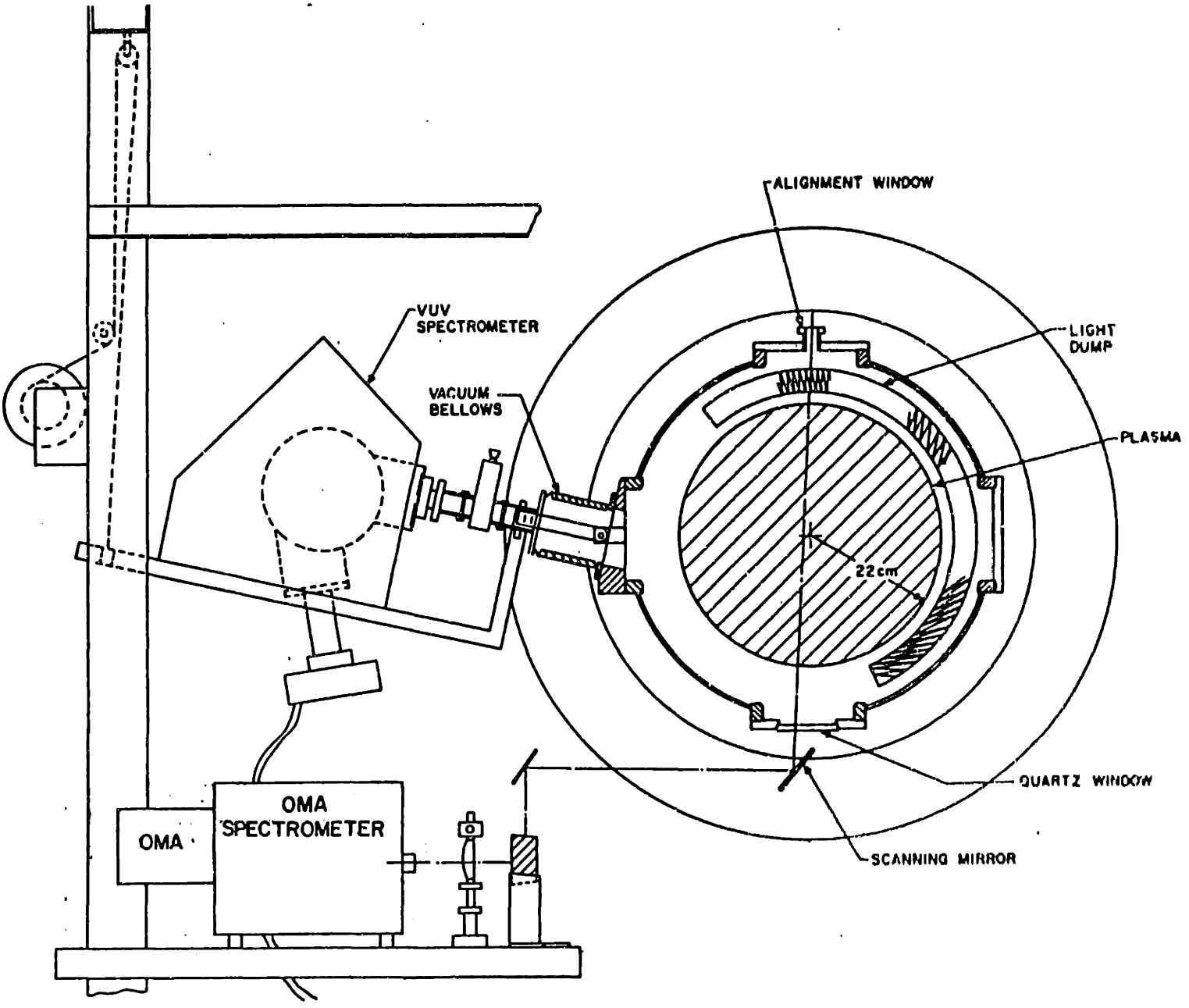

Figure 2.2: Schematic of the vuv spectrometer scanning system and visible spectrometer scanning system at z = 350 cm.

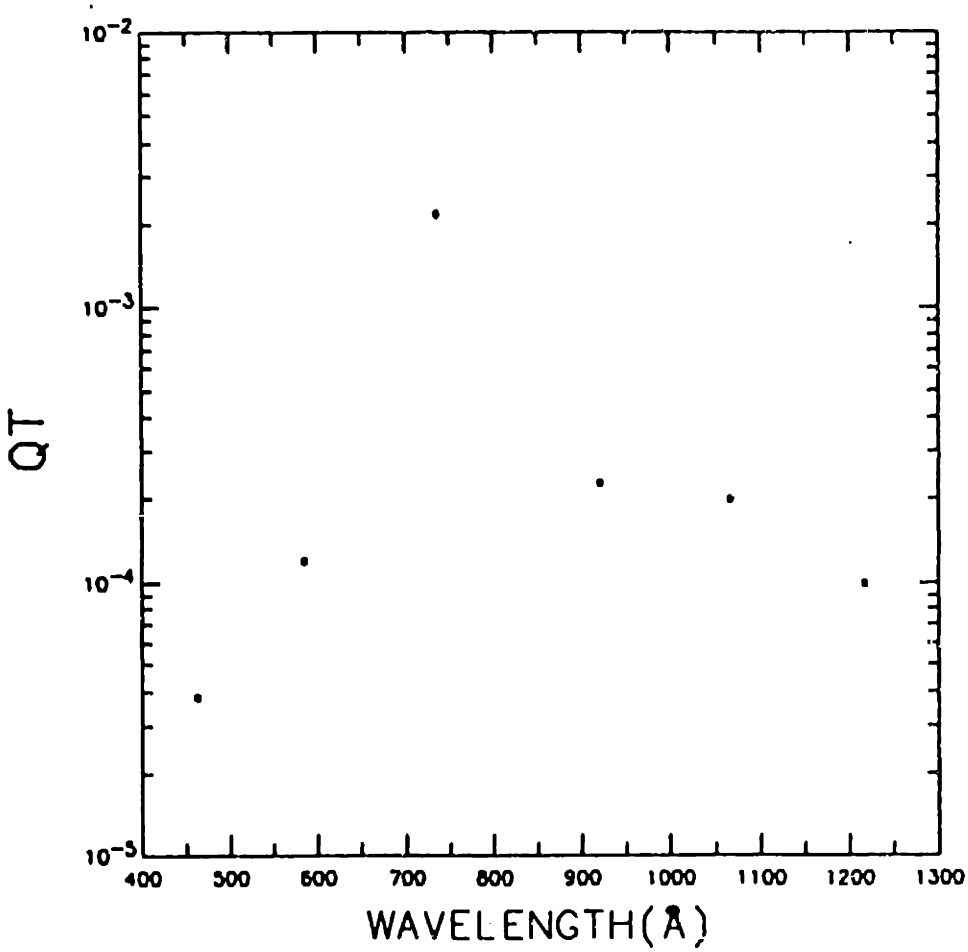

Figure 2.3: Vuv spectrometer calibration

absolutely calibrated at the National Bureau of Standards. This was done several times at six different wavelengths over the instruments range. The ratio of the count rate at a particular wavelength to the absolute photon flux as measured by the diode gives the product of the quantum efficiency of the detector Q and the spectrometer throughput T at that wavelength. A curve of QT is shown in figure 2.3. The accuracy of the standard photodiode is 5%. The variation between calibration results was 12%. The dark count rate of the channeltron is approximately one count per minute. Therefore the total instrumental uncertainty at the calibration wavelengths is determined by the calibration uncertainties and is 13%. At wavelengths between the calibration wavelengths QT is found by interpolation which introduces errors of as much as 100%. There is additional uncertainty due to statistical photon fluctuations. This uncertainty is equal to $1/\sqrt{N}$ where N is

the number of photons counted in the measurement. A typical N measured in the impurity measurements is 500, giving a photon noise of 4%.

The radiated brightness at a particular wavelength is obtained by measuring the number of counts N in an integration time t and dividing by the product of the quantum efficiency QT, the slit area A, and the collection solid angle Ω.

$$B = \frac{(N/t)}{QT\Omega A} \tag{2.1}$$

2.3 Visible Light Grating Spectrometer Systems

The visible grating instruments used were sensitive to radiation from 2000$\AA$ to 7000$\AA$, depending on the window materials and detectors used. Measurements in this wavelength range are much easier than those made in the vuv range, since no vacuum is required. There were three visible light grating instruments used: a film spectrograph, an Oriel Ebert-mounted single channel spectrometer, and an ISA Czerny-Turner-mounted spectrometer equipped with a Princeton Instruments optical-multichannel-analyzer (oma) and optional single channel detector. The first time-resolving measurements were made with the Oriel instrument. Some of those measurements were later duplicated using the ISA instrument and data which had taken dozens of plasma discharges to obtain with the Oriel spectrometer was obtained in one discharge.

The film spectrograph used was a Jarrell-Ash 1.5 meter Wadsworth-mounted instrument. It has a range of 4200$\AA$ to 9700$\AA$ in first order, and 3800$\AA$ to 4850$\AA$ in second order, with the lower limit determined by the glass lens and glass window used. A schematic of the instrument installed on the Tara experiment is shown in figure 2.4. A focussing lens with a 10 cm diameter and 53 cm focal length was used to collect the light exiting the Tara chamber through a 4 cm diameter window. The instrument has an f/20 aperture, which was filled by the input light cone. The spectrometer was aligned using a Helium-Neon laser beam directed into the alignment window and out the center of the collection window at the bottom of the chamber. A mirror is used to send the beam into the input slit of the spectrograph. The spectrograph is adjusted so that the beam hits the center of its collimating mirror and the center of its grating. This alignment is done first without the lens, then with the lens. The beam then passes through the focal plane of the instrument.

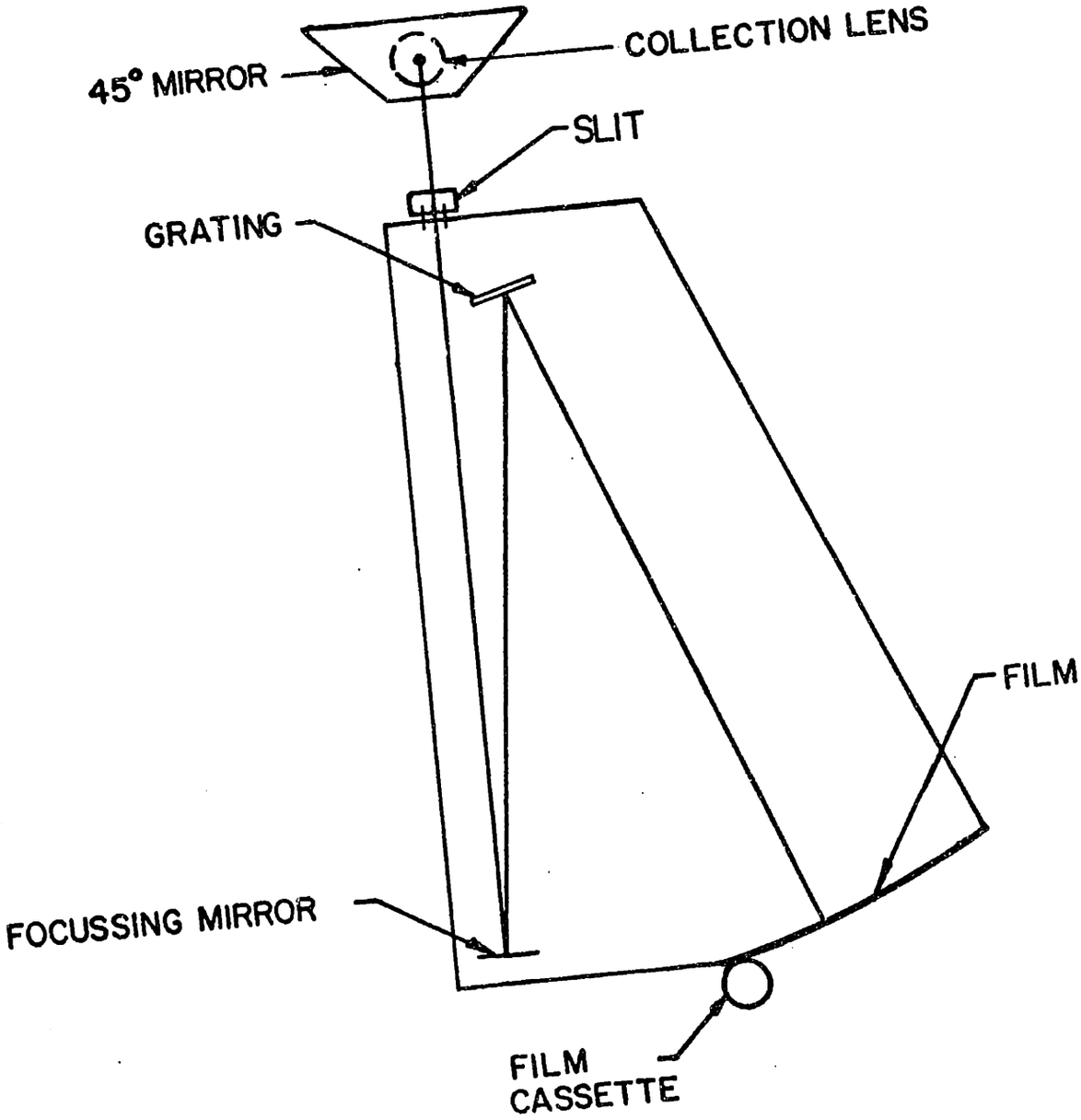

Figure 2.4: Schematic of the Wadsworth film spectrograph installed on the Tara device.

The film used was Kodak 35 mm recording film number 2475, the most sensitive available film in the visible range. The film was not intensity-calibrated, since the measurements were only used for line radiation identification. The spectra on the film was transferred to a paper record using a micro-densitometer. A test of film density vs. illumination time with a discharge lamp showed the response to be linear over the lower 60% of the density range.

The visible scanning system, installed at the z = 350 cm location, is shown in figure 2.2. Visible measurements were also made at the gas port(z = 0 cm), at z = 30 cm and z = 110 cm. The measurements made at the gas port and at z = 30 cm were single chord measurements made through 4 cm diameter quartz windows mounted on the bottom of the chamber. The measurements made at z = 110 cm were made through a 10 cm by 30 cm window installed for the purpose of measuring spectral line doppler shifts caused by plasma rotation.

The light collection system used four mirrors which rotated the image of the spectrometer slit at the plasma 90 degrees in order to view a chord which had a small radial extent, less than .5 cm. The radial chordal resolution is then determined by the collection solid angle, and was typically 1.5 cm., while the axial resolution was 5 cm. The system was aligned by directing a HeNe laser beam down through the alignment window so it hit the rotatable scanning mirror at the rotation axis, and then strikes the center of the other mirrors and the input slit. This was done first without the lens, and then with the lens.

There was a light dump installed behind the section of the column viewed by the visible system constructed of rolled aluminum channel, housing folded .13 mm thick stainless steel shim. The dump is shown in the cross-sectional geometry in figure 2.2. In practice the shim becomes coated with titanium from the getters and becomes less reflective. Light entering a fold makes several reflections, with some absorbtion on each reflection. Therefore the dump absorbs most of the incident light. In order to test the dump, chordal brightness measurements were made of the tenuous, steady-state plasma used in discharge cleaning. The emission profile inferred from the measurements was uniform to within 10 percent, which is consistent with an unmagnetized, tenuous plasma.

A top view of the ISA instrument, which will be called the 'oma spectrometer', alongside the Tara chamber, is shown in figure 2.5. A 125 mm focal length lens images the plasma column onto the slit. The grating used has 2400 lines/mm.

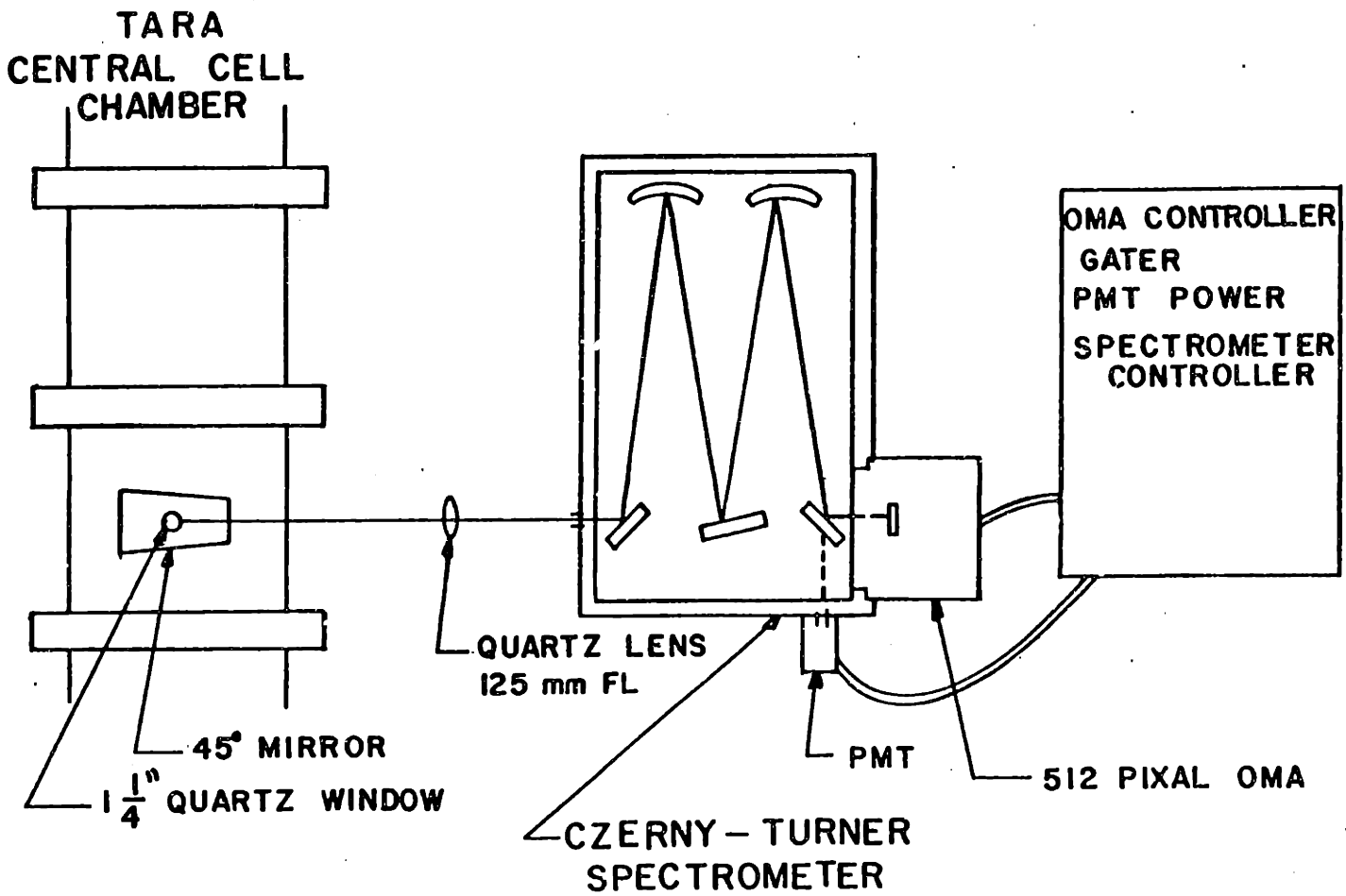

Figure 2.5: Schematic of the oma spectrometer and detector controls mounted alongside the Tara central cell chamber.

and is 10 cm. by 10 cm. The f/number is 4.7. A mirror on the output side of the instrument selects either the single channel detector or the oma. The single detector is an R928 Hamamatsu photomultiplier(pmt) which has an extended wavelength response cathode. It is housed in a nickel-plated magnetic steel box which has a minimum thickness of .25 inches in order to shield it from magnetic fields. There is a 1 mm. thick mu-metal shield inside the steel box for further shielding. To test the effect of the magnetic field a lamp was placed at the entrance slit and the output of the pmt was measured before and during the field pulse. The output was found to be the same, therefore the field had a negligible effect on the pmt. According to manufacturer's specifications, its sensitivity varies less than a factor of 2 over the range used. The voltage applied to the divider chain of the pmt varied between 500 volts and 1000 volts. The output of the pmt is sent to the camac digitizer which stores the data to be accessed by the VAX 11/780. The data was digitized at 100 khz. The selection mirror and the grating drive are controlled by the spectrometer controller, which receives commands from the VAX 11/780.

The oma consists of a 512 pixel diode array at the output end of a 512 pixel linear light intensifier array. The light intensifier has a gatable cathode in front of an array of coated channels, which have a 5000 volt potential between the entrance and exit. Light hitting the cathode ejects a photo-electron with an efficiency of between 1 and 10 percent in the near-uv and visible range. The electron collides with the wall of the tube, creating secondary electrons, which liberate more electrons farther down the tube. The pulse of electrons impinges on a phosphor screen at the back of the tube which causes a pulse of visible wavelength photons to be emitted. The charge generated by pulses of photons at the diodes is measured by the controller which converts the amount of charge to a number. One 'count' roughly equals one photon detected. The controller stores the number of 'counts' for each diode in its memory. The oma controller and the detector head gate are controlled by the VAX which sends a trigger to gate the detector on and sends the commands to prepare the system to take detect radiation. After the data is taken, it is stored in a Camac memory module and then accessed by the VAX.

The diodes are 2 mm in height and 25 μm in width. Since light diverges in the intensifier, the full-width-half-maximum(fwhm) of an arbitrarily narrow line

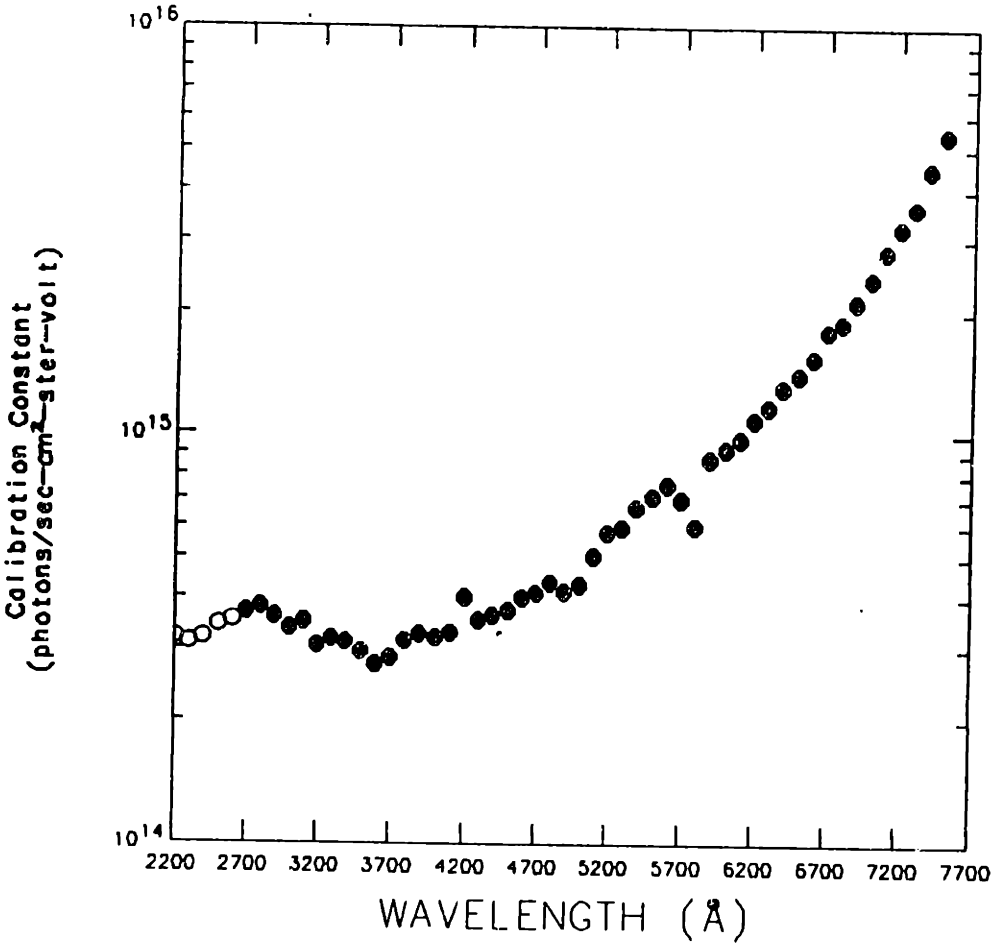

Figure 2.6: Calibration of oma spectrometer in pmt mode.

is four pixels. The best resolution that can be obtained at a wavelength of 6563$\AA$ is .6$\AA$. The best resolution obtainable varies with wavelength since the angular dispersion of the grating varies with wavelength. The smallest fwhm is obtained at the longest wavelengths.

The instrument was absolutely calibrated in the pmt detector mode over its whole wavelength range using an Optronics tungsten ribbon lamp. The same lamp was used to relatively calibrated the spectrometer in the oma mode between 4000$\AA$ and 5000$\AA$. The lamp was absolutely calibrated at the National Bureau of Standards. Order-sorting filters were used to block second order light. Figures 2.6 and 2.7 show the calibration curves for the pmt mode and oma mode respectively.

In operation the calibration coefficient is multiplied by the measured voltage on the pmt to obtain the measured brightness. If the slit area used in data col-

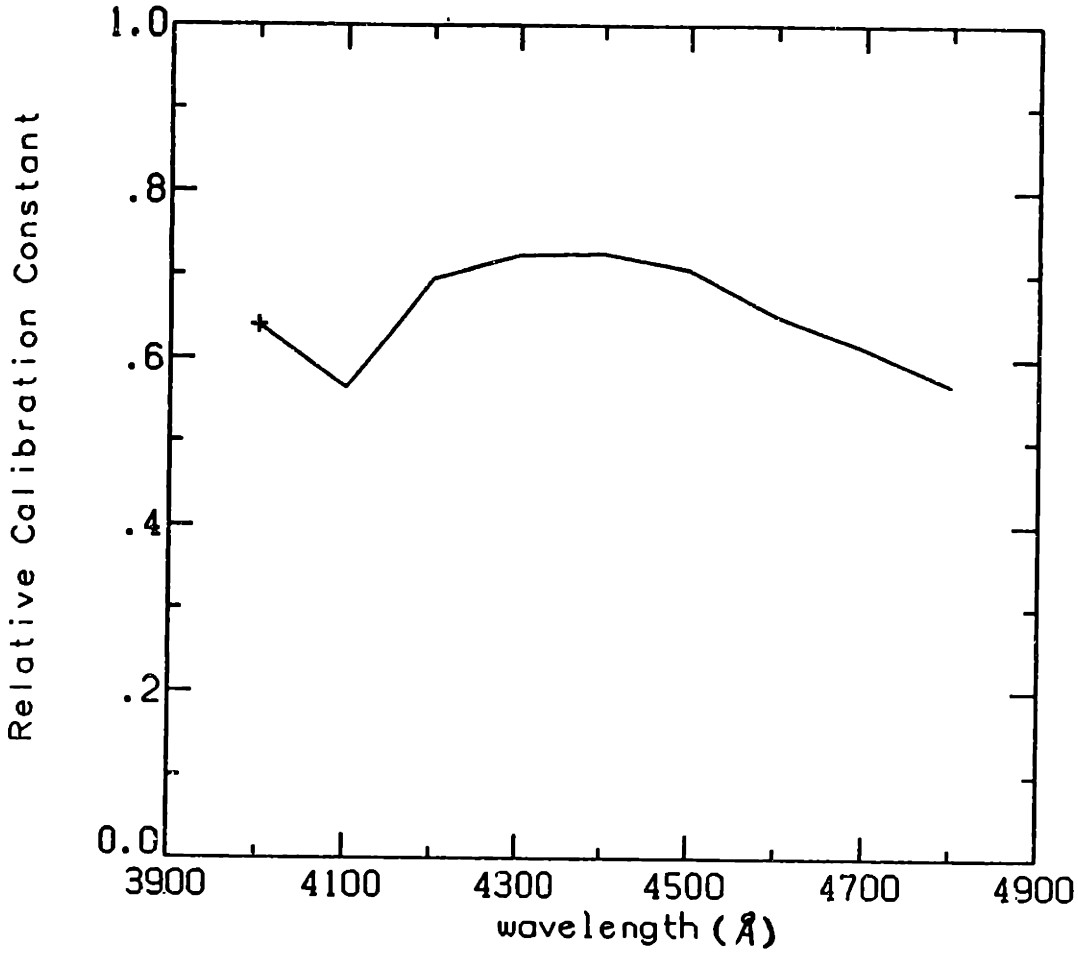

Figure 2.7: Relative calibration of oma spectrometer in multidetector mode.

lection is different from that used in the calibration, the calibration coefficient is multiplied by the area ratio. The spectrometer/pmt system was calibrated while by the author. The spectrometer/oma system was calibrated by another group member, Paul Stek. The spectrometer/pmt calibration curve includes values at wavelengths for which the tungsten lamp intensity was to low to use for a calibration(below 2700Å). For those wavelengths the calibration is estimated based on the manufacturer's specifications of the transmission of the quartz window and quartz lens, the grating transmission versus wavelength, and the efficiency vs. wavelength curve for the pmt used.

The Oriel spectrometer is a 10 cm focal length Ebert-mounted instrument. It also has an R-928 photomultiplier mounted at the exit slit and is housed and shielded in the same manner as the pmt on the ISA instrument. It was absolutely

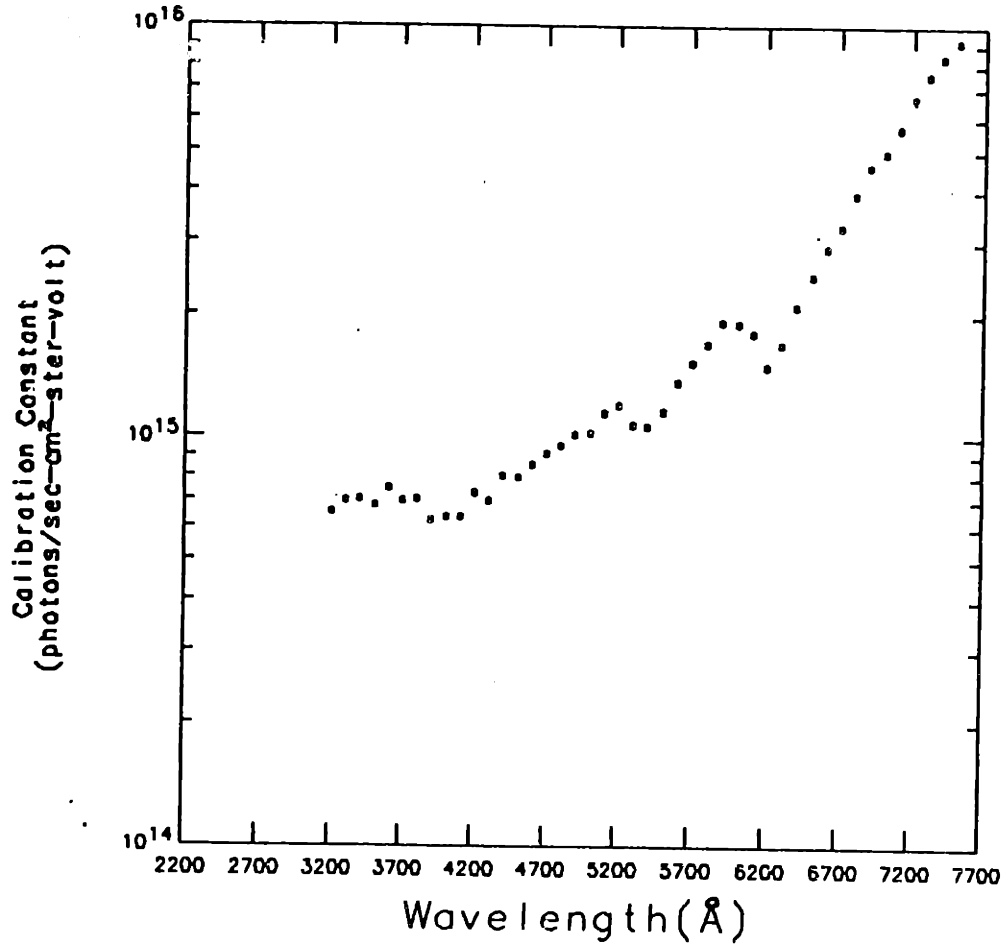

Figure 2.8: Calibration of Oriel spectrometer

calibrated with the same tungsten ribbon lamp which was used to calibrate the ISA instrument. The calibration curve is shown in figure 2.8. It was used with the same quartz lens. It has a minimum fwhm of 5Å in first order and so was only used for low resolution applications.

The absolute uncertainty of the NBS calibrated lamp is 10%. The relative uncertainty (variation of uncertainty with wavelength) of the lamp is $3-5\%$. The pmt calibrations were performed twice and a 4% average variation in calibration number was observed. The absolute spectrometer/pmt instrumental uncertainty is therefore 11%. The relative instrumental uncertainty is due to the relative uncertainty of the lamp. The primary pmt-spectrometer measurement noise is electrical. The oma-spectrometer was not used for absolute intensity measurements. The relative calibration uncertainty is $3-5\%$. Statistical photon noise

Spectrometer	Wavelength Range	Detector
Vuv	$500\mathring{A} - 1250\mathring{A}$	Channeltron
Oriel	$2000\mathring{A} - 7700\mathring{A}$	Pmt
Oma	$2000\mathring{A} - 7500\mathring{A}$	Oma & Pmt
Spectrograph	$4200\mathring{A} - 7500\mathring{A}$	Film

Table 2.1: Spectrometer inventory.

varied from $.3 - 3\%$ for central chord measurements.

A list of the spectrometers, their wavelength ranges, and detectors is contained in table 2.3.

2.4 Visible Fabry-Perot Interferometer System

The grating spectrometers used are ideal for measuring wavelength distributions to resolutions greater than $.2\mathring{A}$. However, this work required the capability to measure the Balmer-alpha line profile under high-resolution, ie. with a fwhm equal to $.13\mathring{A}$. , which is less than 1/50,000 of the length of the central wavelength, $6562.8\mathring{A}$. For that purpose, a Fabry-Perot interferometer was used.

The interferometer used was a Burleigh RC-110 which has a 50 mm aperture and a cavity spacing adjustable from 0-150 mm. It is constructed of super- invar which has high thermal stability. A schematic diagram of the interferometer and alignment set-up is shown in figure 2.9.

In operation, parallel or near parallel light passes through a partially transmitting mirror into a cavity formed by that mirror and a second mirror partially transmitting mirror. The light makes multiple reflections between the two mirrors. The transmission function will be maximum for a particular wavelength when the spacing between the mirrors, d, equals an integral number of wavelengths.

$$d = n\lambda \tag{2.2}$$

A monochromatic source will produce a series of intensity peaks at the pinhole aperture as the distance between the plates is varied. The different peaks represent different orders of interference. The width of the peaks w,is determined by the instrumental finesse F,through the relation

$$w = \frac{FSR}{F} \tag{2.3}$$

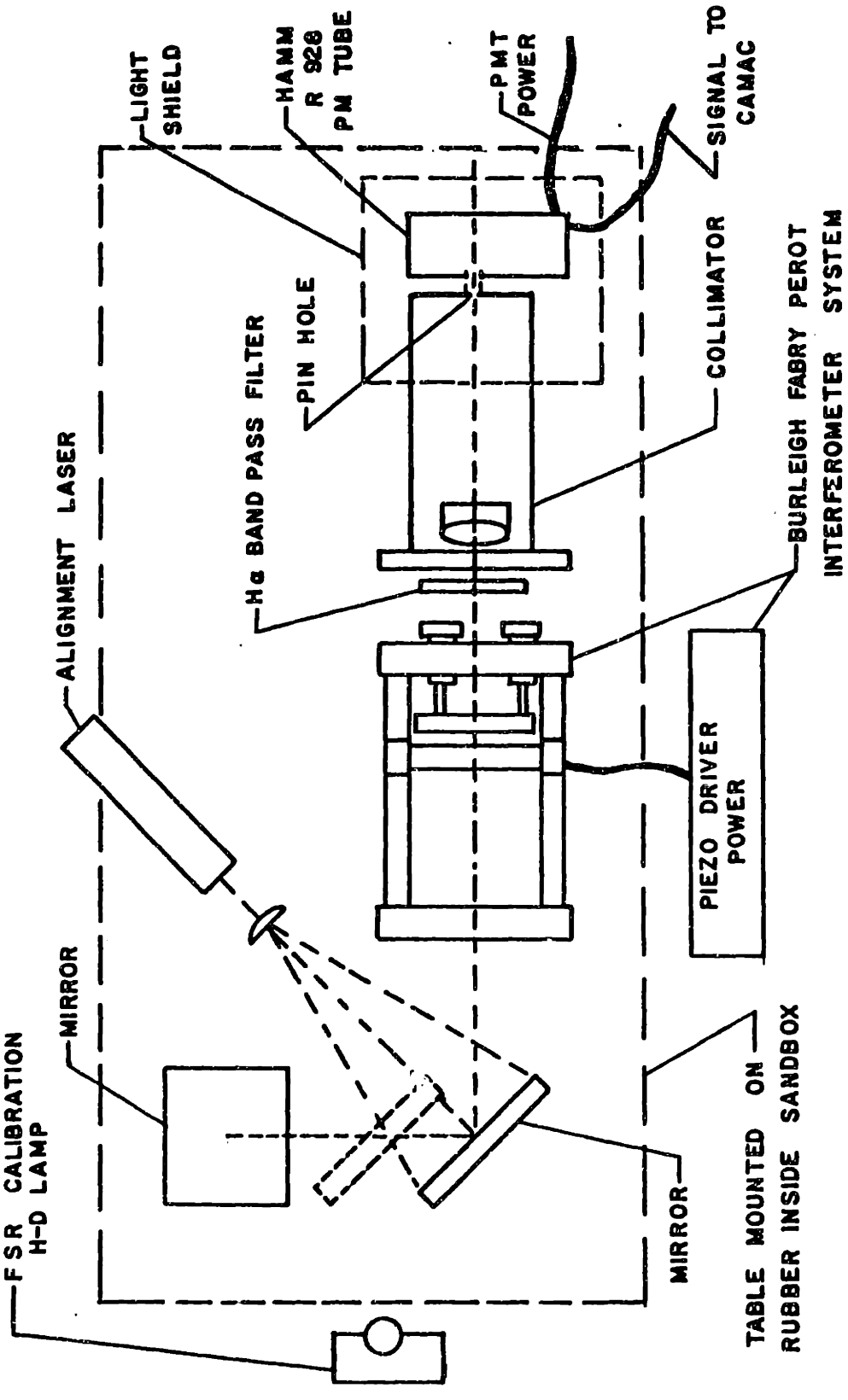

Figure 2.9: Schematic of the Fabry-Perot interferometer, the alignment optics, and calibration optics

where FSR is the free spectral range, or wavelength separation between orders. The instrumental finesse is a function of the plate reflectivity finesse F_r , a function of the reflectivity, the plate flatness finesse F_f, a function of the flatness, and the pinhole finesse F_p, a function of the pinhole diameter D_p, the plate spacing d, the distance from the collimating lens to the pinhole, L, and the wavelength λ.

$$\frac{1}{F^2} = \frac{1}{F_r^2} + \frac{1}{F_f^2} + \frac{1}{F_p^2} \tag{2.4}$$

The reflectivity finesse was 100 and the flatness finesse was 200 according to the manufacturer's specifications. In the measurements presented, the instrumental finesse was determined almost entirely by the pinhole finesse.

$$F_p = \frac{4\lambda L^2}{D_p^2 d} \tag{2.5}$$

The FSR is a function of the wavelength λ and plate spacing d.

$$FSR = \frac{\lambda^2}{2d} \tag{2.6}$$

In practice the FSR varied between 3.6$\AA$ and 21$\AA$, the instrumental finesse varied between 60 and 100, the plate spacing varied between 75μm and 600μm, and the fwhm varied between .05$\AA$ and 1$\AA$. In operation, resolution was degraded by vibrations of the instrument. This will be discussed in chapter 4.

The plate spacing is varied linearly in time by three separate piezo-electric drivers on each of the mirrors, capable of moving one mirror 1.5 μm. Therefore, time corresponds to wavelength. The time to scan the spectral line varied from 3 milliseconds to 20 milliseconds. To ensure that only near parallel light is seen by the detector, a 25 cm long collimator is placed behind the interferometer. The pinhole size used was 2 mm, which solely determined the finesse in some cases. Optical bandpass filters were installed between the collimator and the interferometer to select out only the Balmer-alpha line. A filter with a 10$\AA$ fwhm centered at the Balmer-alpha wavelength was used in studies of the line center and a 40$\AA$ fwhm filter was used in studies of the far wings.

The detector used is an R-928 Hamamatsu pmt identical to the one used in the ISA spectrometer and has also the identical magnetic shielding housing. It is located directly behind the collimator pinhole.There is a light gasket between the collimator and pmt housing as well as a light shield over the collimator and

housing. The pmt output is sent to a Tektronix model 551 differential amplifier and then to a 100 khz digitizer. It is taken into the VAX through the Camac system and stored in the data base. In addition, the piezo driver monitor signal, which is the piezo driver voltage divided by 100, is sent to a 5 khz digitizer and also stored.

Because of the vibrations of the deck on both sides of the Tara chamber, the interferometer was set up on the floor of the cell. The instrument rested on an aluminum table which rested in a box filled with 4 inches of sand. The box rested on 2 inches of rubber. The sand and rubber helped to decrease the vibration of the instrument, but the vibration was never eliminated entirely. Much of the data shows the effect of the vibration as fluctuations on the line profile. The instrument viewed light coming from the window and scanning mirror at z = 380 cm location. Therefore it is able to measure light along different radial chords.

The instrument is aligned is three steps. First the interferometer alone is aligned, then the interferometer, collimator, and mirrors are aligned, and finally the interferometer and collimator are given a fine adjustment. In the first step, the plates are made parallel to within a HeNe laser wavelength by dispersing a HeNe laser beam onto a white card in front of the interferometer and viewing through the back of the interferometer the interference pattern produced at the output side of the instrument. The mirror knobs are then adjusted so that the circular fringe pattern stays constant as the eye is moved parallel to the mirror surface. Secondly, a beam is directed from the alignment window to align all the optical path mirrors and the collimator. Thirdly, the beam is expanded again on a card in front of the interferometer and the wavelength distribution of the HeNe line is measured. The piezo driver bias voltages are then altered so that the maximum finesse is achieved.

The resolution is determined by measuring the instrumental width of the HeNe laser line, which has an actual width of less than .005$\AA$. The time-to wavelength calibration is determined by illuminating the instrument with an H-D lamp. The Balmer-alpha and Deuterium-alpha lines are separated by 1.76$\AA$. The time separation between the two lines then corresponds to a wavelength separation of 1.76$\AA$.

2.5 Balmer-alpha Central Chord Photodiode

A photodiode-filter assembly was constructed in order to measure the relative central chord Balmer-alpha emission at a location 30 cm north of the $z = 350$ cm spectrometer installation. A schematic diagram of the detector is shown in figure 2.10. It contains a UDT model 555 PIN diode with a 1.3 square centimeter sensitive area. An op-amp is contained in the diode housing. The op-amp circuit obtained a current-to-voltage conversion of 10^5. A $100\mathring{A}$ fwhm bandpass filter centered at $6563\mathring{A}$, the Balmer-alpha wavelength, was fixed in front of the diode. The signal was sent to a 5 khz digitizer in the Camac racks and then stored in the VAX database. The detector was operating for all of measurements presented in this study.

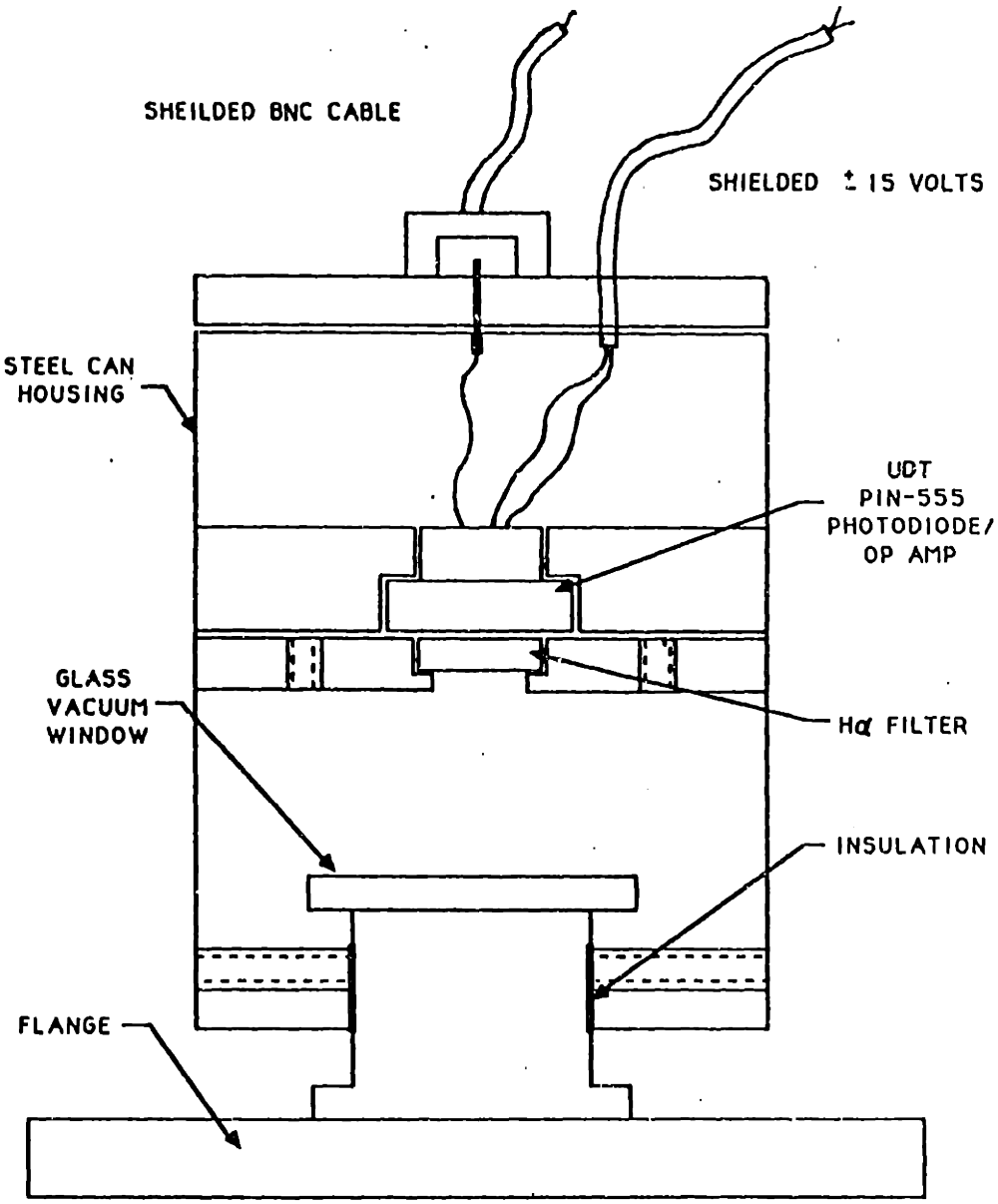

Figure 2.10: Schematic of the central cord Balmer-alpha detector.

Chapter 3

Impurity Emission Measurements

3.1 Introduction

This chapter describes the investigation of the impurity radiation emitted from the Tara central cell plasma. The purpose of these measurements was to obtain the impurity concentrations, estimate the power lost to impurity radiation and ionization, determine the impurity ion temperature and measure impurity drift velocities. Section 3.2 presents absolute impurity spectra measurements and the estimated power lost to impurity processes. Section 3.3 presents the impurity doppler broadening and impurity drift measurements.

3.2 Intensity Measurements of Impurity Spectra

3.2.1 Impurity Spectrum Survey

While the majority of the plasma ions in the central cell plasma are protons, there are impurity ions present, as there are in all confined plasmas. These particles originate at the wall of the chamber and the limiters, and are brought into the plasma by bombardment of those surfaces by plasma particles or neutral atoms, or are contaminants of the hydrogen gas injected to create the plasma. As they enter the plasma, these impurities are dissociated through electron collisions. The product atoms may then be ionized through electron collisions. Once in the plasma, these ions can be ionized further, losing more electrons. The impurity ions then radiate energy from the plasma through collisional excitation.

Impurity ions were studied using the Oriel visible monochromator, the oma spectrometer, the Wadsworth film spectrograph, and the vuv monochromator. The first attempt to identify the impurities present was made with the film spectrograph. A film spectrum of the plasma light was made at a z location of 290 cm. The wavelength range was 4200 $\AA$ to 7500 $\AA$. Second order light was excluded by the glass lens. Three radiating species were identified : atomic hydrogen, carbon III(doubly ionized carbon) and oxygen II(singly ionized oxygen). Impurity lines were identified using ref. [11]. All impurity lines identified belonged to strong multiplets, and in the case of sufficient resolution all lines in the multiplet were observed. All of the impurity lines present on the film spectrum had wavelengths in the region between 4630 $\AA$ and 4660 $\AA$. This region was later studied in detail with the oma spectrometer.

The next attempt to study impurity radiation was made with the vuv monochromator. A shot-by-shot scan of the usable range of the instrument was made consisting of 260 shots. The resolution of the measurements was 6.5 $\AA$ and step size varied between 2 $\AA$ and 4 $\AA$, with the smaller size used when approaching the center of a line. The instrument viewed a chord through the plasma with a 6 cm impact parameter, and below the machine center. The clock was set for a two millisecond counting time. The absolute calibration was used to obtain the radiated brightnesses of the lines. Owing to shot-by-shot nature of the scan, the plasma conditions varied over the range of the scan. The line-average electron density was monitored and was seen to vary 15 percent about its mean. There was no electron temperature monitor at this time. The ratios between ionization states is highly temperature dependent, and the more highly ionized states were seen to vary more widely during a discharge and from day to day. The data for the scan was averaged during the time between 30 milliseconds and 50 milliseconds. The spectrum is shown in figure 3.1 with the lines identified by element and ionization state. Ions of oxygen, nitrogen and carbon are identified on the figure. Not shown in the figure due to its relative weakness is a Ti IV line at 779 $\AA$. The uncertainty in the measurements varies between 14% and 100% depending on the wavelength

The Oriel monochromator was used to measure the spectrum in the near-uv on a shot-to shot scan with a resolution of 30 $\AA$ and a step size of 15 $\AA$. The spectral lines observed with the film spectrograph were also observed with the Oriel instrument. Thus, by combining the film measurements with the Oriel

wavelength scan, the spectrum between 2100 $\AA$ and 7000 $\AA$ was compiled and is plotted in figure 3.2. There were weaker lines present in the Oriel scan which could not be positively identified owing to the resolution used, but the strongest lines are identified as multiplets of the elements observed in the vuv region.

3.2.2 Spatial Profiles

In order to determine the spatial distribution of the impurities the vuv impurity radiation brightnesses of selected lines was measured along multiple radial chords. Visible impurity radiation from selected lines was measured at several axial locations through a central chord and radial brightness profiles were measured at the z = 110 cm and z = 350 cm locations using the oma spectrometer and the Oriel monochromator.

The results showed asymmetries both radially and axially. Figure 3.3 shows radial brightness scans of O III and O V. Radial brightness profiles of O IV and O VI were also measured and showed the asymmetry. The asymmetry could be caused by one of three effects: electron temperature asymmetry , electron density asymmetry, or an asymmetry in impurity confinement. However, the asymmetry is also seen weakly in atomic hydrogen light profiles, which means there is an asymmetry in electron density or electron temperature apart from impurity confinement.

A brightness measurement $B(y)(photons/sec - cm^2 - ster)$,along a particular chord with chordal radius y will contain contributions from all the emitting plasma along the chord. Assuming cylindrical symmetry,

$$B(y) = \int E(y) \frac{r}{\sqrt{r^2 - y^2}} dy \tag{3.1}$$

where $E(y)(photons/sec - cm^3 - ster)$is the local volume emissivity per steradian. The integral is carried out across the plasma column. This equation is known as Abel's integral equation. If E is a function of radius only, the equation may be solved analytically:

$$E(r) = -1/\pi \int_r^R \frac{dB(y)}{dy} \frac{dy}{(y^2 - r^2)^{1/2}} \tag{3.2}$$

The process of solving eq.3.2 is known as 'Abel-inversion'.

The local volume emission rate of a resonance line is dependent on the electron density n_e, the ground state density of the impurity ion n_{imp}, the electron collision

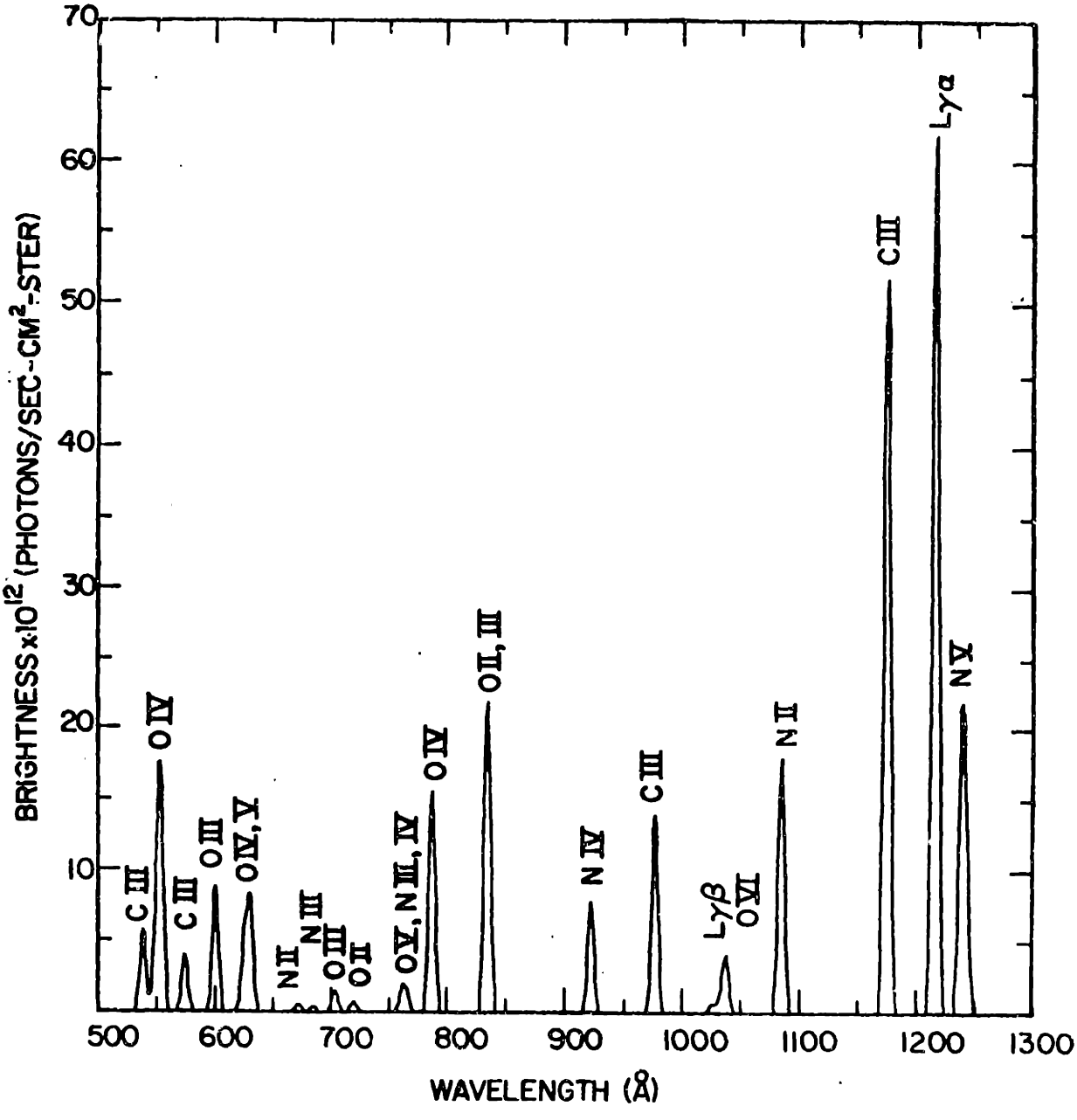

Figure 3.1: Tara central cell vuv spectrum.

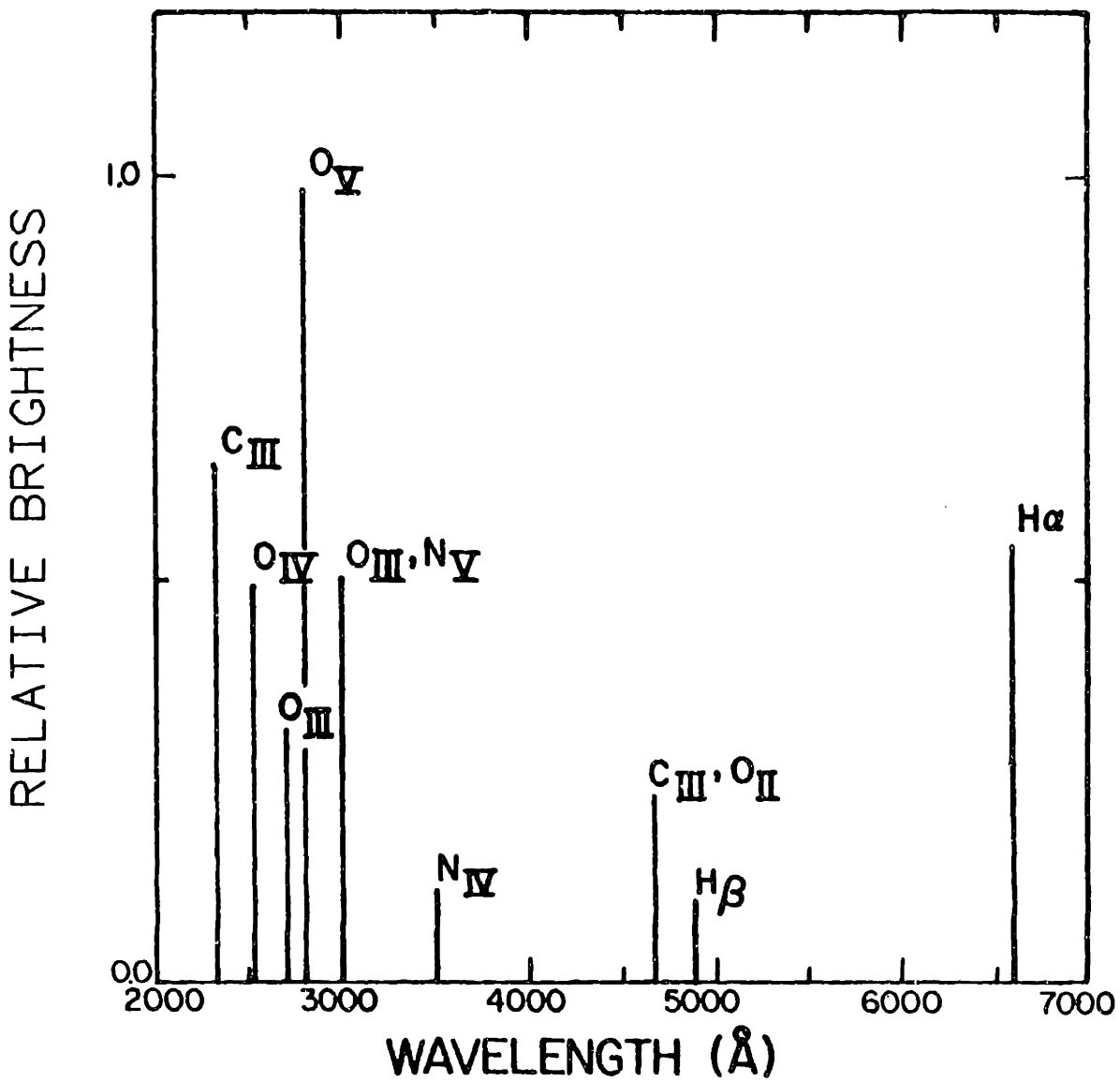

Figure 3.2: Tara central cell visible/uv spectrum.

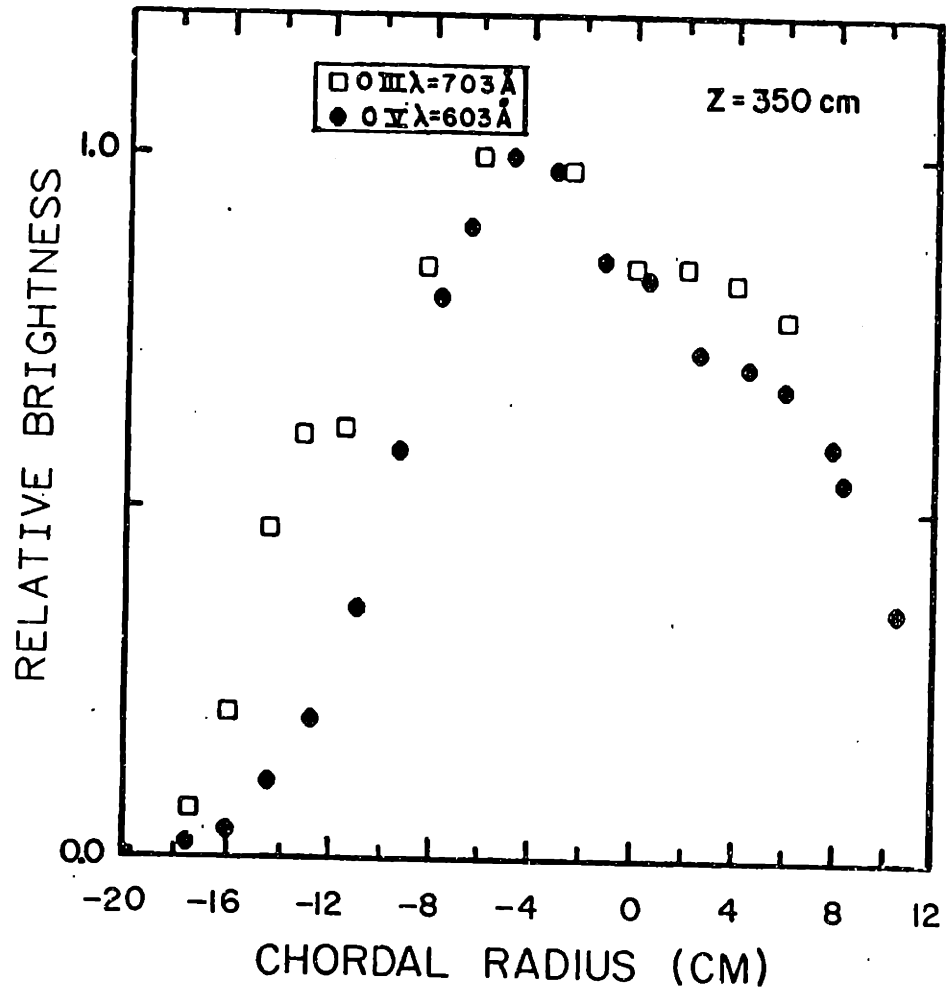

Figure 3.3: Oxygen ion brightness profiles.

excitation rate $< \sigma v >_{ex}$, which is the product of the excitation cross section and electron speed averaged over a maxwellian electron energy distribution, and the branching ratio R_B. [12]

$$E = n_e n_{imp} < \sigma v >_{ex} R_B \tag{3.3}$$

where E now signifies the local volume emission in $photons/(sec - cm^3)$.

The oxygen ion brightness profiles were each separated into a symmetric and an asymmetric component by assuming that the positive chordal radius portion of the profile is symmetric in chordal radius. The symmetric component was then Abel-inverted to obtain the volume emission profile. The asymmetric component of the profile was added on as a correction in determining the oxygen concentrations. The contribution to the concentration from the asymmetric component was estimated

at 5 %. The volume emission profiles were the divided by the product of the local electron density, the local excitation coefficient and branching ratio to obtain the oxygen ion concentrations. The excitation varies a maximum of ten percent over the range of electron temperatures in the plasma. Figure 3.4 shows the resulting normalized oxygen ion density profiles. The accuracy of the inferred density profile depends on the strength of the central emission relative to the outer plasma emission. The greater the central emissivity relative to the average emissivity, the less uncertainty in the inferred central emissivity. Uncertainties in resulting radial emissivity profiles are determined by varying the function which fits the data and performing the Abel-inverted process on the resulting function. The ratio of the central O VI emissivity to the O VI emissivity at 10 cm is accurate to 15% while the ratio of the central O III emissivity to the O III emissivity at 10 cm is accurate to 50%.

In order to determine the axial distribution of impurities, the oma spectrometer was used to measure the relative strengths of several impurity lines at four separate axial locations along a central chord. Owing to the weakness of some lines and the lack of a quartz window at the $z = 110$ cm location, not every line was measured at every location. The line average electron density was monitored for all of the shots and it was seen to vary a maximum of 15 percent about its mean. During the series of discharges in the axial impurity density study a separate detector measured the relative intensities of an O V line and an O III line. These intensities varied a maximum of 50 %. The axial oxygen measurements presented here were normalized to those measurements.

Figure 3.5 shows the plots of impurity density versus axial distance obtained from these measurements. The electron density is independent of axial position. The zero in axial distance corresponds to the gas port location, which was 50 cm north of the center of the central cell. The gas box extends 50 cm on both sides of the origin.

Two trends are readily apparent on viewing the plots. One is that all of the nitrogen and oxygen densities decrease in the direction away from the gas feed. The other is that the carbon III density peaks away from the gas feed, outside of the gas box. The fact that both nitrogen and oxygen are constituents of air, and both have a peak density at the gas port suggests that there was air contaminating the hydrogen gas puffed in to the gas box. Carbon is not a major constituent of

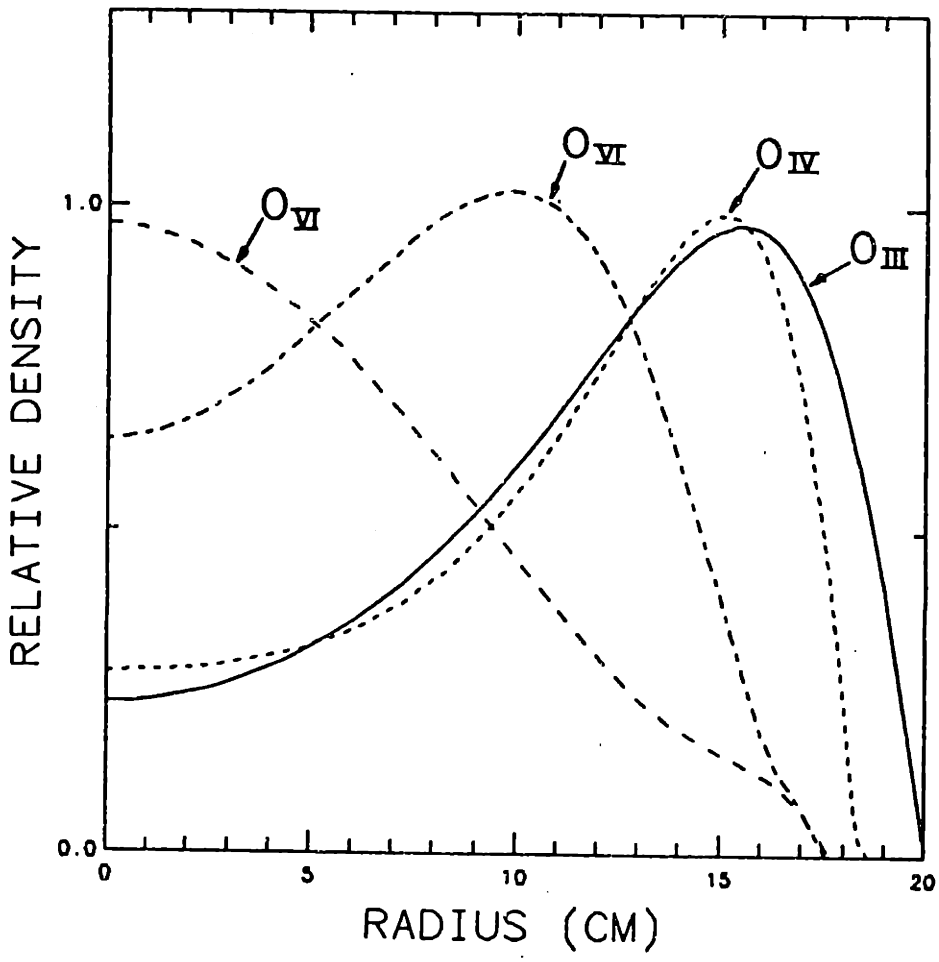

Figure 3.4: Oxygen ion density profiles.

air and it is found to be peaked somewhere between 30 cm and 350 cm. There is a stainless steel limiter at 50. cm. which is the closest limiter to the plasma. It could be the source of the carbon.

The peaking of the lower ionization states of oxygen and nitrogen at the gas feed is easily understood since the mean free path for ionization of N II in a tenuous edge plasma of 3×10^{11} at an energy of 3 ev is 30 cm. From the axial profiles of N II and O II it appears that the gas feed is the source of 50 % of the nitrogen flux into the plasma and is the source of 20 % of the oxygen flux into the plasma, within a factor or two.

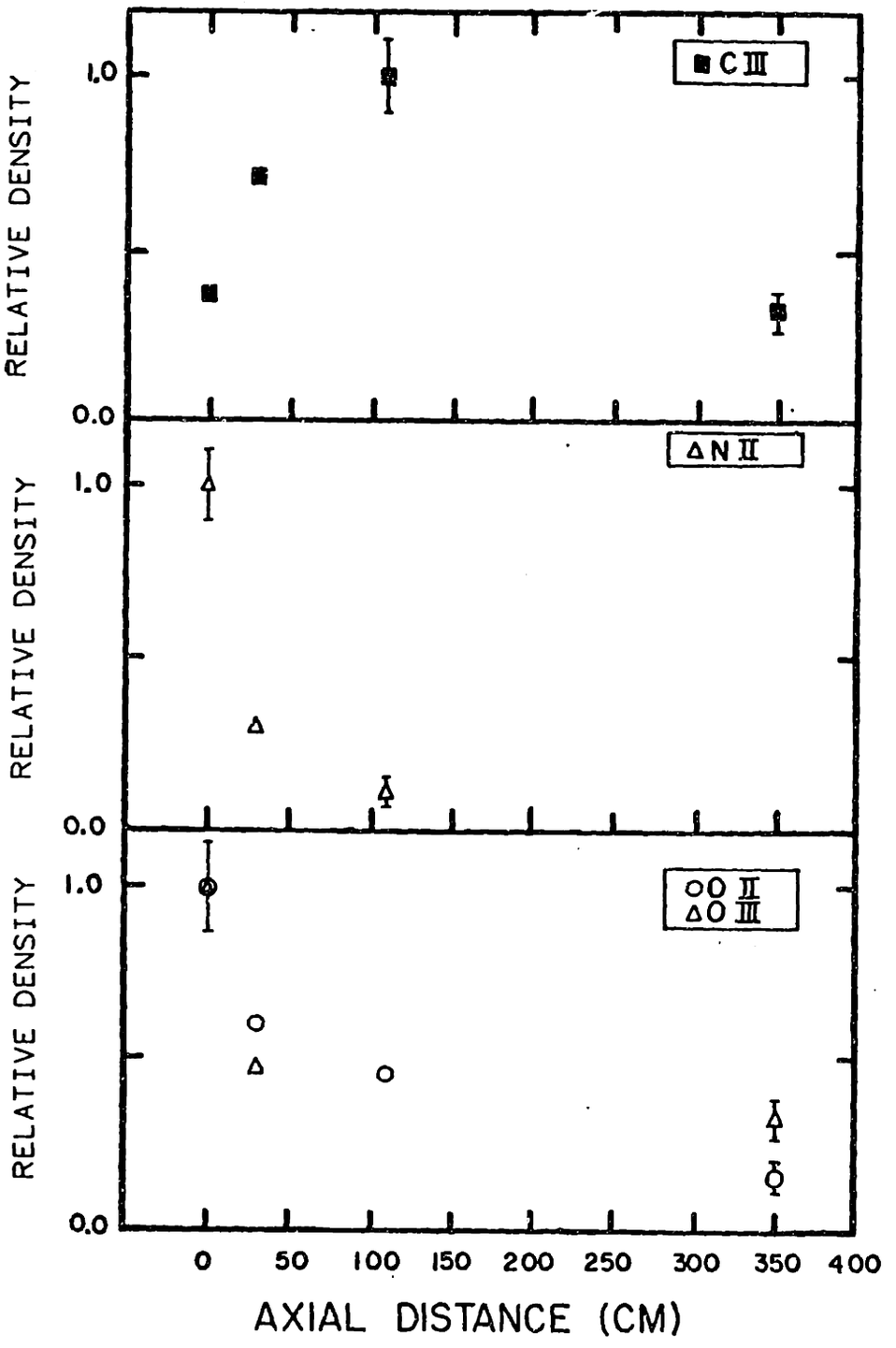

Figure 3.5: Impurity densities versus axial distance.

Impurity	Concentration
Oxygen	.3 %
Nitrogen	.2 %
Carbon	.05 %
Titanium	.02 %

Table 3.1: Impurity concentrations.

3.2.3 Impurity Concentrations

The measured volume emission profiles can be used to obtain absolute ion density profiles and an estimate of power radiated by impurities and power used in ionizing impurities. In the case of several impurity species, metastable ions were observed. Their densities were added to the ground state ions densities to obtain the total densities. In the case of carbon, only two ionization states were observed, since the transitions for other states are weak in the range of the vuv monochromator. In that case the densities of the other states were estimated based on the observed densities in nitrogen and oxygen. Only one line of titanium was observed and the densities of the other states were estimated based on ref [12]

Using the electron density profile, and the excitation rates from ref. [12], the local impurity ion densities are obtained. Using the axial impurity profiles, the average impurity densities and concentrations in the central cell plasma are shown in table 3.1. The total impurity concentration is the sum of the separate concentrations, and is .57% $\pm$ .23%, given an average uncertainty of 40%. THe average ion charge is 2.8. The average effective positive charge of the plasma, Z_{eff}, is 1.04. $\pm$ .016. [13]

3.2.4 Impurity Influx Ratios

Another method of monitoring impurities involves measuring the relative intensities of impurity lines and atomic hydrogen lines as described in ref. [8] The advantages to this method are that an absolute calibration isn't needed and in several cases the impurity lines studied are close in wavelength to the hydrogen lines. The local relative impurity fluxes and local relative proton fluxes are measured using the oma spectrometer. The total relative proton fluxes and impurity are then deduced from the axial profiles.

Particle fluxes into the plasma can be derived by measuring the brightness of line emission B, using the ratio of the ionization coefficient S to the excitation coefficient X

$$\Gamma = 4\pi \frac{S}{XR_B} B \tag{3.4}$$

where R_B is the branching ratio of the observed transition. S/XR_B is the number of ionization events per photon. S/XR_B values for several emission lines in hydrogen, carbon II, carbon III, and oxygen II for a range of electron temperatures are shown in ref. [8].

In the study performed in ref. [3] emission lines from both ground state and metastable levels were measured. In this work, metastable and ground state ratios were not measured for all the impurity species studied. The ground state to metastable population ratios found in ref. were used to calculate the total relative fluxes.

Shown in figure 3.6 is a plot of the emission spectrum between 4305$\AA$ and 4368$\AA$ which includes the hydrogen Balmer γ emission line at 4340 $\AA$ and an O II multiplet. The spectrum was measured at the gas port, where both emissions are peaked. The ratio of the Balmer γ intensity to the O II transition intensity at 4351 $\AA$ is 51. The ratio of axial width of the O II distribution to the axial width of the Balmer γ distribution is 4.9. Therefore the ratio of the Balmer γ average intensity to the O II line average intensity is 10. Since there are 10 ionization events per Balmer α photon [ref. [7]] and the measured ratio of Balmer α intensity to Balmer γ intensity of 40, there are 400 hydrogen ionization events per Balmer γ photon. From ref. [8] ,at an electron temperature of 80 ev., there are 32 O II ionization events per each 4351 $\AA$ photon. This includes ground state and metastable ions, and assumes a ground state to metastable ratio identical to that found in ref. [8] The ratio of oxygen flux Γ_O to proton flux Γ_H is equal to the ionization rate ratios:

$$\frac{\Gamma_O}{\Gamma_H} = \frac{32.}{10. \times 400.} = .008. \tag{3.5}$$

A C II line at 6578$\AA$ was compared to the Balmer α line to infer the relative flux of carbon and protons into the plasma. The spectrum between 6540 $\AA$ and 6580 $\AA$ was measured at the four axial locations on the central cell and the C II line was below detectable strength. Using the axial profiles of Balmer α and C III brightness, the average ratio of the Balmer α emission to the C II line emission is found to be greater than or equal to 520. From ref [8]. there are 28 C II ionization

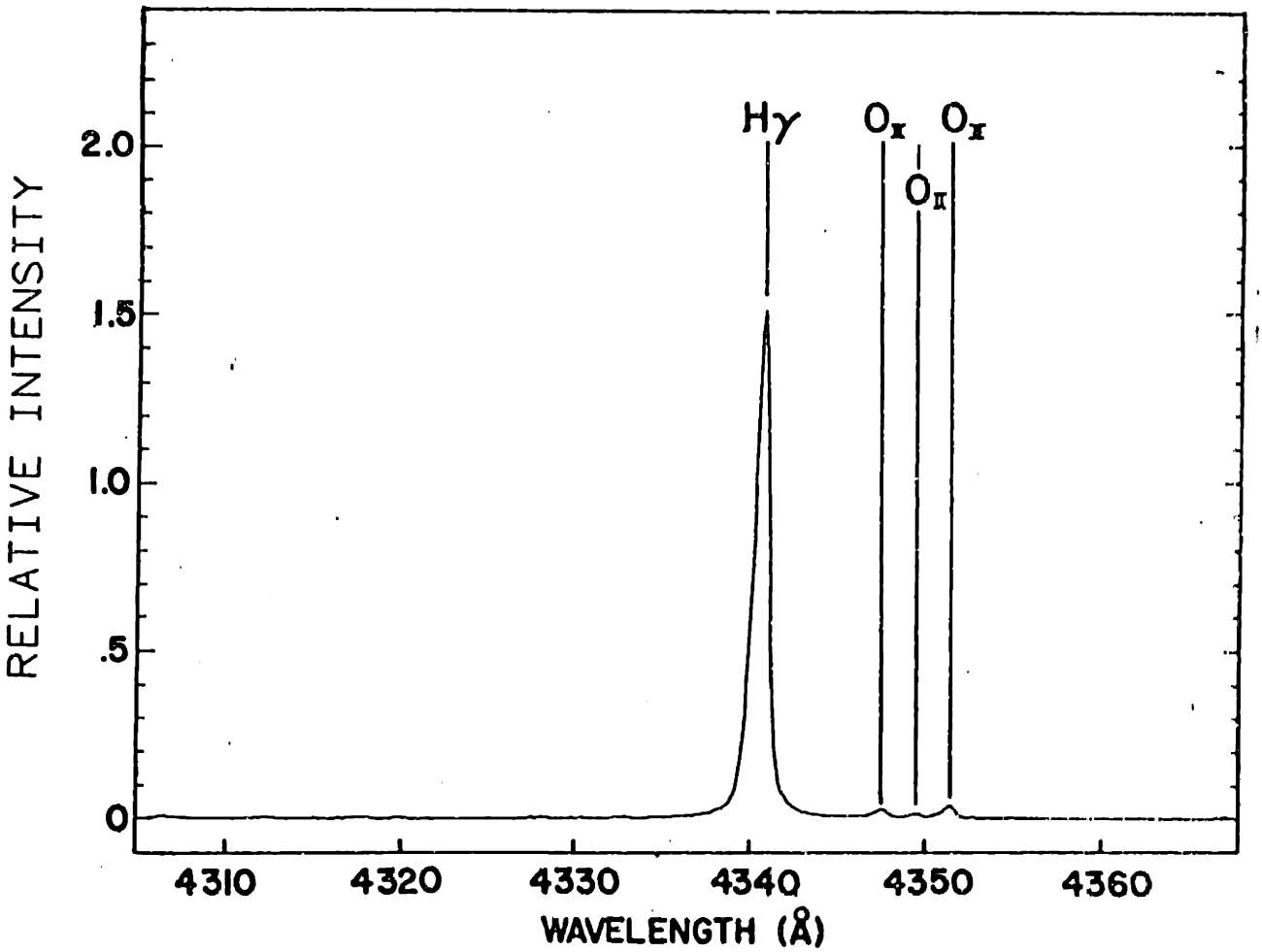

Figure 3.6: Spectrum showing the Hγ line and O_{II} lines.

events per each 6578. $\AA$ photon. That makes the ratio of the carbon III to proton flux less than or equal to 28/(10 × 520), or .0054.

A C III line at 4647. $\AA$ can be compared with the nearby Balmer γ line to obtain the ratio of the flux of C IV to protons into the plasma. The ratio of the average Balmer γ intensity to the average C III line intensity is 14. From ref. [8] the number of ionization events per 4647. $\AA$ photon is 7. including ground state and metastable atoms and assuming the same ratio of ground state ions to metastable ions as found in the work of ref. The ratio of carbon IV flux to proton flux is then 7/(14 × 400) or .0014.

The ratios of O III and C IV influx to proton influx are found to be factors of 2-3 higher than the ratios of these impurity densities to the plasma density. If the impurity confinement time is identical to the plasma particle confinement

Species	Power
O	1.5 Kw
N	1.0 Kw
C	.3 Kw
Ti	3.5 Kw

Table 3.2: Power lost to impurity radiation/ionization.

time the impurity fraction will be identical to the impurity to proton flux ratio, since the ratio of impurity density n_{imp} to plasma density n_e is determined by the ratio of impurity influx Γ_{imp} to plasma influx Γ_p and the confinement times τ_{imp}, the impurity confinement time, and τ_p, the plasma particle confinement time as follows:

$$\frac{n_{imp}}{n_e} = \frac{\Gamma_{imp}\,\tau_i}{\Gamma_e\;\tau_e} \tag{3.6}$$

So, the fact that the density ratio is lower than the flux ratio could be explained by an impurity confinement time which is lower than the plasma particle confinement time. Since the impurity ionization in the lower ionization stages occurs at larger radius on average than the hydrogen ionization, the lower ionization state impurities may be less well confined than the plasma particles. Another explanation of the discrepancy is that the ratio of ground state ions to metastable ions is different from the case in ref. [8] which could alter the flux ratios.

The power lost in radiation from impurities can be estimated from a knowledge of the impurity concentrations and calculated cooling rates. ref. [14,15] Table 3.2 shows the distribution in radiated power. The total power lost to impurities is 7 kilowatts. This represents less than 5 percent of the total rf power injected into the plasma.

3.3 Doppler Broadening and Plasma Rotation Measurements

3.3.1 Ion Temperatures from Doppler Widths

If impurity ion species remain in the plasma for a time long enough to equilibrate with the plasma protons through collisions, they will have the same temperature as the protons. Impurity ions are lost either through diffusion radially or into the loss cone, or through ionization. The ratio of the heating rate to the loss rate

determines whether the impurity ions will have the proton temperature. Impurity heating is described by the following equation:

$$\frac{dT_I}{dt} = \nu(T_i - T_I) \tag{3.7}$$

where T_I and T_i are the impurity ion temperature and the proton ion temperature respectively and ν is the heating rate which is dependent on the impurity ion charge and mass, and the proton density and temperature:

$$\nu = 1.8 \times 10^{-6} \lambda_c \frac{Z^2}{T^{3/2}} \frac{n_i}{\mu_i} \tag{3.8}$$

where μ_i is the impurity ion mass in amu, Z is the impurity charge, n_i is the proton density in cm^{-3} and λ_c is the coulomb logarithm, calculated to be 13.[ref [16]] This expression is approximate and ignores a term in the denominator; $m_i T_I$. Because of the ratio of impurity mass to proton mass this term contributes at most 15 percent to the heating rate and then only when the impurity temperature approaches the proton temperature. This allows an approximate analytical solution to equation.

$$T_I = T_i(1 - e^{-\nu t}) \tag{3.9}$$

Defining a heating time τ_h as $1/\nu$, it follows from equation that after 3 heating times, $T_I = .95T_i$. Therefore, if the particle remains in the plasma for a sufficient time, it will attain the proton temperature. The ratio of the loss time τ_l, defined by $1/\tau_l = 1/\tau_i + 1/\tau_c$, where τ_i and τ_c are the ionization time and the particle confinement time respectively, to the heating time determines the temperature obtained by the impurity ion. The confinement time is estimated to be approximately 1 millisecond. For the lower ionization states, with Z less than 3, the loss time is determined only by the ionization time, while for higher ionization states, the confinement loss contributes.

A spectral line radiated by impurity ions in thermal equilibrium will have a gaussian profile with a half width σ_d determined by the ion temperature and wavelength:

$$\frac{\sigma_d}{\lambda_o} = 7.5 \times 10^{-5} \sqrt{T_I/\mu_I} \tag{3.10}$$

where λ_o is the unshifted wavelength, μ_I is the ion mass in amu, and the temperature is in ev [16].

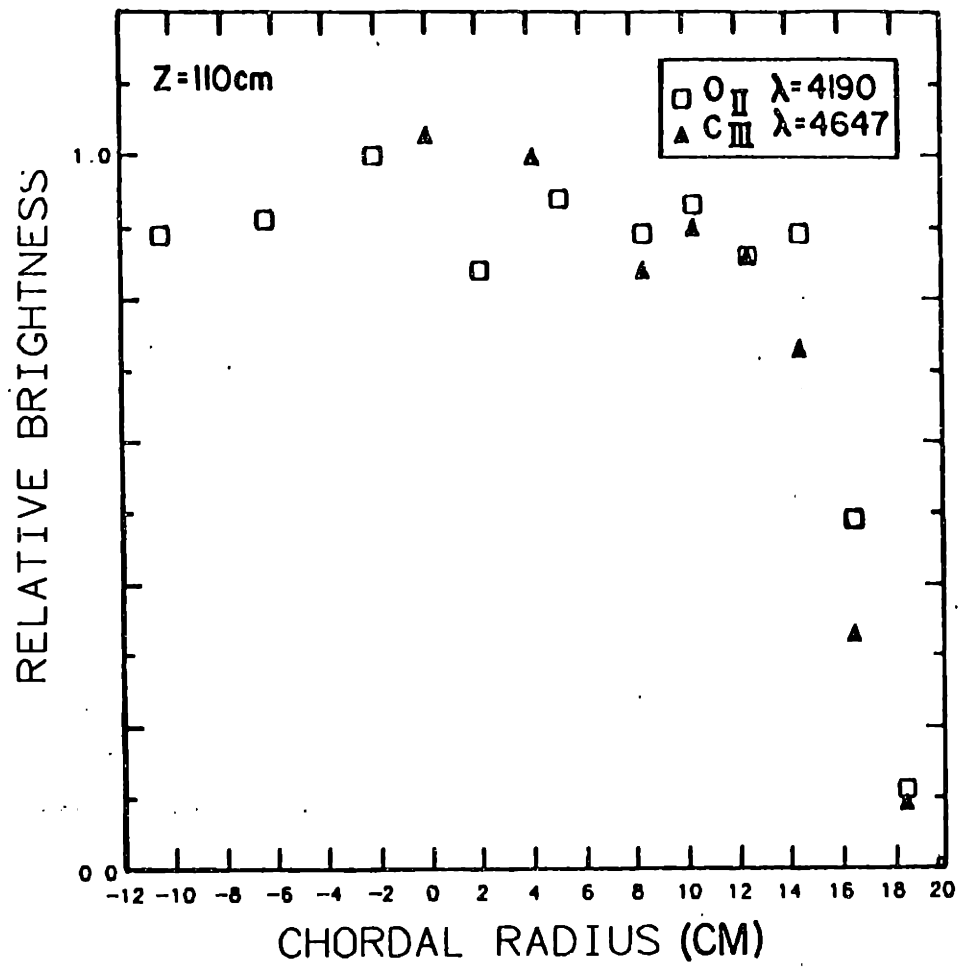

Figure 3.7: Brightness profiles of a C III line and an O II line.

For most of the impurity lines studied for doppler widths, the radial brightness profile of one of the species' lines was measured at either the z = 110 cm location or the z = 350 cm location using either the Oriel monochromator, the oma spectrometer or the vuv monochromator. Brightness profiles of a C III line and an O II line measured at 110 cm are shown in figure 3.7 and a brightness profile of an N IV line measured at 350 cm along with three chordal brightness measurements of a C III line is shown in figure 3.8. The brightness profiles were inverted to obtain the emissivity profiles which are shown in figure 3.9. The mean radius of emission is dependant upon the species.

The wavelength region between 4625$\AA$ and 4685$\AA$ contained both doppler-broadened impurity lines and impurity lines which were not doppler-broadened. A plot of the spectrum in that region measured at the z = 350 cm location is shown

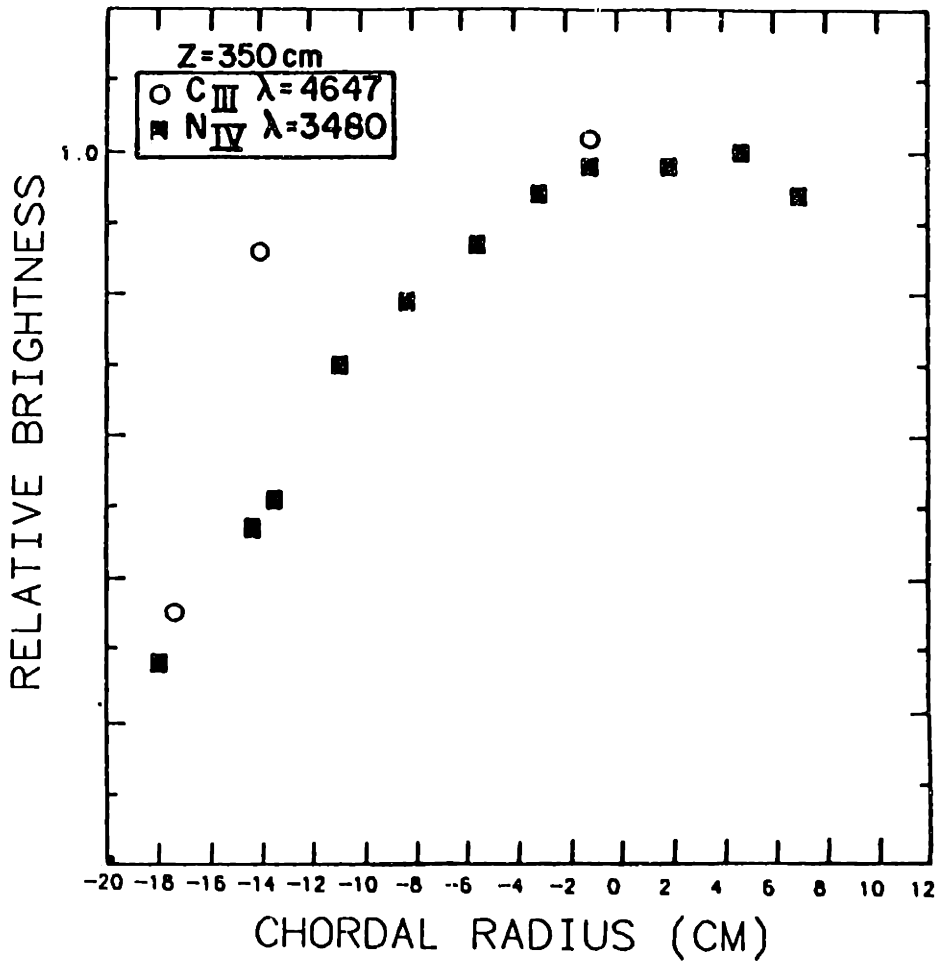

Figure 3.8: Brightness profiles of a C III line and an N IV line.

in figure 3.10. The spectrum is a sum of eight spectra from separate discharges and thus the lines are broadened slightly, .05 $\AA$, over the single discharge broadening due to fluctuations caused by vibrations of the spectrometer system. The C III lines are broader than the Ti I lines and the C IV line is the broadest line. Figure 3.11 shows a spectrum containing an N IV multiplet along with several Ti II lines. The N IV lines are broader than the Ti II lines.

Shown in figure 3.12a is an expanded profile of the 4647.4$\AA$ line of C III from the spectrum measured at 350 cm fitted with a gaussian and shown in figure 3.12b is a profile of the Ti I line at 4681.9 $\AA$ from the same spectrum on the same scale also fitted with a gaussian. The range fitted is always the central portion, and in the case of C III the gaussian is fitted only to the half-maximum point on the long wavelength side due to the interference from other lines. Because of its low

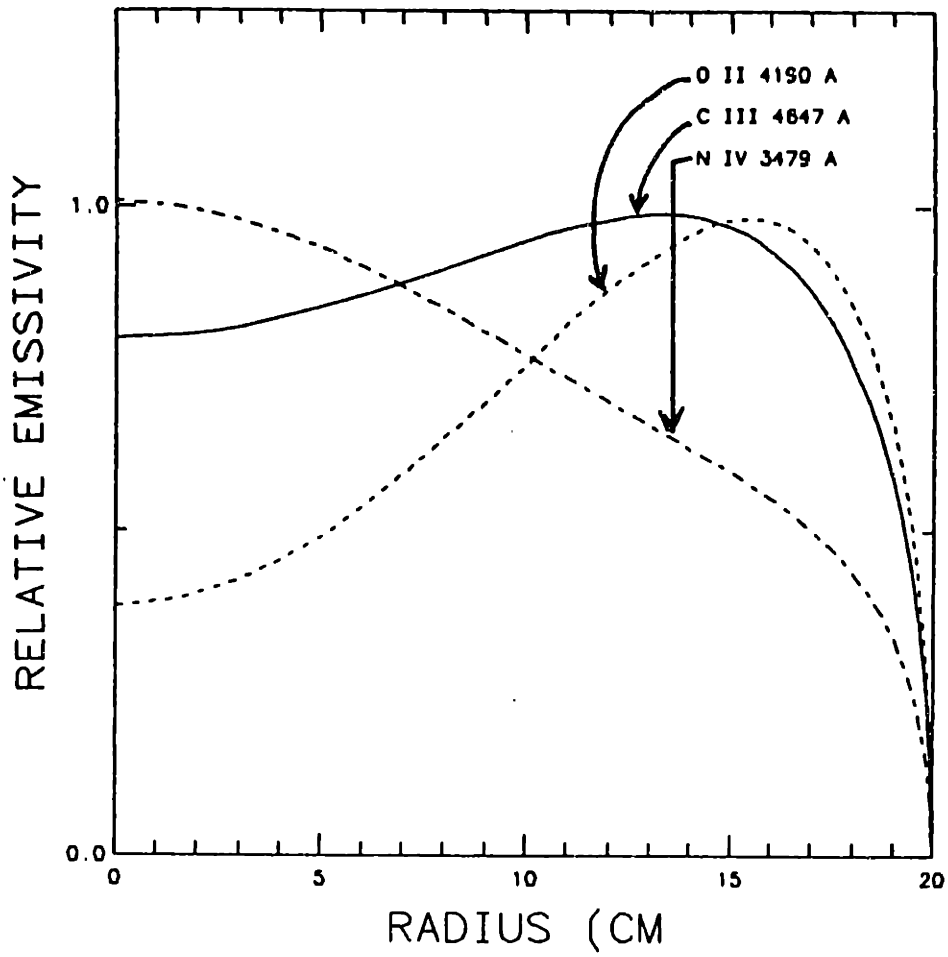

Figure 3.9: Impurity ion emissivity profiles.

temperature and large mass, 48 amu, Ti I has a low velocity spread and its lines have doppler broadening of less than .05 $\AA$. Thus the measured profile of the Ti I line is the instrumental profile and the measured width is the instrumental width. This measurement was consistent with profile measurements of spectral lines radiated from a mercury lamp and from a hydrogen lamp. A line which is broadened by both instrumental and doppler broadening will have a total width σ_t which is dependent on the broadening mechanisms in the following manner:

$$(\sigma_t)^2 = (\sigma_{in})^2 + (\sigma_d)^2 \tag{3.11}$$

where σ_{in} is the instrumental width.

The measured width of the C III line is $1.38\AA$ and the measured width of the Ti I line is $.68\AA$. By equation 3.10 σ_d is $1.18\AA$. By equation 3.9 the C III temperature

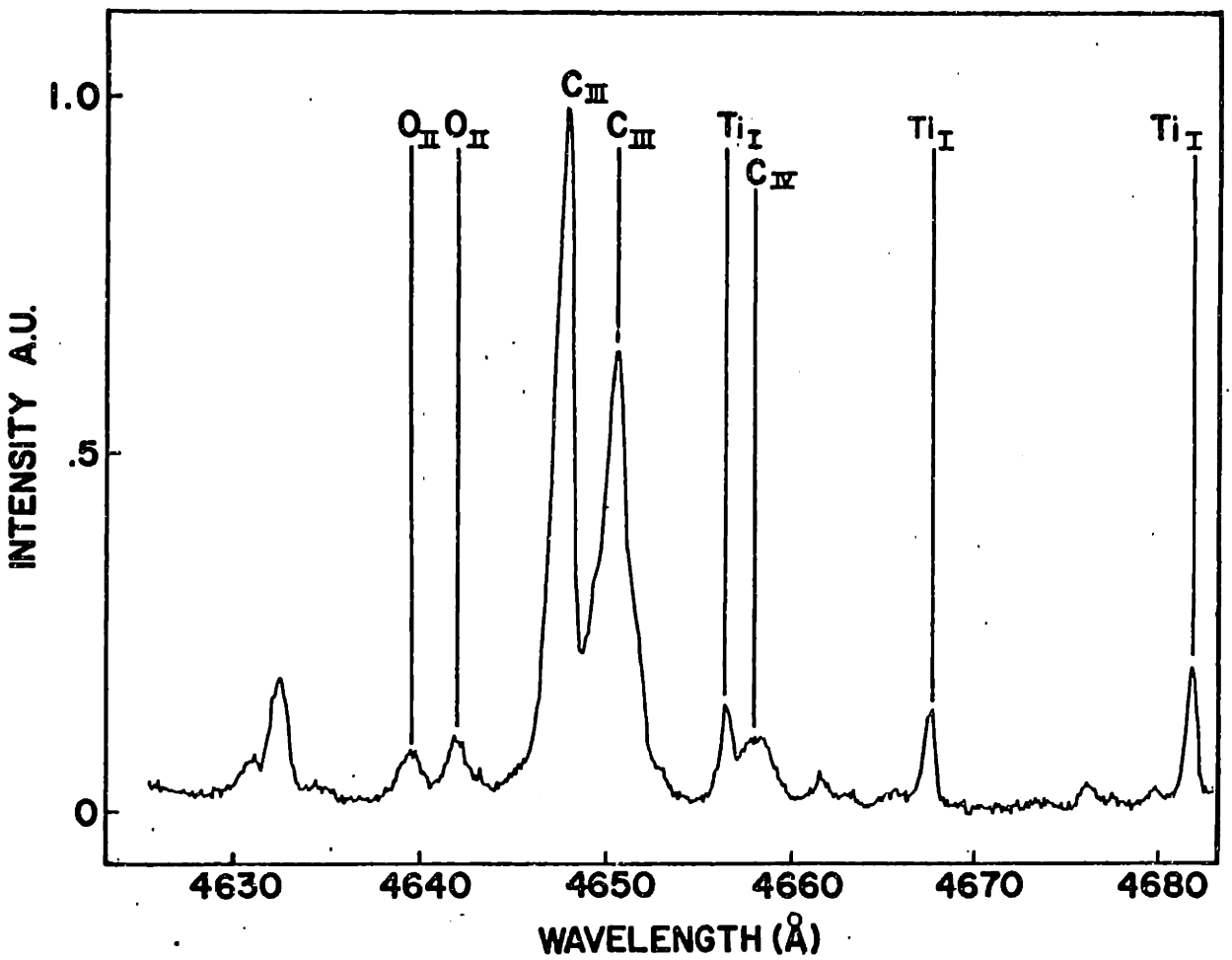

Figure 3.10: Spectrum showing the most intense visible impurity lines.

is 130 ev. In addition to the impurity lines presented, an O V multiplet at 2787$\AA$ was studied and showed broadening beyond the instrumental width.

Table 3.3 contains a list of the impurity ions studied at the z = 350 cm location to determine ion temperatures, along with the ratio of the loss time to the heating time r_τ, the measured impurity temperatures and the mean radius of emission $\underline{r}$ for a series of discharges in which the plasma conditions were held roughly constant. As a measure of the constancy of ion temperature, the diamagnetism and line averaged density were monitored. The ratio, which is proportional to the sum of the 'averaged' electron and ion temperatures, fluctuated a maximum of ten percent about its mean. The measurements are all central chord except for two of the C III measurements which were made at chordal radii of 14.5 cm and 17.4 cm. There is discrepancy between the O II and C III temperatures. The two species

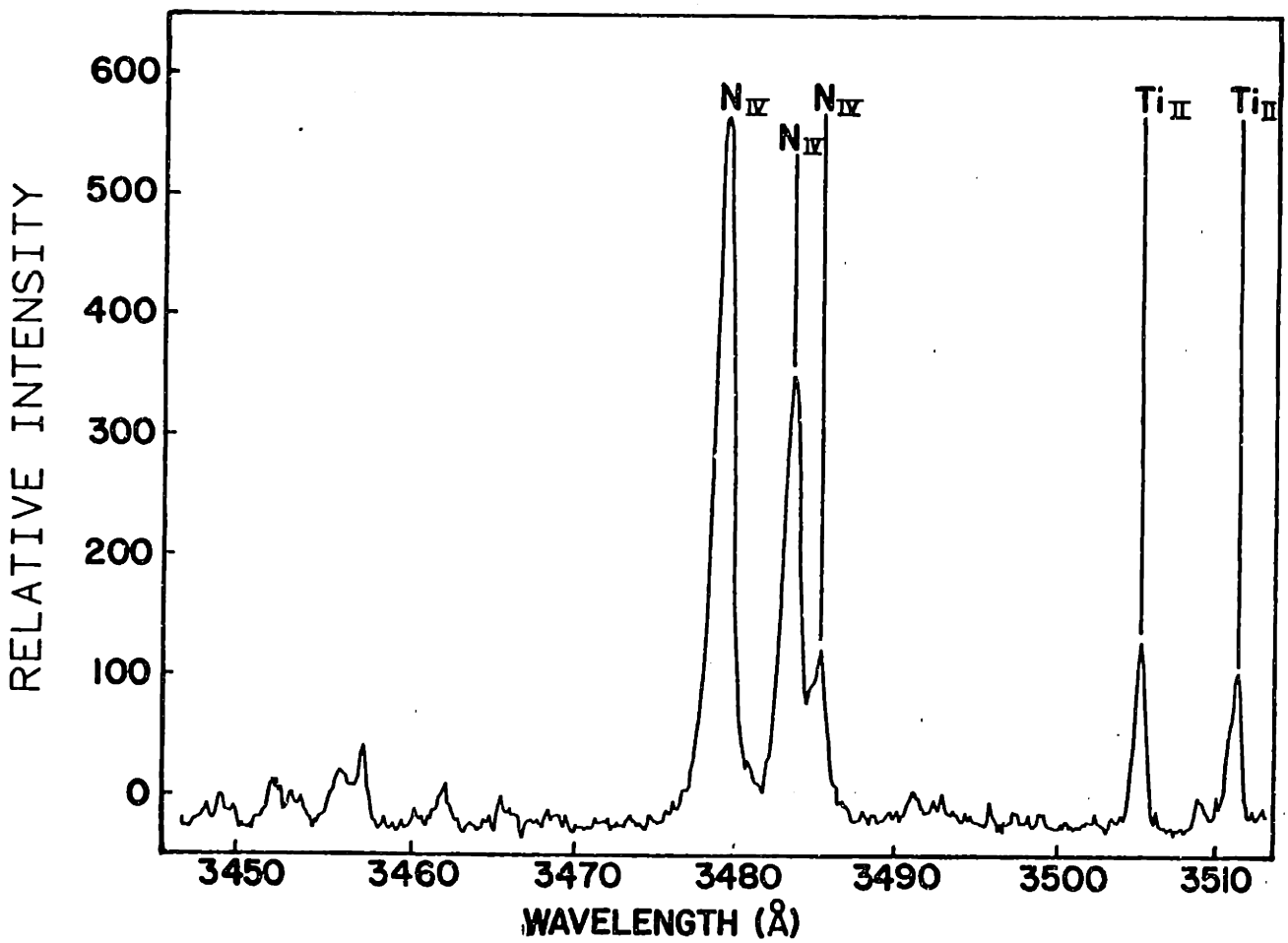

Figure 3.11: Spectrum showing an N IV multiplet and two Ti II lines.

emit in approximately the same radial distribution, yet their temperatures differ by 50 %. According to equation 3.8, their equilibration time is longer than their ionization times, which could explain the difference.

The loss time is longer than the heating time in only two cases. Therefore either equation 3.8 incorrectly determines the heating times, or the loss times are too small. However, the impurity ion temperature profile at z = 350 cm obtained from the line width measurements, shown in figure 3.13, is consistent with the diamagnetism measurements. For this series of discharges the average diamagnetism and average line-integrated density were .0025% and $7 \times 10^{13} cm^{-2}$ respectively. Using equation 1.2., the diamagnetism is obtained by integrating the plasma pressure, defined in equation 1.3, over the loop area and dividing by the magnetic pressure integrated over the same area. Using the electron temperature

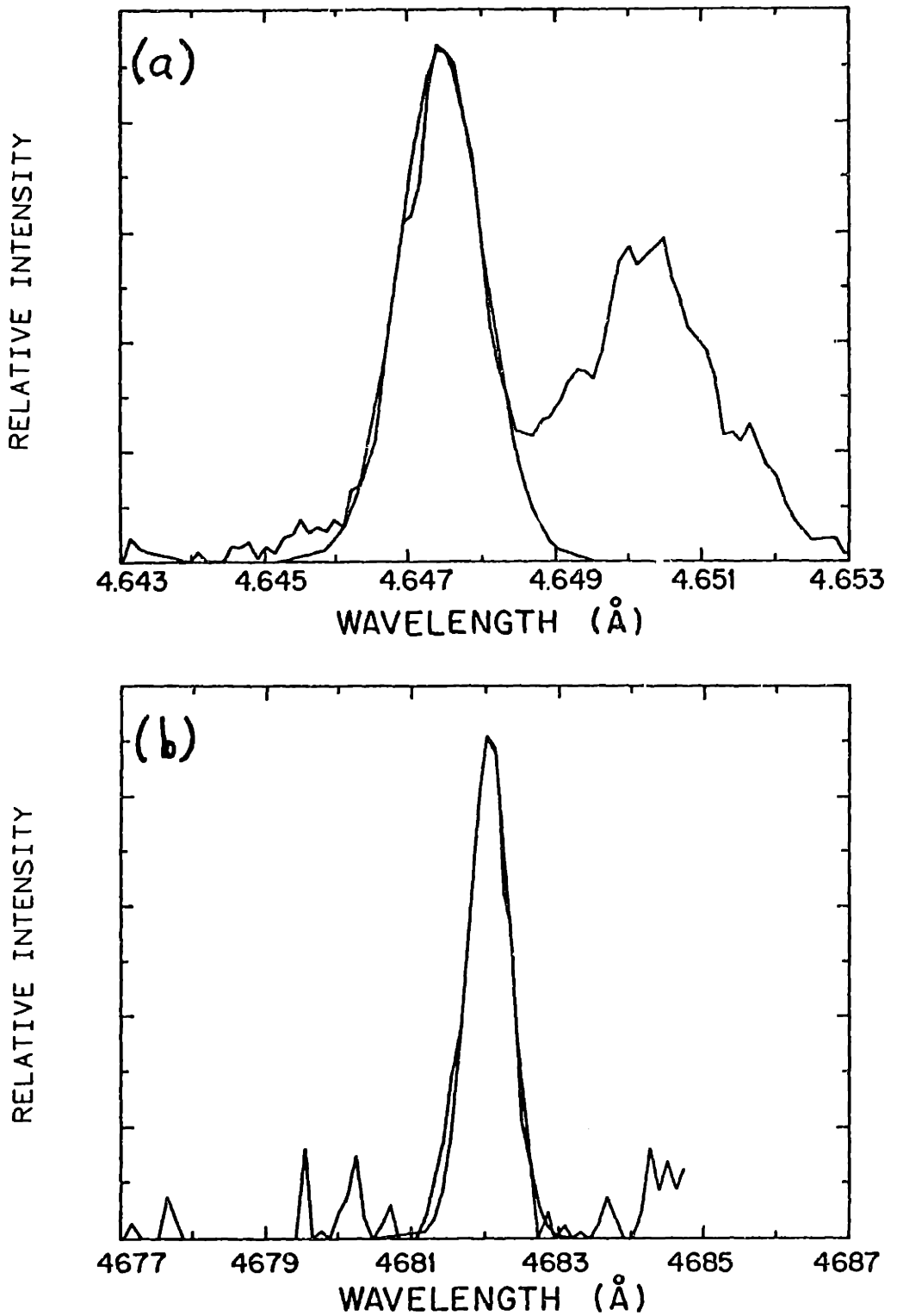

Figure 3.12: (a)Profile of the C III line at 4647.4Å, and (b), the Ti I line at 4681.9Å.

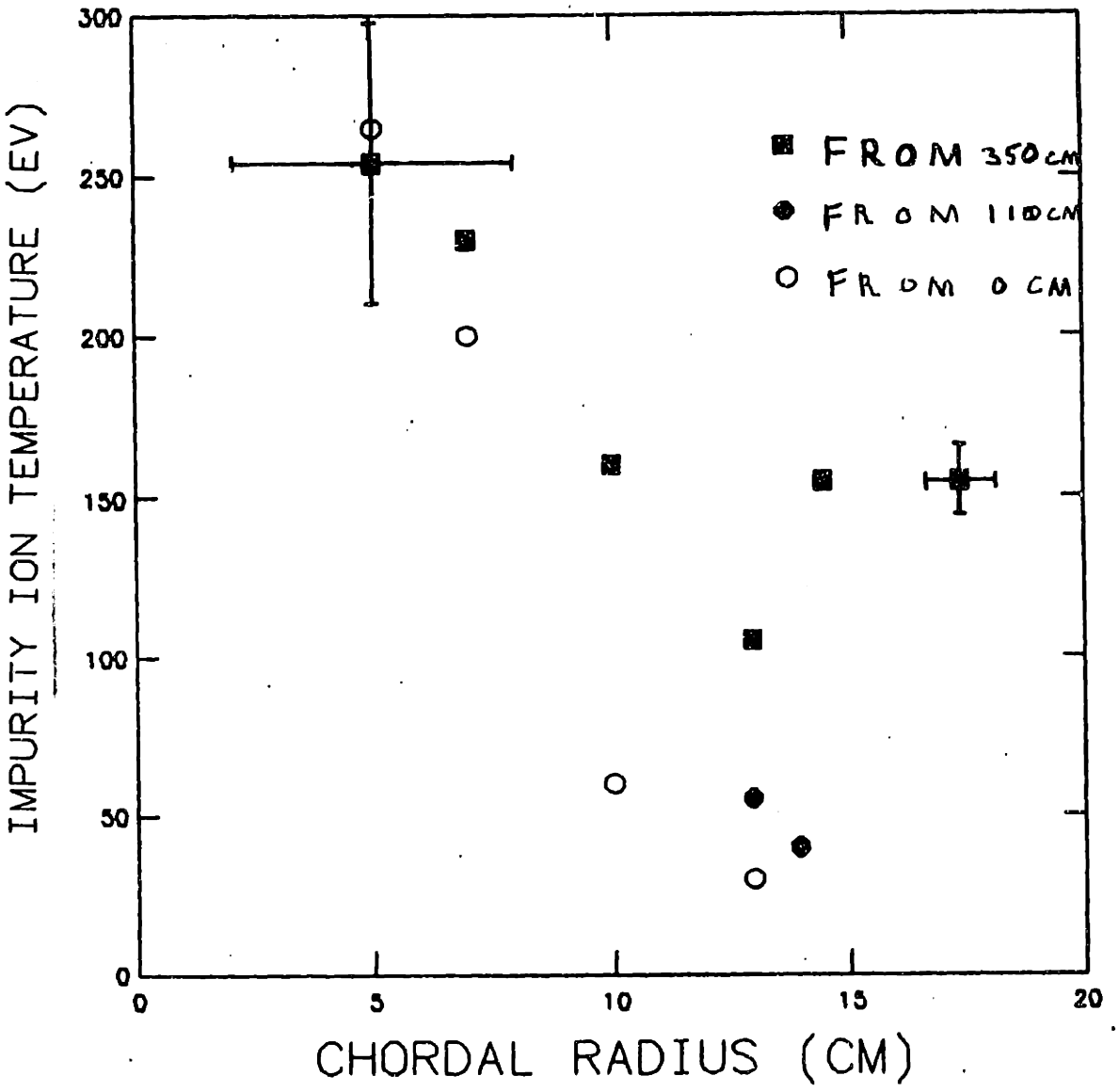

Figure 3.13: Impurity ion temperature profile.

Species	Line	r_τ	r	$T_I(ev)$
O II	4190 $\AA$	.01	13.	105.
O V	2780 $\AA$	1.1	5.	254.
N IV	3480 $\AA$	.3	7.	230.
C III	4647 $\AA$	.4	10.	160.
C III				
"	"	14.5	155.	
C III				
"	"	17.4	155.	
C IV	4658 $\AA$	.3	-	220.

Table 3.3: Impurity ion temperatures.

profile shown in figure 1.3 , the ion temperature profile in figure 3.13, and the electron density profile in figure 1.3 , one obtains a diamagnetism of .0019%. Given a 30 % uncertainty in the temperatures and considering the shot-to-shot variations, the diamagnetism obtained by integrating the measured plasma pressure is consistent with the diamagnetism obtained from the loop measurement. The ion temperature profile obtained from the impurity line doppler widths is also consistent with the measured atomic hydrogen temperatures from the same z location. This will be discussed in chapter 6. Thus, even though an examination of the loss times and heating times would indicate that the impurity ions would not achieve the proton temperature, the impurity temperatures are consistent with the proton temperature. This may be due to an inaccurate calculation of the loss times or to the fact that equation is invalid.

Higher resolution line profiles of the 4647.4$\AA$ C III line were measured with the film spectrograph at z = 260 cm. A slit width of 20 μm was used which afforded a resolution of .4$\AA$. The measured line width was 1.1$\AA$ and the corresponding temperature was 101 ev. The line-averaged density during the discharge studied with the spectrograph was equal to the density during the discharges for the above-mentioned profile and the diamagnetism was 20 % lower.

A radial profile of the C III line was measured at 110 cm in to a 5 cm radius. Central chord measurements of the C III line, the N IV line and the O V line were measured at the gas port and 30 cm north of the gas port. Several temperatures obtained from these measurements are plotted in figure 3.13.

3.3.2 Plasma Rotation Rates from Doppler Shifts

Under standard operating conditions, theory predicts that the central cell plasma in Tara will obtain an electrical potential which is high relative to the wall of the chamber [2]. This higher potential is observed in the ion end-loss measurements. Thus there will exist electric fields in the central cell plasma. If these fields are radial, or have a radial component, there will be a particle drift of both electrons and ions in the azimuthal direction. The drift velocity is independent of mass or charge and is given by $(\underline{E} \text{ X } \underline{B})/(B^2)$, where $\underline{E}$ is the electric field and $\underline{B}$ is the magnetic field. The magnitude is given by:

$$v_E = 10^8 \frac{E}{B} \frac{cm}{sec} \tag{3.12}$$

where E is in volts/cm and B is in gauss. [17]

Since the drift velocity is independent of mass and charge, impurity ions will drift with the plasma ions and electrons. Thus, a measurement of the impurity drift velocity will give the plasma particle drift velocity. Information about the impurity drift velocity can be obtained by measuring the wavelength distribution of a spectral line under sufficiently high resolution. If the ions have a component of velocity along the line of sight of the instrument the wavelength of the emitted photons will be shifted according to $\Delta\lambda/\lambda = v/c$ where $\Delta\lambda$ is the wavelength shift, λ is the wavelength of the photon radiated by the particle at rest, v is the velocity of the particle along the line of sight, and c is the speed of light.

Experiments to measure the impurity drift velocity were made with the oma spectrometer system at the z = 350 cm and z = 110 cm locations. At these locations instrument could view both the edge and the center of plasma cylinder. The spectral lines chosen were the C III line at $4647.4\mathring{A}$ and the O II line at $4190\mathring{A}$. These lines were chosen as the optimum compromise between intensity, instrumental sensitivity, and wavelength.

They are the most among the intense lines with wavelength above $4000\mathring{A}$. It is advantageous to use lines with as high a wavelength as possible, for two reasons. The first is that for a given speed, the wavelength shift is proportional to the unshifted wavelength. The second is that the resolution of the instrument increases with increasing wavelength, since the angular dispersion of the grating increases with wavelength, a factor of three over the whole range of the instrument. Another consideration is detector sensitivity. According to manufacturer's specifications,

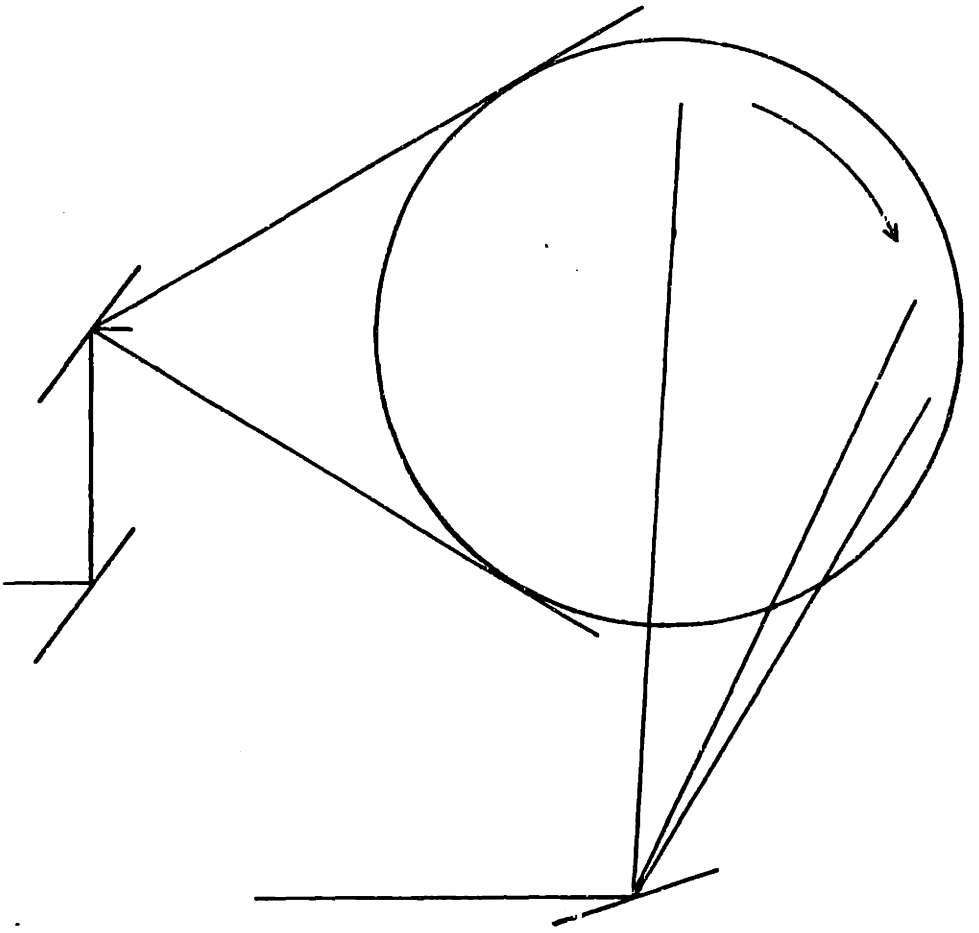

Figure 3.14: Diagram showing the viewing chords for rotation measurements.

the efficiency of the detector is roughly constant from 2000$\AA$ to 5000$\AA$ and falls steeply above that wavelength. The relative calibration between 4000$\AA$ and 5000$\AA$ showed the instrumental sensitivity to vary a maximum of 10% about its mean over the calibrated range.

A schematic drawing of the chamber cross section and viewing chords used in the rotation studies at 350 cm and at 110 cm is shown in figure 3.14. Figure 3.15 shows profiles of the 4647.4$\AA$ line of C III measured as the instrument viewed the plasma along a central chord and a chord at -17.4 cm, at the z = 350 cm location. The inferred C III temperature was 135 ev for the central view and 125 ev for the view at -17.4 cm. The line center is shifted toward the violet for the profile at -17.4 cm.

A plot of the line shifts measured at 350 cm and at 110 cm versus chordal

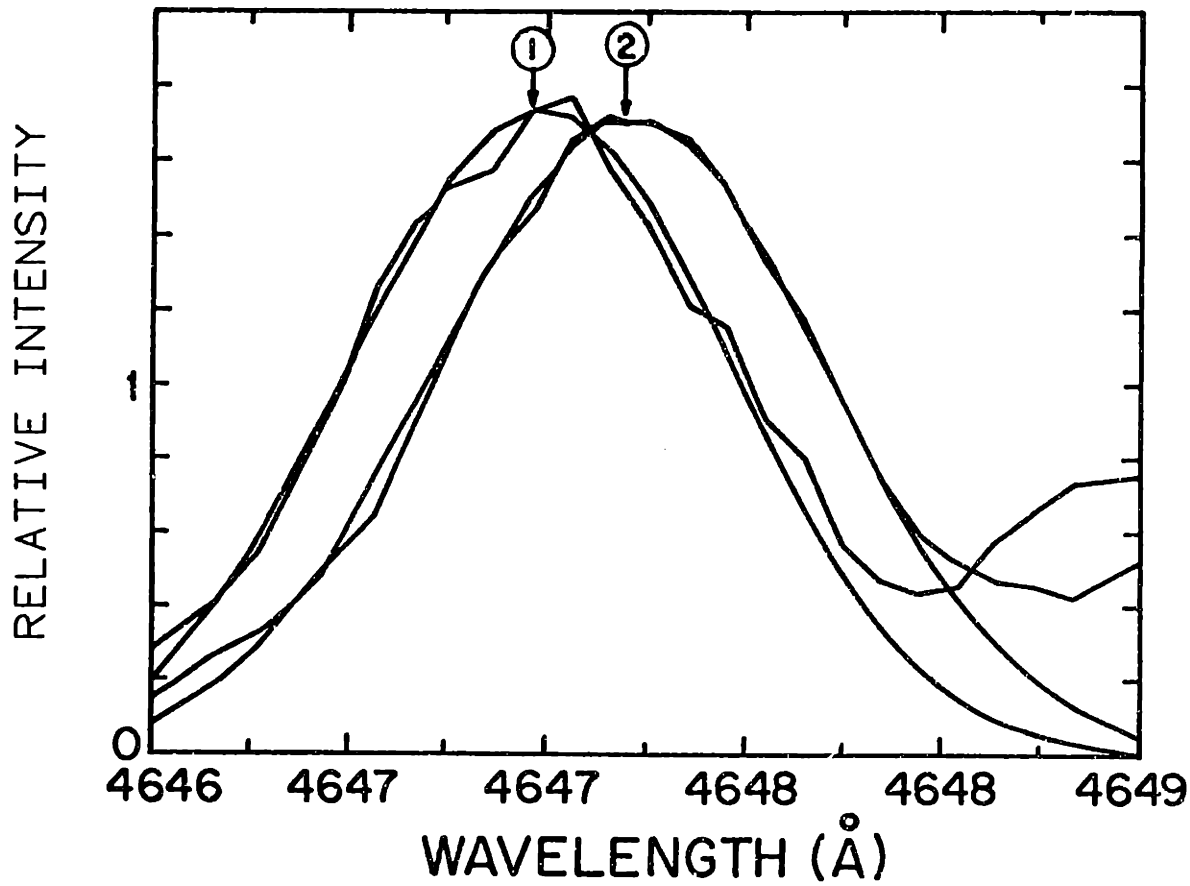

Figure 3.15: (1)C III line profile measured at a chordal radius of -17.5 cm, and (2), measured at 0 cm.

radius is shown in figure 3.16. Negative chordal radius corresponds to the west half of the chamber for the shifts at 350 cm and to the lower half of the chamber for the shifts at 110 cm. The shift at -17.4 cm was $.27\mathring{A}$ which corresponds to a drift velocity of 1.74×10^6 cm/sec $\pm 1.5 \times 10^5$ cm/sec. The direction of rotation is indicated on in figure 3.14. The drift energy is 17.5 ev. Using equation 3.12, the electric field causing the drift would be 38 volts/cm $\pm$ 3 volts/cm. By contrast, the shift measured at a chordal radius of -14 cm corresponds to a velocity of 3.2×10^5 cm/sec $\pm 1.5 \times 10^5$ cm/sec. This does not mean, however, that the C III ions at -14. cm were drifting with that velocity, since the line profile integrates contributions from regions where the plasma is rotating faster.

If the drift measured at 17.4 cm were azimuthally symmetric, the plasma

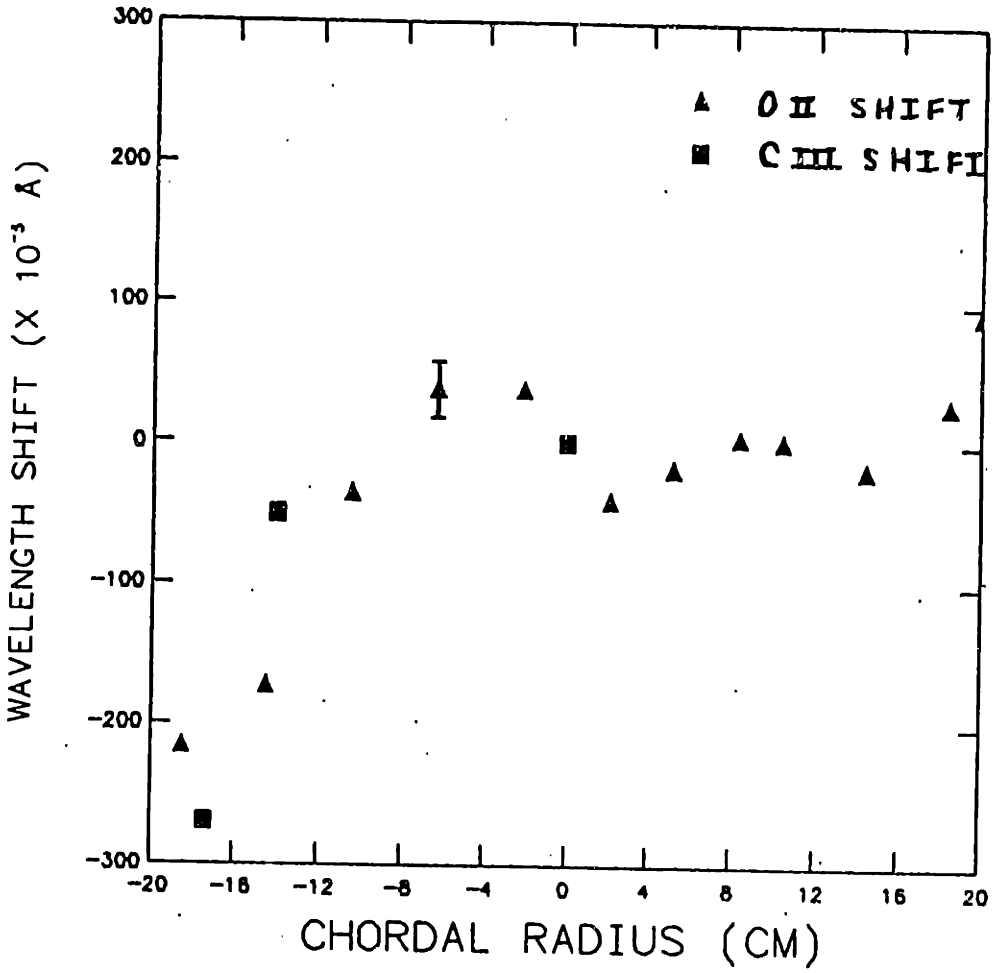

Figure 3.16: Plot of the wavelength shift versus chordal radius.

column would have rotated with a frequency of 16 khz ±1.5 khz. During the same discharge, fluctuations were observed in Balmer α light signals measured at a z of 450 cm on a multichord fiber optic array. The fluctuation frequency at a chordal radius of 8 cm was 23 khz ±1 khz. It is thus unclear whether these fluctuations were caused by a rotating plasma column. The electrical potential profile may have been quite different at the two locations since the fiber array was located at a region of higher magnetic field.

Since no other chordal measurements were made with the oma spectrometer at 350 cm it is unknown whether the shift is symmetric in radius. Since the radial resolution was 1.4 cm the electric field was present over at least that range at that point. Plasma potentials were measured by end-loss analyzers to range from 200 volts to 500 volts. If the electric field causing the observed rotation were constant

between 15 cm and 20 cm it would explain a peak potential of 190 volts.

Radial profiles of an O II line were made at the z = 110 cm location. A plot of the line shift versus chordal radius is shown in figure 3.16. Negative chordal radius corresponds to the south half of the chamber. Since the O II line has a lower wavelength than the C III line, the O II shift will be lower for a given velocity. The O II line shifts have been multiplied by the wavelength ratio for comparison with the C III line measurements. The plot of the O II line shift versus chordal radius shows asymmetries as well as edge shifts which are lower than the edge shifts at 350 cm. The asymmetric drift profile may be due to an asymmetric potential profile. The chordal Balmer α detector at 450 cm which showed 23 khz fluctuations at a radius of 8 cm showed fluctuations of 15 khz $\pm$ 2 khz and 26 khz $\pm$ 2 khz during the discharges at 110 cm. A chordal Balmer α detector at 110 cm collecting light from a chordal radius of 8 cm showed fluctuations of 15 khz $\pm$ 2 khz and 25 khz $\pm$ 4 khz. The shift of the O II line measured at a chordal radius of -18.5 cm corresponds to a rotation speed of 1.4×10^6 cm/sec. The plasma at -18.5 cm rotates at a frequency of 12 khz $\pm$ 1.5 khz. Thus, the observed rotation may be related to the lower frequency light fluctuation. There were some discharges studied during which the diamagnetism and density dropped precipitously during the time interval of measurement. The shifts measured in these discharges differed by as much as .25$\AA$ from shifts measured in discharges with no diamagnetism drops and these measurements were not included in Figure 3.16.

3.4 Summary and Discussion

The impurity spectra study performed on the Tara central cell plasma revealed the presence of oxygen, nitrogen, carbon and titanium. No other impurity elements were observed. Chordal brightness profiles of impurity lines show the higher ionization states of impurity elements are more strongly concentrated in the center of the plasma and the lower ionization states are peaked further out. Axial profiles show that lower ionization states of nitrogen and oxygen are concentrated at the gas port and decrease in concentration with increasing distance from the gas port, indicating the gas port is a source of nitrogen and oxygen, possibly from an air leak into the gas feed system. Carbon emission was found to peak away from the gas port, indicating a source of carbon outside of the gas box, possibly a limiter.

Impurity concentrations were determined from absolute brightness measurements in the vacuum ultraviolet. The total impurity concentration was found to .57%. In the TMX-U tandem mirror experiment, the total impurity concentration was 1.05% and was composed of oxygen, nitrogen and carbon as determined from vacuum ultraviolet spectral measurements. [18,19] Impurity-to-plasma influx ratios were measured directly using a line ratio technique. Assuming that impurity ions and plasma particles have the same confinement time, the impurity fraction inferred from the influx ratio is a factor of 2-3 higher than the fraction obtained from absolute brightness measurements. This may be due to a difference in confinement times, the crudeness of the model used to infer fluxes, or an error in the rates used. The amount of power lost to impurity ionization and radiation is estimated to be less than 5% of the total rf power, therefore impurity radiation and ionization is not a significant power loss channel.

Oma spectrometer measurements showed doppler broadening of impurity lines in the visible and near-uv. Impurity temperatures vary between 30 ev and 255 ev depending on the radial and axial position in the plasma. The ion temperature profile inferred from these measurements is consistent with diamagnetism measurements and atomic hydrogen temperature measurements presented in chapter 4. Oma spectrometer measurements made of particular lines at different chordal radii show the wavelength of the line center varies with chordal radius. This is due to rotation of the plasma about the plasma axis. The maximum velocity observed was 1.74×10^6 cm/sec at a radius of 17.4 cm at the $z = 350$ cm location. This velocity corresponds to an electric field of 38 volts/cm. These measurements were performed at two locations : $z = 110$ cm and $z = 350$ cm. Rotation rates inferred differ by 20% from Hα fluctuation frequencies observed on detector arrays in one case and differ by 30% in another case.

Chapter 4

Atomic Hydrogen Spectral Measurements

4.1 Introduction

Most plasmas studied in plasma confinement experiments are created by ionizing hydrogen gas. Atomic hydrogen emission from those plasmas has been well studied. [8,9,10,20] The emission measurements have been used to determine atomic hydrogen densities and ionization rates, and to gain knowledge of the atomic kinetic energy distribution. [8,9,10,20]

This work presents a detailed analysis of the atomic hydrogen emission from the Tara central cell plasma. It includes an investigation of the atomic hydrogen emission in the visible and vacuum ultraviolet and includes both low- and high-wavelength-resolution measurements. There were radially-resolved measurements made at two axial locations and central chord measurements made at four axial locations. In addition, a video camera recorded the two dimensional axially-integrated atomic hydrogen light profiles.

The data gained was used to determine atomic hydrogen densities, ionization rates, and energy distributions. This information was used to estimate the power lost to atomic radiation, ionization and charge-exchange. This analysis is contained in chapter 6.

4.2 Theory of Atomic Hydrogen Spectra

The energy level structure and spectra of the hydrogen atom are described by the Schrödinger equation:

$$H\Psi_n = E_n\Psi_n \tag{4.1}$$

where H is the Hamiltonian of an electron in the field of a proton, Ψ_n is the wave function of state n and E_n is the energy of state n. In the absence of external fields and ignoring the interaction between the electron's orbital angular momentum and its spin, the energy levels are expressed as:

$$E_n = -\frac{13.6}{n^2}(ev) \tag{4.2}$$

Each n level has a degeneracy of $2n^2$. When the spin-orbit interaction is included as a perturbation, the levels are no longer totally degenerate and are split between states of different total angular momentum j. The presence of external fields will also remove degeneracies and cause additional line splitting.

In these low density plasmas, atoms put into excited states will decay spontaneously to a lower state and radiate a photon. The spectral lines resulting from decays to the ground state are called the Lyman series. The first transition in the series is the $n = 2$ to $n = 1$ decay which results in a 10.2 ev photon at a wavelength of $1216\mathring{A}$, which is in the vacuum ultraviolet. The lines are called Lyman α, β, γ etc. in order of increasing initial quantum number. The first transition is called Lyman α. The spectral lines resulting from decays to the $n = 2$ level are known as the Balmer series. The first transition in the series, $n = 3$ to $n = 2$, called Balmer α, or Hα, has a photon energy of 1.9 ev and occurs at a wavelength of 6563 $\mathring{A}$. An energy level diagram of the hydrogen atom is shown in figure 4.1. The Lyman α, Hα, and Hβ transitions are noted.

Due to the spin-orbit splitting, each 'line' is actually several lines. Their number is determined by the selection rule, $\Delta j = \pm 1$, and their separations are determined by magnitude of the spin-orbit interaction. When no other line splitting or broadening mechanisms are present, the separate 'fine structure' lines can be resolved. When other broadening mechanisms are operative, such as thermal broadening, the fine structure lines will be "washed out" and a single feature will be observed.

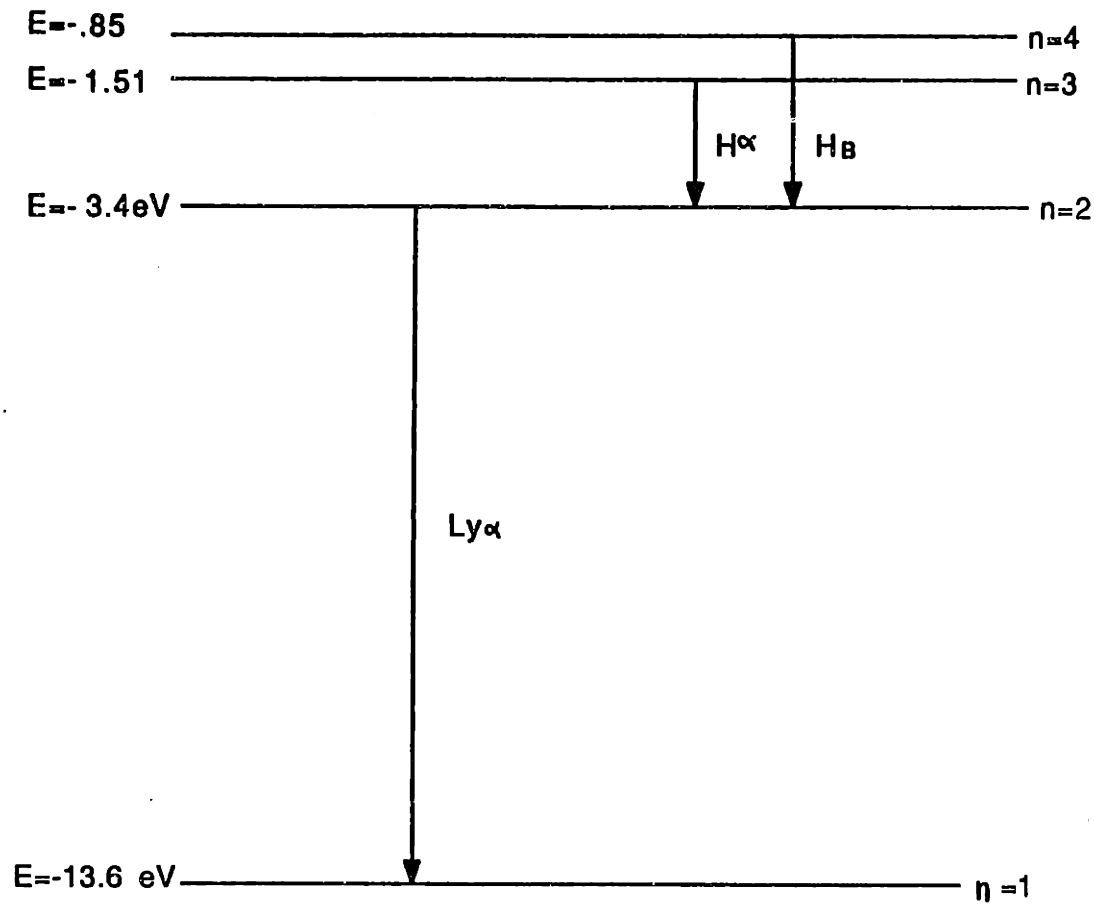

Figure 4.1: Atomic hydrogen energy level diagram.

Several mechanisms can change the energy level. They are collisional excitation or de-excitation, or decay from higher states or the continuum. Decay from the continuum is called 'recombination', in which an electron combines with a proton to form a hydrogen atom. At the electron densities and temperatures found in the Tara central cell plasma and at its edge, the primary population mechanism is electron collisional excitation from the ground state. For example, to populate the n = 3 level:

$$e + H_{n=1} \rightarrow e + H_{n=3} \tag{4.3}$$

The temperatures are a factor of 20 too high for recombination to be significant during the rf pulse. After the rf pulse the electron temperature drops to below 5 ev and recombination takes place. Once in an excited state, the atom decays to a

lower state and emits a photon. The decay lifetimes range from 1.6 nanoseconds for the Lyα decay to 88 nanoseconds for the Hγ decay.

Another way to create an excited atom in the plasma is dissociate a hydrogen molecule. There are several channels of dissociation which can produce ground state atoms, protons, or excited atoms. For example, a molecule may be excited to a state which dissociates into a ground state atom and an atom in the n = 3 state:

$$e + H_2 \rightarrow e + H_2^* \tag{4.4}$$

$$H_2^* \rightarrow H_{n=1} + H_{n=3} \tag{4.5}$$

The excited atom will then radiate an Hα photon within a mean time of 10 nanoseconds. This process is known as dissociative-excitation.

4.3 Atomic Hydrogen Low-Resolution Spatial Profiles

Measurements of atomic hydrogen emission were made with the Oriel monochromator at z = 350, the vuv monochromator at the z = 350 cm , and with the oma spectrometer at z = 0 cm, 30 cm, 110 cm, and 350 cm.

The vuv monochromator was used to measure the Lymanα emission. The measurements were made using a resolution of 6 $\AA$. High resolution measurements of the Hα line to be discussed in the next section showed that the broadest component of the Lyα line would have a width of .55 $\AA$. Therefore the vuv measurement is the integral of the total line intensity. The Hα temporal and spatial intensity profiles were measured first with the Oriel monochromator. The instrument was operated with a slit width of 300 μmeters which corresponded to a resolution of 30 $\AA$ fwhm. Since this width is much greater than the widest wavelength component as measured in the high resolution studies, 3 $\AA$, the Oriel measurement includes the total line intensity.

The Hα brightness was also measured by the central chord Hα detector located 30 cm north of the 350 cm location. This detector was calibrated by comparing the signal intensity with the absolute brightness measurement from the Oriel instrument, with the Oriel tuned to measure Hα brightness. The behavior of the intensity in time was identical at the two locations. Since the ratio of brightness

between 350 cm and 380 cm was expected to remain constant, the central chord detector yielded the central chord Hα brightness for all of the discharges studied.

A plot of the Lyα brightness versus time at the 350 cm location is shown in figure 4.2 along with a plot of the Hα brightness versus time at 350 cm and a plot of the line-integrated density at 200 cm vs time for the same discharge. The Lyα brightness measurement is accurate to 14% and the Hα brightness measurement is accurate to 10%. The brightness plots are characteristic of all the atomic hydrogen spectra plots measured at this location. There is a sharp rise and fall in emission at the start of the discharge, the 'burnout spike', followed by period of nearly constant emission. The increase in electron density at 33 milliseconds was due to a 50% increase in the gas injection rate. The brightness during the discharge varied in proportion to the electron density variation. The difference in the ratio of the burnout spike to the emission during the steady state for the two lines is due to a difference in the time resolution of the two instruments. The resolution of the vuv instrument was 1 msec and the resolution of the Oriel instrument was 10 μseconds.

The chordal brightness profile of the Lyα emission was measured before and during the gas injection increase. The chordal profile before and during the injection increase is shown in figure 4.3. The profile before the increase shows the same type of asymmetry as in the impurity brightness profiles. Since the emission asymmetry is observed in both the neutral spectra and the impurity ion spectra, the asymmetry must be due to either an asymmetry in the excitation rate or in the electron density and not in atomic density. During the period of increased fueling the emission profile is higher and more symmetric.

This measurement was performed four times with the line integral of the electron density varying from $.5 \times 10^{14} cm^{-2}$ to $.75 \times 10^{14} cm^{-2}$. The brightness profile inside 10 cm did not vary with line-average density. The radius where the emission equaled one half of the peak emission varied between 14 cm and 15.5 cm. The multichord interferometer, which did not operate during these measurements, showed the half-width of the radial density distribution typically varied as much as 2 cm. Therefore, the variation in the Lyα emission profile might have been caused by variation in the electron density profile.

Chordal brightness measurements of the Hα emission were made at $z = 350$ cm with the Oriel instrument and $z = 110$ cm with the oma spectrometer. The

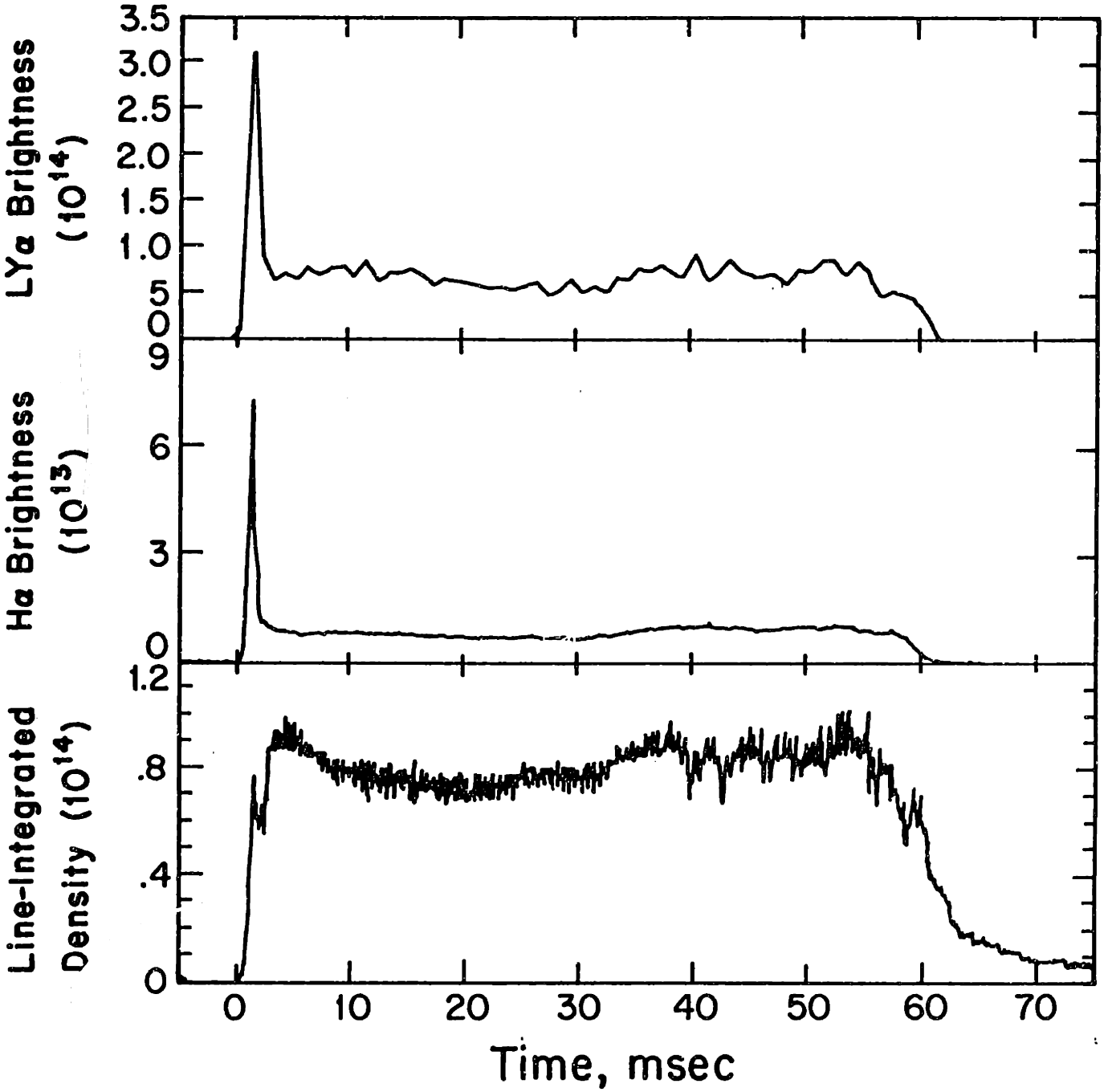

Figure 4.2: Lyα and Hα brightnesses and line-integrated density versus time.

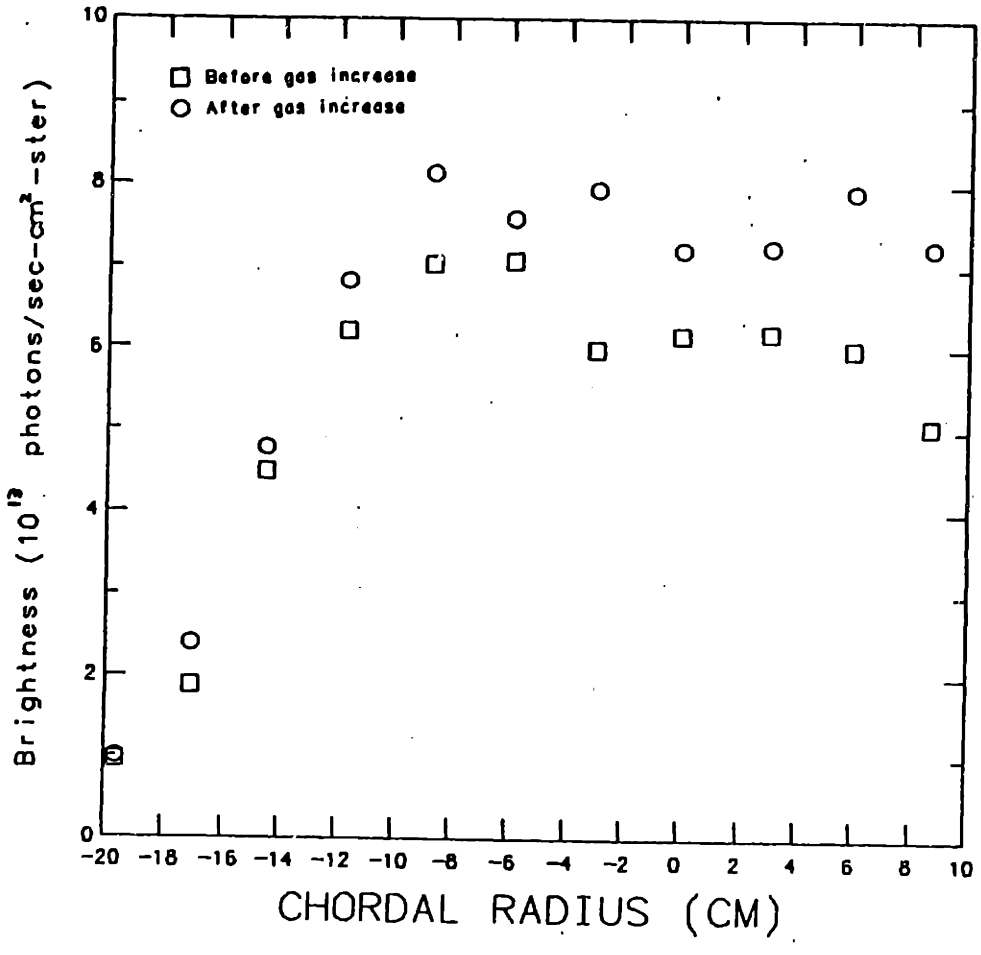

Figure 4.3: Lyα chordal brightness profile.

oma spectrometer measurements were made using the multidetector array. The resolution used was .65 Å. Figure 4.4 shows the normalized brightness profile measured at 350 cm and the normalized profile measured at 110 cm on the same plot. The chords used in the 350 cm measurement originate at a point underneath the chamber and the chords used in the 110 cm measurement originate at a point on the east side of the chamber.

Again, both brightness profiles were consistent inside a 10 cm chordal radius and the radius where the emission equaled half the peak emission varied 1.5 cm. There is an asymmetry in emission showing greater emission east of the center of the chamber. The volume emission profile inferred from these profiles will be presented and discussed in chapter 6.

The Hα chordal profile at 350 cm differs from the Lyα profile at 350 cm. The

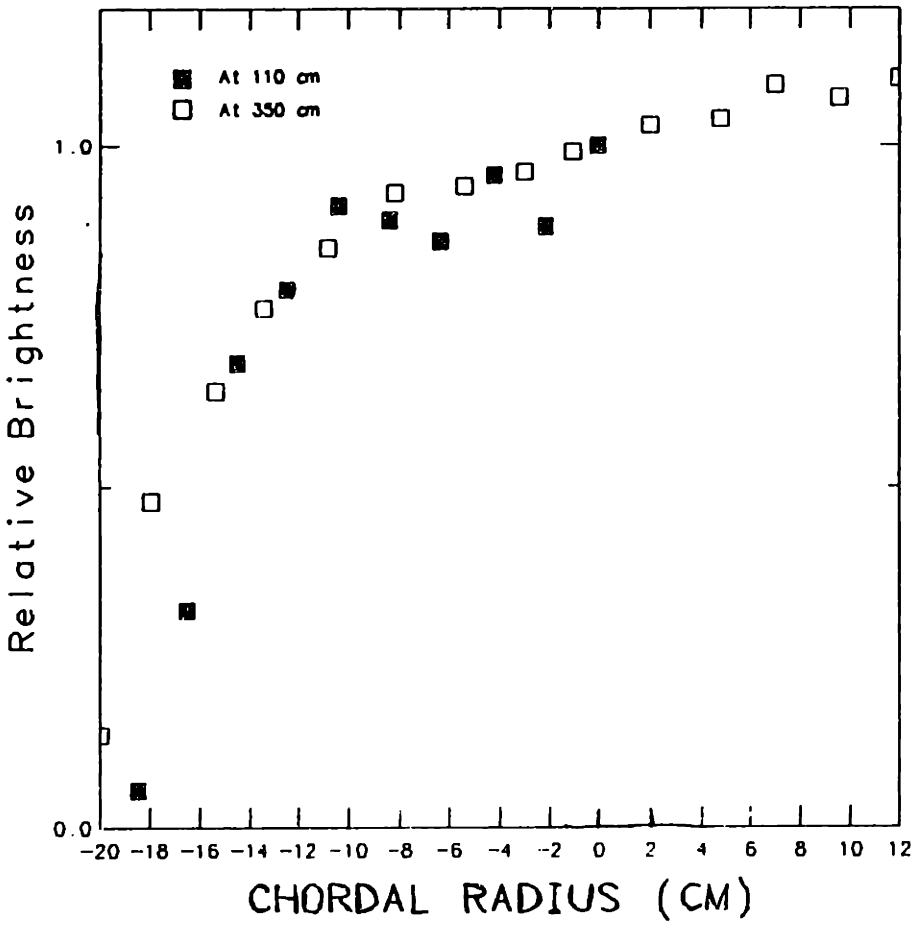

Figure 4.4: Hα chordal brightness profile.

Hα brightness is half its maximum at a chordal radius of 17 cm while the Lyα brightness is half its maximum at a chordal radius of 15 cm. In addition, the Lyα profile does not show the increase in brightness for positive values of chordal radius. These differences may be due to azimuthal asymmetries since the Hα profile is east-west while the Lyα profile is up-down.

Shot-to-shot single chord brightness measurements were made at z = 0 cm and z = 30 cm using the oma spectrometer with the photomultiplier. Figure 4.5 shows plots of the Hα, Hβ, Hγ(n = 5 to n = 2), and Hδ(n = 6 to n = 2) brightnesses versus time at z = 0 cm for a series of discharges. Figure 4.6 shows plots of the Hδ, Hϵ (n = 7 to n = 2),Hζ(n = 8 to n = 2), and Hη(n = 9 to n = 2) brightnesses versus time measured from the same series of discharges. All of these brightness measurements are accurate to 10%.

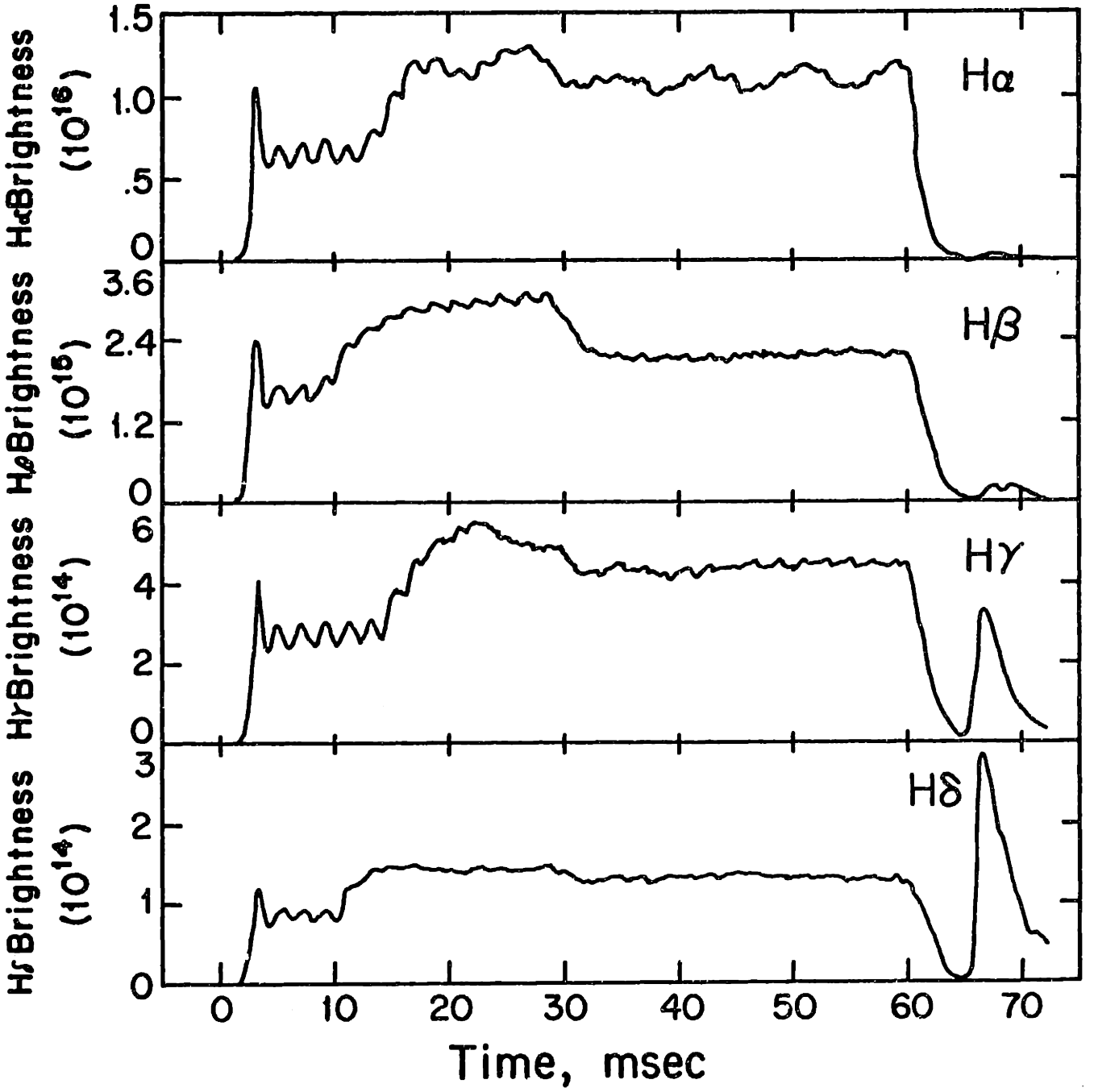

Figure 4.5: Plot of the first four lines of the Balmer series versus time.

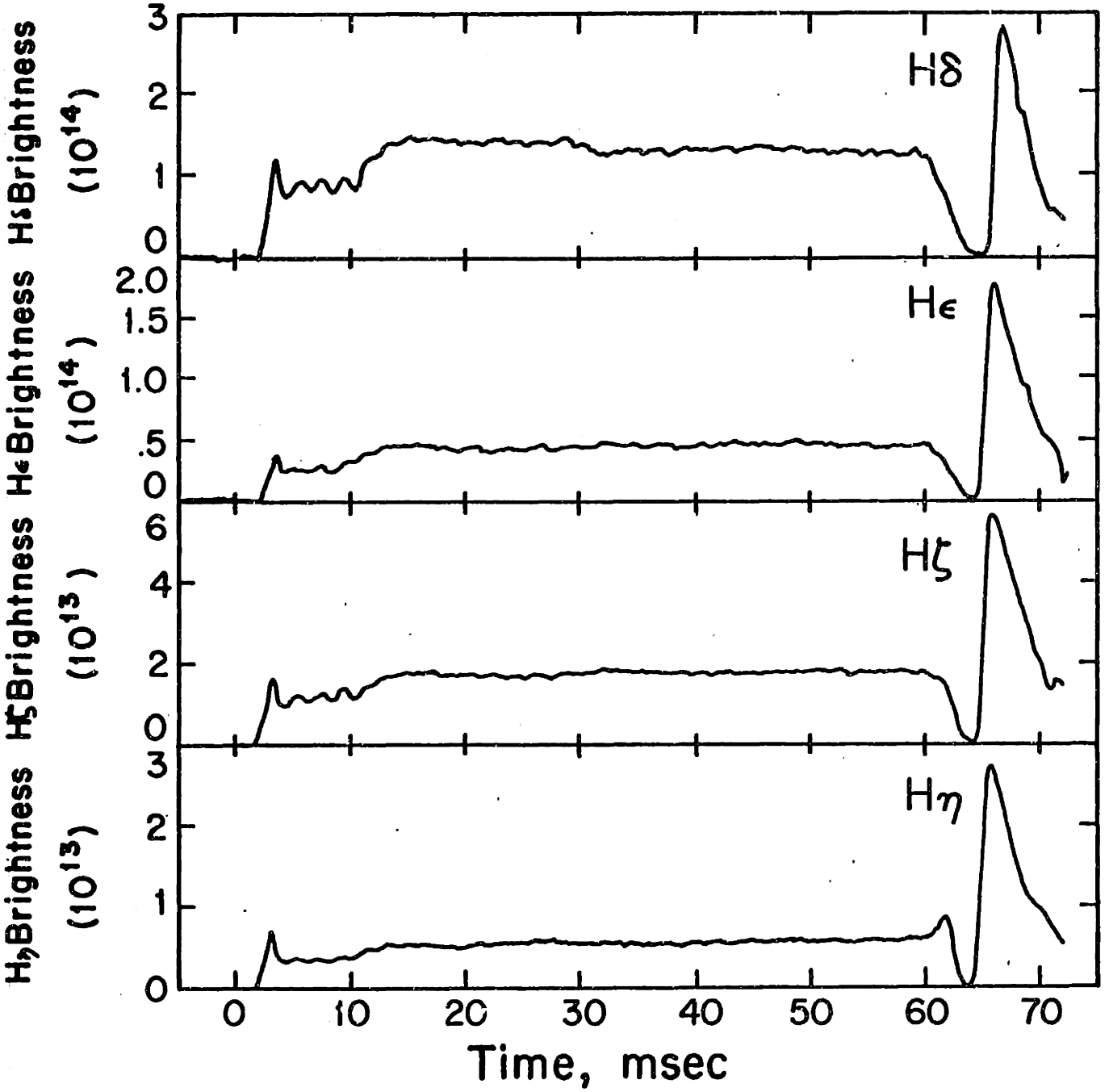

Figure 4.6: Plot of the n = 6 through n= 9 Balmer line brightnesses versus time.

The different brightnesses show the same temporal behavior during the discharge. Oscillations in emission during the first 15 milliseconds are probably due to an oscillation in the local atomic density since the electron density does not show the oscillations. The temporal behavior after the end of the rf pulse is different for each transition in the series. A few milliseconds after the end of the rf pulse at 60 milliseconds the emission decays to almost zero emission and then rises sharply. The ratio of the emission during this rise to the emission during the discharge depends on the initial quantum number of the transition. The higher the initial quantum number, the greater the proportionate rise in emission following the end of the rf pulse.

This is due to a difference in population mechanisms for the two periods. During the discharge the excited state levels are populated by mainly by excitation from the ground state. After the rf pulse the plasma cools and the electron temperature falls to a few ev. The ratio of Hβ to $H\alpha$ emission increases to .33, which is consistent with a 1-3 ev electron temperature. [7] Recombination then takes place and the levels are populated by recombination from the continuum.

The dependence of Hα brightness on z is seen in figure 4.7. The figure shows the intensity measured at z = 0 cm, 30 cm, 350 cm, and the line-integral along z. The data presented from z = 0 cm, z = 350 cm, and the line-integral along z were all collected from the same discharge. The data presented from z = 30 cm was collected from a different discharge which had different gas injection timing.

The brightness shows a strong dependence on z, with the intensity during the steady state greatest at z = 0 with a brightness of $1.1 \times 10^{16} photons/(sec - cm^2 - ster)$ and falling to a brightness of $1. \times 10^{13} photons/(sec - cm^2 - ster)$ at z = 350 cm. The brightness at the start of the discharge decreases less with z, falling to $2 \times 10^{14} photons/(sec - cm^2 - ster)$. These measurements will be discussed in chapter 6.

4.4 Atomic Hydrogen High-Resolution Line Shape Measurements

The wavelength distribution of the Hα line was studied under high resolution, .13$\mathring{A}$ to .65$\mathring{A}$, in order to determine the energy distribution of the radiating particles. The instruments used were the Wadsworth film spectrograph, the Fabry-Perot

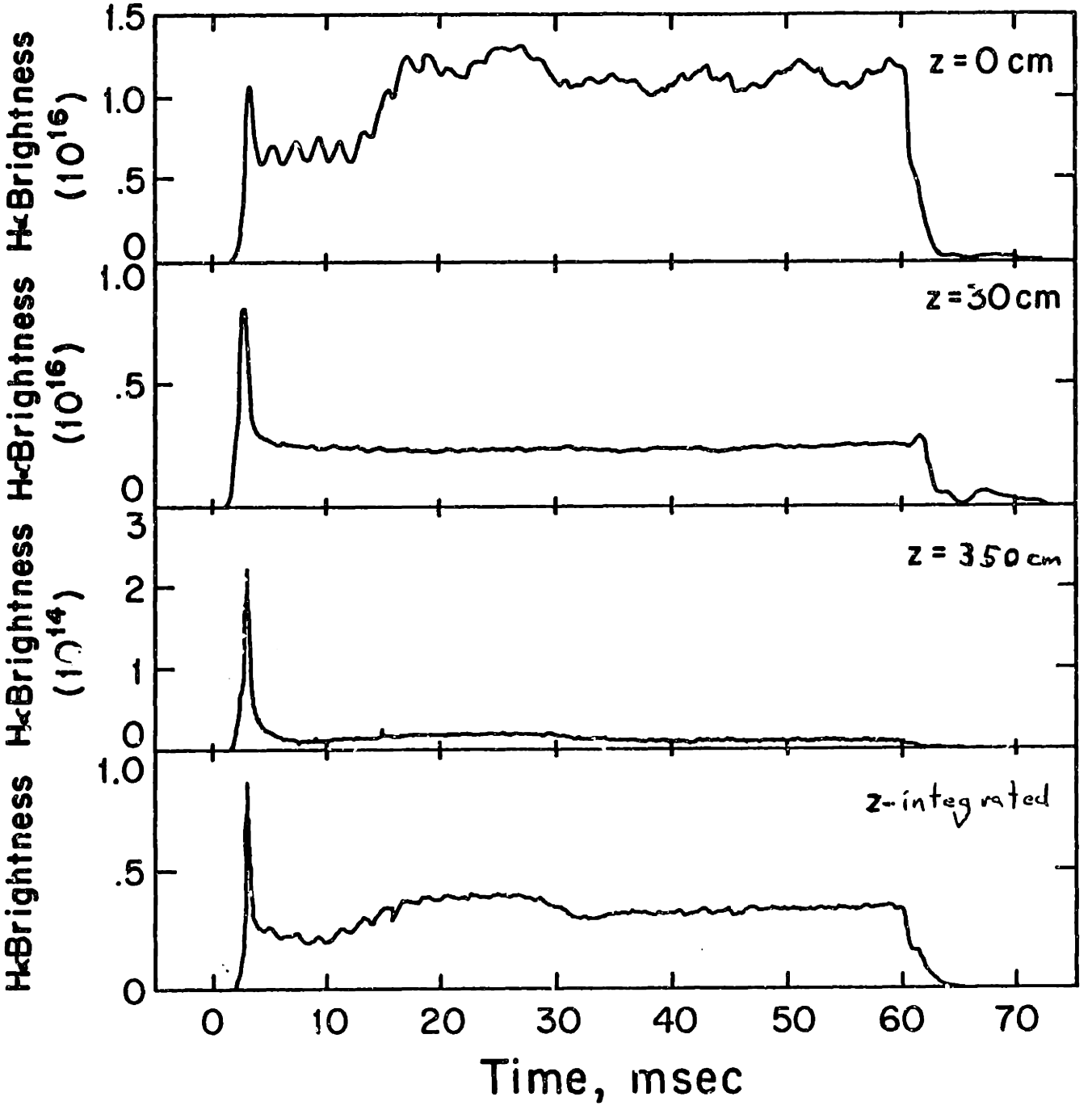

Figure 4.7: Plots of the Hα brightness at z = 0, 30, and 350 cm, and the axially-integrated brightness.

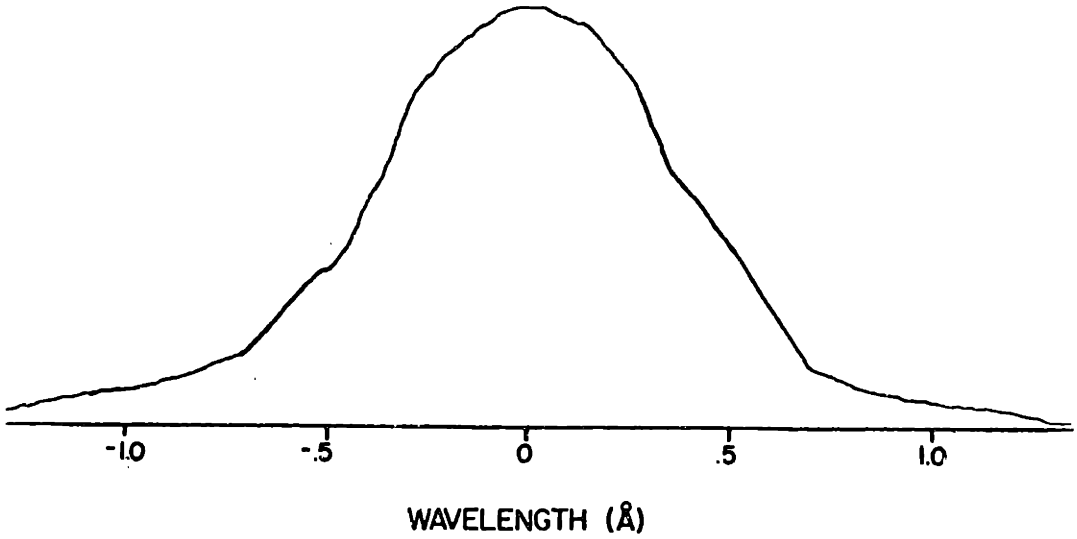

Figure 4.8: Film spectrograph Hα line profile.

interferometer, and the oma spectrometer. Initial m surements were made with the film spectrograph.

The film spectrograph was exposed to plasma emission exiting a 3 cm window located at z = 290 cm. The film was exposed to light from ten discharges. Since the shutter remained open for the entire discharge, the measurement is an average for the entire discharge. From measurements of the Hα versus time at 350 cm, the radiation from the initial burnout spike is between 10 and 30 percent of the total time- integrated emission.

The resolution obtained was .2Å. A plot of the intensity versus wavelength obtained with the densitometer is shown in figure 4.8. There is a central component with a width of .75Å which extends to .8Å from the line center and a broader component with a width of approximately 2Å which extends to 1.4Å from the line center. The inner width corresponds to an atomic temperature of 1.5 ev and the outer width corresponds to a temperature of 16 ev. The lower energy component was then studied at higher resolution with the Fabry-Perot interferometer, which was located at z = 350 cm.

The interferometer was operated in a voltage-sweep mode during the discharge. The voltage on the piezoelectric crystals was varied linearly in time. The mirror spacing and the resonant wavelength therefore changed linearly in time during the scan. In order to ensure that the wavelength integrated Hα line intensity did

not vary during the sweep, the total line intensity was monitored with the central chord photodiode.

The 'effective' resolution obtained was a function of the instrumental finesse and of the vibration of the apparatus. Installing the instrument table in a sandbox sitting on two inch thick rubber mats decreased the vibration but did not eliminate it entirely. The mirrors vibrated with approximately a one kilohertz frequency. The vibration was manifested by intensity spikes on the pmt output while the interferometer was scanning over a wavelength region of changing intensity. Due to these spikes, the scan time was maximized so that the spikes could be averaged out in the data processing.

The measurements made of the central portion of the line were made using a 2 mm diameter pinhole and a 10 $\mathring{A}$ fwhm $H\alpha$ bandpass filter. The resolution obtained was .13$\mathring{A}$. This was determined by measuring the line profile from a HeNe laser during a discharge with the instrument set up in the data collection mode.

In order to determine the free spectral range and the time-to-wavelength conversion factor, the spectrum from a lamp containing both hydrogen and deuterium was measured during a discharge with instrumental conditions identical to those used in data collection. The deuterium alpha line has a wavelength of 6561.03$\mathring{A}$ and the hydrogen alpha line has a wavelength of 6562.79$\mathring{A}$. [11] Both lines appear in the spectrum during the sweep. Since Dα has a shorter wavelength than Hα, the line appearing before Hα in time must be Dα. The wavelength separation is used to determine the free spectral range and the conversion from time to wavelength. The free spectral range was 3.3$\mathring{A}$ which implies the mirror spacing was 653 mμ.

The signal was filtered with a 100 khz filter and digitized at 100 khz. Figure 4.9 shows a plot of interferometer output with the instrument viewing along a central chord, the central chord detector output, and the piezoelectric driving voltage. The wavelength scale is indicated on the figure.

Several features are notable in the wavelength scan. (1) The line profile is symmetric after the initial burnout spike, indicating that the wavelength distribution is constant over the scan interval. (2) The burnout spike is a factor of three higher than the light intensity following the spike, while in the measurement of the wavelength-integrated emission, the burnout spike is a factor of forty higher than

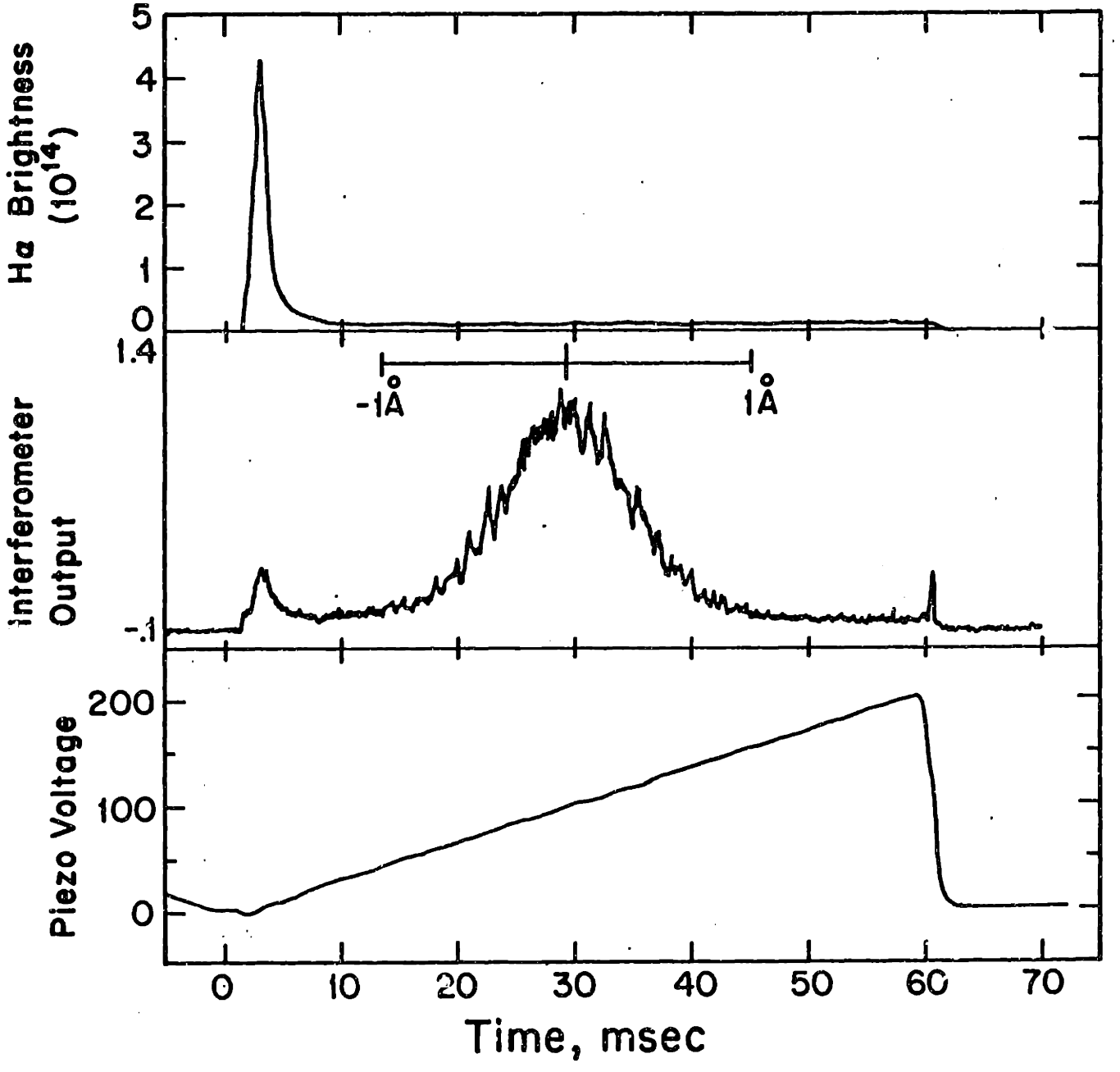

Figure 4.9: Wavelength-integrated Hα brightness, pmt output, and sweep voltage.

the emission after the spike. This indicates the time behavior of the Hα emission radiated with a wavelength shift of between 1.4$\AA$ and 1.7$\AA$ is different than the time behavior of the emission with shifts of less than .5$\AA$, which includes most of the light. Indeed, the initial spike in emission on the interferometer output may be from light with shifts of less than .5$\AA$, since the instrument has a finite wavelength contrast. (3) The emission does not reach a zero value during the scan. Since the free spectral range is 3.3$\AA$ the halfway wavelength between orders is 1.65$\AA$ from the line center. This suggests there was emission with shifts greater than or equal to that value. This was observed in interferometer measurements made with a wider free spectral range, and in oma spectrometer measurements, both of which are presented later in this section.

Figure 4.10a shows a plot of the wavelength scan of the plasma emission shown in figure 4.9 along with a plot of the spectrum of the hydrogen-deuterium lamp used to determine the time-to-wavelength conversion, shown in figure 4.10b. The plasma emission has been smoothed using a digital filter. The plasma profile is broader than the lamp profile, which itself is broader than the instrumental profile. The width of the Hα and Dα lines in the lamp profile indicates an atomic temperature of 3000 degrees Kelvin.

In order to determine the instrumental function of the interferometer, the instrument was set up to measure the profile of the Helium-Neon laser line at 6328$\AA$ during a discharge. This wavelength falls within the range of the interferometer plates. Figure 4.11a shows a plot of the emission shown in figure 4.9 plotted along with a scan of the HeNe laser line, shown in figure 4.11b. The laser line has an actual width of less than .01$\AA$, which is negligible in comparison to the instrumental width. Thus, the measured distribution of the laser line is the instrumental function. It is smaller than the measured plasma emission width by a factor of eight. The measured plasma emission wavelength distribution therefore approximates the radiated distribution. The half-width of the Hα line is .77$\AA$ which would correspond to a temperature of 2.5 ev. The diamagnetism and line-integrated density during the scan were .003 % and $5 \times 10^{13} cm^{-2}$. The wavelength distributions will be examined in more detail in chapter 6.

Line profiles of Hα were measured under various conditions and were observed to vary according to the conditions. Figure 4.12a shows the distribution measured when the diamagnetism was .0025 % and the line-integrated density was

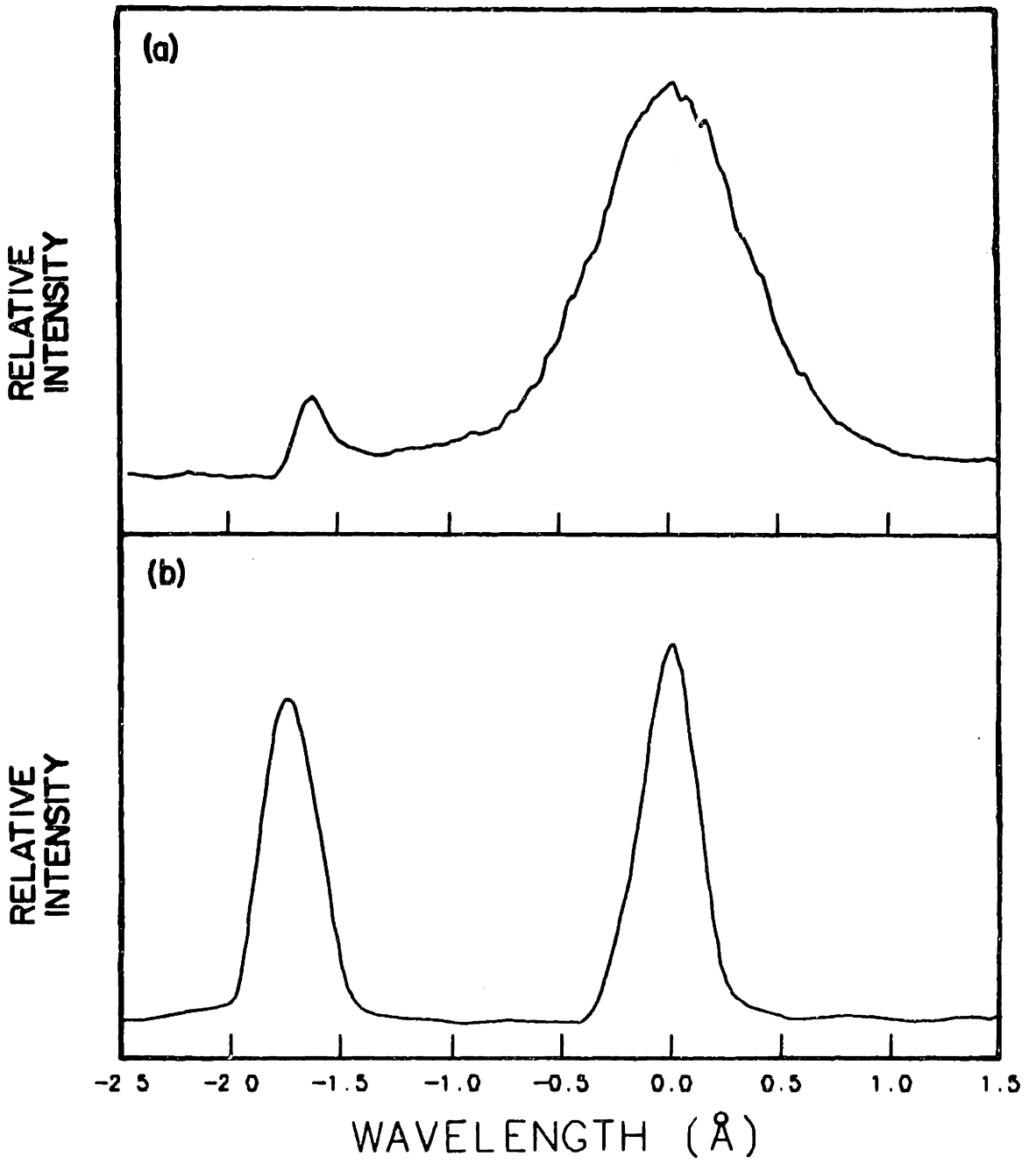

Figure 4.10: (a) Hα line profile, and (b), H-D lamp scan.

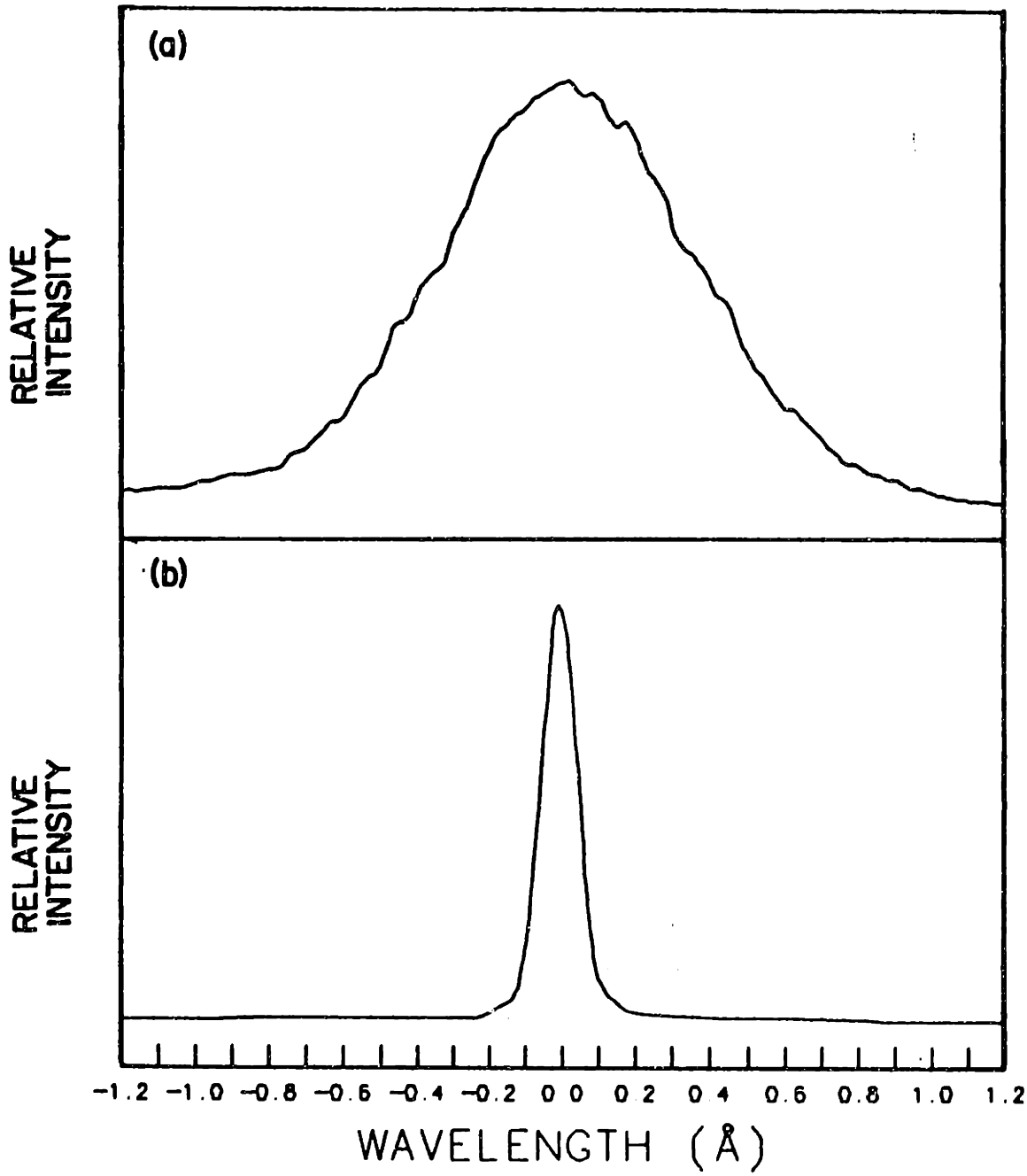

Figure 4.11: (a)Hα line profile, and (b), HeNe laser line profile.

$7 \times 10^{13} cm^{-2}$. Since the diamagnetism is lower and the line-integrated density is higher than in the case presented in figure 4.11, the ion temperature, or electron temperature, or both may be lower. The half-width of the profile is .48$\AA$, which is narrower than the width of the higher diamagnetism/lower density case. This width would correspond to a temperature of .9 ev if the distribution were thermal. The wavelength distribution will be analyzed in chapter 6. Hα profiles virtually identical to this profile were measured in experiments performed on the EBT device [20,21,22,23,24]. Figure 4.12b shows the profile measured from a very weak discharge in which the injected rf power was less than ten percent of the normal power, the line-integrated density was a factor of ten lower than normal, and which had no measurable diamagnetism. The gauge pressure was a factor of five higher than normal in the beginning of the scan, indicating higher molecular or atomic densities. The gauge pressure and central chord brightness decreased over the scan interval. The line shape, which was obtained by dividing the interferometer output by the central cord detector output, shows an asymmetry which indicates the distribution changed during the scan interval. The narrow profile measured early in the scan was never seen in plasma measurements and may indicate a high molecular dissociative excitation contribution. While the instrument swept through the center of the line, the pressure and central chord emission decreased, indicating a lower molecular or atomic density. After the gauge pressure and central cord emission decreased, the profile resembled those measured during successful discharges.

In order to determine the radial variation of the Hα inner line profile, the instrument was set up to view the plasma in the radial scanning mode for a series of discharges which had constant plasma conditions. Figure 4.13a-d shows these profiles. They did not vary within the experimental uncertainty, which was due mainly to electronic noise and statistical fluctuations. These profiles will be discussed in chapter 6.

The measurements made with a free spectral range of 3.3$\AA$ suggested the presence of Hα emission with wavelength shifts beyond 1.65$\AA$. In order to measure the distribution of the complete line, the interferometer mirror spacing was changed to 150 μm, as determined from free spectral range measurements. The free spectral range was then 14.5$\AA$. Figure 4.14 shows a plot of a wavelength scan in this mode during a discharge with diamagnetism of .0025 % and a line integrated density of

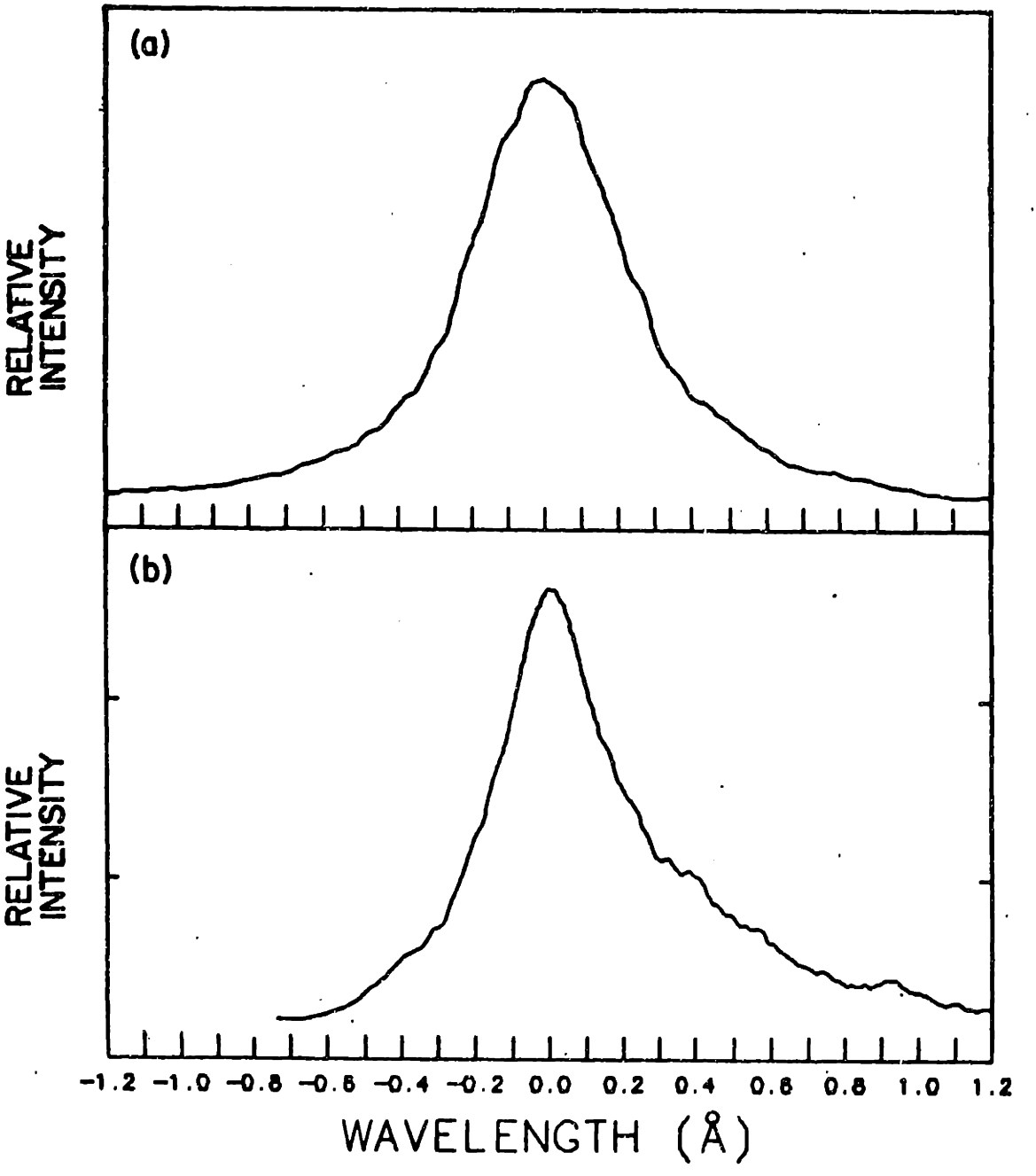

Figure 4.12: Hα line profiles under (a),typical conditions and (b), weak plasma conditions.

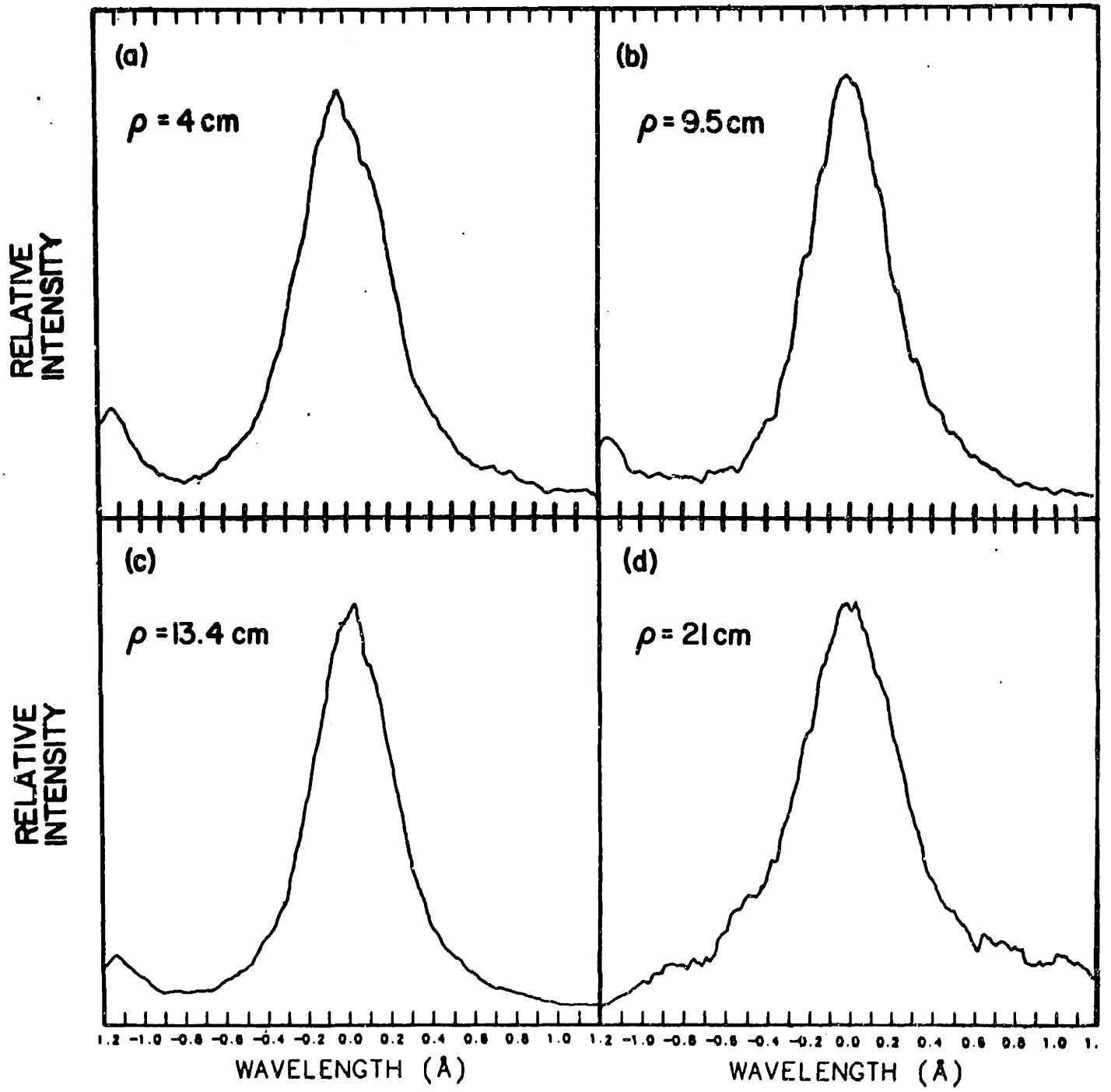

Figure 4.13: Plots of the Hα profile measured along four radial chords.

$7 \times 10^{13} cm^{-2}$. There are wings present in the profile which are consistent with the smaller free spectral range measurements. Emission was seen to decrease to zero at a wavelength shift of $5\mathring{A}$. The asymmetries in the profile are due to vibrations of the interferometer. The inner portion of the line is broadened beyond the instrumental width due to vibrations of the interferometer. Vibration-free measurements were never obtained. Therefore, the oma spectrometer was used to study the complete line shape.

Measurements of the Hα line profile using the oma spectrometer were made using a resolution of $.65\mathring{A}$, which was sufficient to measure the shape of the wide component. Since it was not affected by vibration, the oma spectrometer measurement was more reliable than the wide-sweep interferometer measurement. Figure 4.15 shows the profile measured with the instrument viewing along a central chord at z = 350 cm. The instrument collected light for the second twenty milliseconds of the discharge. The far wings seen on the wide-sweep interferometer profile are present. The oma profile is similar to the wide-sweep interferometer profile, with the difference being that the central component is narrower, due to the lack of vibrational effects. Plotted along with the data in figure 4.15 is a five parameter fitting function. The fitting function is a sum of two functions : (1) a gaussian function and (2) a function which is the convolution of the interferometer-measured profile shown in figure 4.12a, and the oma instrumental function. The oma-convoluted interferometer profile fits the inner portion of the oma measured profile well. The oma measurement is therefore consistent with the interferometer measurement. This fitting procedure is part of the analysis discussed in chapter six.

The profiles obtained from the spectrograph measurement at z = 290 cm, the interferometer measurement at z = 350 cm, and the oma measurement at 350 cm all show the presence of 'far' wings. These wings suggest that there were two energy components: a 'cold' component with a width of $.45\mathring{A}$ and a 'hot' component with a width of $3\mathring{A}$. The presence of two energy components implies there were at least two different mechanisms determining atomic energies. This will be further discussed in chapter 6.

In order to measure the radial variation in the complete line profile, the oma spectrometer was set up in the radial scanning mode. Figure 4.16a-d shows the Hα profiles measured along four non-central chords during a series of constant

condition discharges. Each profile is fitted with the five parameter fitting function. The normalized profiles do not vary with chordal radius within the uncertainty, which is due to statistical fluctuations. The measurements suggest that the kinetic energy distribution of the emitting atoms was constant in radius. This will be further discussed in chapter 6.

In order to study the axial variation of the Hα profile, the instrument was set up at several locations along the axis of the central cell. At the gas box, only central chord measurements were possible. At the z = 110 cm location a radial scan was performed. Figure 4.17a-d shows the Hα line profile measured through a central chord at the z = 0, z = 30, z = 110 during the discharge, along with a plot of the profile measured after the discharge during the recombination phase. The light collection times varied from 500 microseconds at z = 0 to 20 milliseconds at z = 350. The profiles measured during the discharge were all collected in the second 20 milliseconds of the discharge. Profiles were measured at varying times during the discharge and were found to be consistent. Radial measurements of the Hα profile at z = 110 cm showed the profile was independent of radius at that location.

The Hα profiles measured at z = 0 cm, 30 cm, and 110 cm differ from the profiles measured at z = 350 cm in their lack of far wings. The wide component was only present at z = 350 cm. Thus, the kinetic energy distribution of the radiating atoms depends on axial position. This will be discussed in chapter 6.

Any broadening mechanisms affecting the Hα line profile must also affect the other Balmer series lines. In order to gain information about broadening mechanisms, central chord measurements of higher n Balmer lines were made at several axial locations. Figure 4.18a-d shows plots of the Hβ line measured through a central chord at 350 cm, along with plots of the Hβ, Hγ, and the Hζ line (n = 8 to n = 2) measured at z = 0. The Hβ profile measured at z = 350 cm shows a wide component, partly obscured by impurity lines, similar to the Hα profile. The width of the hot component is impossible to determine due to impurity line contamination. The Hβ, Hγ and Hζ line profiles measured at z = 0 cm do not have the hot component, consistent with the Hα profiles measured there. The width of the central portion of the higher n Balmer lines does not vary. The broadening of all of the Balmer line profiles measured is consistent with doppler, instrumental, and fine structure broadening, as will be discussed in chapter 6.

4.5 Summary and Discussion

Radial wavelength-integrated atomic hydrogen emission brightness profiles have been measured at 2 axial locations. The profiles varied only 2 cm in width, which might be due to variations in the electron density profile. The brightness at a particular axial location does not vary more than 20% inside a chordal radius of 10 cm. Central chord measurements of $H\alpha$ brightness made at four axial locations indicate the atomic emission is peaked at the gas port and decreases with distance from the gas port by a factor of 700.

The Hα line profile was measured using three instruments: a film spectrograph at z = 290 cm, a Fabry-Perot interferometer at z = 350 cm, and an oma spectrometer at z = 350 cm. All three profiles showed a central 'cold' component extending to 1 $\AA$ from the line center and a wider 'hot' component extending to 3 $\AA$ or more from the line center. The central 'cold' component measured under certain conditions is similar to profiles measured in experiments at the EBT device. [20,?,22,23,24] At the z = 0 cm, 30 cm, and 110 cm locations, only the 'cold' component was observed. The wide wings observed on the profile at 350 cm have not been observed conclusively in Hα profiles measured in magnetic confinement experiments to date. The far wings indicating the presence of a hot component were was observed only at 290 cm and 350 cm. Profiles of higher n Balmer lines were similar to the Hα profiles from the same locations. Measurements made of the line shape through several non-central chords at z = 350 cm and z = 110 cm with the Fabry-Perot interferometer and the oma spectrometer show the profile was independent of chordal radius.

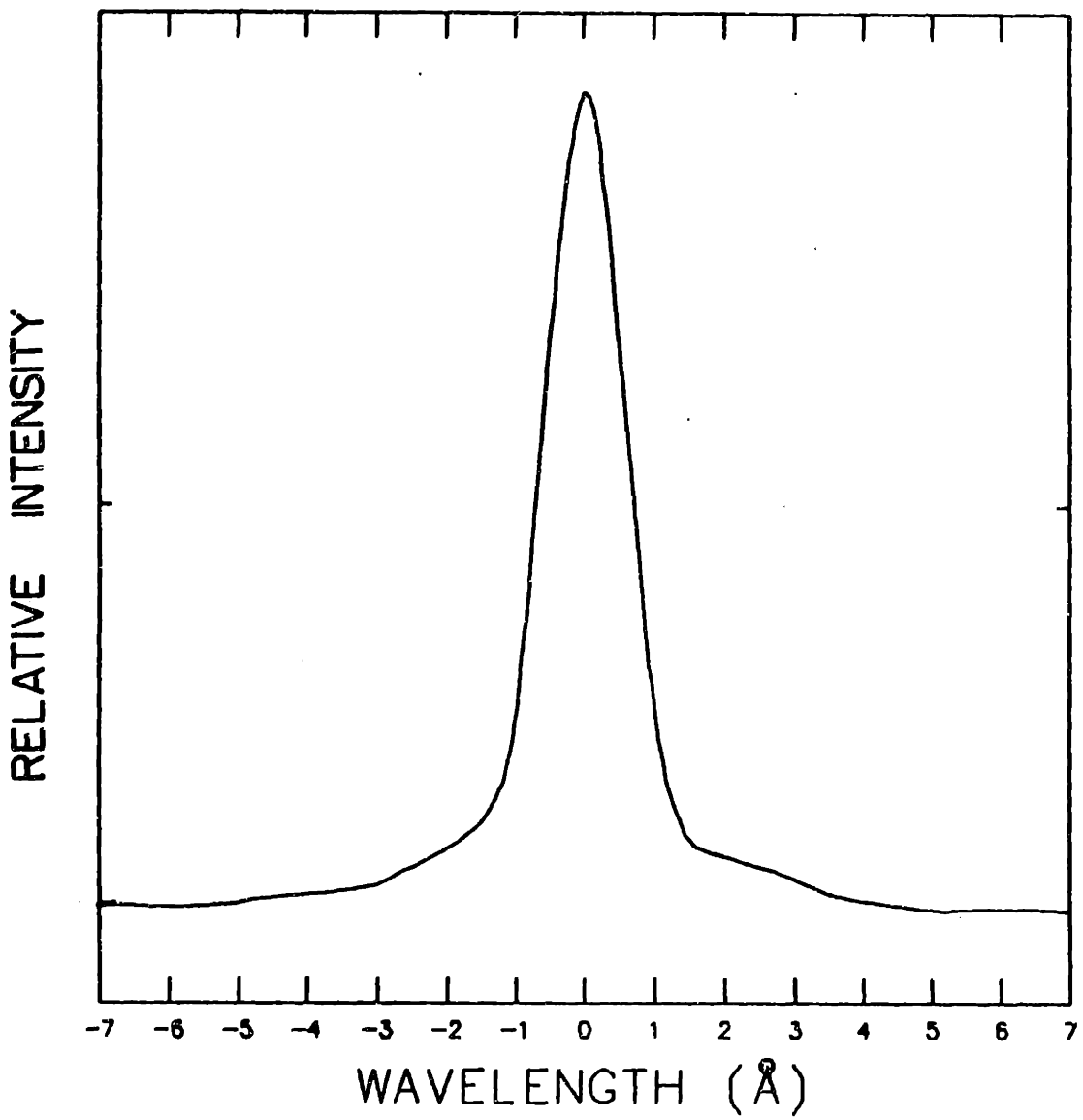

Figure 4.14: Wide free-spectral-range scan of the Hα line.

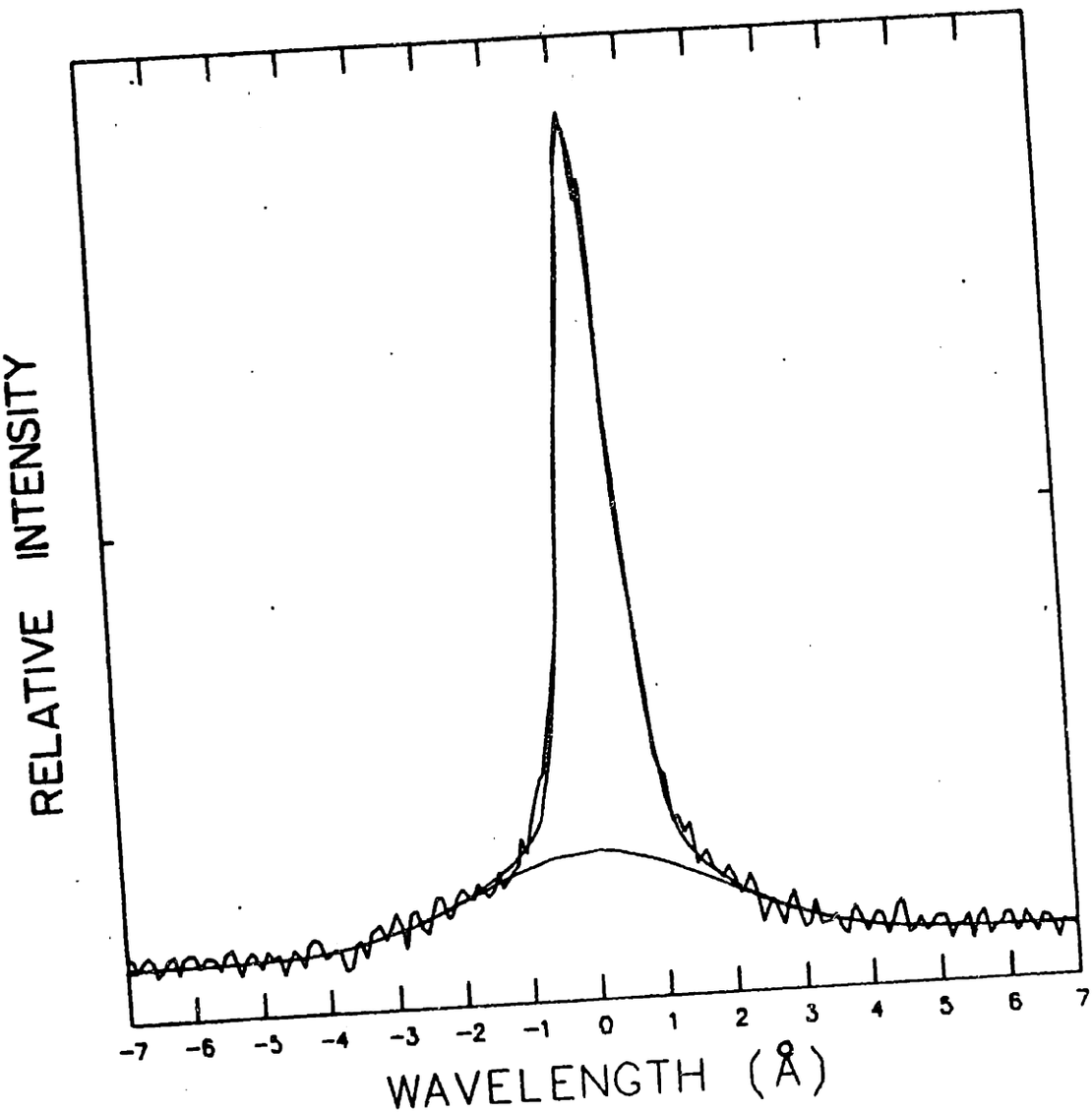

Figure 4.15: The Hα line profile measured at z = 350 cm along a central chord.

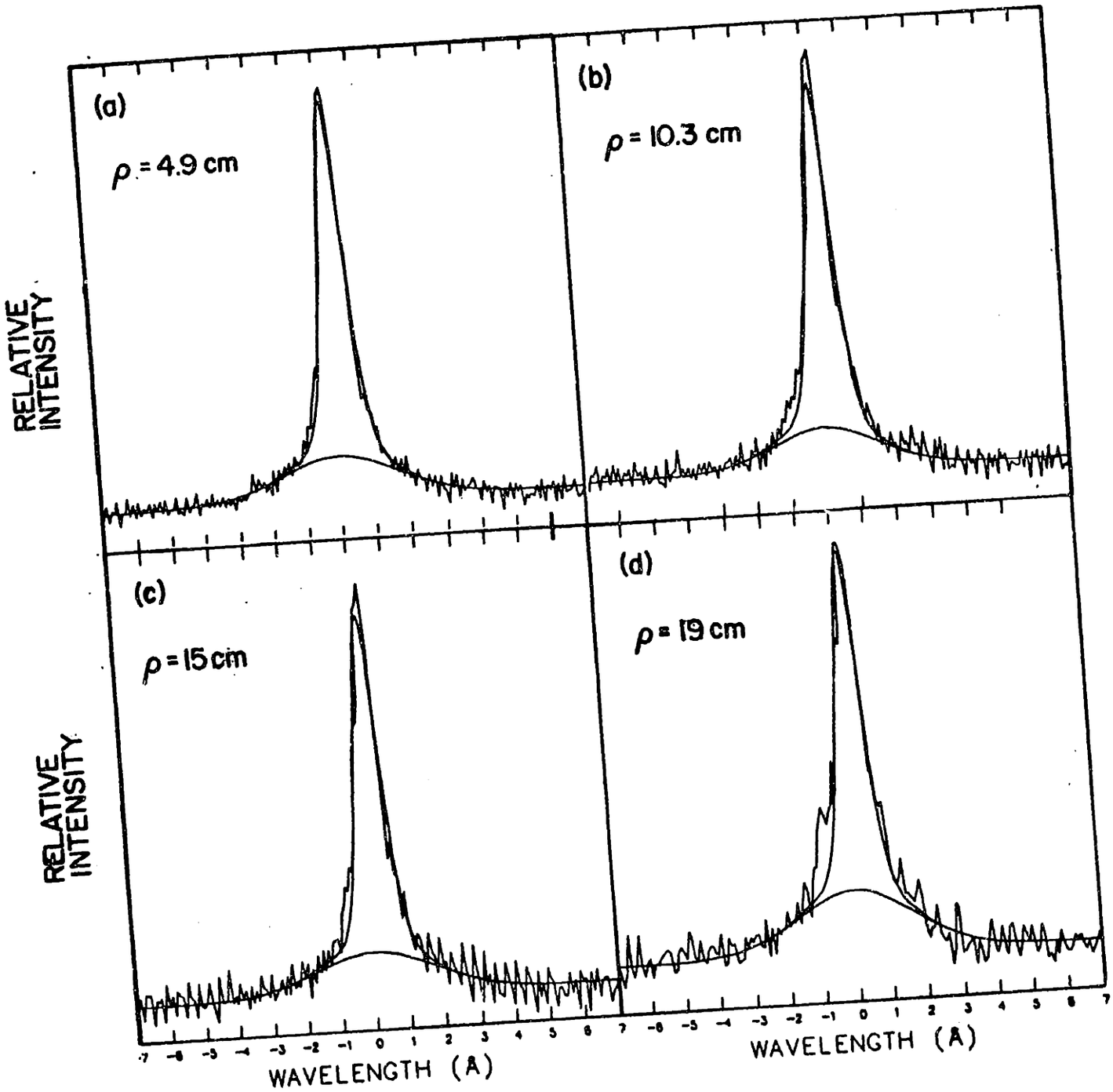

Figure 4.16: Hα line profiles measured along several radial chords at the z = 350 cm.

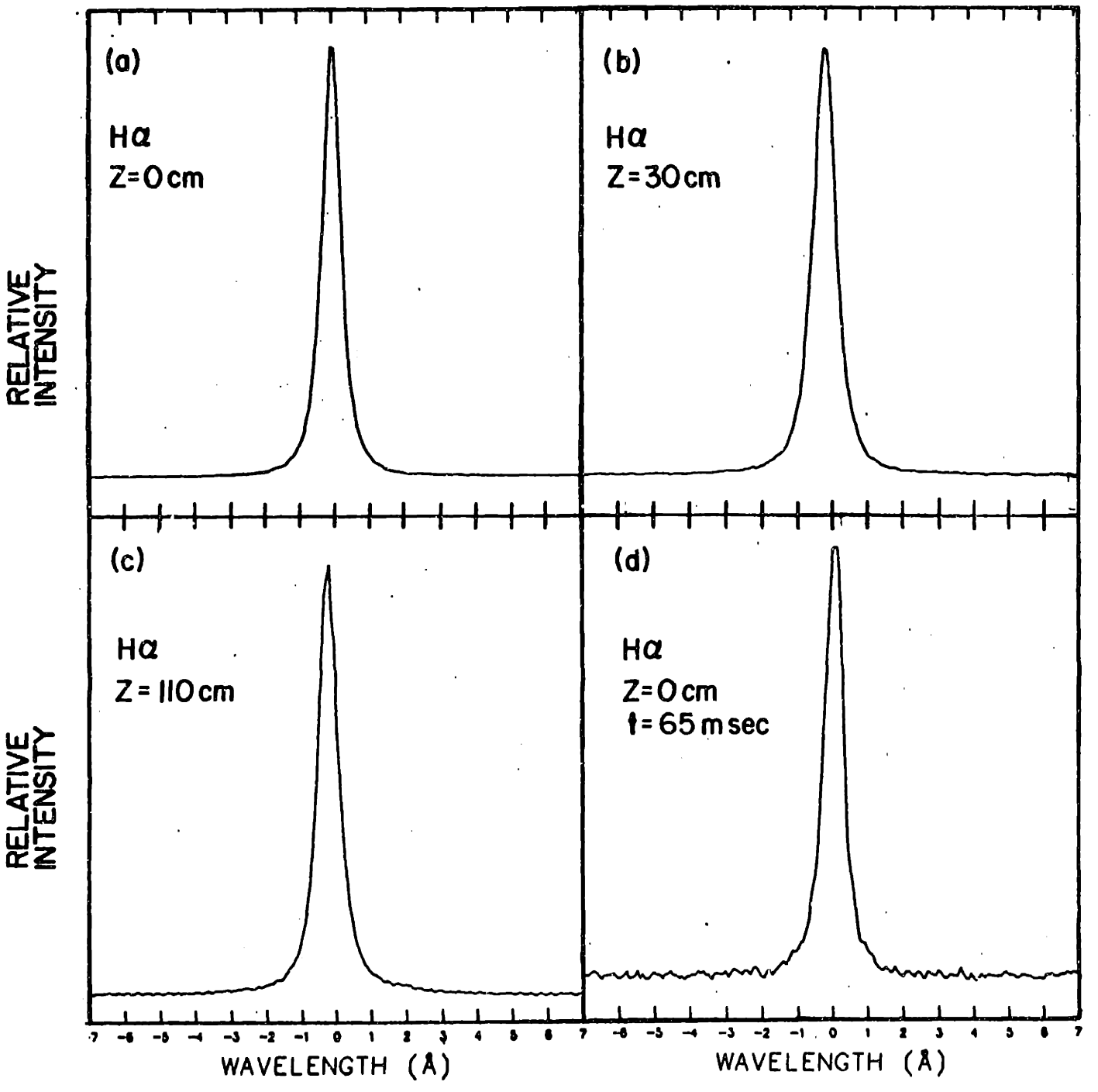

Figure 4.17: Plots of the Hα line profile measured at several axial locations.

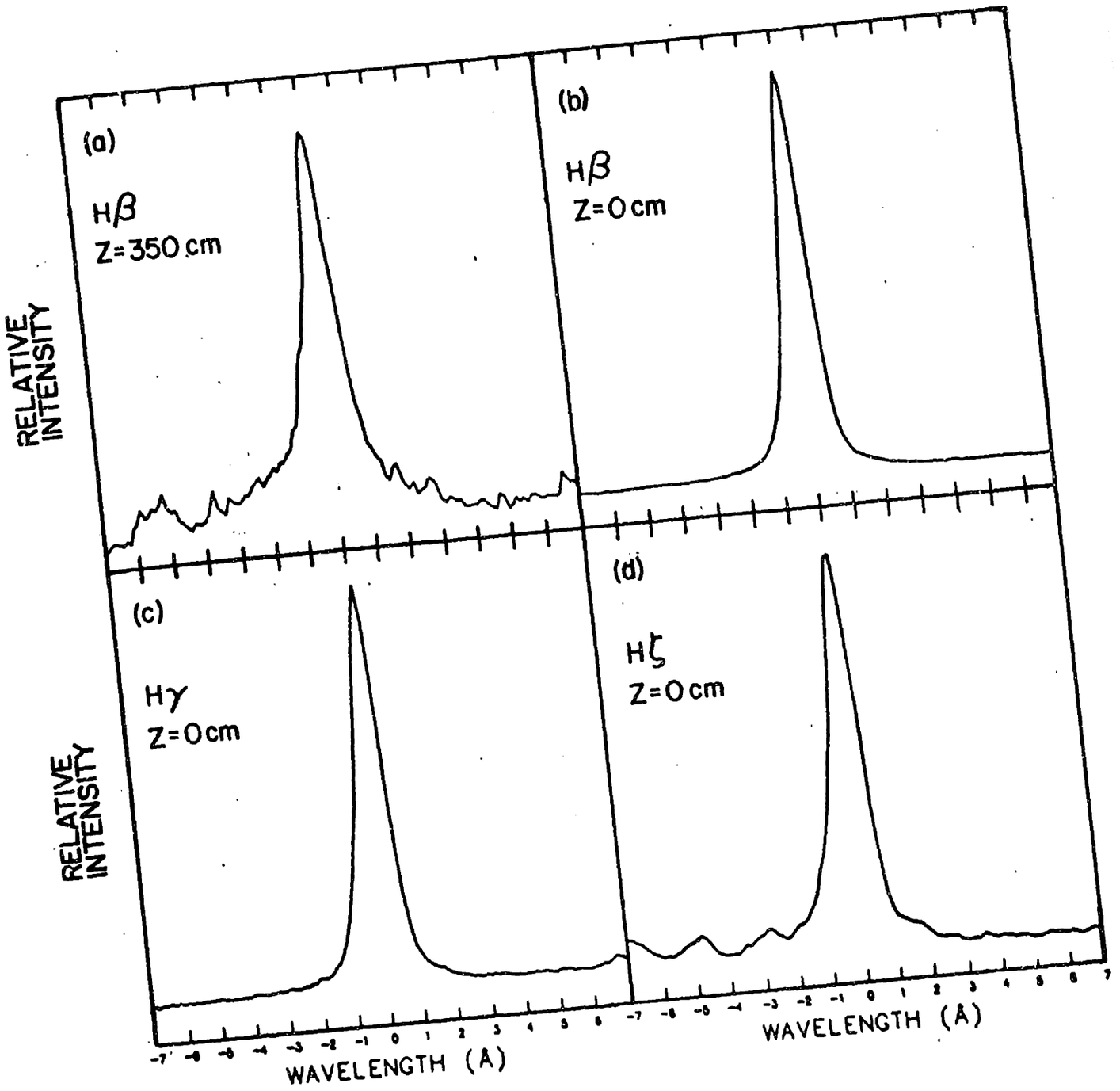

Figure 4.18: Plots of Balmer line profiles measured at z = 350 cm and z = 0 cm.

Chapter 5

Molecular Hydrogen Spectra Measurements

5.1 Introduction

Hydrogen plasmas are created by dissociating molecular hydrogen, which is injected into the plasma in gas form. It is almost always present at the edge of hydrogen plasmas. However, owing to the low density of molecular hydrogen in most magnetically-confined plasmas, and the relatively low intensity of molecular emission lines in plasma spectra, molecular emission has not been well studied in these plasmas. The Tara central cell plasma is better suited for a study of molecular spectra than the higher density plasmas present at most confinement experiments since the molecular density is higher in Tara, due to the lower electron density. This chapter presents a study of the molecular emission from the Tara central cell plasma.

Molecular emission from confined plasma experiments has been studied in the visible and vacuum ultraviolet regions at two experiments. The studies have included molecular bands in the vacuum ultraviolet at the Alcator C Tokamak [25] and individual visible spectral lines at the EBT device [20,26]. The work presented here includes the first intensity measurements of the strongest visible molecular bands(under some conditions), and the first wavelength distribution measurement of molecular hydrogen dissociative-continuum emission from confined plasma experiments. The data gained was used to infer molecular hydrogen densities, dissociation and ionization rates, and information about molecular temperatures.

This chapter presents the basic theory of molecular hydrogen spectra, the results of the molecular line spectra and molecular continuum spectra measurements made on the Tara central cell plasma and a discussion of those results.

5.2 Theory of Molecular Hydrogen Spectra

The theory of the hydrogen molecule is presented in detail in ref. [27,28]. A summary of the theory is presented here.

The energy level structure of the hydrogen molecule is determined by the solving the Schrödinger equation for the total molecular wave function $\Psi(\underline{r},\underline{R})$, where r represents the coordinates of both electrons and R the coordinates of both nuclei.

$$\left(-\frac{\hbar^2}{2\mu}\nabla^2-\frac{\hbar^2}{2m}\nabla_1^2-\frac{\hbar^2}{2m}\nabla_2^2+V\right)\Psi(\underline{r},\underline{R})=E\Psi(\underline{r},\underline{R}) \tag{5.1}$$

where E is the total energy, μ is the reduced nuclear mass, m is the electron mass and V is the total potential energy.

$$V=V_{ee}+V_{eN}+V_{NN} \tag{5.2}$$

where V_{ee} represents the electron-electron repulsion, V_{eN} represents the electron-nuclear attraction, and V_{NN} represents the nuclear-nuclear repulsion.

The wavefunction can be expressed in the form

$$\Psi(\underline{r},\underline{R})=\psi(\underline{r},R)\xi(\underline{R}) \tag{5.3}$$

where $\psi(r,R)$ is the electronic wavefunction, which depends on the nuclear separation as a parameter, and $\xi(\underline{R})$ is the nuclear wavefunction, which depends only on the nuclear coordinates $\underline{R}$. Since the electronic wavefunction varies slowly with internuclear distance, one assumes that

$$\nabla^2\psi(\underline{r},R)\xi(\underline{R})\simeq\psi(\underline{r},R)\nabla^2\xi(\underline{R}) \tag{5.4}$$

neglecting any contributions from the derivatives of $\psi(\underline{r},R)$ with respect to R. Using this approximation, known as the Born- Oppenheimer approximation, eq. 5.1 can be separated into two equations, one determining the nuclear wavefunction and one determining the electronic wave function. The following equation determines the electronic wavefunction:

$$\left(-\frac{\hbar^2}{2m}\nabla_1^2-\frac{\hbar^2}{2m}\nabla_1^2+V(r,R)\right)\psi(\underline{r},R)=E_e(R)\psi(\underline{r},R) \tag{5.5}$$

where $V(\underline{r}, R)$ is the potential energy for a particular nuclear separation, and $E_e(R)$ is the total electronic energy.

At infinite nuclear separation the electronic states $\psi(\underline{r}, R)$ are simply products of separate atomic hydrogen states. At closer distances they are approximated by linear combinations of products of hydrogen atom wave functions. Each molecular state has an energy which is dependent on the nuclear separation R. If the energy has a minimum with respect to the separated atom energy, the state will be bound, and if the state has no minimum the state will be unbound and the molecule will be unstable and will separate into two atoms.

The minimum energy of the molecular ground state is 4.5 ev below the energy of the separated atoms at rest. There are also bound and unbound excited states which dissociate into a ground state atom and an excited atom, or two excited atoms. The first bound excited state has its energy minimum 10 ev above the minimum of the ground state.

The nuclear wavefunction obeys the following equation:

$$\left(-\frac{\hbar^2}{2\mu}\nabla^2 + E_e(R)\right)\xi(\underline{R}) = E_N\xi(\underline{R}) \tag{5.6}$$

where E_N is the energy of the nuclear motion. Thus, the nuclear motion is independent of the electron motion, whose effect appears only through the term $E_e(R)$, which is the electronic energy as a function of the nuclear separation and serves as the potential energy for the two nuclei.

The nuclear wavefunction can be further separated into a radial part and an angular part.

$$\xi(R, \theta, \phi) = \frac{\chi(R)}{R} S(\theta, \phi) \tag{5.7}$$

The nuclear Schrödinger equation can then be separated into an equation for the radial wave function and the angular wavefunction. The angular wavefunction obeys the equation

$$M^2 S_{J,M}(\theta, \phi) = J(J+1)\hbar^2 S_{J,M}(\theta, \phi) \tag{5.8}$$

where M^2 is the operator for the square of the total molecular rotational angular momentum, J is the quantum number for the total molecular rotational angular momentum, M is the quantum number for the z-component of that momentum, and the eigenvalues $J(J+1)\hbar^2$ are the squares of the total molecular angular

momentum for different J states. The eigenfunctions $S_{J,M}$ are the associated Legendre polynomials.

The molecular rotational energy E_J can be expressed in terms of J:

$$E_J = \frac{\hbar^2}{2I} J(J+1) \tag{5.9}$$

where I is the moment of inertia. Thus, a rotational level is separated from the next highest level by an amount of energy ΔE_J

$$\Delta E_J = (J+1)\frac{\hbar^2}{I} \tag{5.10}$$

The average moment of inertia, I_a, depends on the electronic state since the equilibrium separation varies between different electronic states. Average molecular rotational energy E_{rot} is defined in terms of the average moment of inertia.

$$E_{rot} = \frac{J(J+1)\hbar^2}{2I_a} \tag{5.11}$$

The average rotational energy can be substituted into eq.5.6 in place of the rotational energy term. The equation for the radial wavefunction can then be written

$$-\frac{\hbar^2}{2\mu}\frac{d^2}{dR^2}\chi_{v,J} + \left[E_{el}(R) + \frac{J(J+1)\hbar^2}{2\mu R^2} - E_{v,J}\right]\chi_{v,J} = 0 \tag{5.12}$$

where the energy of nuclear motion E_n is the sum of the rotational and vibrational energies.

$$E_n = E_{rot} + E_{vib} \tag{5.13}$$

By expanding $E_e(R)$ as a quadratic function about the equilibrium internuclear distance, R_e, eq.5.12 takes the form of the harmonic oscillator equation. The solutions are the harmonic oscillator wave functions. Their corresponding eigenvalues are given by

$$E_{vib} = (v + \frac{1}{2})h\nu_e \tag{5.14}$$

where ν_e is the vibration frequency. The levels are separated by a fixed amount of energy ΔE_{vib}

$$\Delta E_{vib} = h\nu_e \tag{5.15}$$

Since the potential well is not perfectly quadratic the levels are actually separated by slightly varying amounts of energy. The two lowest vibrational states in the

electronic ground state of H_2 are separated by .45 ev. There are 14 vibrational states below the dissociation limit of the electronic ground state.

Thus, the total energy of a molecular state E_T is the sum of the electronic energy and the energy of nuclear motion.

$$E_T = E_e + E_{vib} + E_{rot} \tag{5.16}$$

In the hydrogen molecule, the minima of the electronic energies are two to five ev below the dissociative limits of the various states and the states are separated from each other by a fraction of an ev to 20 ev. Neighboring vibrational levels of a particular electronic state in H_2 are separated from each other by .2 ev to .45 ev. The first rotational excited state in the ground state of H_2 is .0076 ev above the lowest rotational state, which corresponds to a temperature of 176 degrees Kelvin. Each electronic state has several vibrational states with energies below its dissociation limit and each vibrational state has several rotational states with energies below the energy of the next vibrational state.

In considering transitions between electronic states ref. [27] shows that rotation can be neglected in computing the relative strength of a particular vibrational transition. Since the electronic dipole operator does not operate on χ and does not vary with R, the transition matrix element T for a transition between Ψ and Ψ' can be expressed as

$$T = \int \chi^* \chi' \left[\int \psi^* M_e \psi' d\tau_e \right] dR \tag{5.17}$$

where the integral is over the coordinates of the electrons, τ_e and internuclear distance, R, and M_e is the electronic dipole operator. Assuming that the integral in brackets varies only slowly with R, the probability P, of a transition between a vibrational state v'' in the initial electronic state to a vibrational state v' in the final electronic state is proportional to the square of the overlap integral.

$$P \propto \left[\int \chi_{v''} \chi_{v'} d\mathrm{R} \right]^2 \tag{5.18}$$

The integral depends on the overlap of the two functions, and will be maximized for two functions which are peaked at the same internuclear separation. This ensures that transitions in the molecule will occur without a change in internuclear separation. This is known as the 'Franck-Condon principle' and the square of the overlap integral is known as the 'Franck-Condon factor'. Figure 5.1 shows a

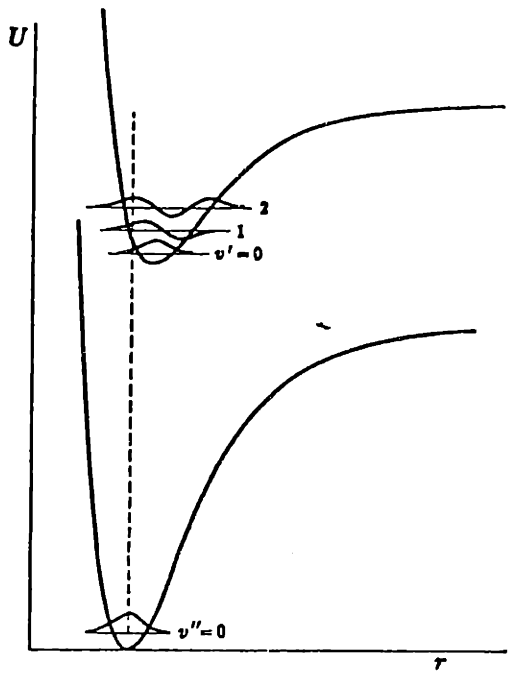

Figure 5.1: Molecular energy diagram showing vibrational wave functions and a transition. Reproduced from ref.[27].

diagram of two potential curves with the ground vibrational state in the lower level and three vibrational states in the upper level(reproduced from ref. [27]). The overlap is greatest between the lower ground vibrational state and the upper second vibrational state of the upper electronic state.

The probability of transition between particular rotational states depends on the type of electronic transition. The allowed change in J will be either ± 1, or 0 and ± 1. The spectral lines arising from rotational transitions between two particular electronic and vibrational states is known as a 'band'. The spectral lines resulting from decays to lower levels may be resolvable as separate lines or they may appear to be part of a continuous wavelength distribution.

Transitions may also occur between bound discrete states and unbound continuum states. The molecule will then dissociate into separate atoms. If the continuum state has a lower energy than the initial bound state, a photon may be emitted. This type of transition produces a continuous spectrum.

5.3 Molecular Hydrogen Line Spectra Measurements

Several bands in the spectrum of molecular hydrogen have been studied previously in plasma confinement devices. Terry [25] measured emission from the Alcator C Tokamak plasma in the Lyman and Werner bands, which result from decays from the bound singlet states $B^1\Sigma_u^+$ and $C^1\Pi_u^+$ to the ground electronic state $X^1\Sigma_g^+$. These bands are in the vuv region between 850 $\AA$ and 1650 $\AA$. Individual lines were not resolved.

McNeill [20,26] measured emission from the EBT plasma in the Fulcher bands, which result from decays from the triplet $d^3\Pi_u^+$ state to the triplet $a^3\Sigma_g^+$ state. Emission in these bands was responsible for the background light present in the Thomson scattering experiment, which measured the electron temperature. Individual lines were resolved and identified. These bands are in the visible region between 5800$\AA$ and 6300$\AA$.

Several of the lines observed by McNeill were among the lines noted in one the earliest studies of molecular hydrogen spectra [29]. In this study, molecular gas was excited by electron collision. The electrons were in a beam whose energy was controlled. The spectrum was measured with a film spectrograph. A plot of the film densities of several of the most the prominent lines versus beam energy is shown in figure 5.2. There are two classes of lines. One class has a maximum in intensity below 30 ev, the lower limit of the energy range of the experiment. The other class has an intensity maximum between 30 ev and 40 ev. The lines with the lower energy peak have wavelengths between 6010$\AA$ and 6330$\AA$. The lines with the higher energy peak have wavelengths between 4200$\AA$ and 5020$\AA$. The densities of lines with the lower energy peak decrease more sharply with increasing electron energy than the densities of lines with the higher energy peak. The lower-peak line densities decrease approximately as the reciprocal of the square of the electron energy. The wavelength resolution used in these measurements is unknown, so the 'lines' may represent more than one molecular line. The lines with the lower energy peak belong to the Fulcher bands. The transition does not conserve spin. Therefore, the cross section has a strong dependence on electron energy, as seen in figure 5.2.

The Fulcher band lines in figure 5.2 were observed with the Oriel spectrometer

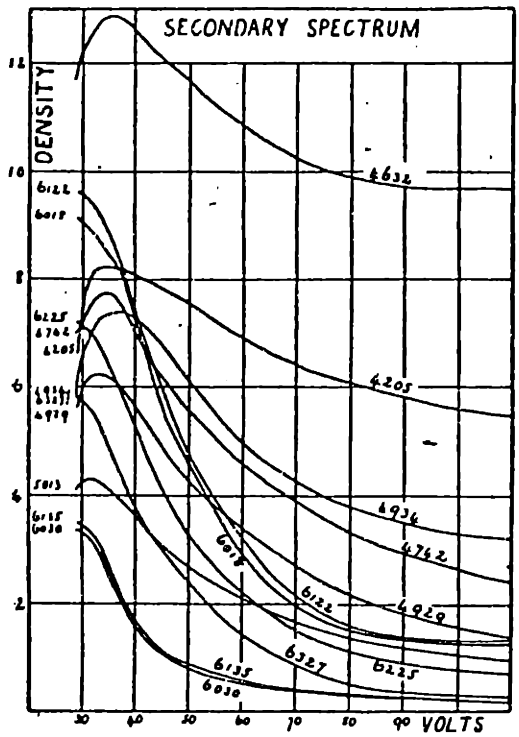

Figure 5.2: Plots of film density versus electron impact energy for various H_2 lines. Reproduced from ref.[29].

in the Tara discharge cleaning plasma spectrum. This plasma was created by a dc discharge in hydrogen gas and had a low estimated electron density (less than $10^{11} cm^{-3}$) and low estimated electron temperature (less than 5 ev). The lines with a higher energy maximum were not observed in the discharge cleaning plasma, which is consistent with the low temperature.

Several of the lines in the class with a higher energy peak belong to bands which arise from excitation from the ground state to the bound singlet state $G^1\Sigma_g^+$ and subsequent decay to the singlet state $B^1\Sigma_u^+$. As seen in figure 5.2, these lines will be more intense than the Fulcher band lines at higher electron energies, since the film densities of the singlet state transitions are higher for electron energies above 60 ev. At higher energies these will be the most intense H_2 lines in the visible region. These bands were studied in detail by Anderson etal. [30,31]

The first attempt at molecular spectroscopy on the Tara plasma was made with the vuv spectrometer at the z = 350 cm location. The wavelength region between $850\mathring{A}$ and $1250\mathring{A}$ was scanned on a shot-by-shot basis. The Lymanα and Lymanβ lines were observed but the Werner and Lyman bands were not in evidence. This is not surprising since the molecular and atomic emission is weakest at the z = 350 cm location. All subsequent studies of molecular spectra were in the visible and near-uv, with instruments which could be installed at several axial locations.

The next attempt to make molecular spectra measurements was made using the Oriel instrument at the $z = 30$ cm location in an attempt to observe the $G_0 \rightarrow B_0$ (the subscript indicates vibrational quantum number v) band at $4632\mathring{A}$. The wavelength region between $4600\mathring{A}$ and $4700\mathring{A}$ was scanned using a $5\mathring{A}$ resolution. Intensity peaks were measured at $4632\mathring{A}$ which indicated the presence of the $G_0 \rightarrow B_0$ band and the $K_0 \rightarrow B_0$ band at 4661 $\mathring{A}$. Individual rotational transitions were not resolvable owing to the resolution used. The oma spectrometer was then set up to make higher resolution measurements of these bands.

The wavelength region containing lines from the above-mentioned bands and a wavelength region containing lines from other prominent bands were studied using the oma spectrometer at the 0 cm, 30 cm, 110 cm, and 350 cm axial locations. A resolution of $.7\mathring{A}$ was used. The wavelength regions studied were $4625\mathring{A}$ – $4675\mathring{A}$ and $4180\mathring{A}$ – $4230\mathring{A}$. The two spectra contain lines from the following bands: $G_0 \rightarrow B_0, G_1 \rightarrow B_0, I_1 \rightarrow B_3, K_0 \rightarrow B_0, K_1 \rightarrow B_0$. Several lines in these bands are listed in Table 5.1, reproduced from ref. [31]. The bands observed

Rydberg states					Doubly excited states				
Transition ($X_{v'} \rightarrow B_{v''}$)	Rotational line	Wavelength (Å)	Lifetime (ns)	Cross section (10^{-18} cm^2)	Transition ($X_{v'} \rightarrow B_{v''}$)	Rotational line	Wavelength (Å)	Lifetime (ns)	Cross section (10^{-20} cm^2)
$\underline{G_0 \rightarrow B_0}$	$R0$	4628.0	20.8	1.7	$\underline{K_0 \rightarrow B_0}$	$R0$	4661.4	67.6	1.0
	$R1, R4$	4631.6	22.7[a]	1.7		$R1$	4660.4	68.1	0.3
	$R2, R3, P1$	4634.4	21.3[a]	3.3		$R2$	4662.8	69.4	0.8
						$P2$	4687.8	68.4	0.7
$\underline{G_1 \rightarrow B_0}$	$R0$	4195.7	36.1	1.2					
	$R1, P1$	4200.0	35.7[a]	0.9	$K_1 \rightarrow B_0$	$R2$	4223.9	68.5	0.8
	$R2$	4205.1	37.6	3.0		$P2$	4243.3	69.1	0.4
	$R3$	4210.1	32.1	0.5	$K_2 \rightarrow B_1$	$R0$	4078.8	38.8	1.3
	$R4, R5$	4212.2	32.1[a]	0.4		$R1$	4082.4	39.1	0.6
$G_2 \rightarrow B_0$	$R0, R1, R2$	3859.8	42.5[a]	0.6		$R2$	4087.8	44.2	1.3
$G_2 \rightarrow B1$	$R0, R2$	4066.9	39.7[a]	2.9	$M_0 \rightarrow B_0$	$R0$	4306.3	74.7	0.4
	$R1$	4065.6	39.7	0.6		$R1, R2, R3$	4303.7	56.7[a]	0.7
	$R4$	4074.1	42.5	0.3	$N_1 \rightarrow 2B_0$	$P2$	4028.3	45.5	0.7
$G_3 \rightarrow B_3$	$R0$	4201.0	29.7	0.4		$P3$	4035.6	47.0	0.2
$G_3 \rightarrow B_5$	$R0$	4670.7	32.1	0.4		$P4$	4043.6	46.6	0.4
$G_3 \rightarrow B_7$	$R0$	3222.9	32.7	0.4	$N_2 \rightarrow 2B_2$	$R0$	4113.5	54.8	0.1
						$R1, R2, R3$	4110.2	49.1[a]	0.2
$I_0 \rightarrow B_0$	$Q1, Q2$	4579.8	21.7[a]	1.6		$P2$	4131.5	56.7	0.2
	$P2$	4582.6	21.7	0.6					
	$P3$	4575.9	21.7	0.4					

[a]Measurements obtained from observation of an unresolved rotational line blend

Table 5.1: H_2 line spectra wavelength table. Reproduced from ref.[31].

are underlined. Several lines not listed in the table were identified using Dieke's wavelength tables [32].

The table lists the lines by electronic transition, vibrational transition, and rotational transition. R_n indicates a decay from the nth rotational level of the upper electronic and vibrational state in which j increases by one, while P_n indicates a decay in which j decreases by one. Some of the lines are blends of several rotational transitions. The lifetime of the states are listed along with the cross section for excitation of room temperature molecules at an electron energy of 50 ev. The reference also includes a plot of the cross section versus energy for energies between 15 ev and 300 ev.

In ref. [30] Anderson published a spectrum of the wavelength region between 4590$\mathring{A}$ and 4665$\mathring{A}$ obtained by bombarding H_2 with 100 ev electrons. This plot

is reproduced in figure 5.3. The bands are labeled. The spectrum was produced using a .9$\mathring{A}$ resolution.

A plot of the spectrum from the 4625$\mathring{A}$ – 4675$\mathring{A}$ region measured from the Tara plasma at the z = 0 cm axial location with the instrument viewing along a central vertical chord is shown in figure 5.4. All the lines in the spectrum obtained by electron bombardment of H_2 in the overlapping wavelength region are present in the Tara spectrum. The molecular lines in the Tara spectrum are labeled. Five lines from the $G_0 \rightarrow B_0$ band are resolvable. Several 'lines' are blends of several individual lines. Four lines from the $K_0 \rightarrow B_0$ band are resolvable. Other lines are identified as impurities. At z = 0, the molecular line at 4634.4$\mathring{A}$ (which is blend of three lines) is the strongest of all lines in the visible region except for the atomic hydrogen Balmer lines.

Figure 5.5 shows a plot of the spectrum from the 4180$\mathring{A}$ – 4230$\mathring{A}$ region measured at the z = 0 location through the same chord. Six lines from the $G_1 \rightarrow B_0$ band are resolvable. The molecular lines as well as the impurity lines are labeled. The strongest line is half as intense as the line at 4634.4$\mathring{A}$.

The relative intensities of several molecular lines at z = 0 cm were sufficiently strong to rule out significant contribution from impurity radiation. The intensities of these lines relative to other lines in the same band, and to other lines in different bands can be compared with the relative sizes of cross sections for those lines listed in Table 5.1. The ratio of the intensity of the 4634.4$\mathring{A}$ line to the intensity of the 4631.6$\mathring{A}$ line is measured to be 1.7. The ratio between their respective cross sections listed in the table is 1.94. The ratio of the intensity of the 4634.4$\mathring{A}$ line to the intensity of the 4628.0$\mathring{A}$ line is measured to be 2.3 while the ratio of their listed cross sections is 1.94. The ratios of intensities of the lines in the $G_0 \rightarrow B_0$ band relative to each other are approximately the same as the ratios of their listed cross sections, with an average difference of 15%. Likewise, the ratios of intensities of lines in the $G_1 \rightarrow B_0$ band relative to each other are approximately the same as the ratios of their respective cross sections.

The ratios of intensities between rotational lines in a band are functions of the distribution in rotational levels in the excited state, which is dependent on the rotational level distribution of the ground state. Since the emitting molecules in the cross section measurement experiment were at rotational room temperature, the emitting molecules in the Tara plasma must have been near rotational room

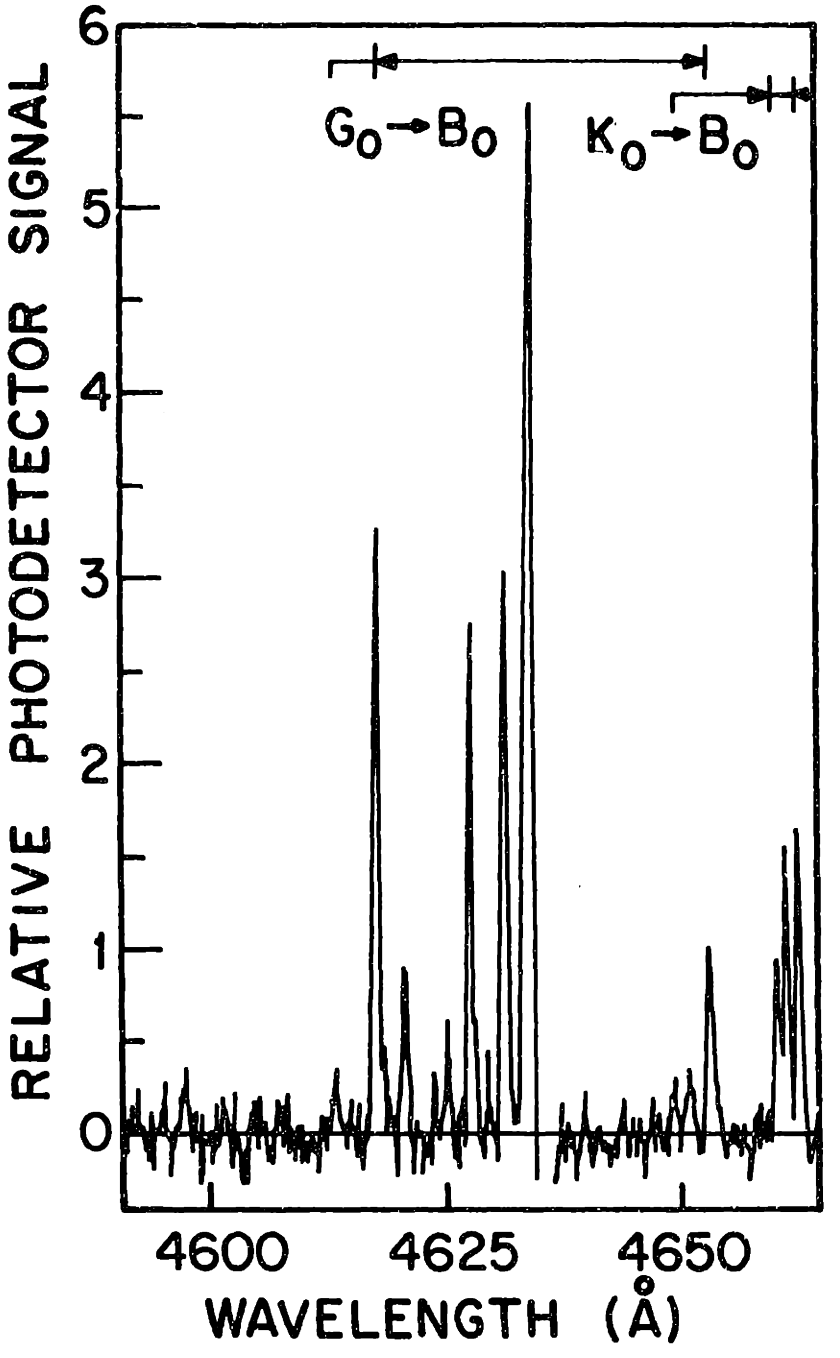

Figure 5.3: H_2 spectrum showing two bands, also observed in the Tara spectrum. Reproduced from ref.[30]

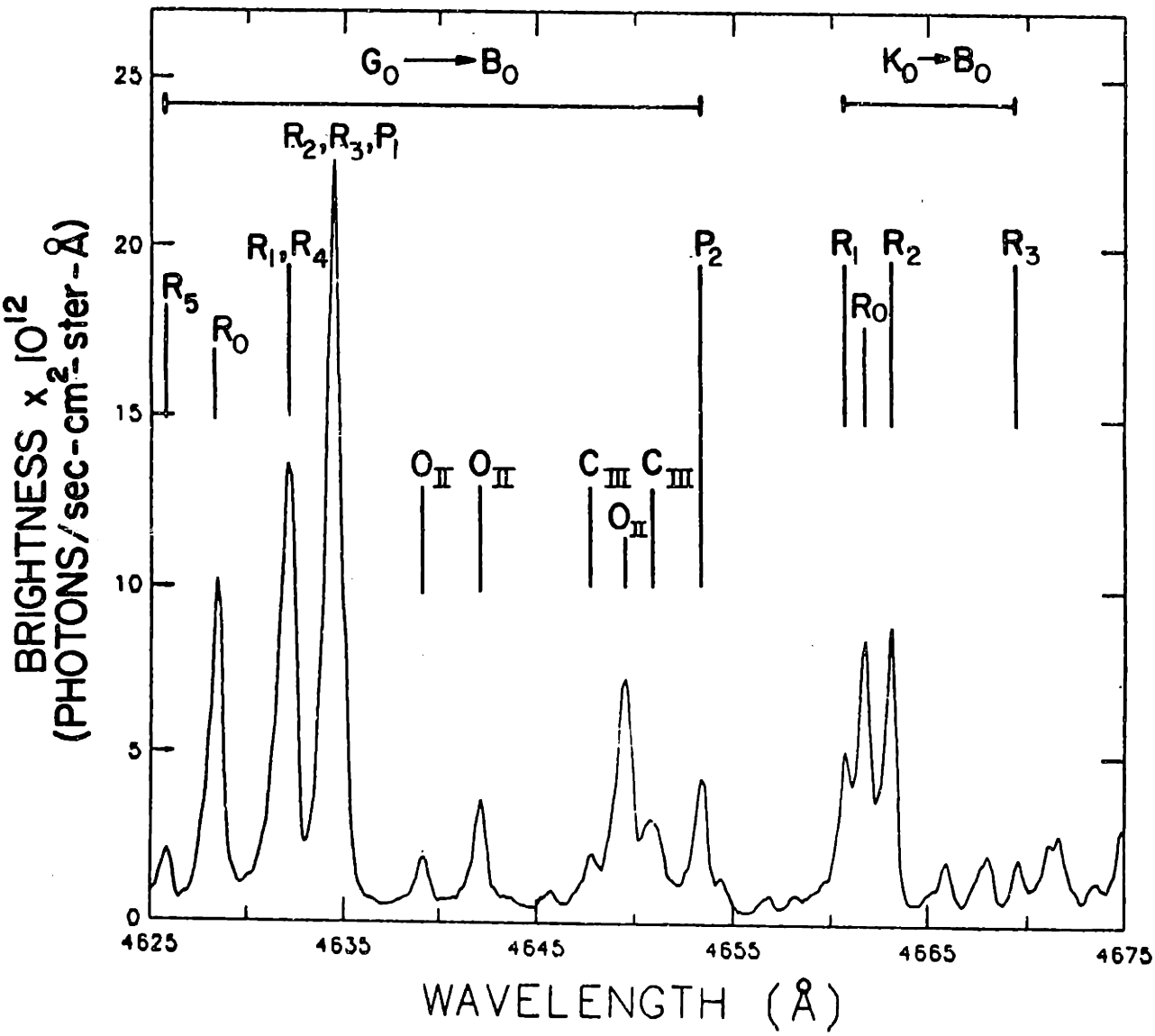

Figure 5.4: Plot of the spectrum between 4625$\AA$ and 4675$\AA$ measured at z = 0.

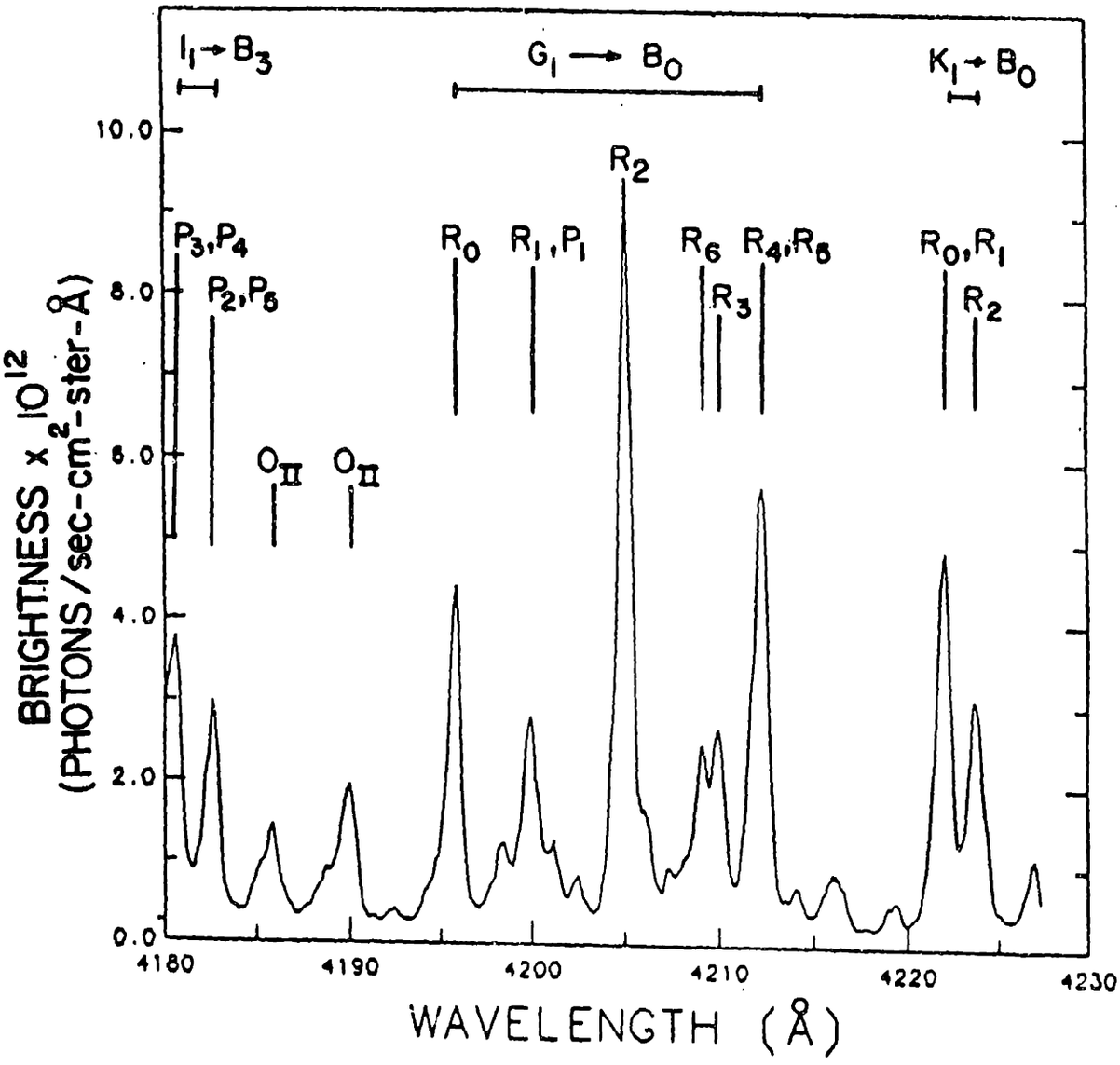

Figure 5.5: Plot of the spectrum between 4180Å and 4230Å measured at z = 0.

temperature, 300 degrees Kelvin. A knowledge of the individual line excitation rates would be necessary in determining the rotational temperature from the line spectra measurements.

In contrast with the distribution of emission among rotational lines in a particular band, the ratios of the intensities of lines in one band to line intensities in another band in the same electronic system are different from the corresponding ratios of their respective cross sections given in Table 5.1. Transitions populating the ground vibrational state of the G electronic state are enhanced over transitions populating excited vibrational states of the G electronic state, in comparison with cross sections in table 5.3. The ratio of the 4634.4$\AA$ line intensity to the 4205.1$\AA$ line intensity is 2.3, while the ratio of their listed cross sections is 1.1.

Enhancement of transitions to the ground vibrational state of the upper electronic state over transitions to excited vibrational states could be due to the fact that a fraction of the ground state molecules were in excited vibrational states. The wavefunctions of these states have maxima at larger internuclear distance than the equilibrium radii of the lowest vibrational state wavefunction. Also, as in the case illustrated in Figure 5.1, the wavefunction of the lowest vibrational state of the upper electronic state has a maximum at larger internuclear separation. Therefore, the overlap between these higher vibrational state wavefunctions, and the wave function of the lowest vibrational state of the upper electronic state, may be greater than the overlap between the two lowest vibrational states. Therefore, transitions to the lowest vibrational state of the upper electronic state may be enhanced over transitions to excited vibrational states of the upper electronic state.

The vibrational and rotational energy level distributions of ground state hydrogen molecules in plasma bucket sources have been studied using the laser resonance technique [33,34]. Thermal equilibrium rotational distributions corresponding to rotational temperatures of 340 – 530 degrees Kelvin were observed. These temperatures are consistent with the line spectra measurements on Tara. Vibrational energy level distributions were not found to be in thermal equilibrium, and had distributions corresponding roughly to vibrational temperatures of 1300 – 2500 degrees Kelvin , which means 2 % to 15 % of the molecules were in excited vibrational states.

The presence of molecules in excited vibrational states may affect the total

dissociation and ionization cross sections. They would most likely increase, since the internuclear separation, R_e, of the molecular ion and that of the of a molecule in the bound triplet state is larger than the R_e of the ground vibrational state. For the purpose of inferring the ionization rate, the line at $4634.4\mathring{A}$ will be used, since the increased excitation from excited vibrational states may be closer in ratio to the increased ionization from those states. For the purpose of inferring molecular densities both bands will be averaged.

The molecular line spectra shows that molecular lines resulting from single rotational transitions show only instrumental broadening, and no doppler-broadening.. This places a limit of 1 ev on the molecular translational temperature.

Figure 5.6 shows a plot of several cross sections and rate coefficients of molecular excitation processes:the molecular ionization cross section σ_i versus energy, the maxwellian-averaged rate coefficient for that process Q_I [6], the cross section for excitation of the $4634.4\mathring{A}$ line σ_{ex}[32], multiplied by 3800, the cross section for dissociation through the $a^3\Sigma_g^+$ state σ_d, and the maxwellian- averaged rate coefficient for that process Q_d [6]. The cross section for the line excitation has almost the same energy dependence as the cross section for ionization. The rate coefficient for the line excitation for an electron temperature of 100 ev is lower than the rate coefficient for ionization by a factor of 3650. Therefore, for every $4634.4\mathring{A}$ photon emitted from molecules in a 100 ev plasma, 3650 ionization events take place.

Measurements made of the $4625\mathring{A} - 4675\mathring{A}$ region at z = 30 cm and z = 110 cm through central chords are shown in figure 5.7. The $4634.4\mathring{A}$ line intensity decreases by a factor of 42 between the gas port and the z = 110 cm location. Figure 5.8 shows a plot of the spectrum from the $4180\mathring{A} - 4230\mathring{A}$ region at z = 30 cm and z = 110 cm through central chords. The $4205.1\mathring{A}$ line intensity decreases by a factor of 38 between z = 0 and z = 110 cm. The discrepancy between the two lines is within the experimental uncertainty, given the shot-to-shot nature of the data. Emission measured at z = 350 cm showed no molecular line radiation. A spectrum of this region is presented in chapter 3.

In all of the oma spectra collected, the spectrum measured during the discharge contained dark counts. In order to measure the dark count level, the detector was gated on for an time interval equivalent to the data collection interval and the

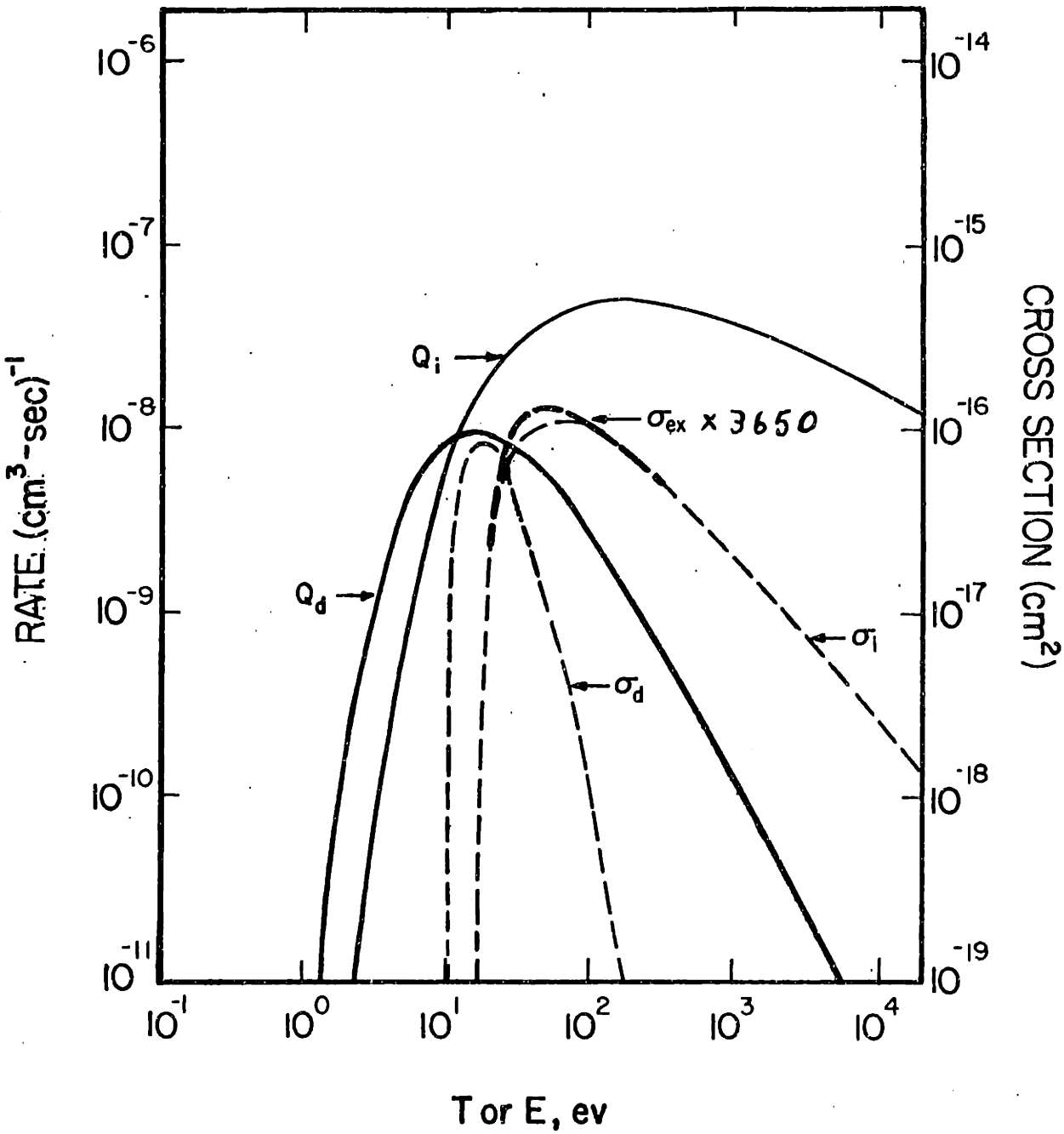

Figure 5.6: Molecular cross sections and rates for ionization, continuum dissociation and line excitation. From refs.[6,31].

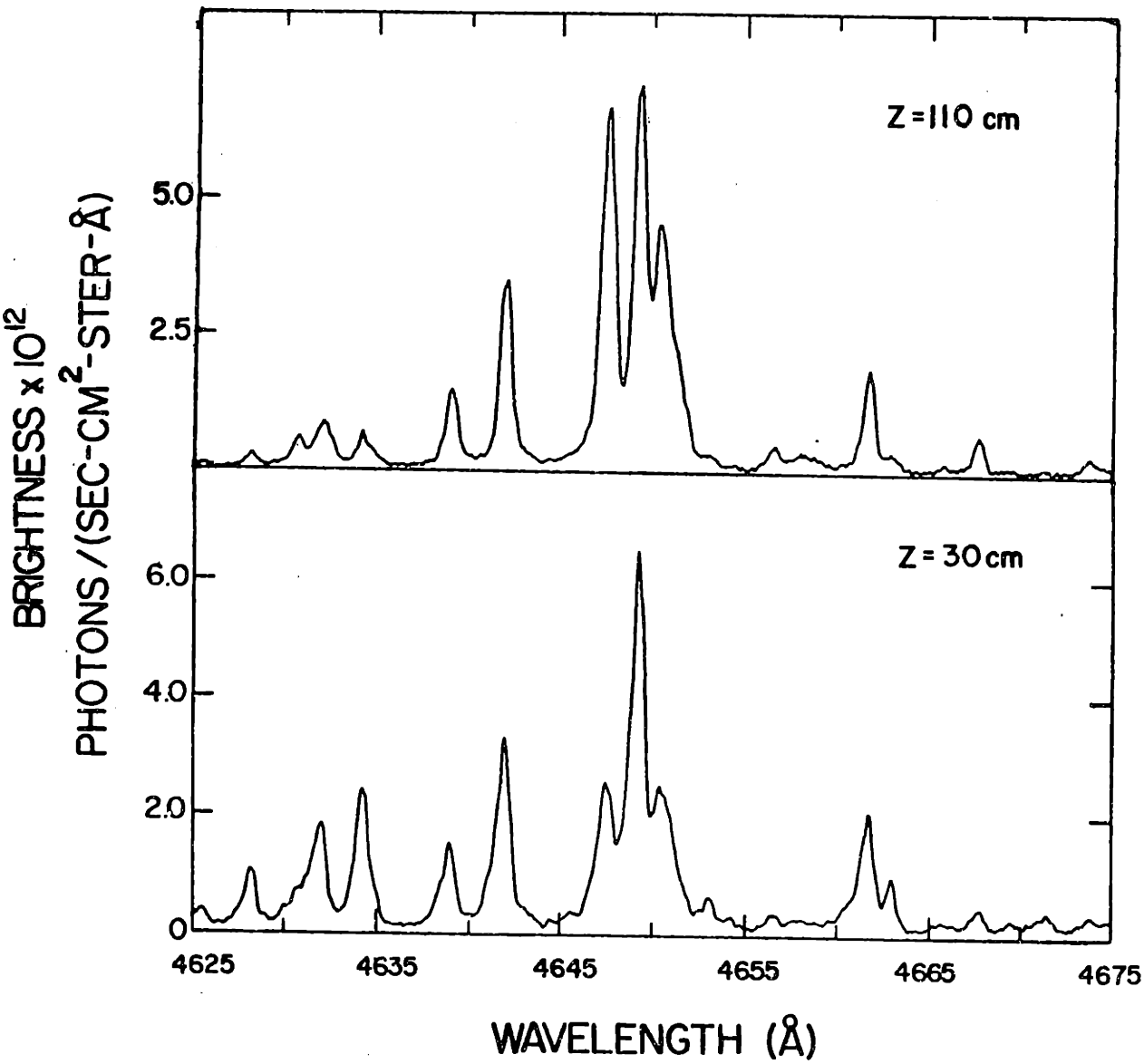

Figure 5.7: Plots of the spectrum between 4625$\AA$ and 4675$\AA$ measured at z = 30 cm and z = 110 cm.

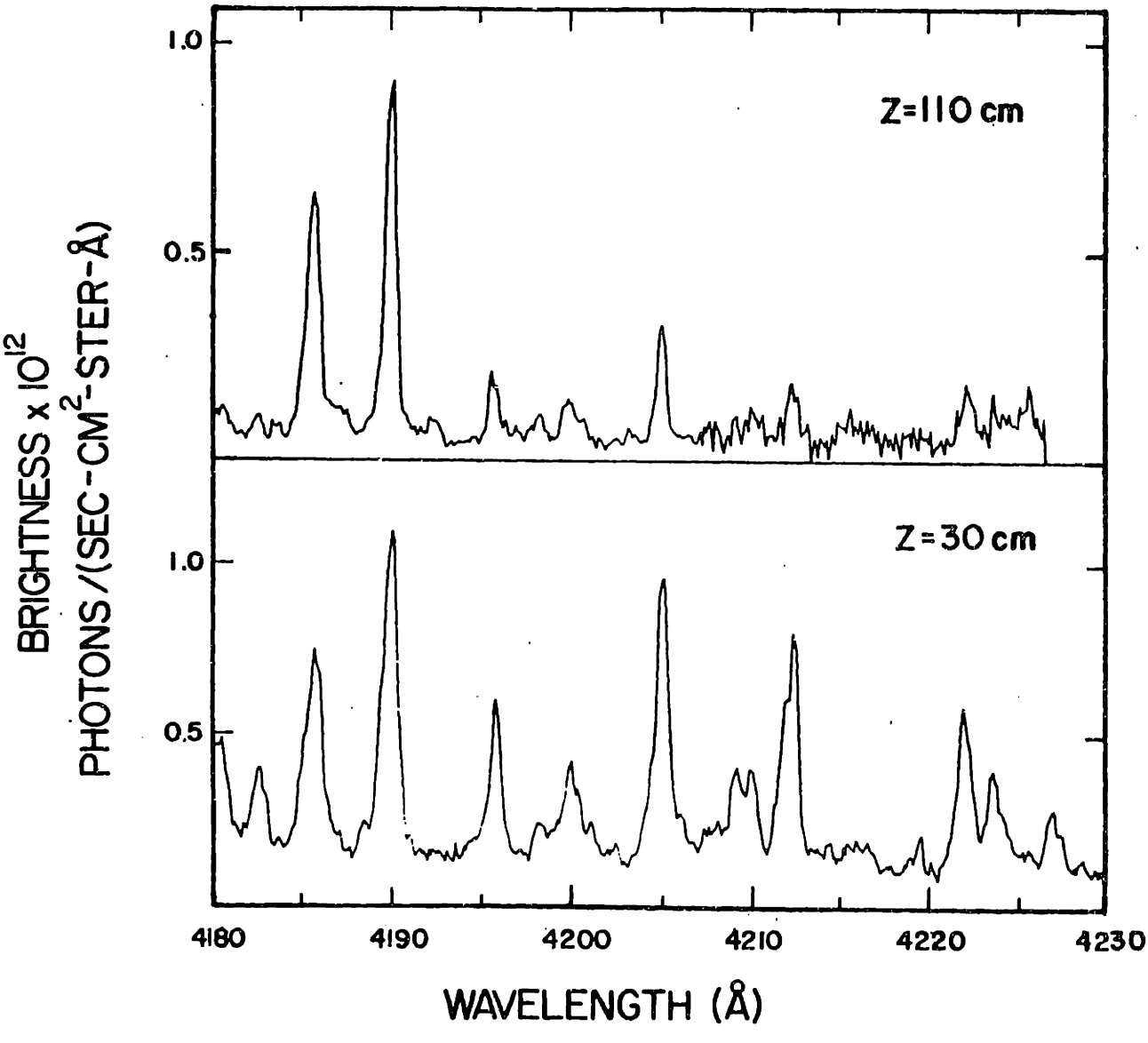

Figure 5.8: Plots of the spectrum between 4180$\mathring{A}$ and 4230$\mathring{A}$ measured at z = 30 cm and z = 110 cm.

dark spectrum was subtracted to obtain the emitted spectrum. Background drift caused the offset to vary, causing error in the background measurement. This problem was solved before the measurements at z = 110 cm. In the measurements made at 0 cm and 30 cm the background intensity level is uncertain to within a factor of two. The ratio of the line intensities to the background is uncertain for these data. The ratios of line intensity to background intensity measured at z = 110 cm are correct.

At the z = 110 cm location, the mirror scanning system was used to obtain a radial brightness profile of the 4205.1$\AA$ molecular line. Figure 5.9 shows that profile. It differs from the Balmer line profiles measured at both 110 cm and 350 cm in that the brightness is higher in the outer region of the plasma. The atomic brightnesses are higher in center. The profile will be analysed in chapter 6.

5.4 Molecular Hydrogen Continuum Spectral Measurements

In addition to molecular hydrogen line emission, molecular continuum emission from the Tara plasma was also observed. The observed emission is known as the 'molecular hydrogen continuum'. While this continuum has been well studied in investigations of molecular hydrogen spectra [35,36], it has not been reported in spectra from magnetic confinement devices in the last twenty years, owing to its relative weakness. Investigators working on the Deca II confinement device [37] measured the brightness of the radiation between 2000$\AA$ and 4000$\AA$ using wide band optical filters(700$\AA$ bandpass)and determined that the emission was too intense to arise from either bremsstrahlung or recombination. They attributed the emission to the molecular dissociative continuum process and obtained a value for the product of electron density and molecular density from intensity measurements. The measurements performed on the Tara plasma are the first measurements of the continuum wavelength distribution made on a magnetic confinement device and allow the first positive identification of the continuum in the spectra measured from such devices.

The continuum arises from excitation of molecules in the ground electronic state $X^1\Sigma_g^+$ to the bound triplet state $a^3\Sigma_g^+$ through electron collision. This transition violates conservation of spin, and therefore the cross section is proportional

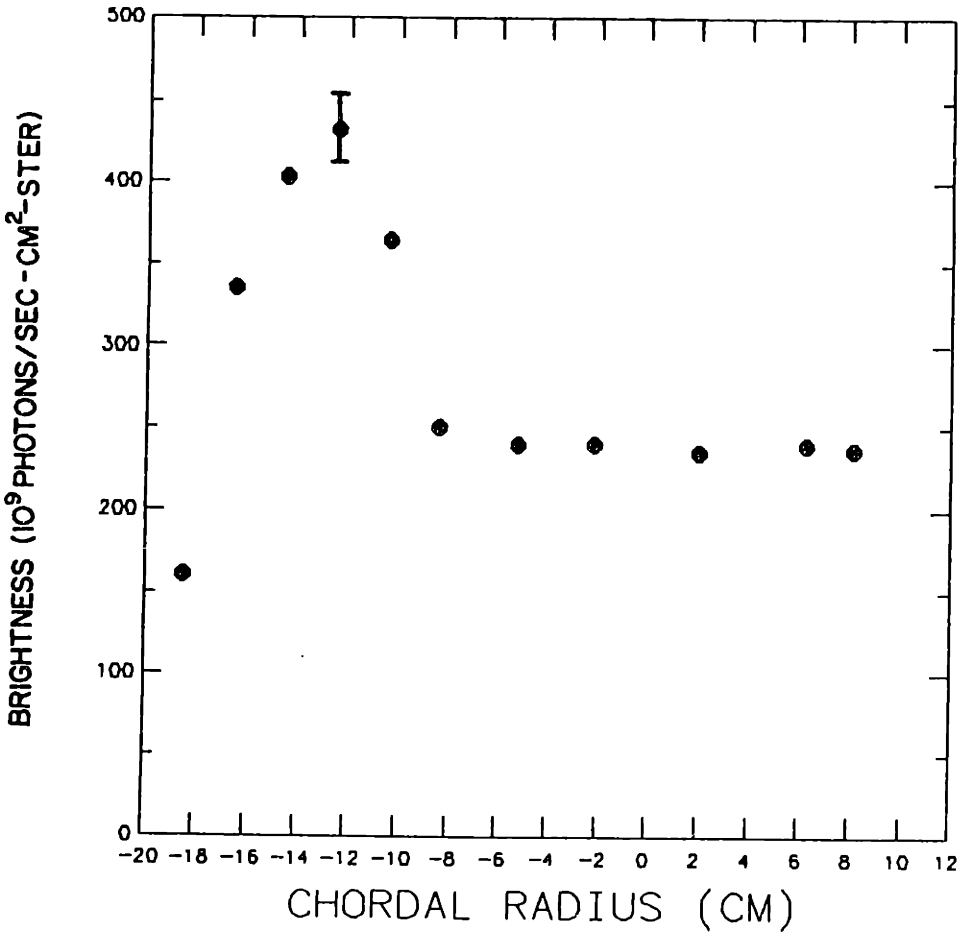

Figure 5.9: Chordal brightness profile of the 4205$\AA$ line of H_2.

to the reciprocal of the square of the electron energy. [6] Once in the triplet state $a^3\Sigma_g^+$, the molecule decays to the unbound triplet state $b^3\Sigma_u^+$ and emits a photon whose energy equals the energy difference between the initial and final molecular energies. Since there are a continuum of final states, the radiated spectrum is continuous in wavelength. Molecules in the unbound state will dissociate into two ground state hydrogen atoms.

Figure 5.10 shows a diagram of the ground state potential curve, the bound triplet potential curve and the unbound triplet potential curve, taken from ref. [38]. The transitions which lead to the continuum radiation are noted by arrows. Molecules can be excited to any of the vibrational levels of the $a^3\Sigma_g^+$ state. Decay from a particular vibrational state will produce a particular continuous spectrum. Figure 5.4a shows the individual spectra produced by decays from the first four

vibrational levels and figure 5.4b shows the individual spectra produced by decays from the fifth through ninth vibrational levels. These figures are reproduced from ref. [39]. When more than one vibrational level is populated, the continuous spectrum will be a combination of the individual spectra produced by decay from each level. populated.

After decay to the unbound triplet state, the molecule has an energy ΔE_k, which is noted on the figure 5.10. This energy ΔE_k becomes the kinetic energy of the two product atoms and is divided equally between them. Since there are a continuum of final states, the atoms produced by this process will have a continuum of kinetic energies.

Shot-to-shot continuum emission measurements on the Tara plasma were initially made at z = 30 cm with the Oriel spectrometer using a 30$\AA$ resolution. The general shape of the continuum was measured, but the spectrum was strongly contaminated by impurity lines, due to the resolution used. These measurements were later repeated at z = 0 cm with the oma spectrometer in photomultiplier mode using a resolution of was 3$\AA$. The continuum was more intense at z = 0 cm and the higher resolution made it possible to make measurements free of impurity line contamination.

In order to positively identify the continuum, several criteria must be satisfied: (1)It must have a wavelength distribution consistent with an expected distribution, (2) its time behavior must be consistent with the time behavior expected of molecular emission, (3) its emission must be much more intense than other known continua emission, and (4) it must have the same spatial distribution as the molecular line emission, given an absence of electron temperature-induced effects. These criteria have been satisfied.

Figure 5.12 shows a plot of the continuum spectrum between 2200$\AA$ and 3600$\AA$ measured through a central vertical chord at z = 0 cm with a resolution of 3$\AA$. The measurements were made on a shot-by-shot basis with the wavelength changed each discharge. The data were collected with plasma conditions remaining unchanged. Although care was taken to avoid the impurity lines identified in chapter 3, several of the emission measurements were contaminated by impurity line emission. These measurements were characterized by a higher ratio of steady-state emission to initial spike emission, and brightness values above the continuum brightness at nearby wavelengths. The measurements were not included in the

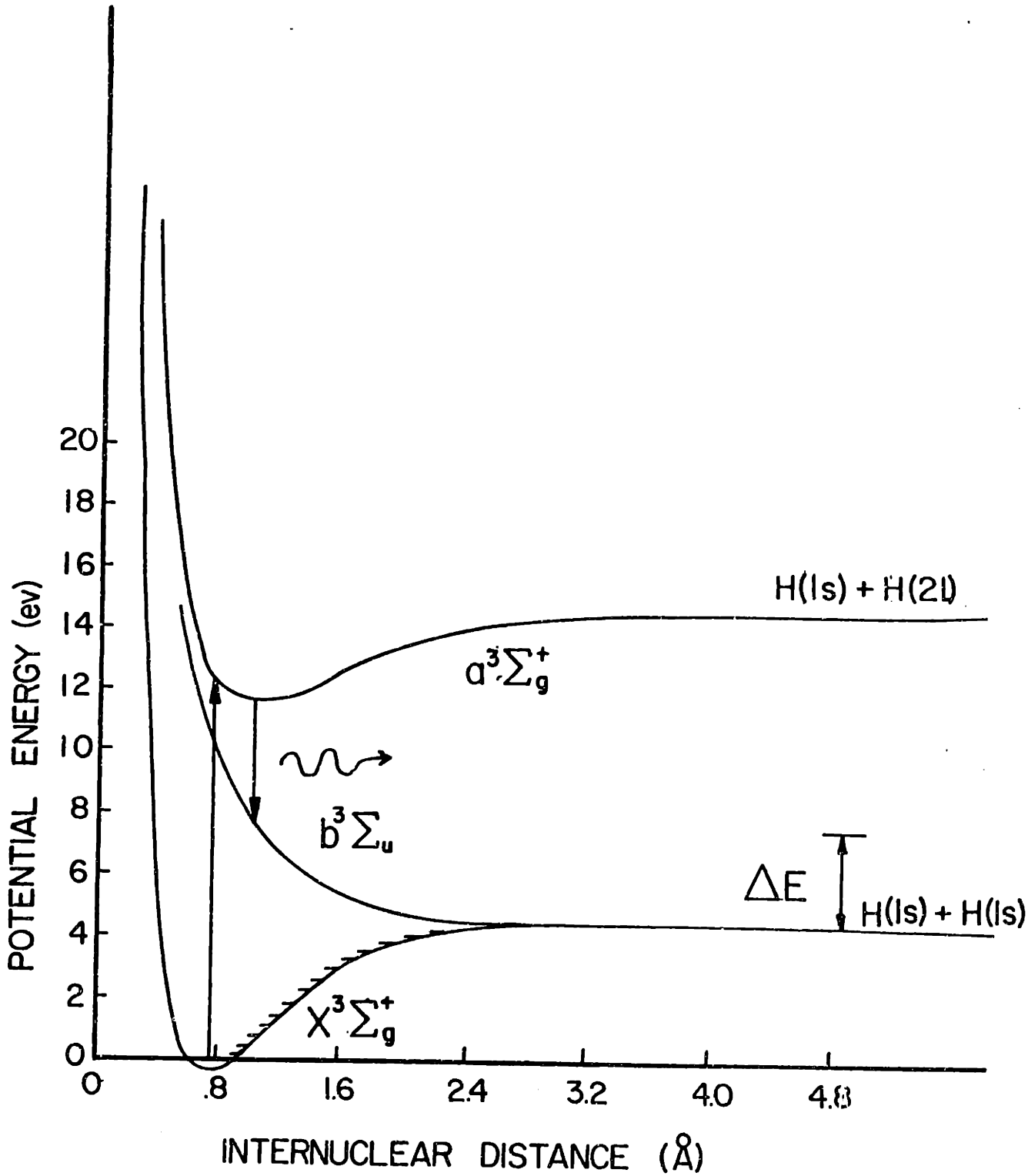

Figure 5.10: H_2 potential curves showing continuum production and dissociation. From ref.[38].

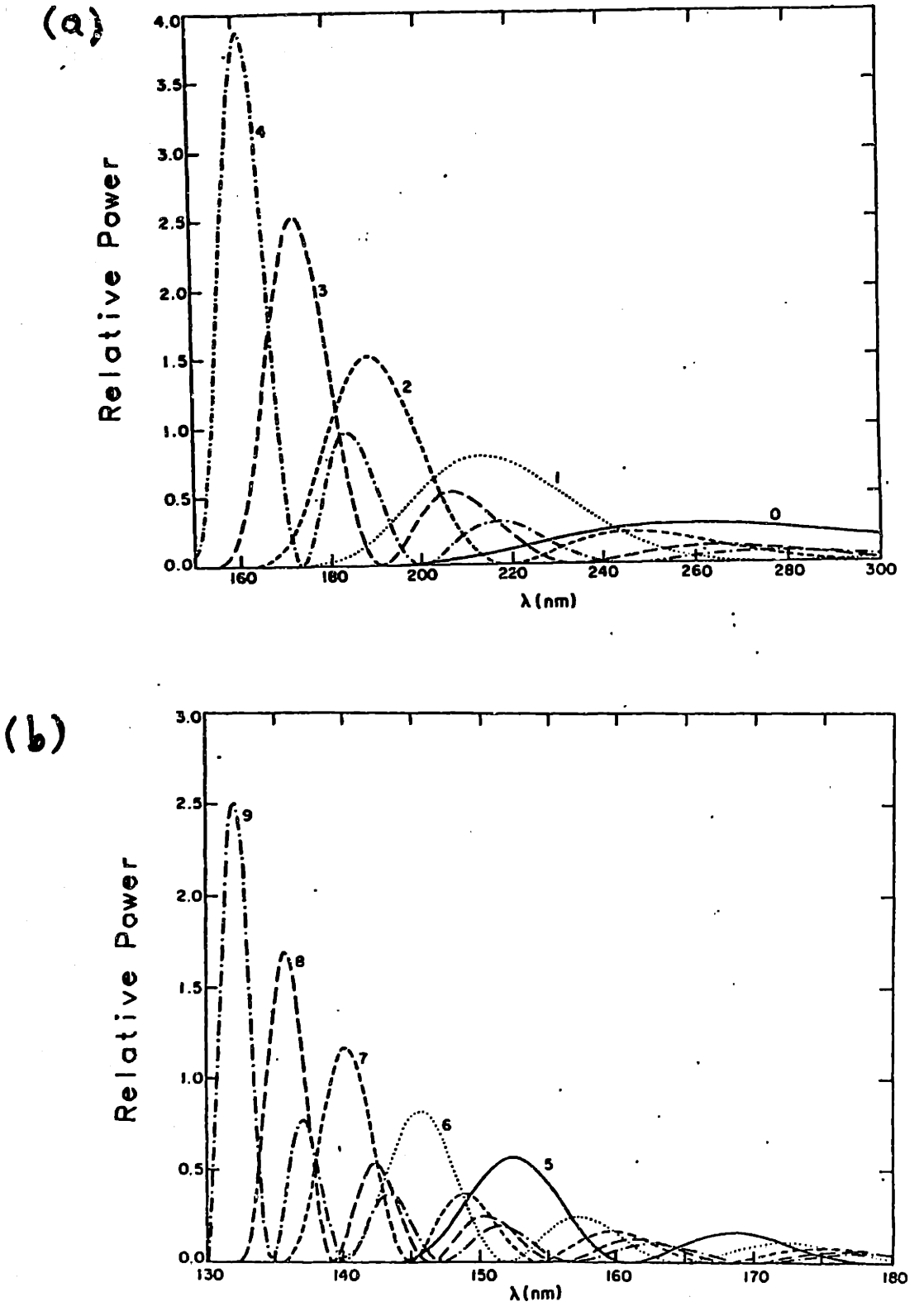

Figure 5.11: Continuum spectra for decays from (a), the first five and (b), the second 5 vibrational levels of the $a^3\Sigma_g^+$ state. From ref.[39].

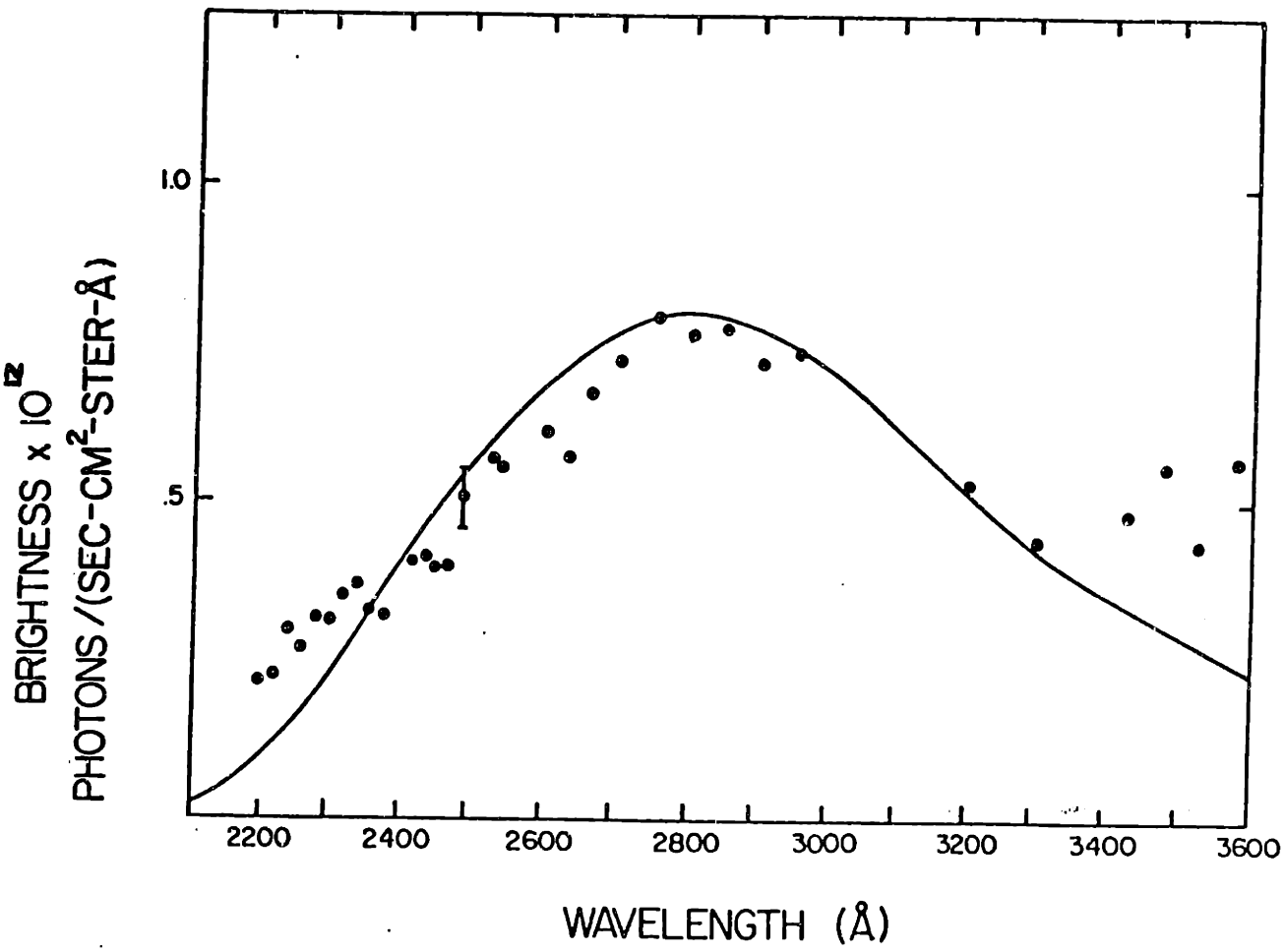

Figure 5.12: H_2 continuum brightness distribution measured at $z = 0$ cm and calculated brightness curve from ref.[40].

data shown in figure 5.12.

Plotted along with the measured continuum distribution is the relative brightness versus wavelength calculated for decay from the first vibrational state of $a^3\Sigma_g^+$ to the unbound state $b^3\Sigma_u^+$ taken from ref. [40]. The intensity curve in ref. [40] has been multiplied by the wavelength in order to convert from relative power to relative photons/sec. In this case the spectrum contains only the contribution from the curve labeled 0 in figure 5.11. However, in the case of the Tara spectrum, all vibrational levels of the state $a^3\Sigma_g^+$ can be excited owing to the energies of the plasma electrons. Therefore, in general, the Tara spectrum will be a combination of the individual continua spectra shown in figure 5.11. The close correspondence between the Tara spectrum and the calculated spectrum suggests that much of

the continuum radiating from the Tara plasma arises from decays from the $\nu = 0$ vibrational state.

Molecular hydrogen has another emission continuum which results from decays from the $B^1\Sigma_u^+$ and $C^1\Pi_u^+$ states to unbound vibrational states of the electronic ground state. [41,42] However, this continuum peaks at $1650\mathring{A}$ and has negligible strength in the wavelength region of the measured continuum.

There are other continua present in spectra radiated from confined plasmas: bremsstrahlung and recombination. At an electron temperature of 80 ev, bremsstrahlung emission will be 100 times as intense as recombination emission. [13] The bremsstrahlung emissivity from a plasma with an electron temperature $T_e(ev)$, at wavelength $\lambda(\mathring{A})$, with electron density $n_e(cm^{-3})$ and effective ion charge Z is:

$$E_{brem} = \frac{C_b}{\lambda} \frac{n_e n_i Z_{eff}^2 g_{ff} e^{-hc/\lambda T_e}}{T_e^{1/2}} photons/(sec - cm^3 - \mathring{A} - ster) \qquad (5.19)$$

where C_b is $9.5 \times 10^{-14}/(4\pi)$, g_{ff} is the free-free Gaunt factor averaged over a maxwellian electron distribution at temperature T_e, Z_{eff} is the effective Z, which is 1.05, from chapter 3. From ref. [13], the Gaunt factor for emission at $2700\mathring{A}$ and for a temperature of 80 ev is 2, within a factor of 1.2. Using the Tara plasma parameters, the average bremsstrahlung emissivity per angstrom at z = 0 cm would be $2.2 \times 10^6 photons/(sec - cm^3 - \mathring{A})$ at a wavelength of $2700\mathring{A}$. The line-integrated central chord brightness would be $6.6 \times 10^7 photons/(sec - cm^2 - \mathring{A} - ster)$. Therefore, the measured continuum brightness is a factor of 10^4 higher than the continuum brightness expected from bremsstrahlung.

A plot of the continuum brightness at $2700\mathring{A}$ versus time is shown in figure 5.13 along with plots of the axially-integrated $H\alpha$ emission and line-integrated density. The time behavior of all the continuum emission measurements presented in figure 5.12 was identical.

The continuum time behavior is characterized by several features. The ratio of the initial burnout spike to the steady state emission is larger than the corresponding ratio for the atomic emission. The time evolution during the discharge resembled the atomic emission evolution, although it was not identical. The continuum light emission rose at the end of the discharge, increasing by a factor of four. The atomic emission did not rise at this time. The molecular emission increase may have been caused by either a decrease in electron temperature, since the excitation rate increases with decreasing electron temperature at a temper-

ature of 100 ev, as seen in figure 5.6, or an increase in molecular density in the plasma. Figure 5.14 shows a plot of the quantities plotted in figure 5.13 plotted at the start of the discharge. The molecular emission rose earlier than the atomic emission, reaching its half-maximum point 200μsec before the atomic emission. The electron density reached 80% of its peak by the time the atomic emission peaked and continued increasing while the atomic and molecular emission decreased. Thus, the decrease in atomic and molecular emission is probably due to a decrease in atomic and molecular concentration or a decrease in electron temperature. Since it is not likely that the electron temperatures decreased enough to cause the decrease in emission, the atomic and molecular densities probably decreased after the initial spike.

The total brightness of the continuum is obtained by integrating the brightness per unit wavelength in the wavelength region where the continuum is non-zero. The continuum extends from 1600$\mathring{A}$ to 5000$\mathring{A}$ [43]. Thus, there are two ranges over which the brightness was not measured: $1600\mathring{A} - 2200\mathring{A}$, and $3700\mathring{A} - 5000\mathring{A}$. The brightness per unit wavelength is assumed to be constant over those regions, with the brightness value being the brightness measured at the upper and lower limit of the ranges respectively. The total brightness obtained at z = 0 cm is $1.5. \times 10^{15} photons/(sec - cm^2 - ster)$. At z = 30 cm the continuum brightness was measured at several wavelengths and the total brightness was calculated to be a factor of 10.1 less than the brightness at z = 0. Thus, the ratio of the continuum intensity at 30 cm to the continuum intensity at 0 cm is approximately the same as the corresponding ratio of the line emission.

As seen in figure 5.6, the rate coefficients for ionization and continuum dissociation have a different energy dependence. The ratio of continuum dissociation to ionization is therefore electron temperature dependent. Since the cross section for continuum dissociation is proportional to the inverse of the square of the electron energy and the cross section for ionization is roughly proportional to the inverse of the electron energy, the rate ratio is roughly proportional to the inverse of the electron temperature. Figure 5.15 shows a plot of the ratio of continuum dissociation rate to the ionization rate versus electron temperature. [6]. The ratio of continuum dissociation to ionization may be calculated from the measured line

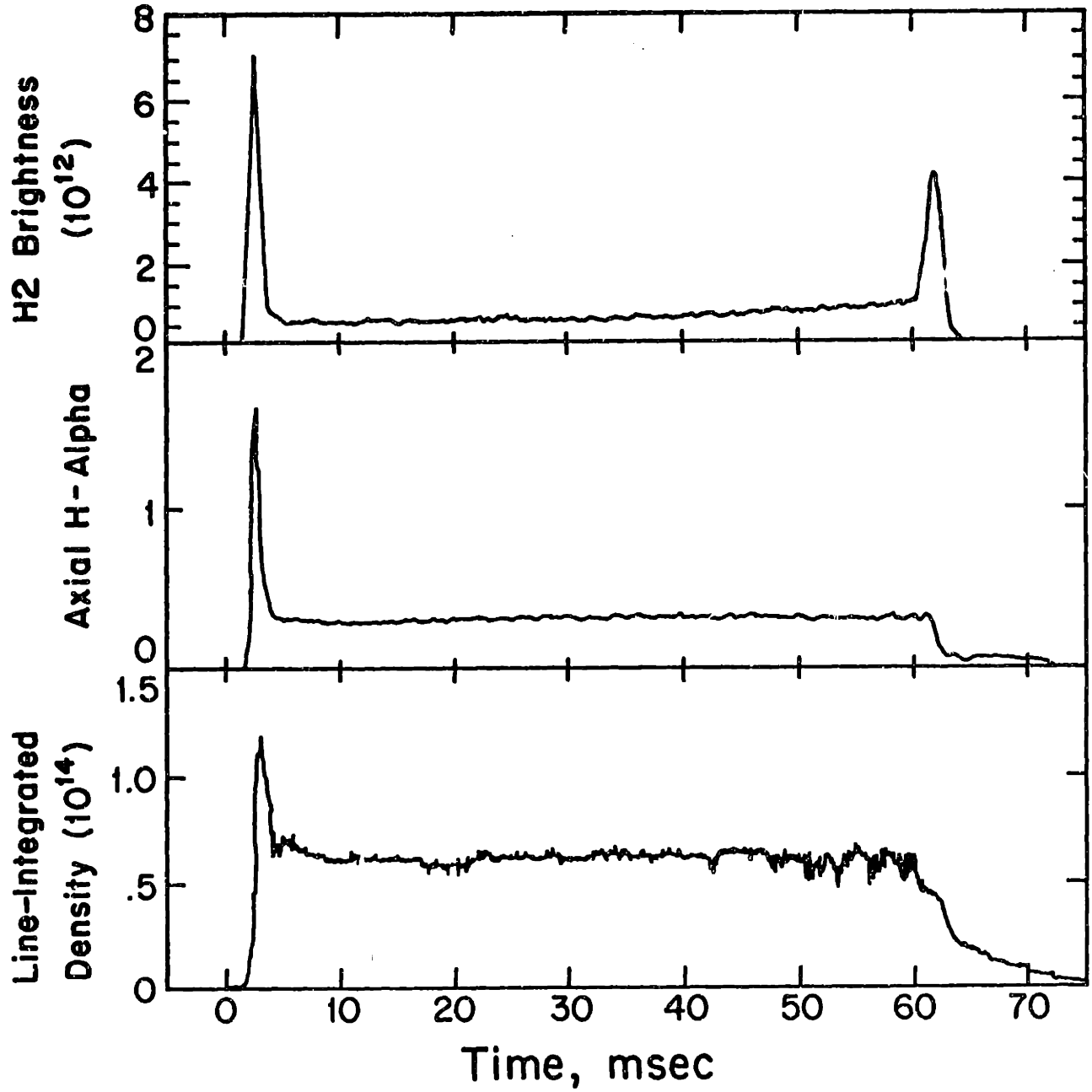

Figure 5.13: H_2 continuum brightness, $H\alpha$ brightness and line-integrated electron density versus time.

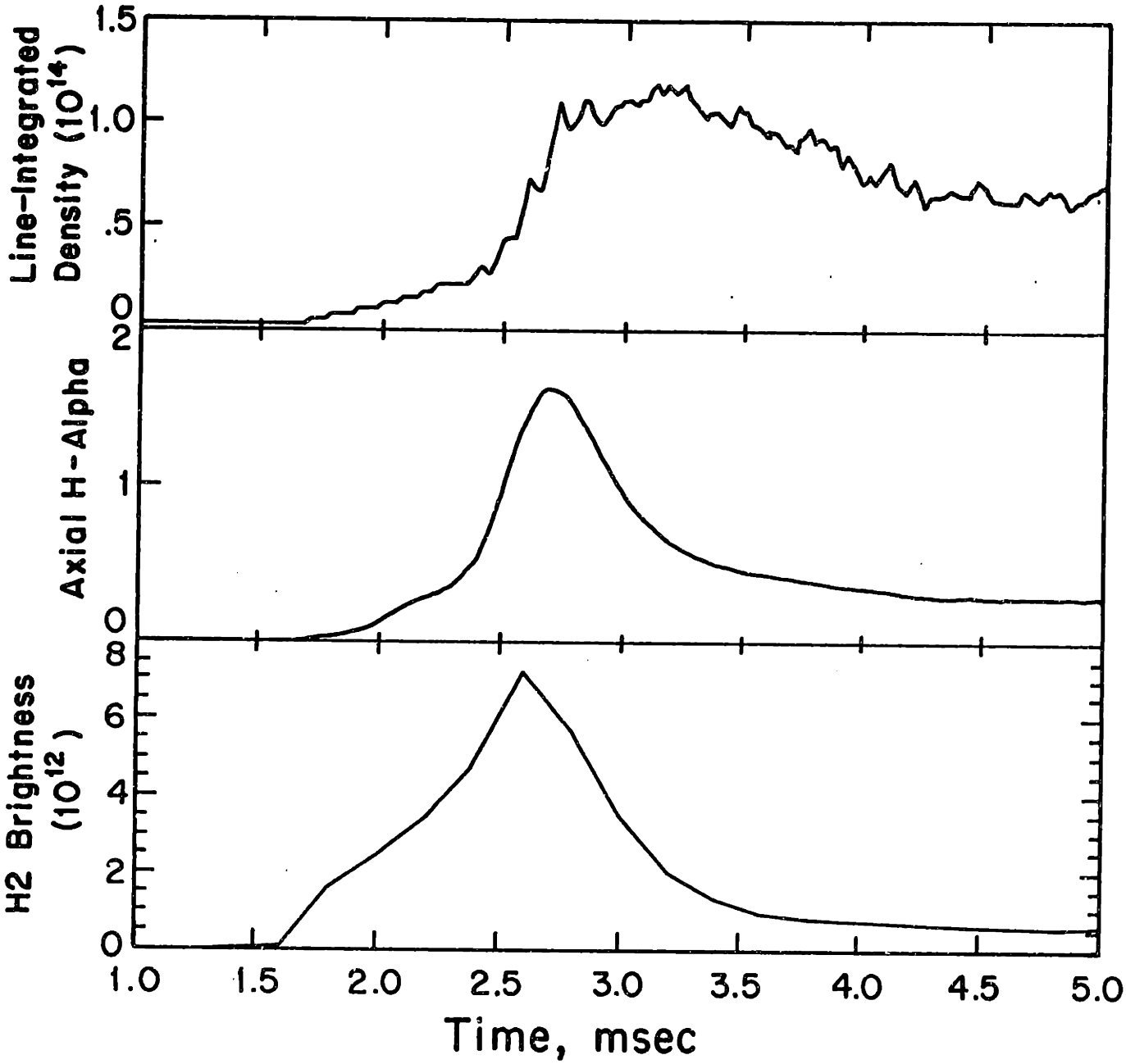

Figure 5.14: H_2 continuum brightness, $H\alpha$ brightness and line-integrated electron density during start-up.

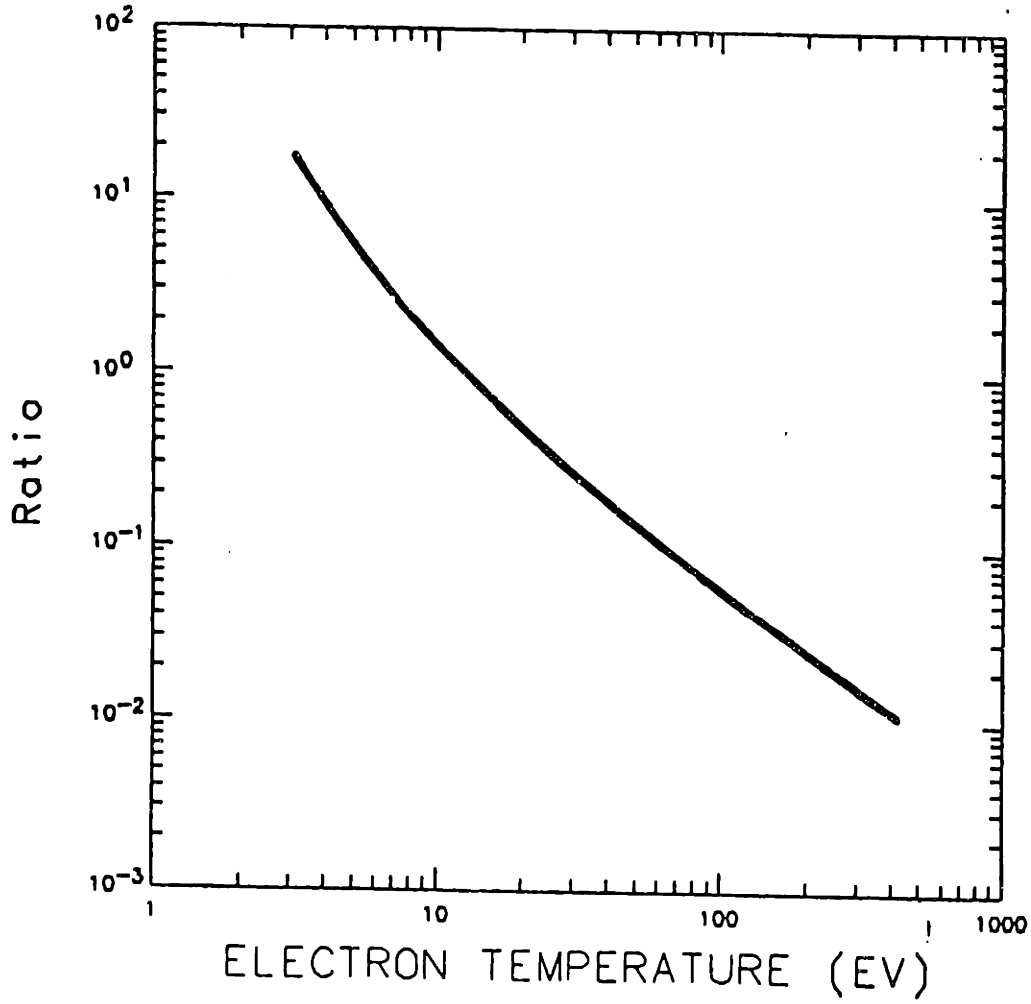

Figure 5.15: Ratio of continuum dissociation to ionization. From ref.[6]

brightness at 4634.4Å, $B_{4634.4\mathring{A}}$, and the continuum brightness B_{cont}.

$$ratio = \frac{B_{cont}}{B_{4634.4\mathring{A}} \times 3650} \tag{5.20}$$

since there are 3650 ionization events per 4634.4Å photon. The ratio is .025, which indicates an electron temperature of 190 ev. The temperature has been measured at 100 ev at the plasma edge. Possibly the discrepancy is due to the fact that the continuum intensity was estimated in the wavelength region not included in the scan, or that the ionization rate determined from the line emission is incorrect.

5.5 Summary and Discussion

Line spectra from the $G \rightarrow B, K \rightarrow B$, and $I \rightarrow B$ bands in molecular hydrogen have been observed in the Tara central cell plasma visible spectrum. Many distinct rotational transitions within the bands have been resolved. These bands have not been previously reported in measurements made on magnetic plasma confinement devices. The emission from these bands may be used to infer the molecular ionization rate since the excitation cross section has the same dependence on electron energy as the ionization cross section. If the electron temperature is sufficiently high, lines in these bands will be the most intense lines in the visible molecular spectrum. Central chord measurements at four axial locations show the molecular emission is strongly concentrated at the gas port. It is down a factor of ten at 30 cm and by a factor of 40 by 110 cm. At 350 cm the emission is below the level of detection. Radial profiles at 110 cm show the emission is concentrated on the edge of the plasma, unlike the atomic emission, which is concentrated in the center. The relative intensities of different vibrational bands within the $G \rightarrow B$ system indicate a fraction of the ground state molecules are in excited vibrational states. The ratios between intensities of lines in the same band indicate that the rotational temperature is approximately consistent with a temperature of 300 degrees Kelvin. Higher vibrational temperatures will change the rates of dissociation and ionization, although the amount of change is unknown. Widths of spectral lines indicate the molecular translational temperature is below 1 ev.

Molecular hydrogen dissociative continuum emission has been observed in the Tara central cell plasma spectrum. It has been identified through a measurement of its absolute brightness, its wavelength distribution and its time evolution. The brightness at $2700\mathring{A}$ was a factor of 10^4 above the brightness expected from bremsstrahlung continuum, its wavelength distribution matched approximately the wavelength distribution of the H_2 molecular continuum under certain conditions, and its time evolution was similar to the time evolution of the atomic emission, except that the molecular emission peaked earlier and increased at the end of the discharge.

Each continuum photon is accompanied by a dissociation event. The ratio of the wavelength-integrated continuum brightness to the $G \rightarrow B$ brightness gives the ratio of continuum dissociation to molecular ionization, which is .025. The

ratio of these two processes is a function of electron temperature, and the ratio determined from the measurements indicates an electron temperature of 190 ev. This is higher than the temperatures measured in the device and may indicate that the total continuum intensity was estimated incorrectly or that the ratio of dissociation to ionization obtained from the measurements is incorrect.

Chapter 6

Analysis and Modeling

6.1 Introduction

In this chapter, the information gained from the atomic and molecular emission measurements is used to determine particle densities and ionization rates, as well as energy distributions of emitting atoms. The neutral particle spatial emission profiles are analysed to obtain the ionization and density profiles, which are used to estimate the power lost to the plasma due to neutral processes. Hα line profile measurements are used to determine the energy distributions of the emitting atoms. The spatial profiles and energy distributions are compared with the results of a transport simulation.

6.2 Atomic and Molecular Ionization Profiles

The spatial distributions of the atomic and molecular ionization are determined from the distributions of atomic and molecular line radiation, since the ionization rates are proportional to line excitation rates. A plot of the central chord brightnesses of the $H\alpha$ line and the molecular line at 4634.4$\AA$ versus axial distance is shown in figure 6.1. Atomic line brightness was measured at z = 0 cm, 30 cm, 110 cm, and 350 cm. Molecular line brightness was measured at z = 0 cm, 30 cm, and 110 cm. The molecular brightness at 350 cm was below the limit of measurement.

The Hα brightness decreases almost three orders of magnitude between z = 0 cm and z = 350 cm. The molecular line brightness axial profile is similar to the atomic brightness profile, with the difference being that the molecular brightness

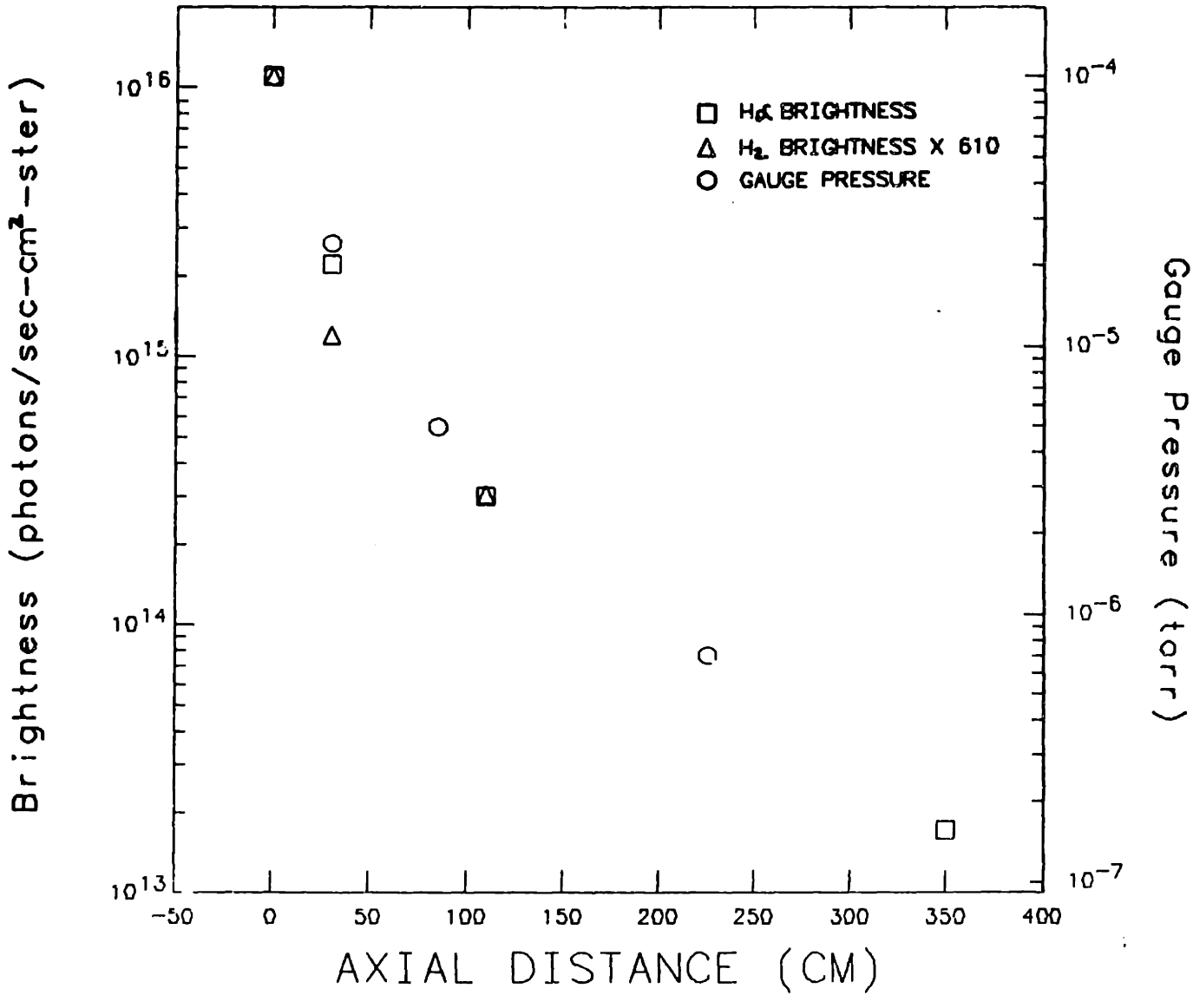

Figure 6.1: Hα brightness, H_2 4634.4$\AA$ brightness and gauge pressure versus z.

decreases a factor of ten between z = 0 cm and z = 30 cm, while the atomic brightness decreases a factor of 4.5. The molecular brightness decrease is less than the atomic brightness decrease between z = 30 cm and z = 110 cm, and the ratios of molecular to atomic brightness at 0 cm and at 110 cm are the same. Also plotted in figure 6.1 is the pressure as measured on the fast ion gauges during the discharge. The pressure profile roughly matches the light profiles. The pressure decreases a factor of four between 0 cm and 30 cm. This is more consistent with the atomic light profile than with the molecular profile, indicating the pressure may be a measurement of atomic edge density rather than molecular edge density.

Radial brightness profiles of both atomic and molecular emission were obtained at z = 110 cm and were shown in figures 4.3, 4.4, and 5.9. Both profiles were Abel-inverted in order to obtain the volume emissivity profiles. Figure 6.2 shows the volume emissivity profiles of the Hα line and the H_2 line at 4205.1$\AA$. The H_2 line emissivity has been multiplied by 500. The Hα emissivity extends to the center of the plasma, and varies a maximum of twenty percent between 0 cm and 18 cm in radius. The H_2 emissivity in concentrated in the outer 10 cm in radius. The emissivity for radii less than 9.4 cm has been given a value of zero, since the Abel-inversion procedure obtained a small negative emissivity for this region. This shows the error inherent in inverting an absolutely hollow light profile.

Measurements of the axially-integrated Hα volume emissivity profile were made with a video camera fitted with a .5 meter focal length telephoto lens and an $H\alpha$ bandpass filter mounted at a window at the north end of the Tara device. [44] The camera/filter assembly was absolutely calibrated using the same tungsten lamp used to calibrate the visible/uv spectrometers. Figure 6.3a shows a x-cut of the profile and Figure 6.3b shows a y-cut. The camera profiles are similar to the inverted Hα profile measured at 110 cm except that the half-intensity radius of the camera profile is smaller. The maximum emissivity occurs at 14 cm for the profile at 110 cm and at 8 cm for the axially-integrated profile. This is due to the higher magnetic field in the gas box, where 90 percent of the radiation is emitted. The field in the gas box is a factor of 1.7 higher than the field at 110 cm and 350 cm. The radius of a flux line will then be a factor of 1.3 higher at 110 cm and 350 cm. The profile at these locations is 3 cm broader than the scaled gas box profile. However, the general shape of the profile obtained by Abel-inversion is the same as that obtained from the video camera profile. Therefore, the Abel-inversion

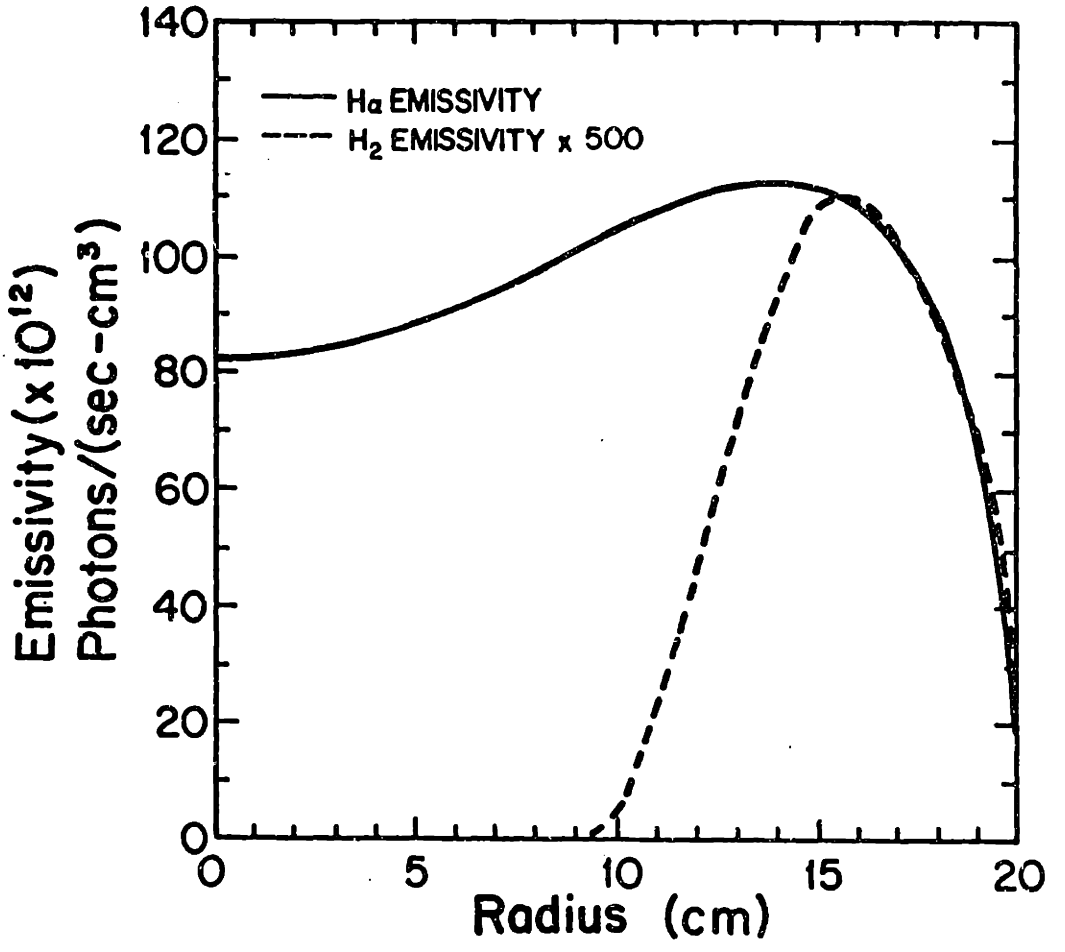

Figure 6.2: Hα and H_2 4205.1$\AA$ line emissivity profiles.

procedure is valid.

The radial ionization profile at 110 cm is obtained from the radial atomic and molecular emissivity profiles. Since the rate for electron impact excitation of the n = 3 level in atomic hydrogen is proportional to the rate for electron impact ionization for electron temperature above 10 ev, a measurement of the local atomic $H\alpha$ emissivity $E_{H,H\alpha}$ may be used to obtain the local atomic ionization rate S_H [7]. The number of ionizations per $H\alpha$ photon is 10 for plasmas with an electron density of $10^{12} cm^{-3}$ and an electron temperature above 10 ev.

$$S_H = 10 \times E_{H,H\alpha} \tag{6.1}$$

A fraction of the Hα emission measured is radiated by atoms arising from dissociation reactions which leave one atom in an excited state. Therefore, this

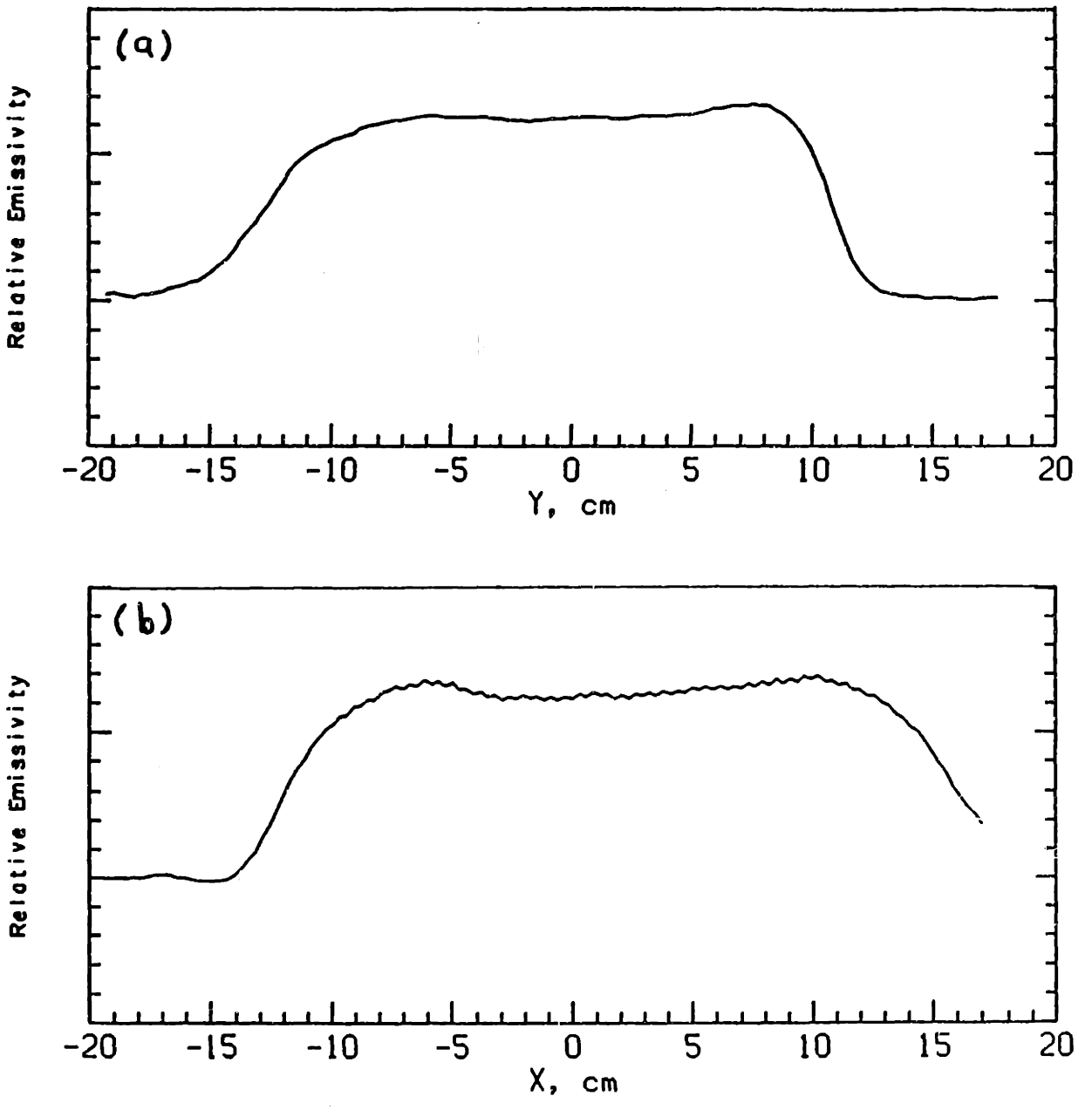

Figure 6.3: (a)Y-cut of the video Hα profile and (b), X-cut of the video profile. From ref.[44].

emission level should be subtracted from the measured Hα emissivity in order to obtain the electron impact excitation Hα contribution. The molecular line emission at 4634.4Å is used to determine the molecular contribution to the Hα light. The number of dissociative events which lead to an Hα photon per 4634.4Å photon is 310. The ratio r of molecular dissociative $H\alpha$ emission to atomic $H\alpha$ emission is then:

$$r = \frac{310}{10} \frac{E_{4634.4\mathring{A}}}{E_{H,H\alpha}} \tag{6.2}$$

where $E_{4634.4\mathring{A}}$ is the emissivity of the 4634.4Å line. Since the ratio of central chord Hα brightness to 4643.4Å brightness is 610, five percent of the central chord $H\alpha$ emission was due to dissociative excitation. The atomic ionization source profile at 110 cm obtained is shown in figure 6.4.

As discussed in chapter 5, the molecular ionization rate is computed in the same manner. The number of ionization events per 4643.4Å photon is 3650. The local molecular ionization rate per unit volume at z ,$S_{H_2}(z)$, is obtained from a measurement of the local molecular line emissivity $E_{4634.4\mathring{A}}$.

$$S_{H_2}(z) = 3650 \times E_{4634.4\mathring{A}} \tag{6.3}$$

The molecular ionization source profile at 110 cm is shown in figure 6.4 along with the total ionization source profile $S_T(z)$ at that axial location, which is the sum of the atomic and molecular contributions.

The molecular contribution to the ionization becomes dominant at the plasma edge. It has a maximum at 14.5 cm and is lower by a factor of 2 at the plasma center. The ionization source rate per axial distance $S_{sym}(z)$ at z = 110 cm is obtained by integrating the local ionization source over the plasma cross section:

$$S_{sym}(z) = \int_0^R S_{T,z} 2\pi r dr \tag{6.4}$$

where R is the maximum radius of emission. The atomic ionization rate at 110 cm is 1.22×10^{18} electrons/(sec-cm) and the molecular ionization rate is 1.1×10^{18} electrons/(sec-cm). The total rate is 2.32×10^{18} electrons/(sec-cm). The ratio of atomic to molecular ionization at 110 cm is 1.1.

The central chord Hα brightnesses at 0 cm and 30 cm are used to calculate the atomic ionization source per unit length at those locations. Radial emissivity profiles obtained by the video camera are used to construct radial atomic ionization profiles at those locations. The atomic ionization source per unit length at

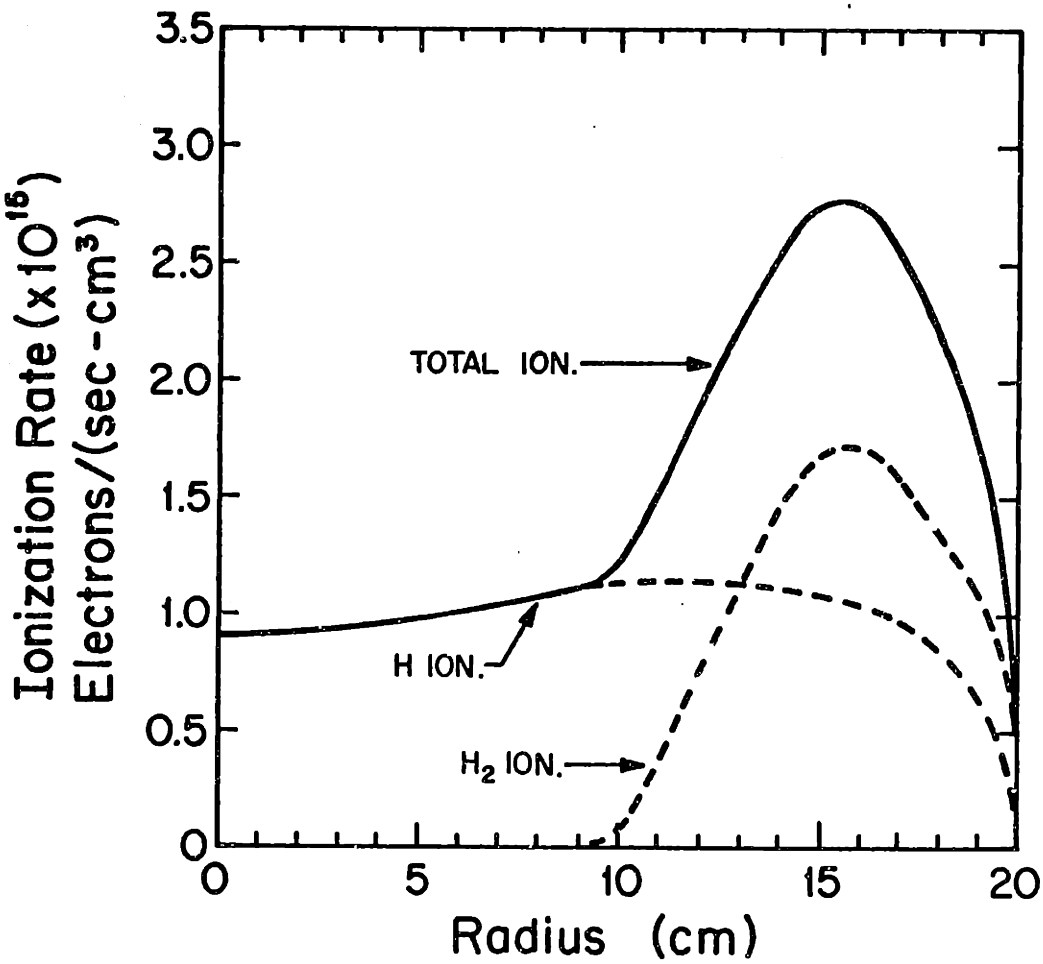

Figure 6.4: Atomic ionization, molecular ionization, and total ionization radial profiles at z = 110 cm.

0 cm and 30 cm is calculated by reducing the radial scale of the profiles at 110 cm by a factor of .74 in order to match the atomic emission profile at 110 cm to the atomic emission profile obtained by the video camera. The emissivities are scaled up by a factor which ensures the central chord brightness value obtained from the scaling procedure is the same as the measured brightness. The atomic ionization source profiles at 0 cm and 30 cm are then computed. The ionization source per unit length at those locations is then obtained using equation 6. The atomic ionization source per unit length at 350*cm* is obtained in the same manner.

The molecular ionization rate per unit length at z = 0 cm and z = 30 cm cannot be computed in the same way, since molecular radial emission profiles at z = 0 cm and 30 cm were not measured. Since molecules were injected through

two ports on each side of the chamber, these profiles are expected to be very azimuthally-asymmetric. The mean free path for a molecule in the plasma is less than 4 cm, as seen in figure 6.2. Therefore, all of the molecules injected through the side ports would be ionized or dissociated within 4 cm of the ports. All of the emitting molecules observed in the up-down central chord measurements at z = 0 cm and 30 cm must have originated on the wall of the chamber, since the molecules injected through the side ports would not reach the viewing chord. Assuming that the molecules desorbed from the wall, known as 'recycled' molecules, are in the same radial profile at z = 0 cm and 30 cm as the molecules at 110 cm, corrected for profile narrowing, the ionization rate per unit length at 0 cm, 30 cm, and 350 cm due to this symmetric component may be computed using eq. 6.4.

The total azimuthally-symmetric ionization source is then obtained by integrating the azimuthally-symmetric ionization source per unit length along the length of the plasma.

$$S_T = \int S_{T,sym}(z)dz \tag{6.5}$$

where the integral is carried out over the length of the central cell plasma. The z-dependence is assumed to be exponential between the measurement locations and an exponential function is fitted to each region between the observation points. The e-folding length of the regions between 0 cm and 30 cm, 30 cm and 110 cm, and 110 cm and 350 cm are 19 cm, 40 cm, and 86 cm respectively for the Hα emission, and 13 cm, 61 cm and 86 cm respectively for the H_2 emission. Figure 6.5 shows the total azimuthally-symmetric ionization current per unit length versus axial distance. Integrating along z gives an atomic ionization source of 1.3×10^{21} electrons/second or 208 amps, and an azimuthally-symmetric molecular ionization rate of 9.6×10^{20} electrons/second or 154 amps. The total symmetric ionization current is then 362 amps.

The atomic ionization rate was also determined from the video camera measurements. The camera measured a total radially- and axially-integrated ionization of 200 amps. [45] Considering the assumptions made in calculating the total atomic ionization rate from central chord measurements, the agreement is quite good.

The atomic ionization rate was twice the molecular particle injection rate. Molecular particle injection rate is calculated from the gas injection rate Γ_{gas}, measured in torr-liters/second. The molecular particle injection rate $\Gamma_{H_2,p}$ is pro-

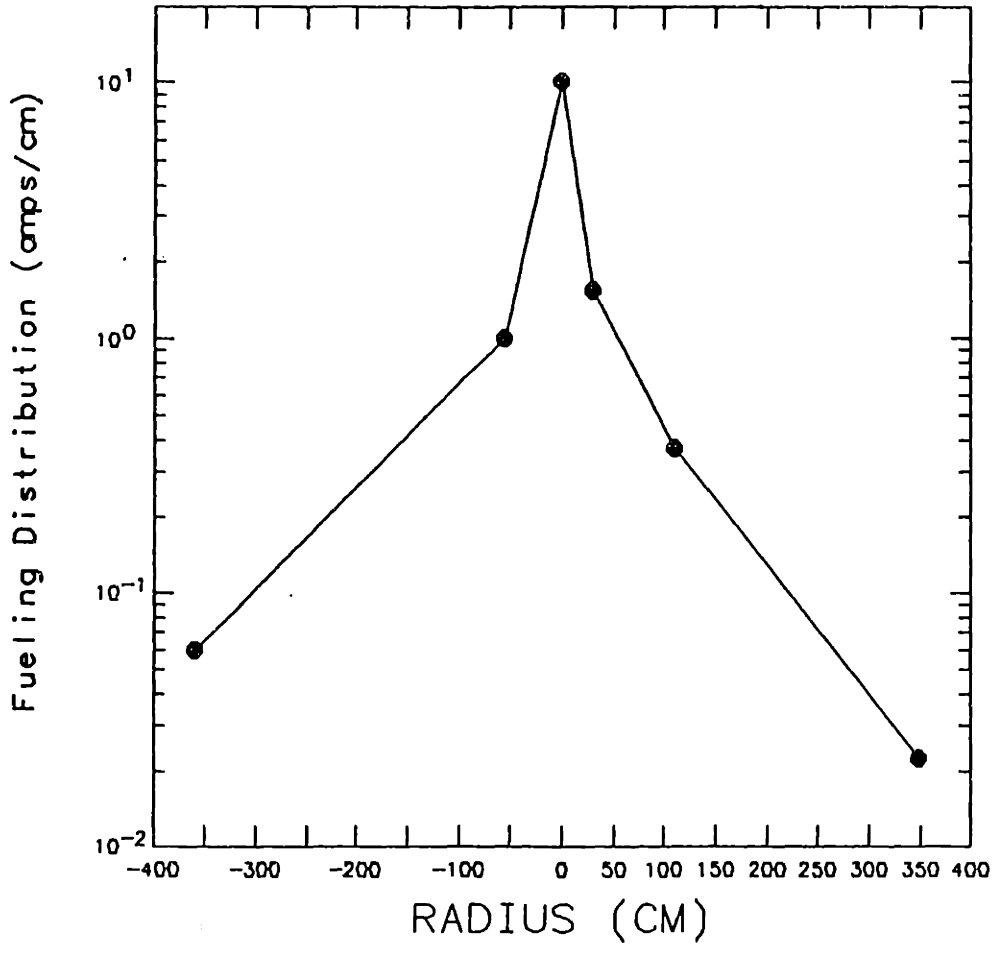

Figure 6.5: Radially-symmetric axial fueling profile.

portional to the gas injection rate:

$$\Gamma_{H_2,p}(amps) = 5 \times \Gamma_{gas} \tag{6.6}$$

The gas injection rate during the discharges from which this data was obtained was 20 torr-liters/second. Thus, the molecular particle injection rate was 100 amps.

The total molecular ionization can be estimated as the sum of the symmetric and asymmetric component. The asymmetric component, which enters through the side ports, must equal the molecular particle injection rate, since virtually all of the injected molecules are ionized. The total molecular ionization rate is then equal to the sum of the non-recycled contribution, 100 amps, and the recycled

contribution, 154 amps, for a total of 254 amps of molecular ionization current. The total ionization current is then 462 amps.

The values of the total plasma ionization source and the total plasma number may be used to compute the global plasma confinement time τ_p:

$$\tau_p = \frac{\int n_e dV}{S_T} \tag{6.7}$$

where the integral is carried out over the whole plasma volume. The total plasma number is 1.5×10^{18} particles and the total plasma source, S_T, is $462 \times 6.25 \times 10^{18}$ particles/sec, which gives a global confinement time of .52 milliseconds. Since the edge plasma has a lower density and higher source, the local confinement time there will be smaller than the global confinement time. Since the core plasma has a higher density and lower source, the local confinement time there will be higher.

Using the rates of molecular and atomic ionization, one can obtain an estimate of the power expended due to ionization, as well as of the power expended in molecular and atomic radiation. Each atomic ionization requires 13.6 ev of energy, and 11. ev of energy is radiated in Lyman series photons. Thus the energy cost of one atomic ionization is 24.6 ev. The total power cost is the product of the energy cost per ionization and the ionization current, or 5.1 kilowatts. Each molecular ionization requires 16 ev of energy, and is accompanied by an average of 7.2 ev of energy lost in radiation, for a total of 23.2 ev. Molecular ions have a short mean free path for dissociation. Therefore, each will be dissociated by electron collision. The energy cost per molecule is 10 ev. 8 ev of this energy becomes the kinetic energy of the proton and atom and thus is not all lost to the plasma. The total power cost in molecular ionization, dissociation, and radiation is 8.4 kilowatts.

The Hα radial and axial profiles are used along with axial pressure measurements and axial diamagnetism measurements to estimate the power lost in charge-exchange with plasma protons. For a given ion temperature, the charge exchange rate is proportional to the atomic $H\alpha$ emission rate. The number of charge-exchange events per $H\alpha$ photon κ varies between 14.3 and 30. for the ion temperatures involved, 30 ev - 700 ev. [6,46] The local charge-exchange power P_{cx} is then:

$$P_{cx} = \kappa E_{H,H\alpha} T_i \tag{6.8}$$

The impurity ion temperature profiles in figure 3.13 were used in the calculation. The local charge exchange power is integrated over the plasma cross section to

H_0 Ion.,Rad.	5.1 Kilowatts
H_2 Ion.,Dis.,Rad.	8.4 Kilowatts
Charge-Exchange	76.2 Kilowatts
Total Power Loss	89.7 Kilowatts

Table 6.1: Neutral Particle Power Losses

obtain the charge-exchange power loss per unit length at the 0 cm, 30 cm, 110 cm, and 350 cm. Comparisons of pressure gauge measurements made in the south half of the device were used to estimate the local ionization profiles. Comparison of the diamagnetic loop measurements were used to compute local ion temperature profiles in the south region. Both the gauge reading and the diamagnetism measurement were higher in the south half. Hotter ions in the south may cause higher rates of gas flux from the walls.

Figure 6.6 shows a plot of the charge-exchange power loss per unit length as a function of axial distance. Exponentials functions were fitted between the measurement locations. The axially-integrated charge-exchange power loss was 76.2 kilowatts. 76% of the power is lost from the south half of the machine according to the estimation. The total power expended in neutral particle processes was estimated at 90 kilowatts. The uncertainty is estimated to be 40 %. The total injected rf power was 300 kilowatts.

A list of the neutral power losses is shown is table 6.2.

6.3 Analysis of the High Resolution Balmer-Alpha Line Profile

The high and medium resolution measurements of the Hα line profile show wavelength broadening beyond the instrumental width. This broadening is mostly all doppler and instrumental. Analysis of the line shape thus yields information about the radiating atoms, which is related to the source of the atoms as well as their interaction with the plasma and the wall.

Spectral lines can be broadened through several mechanisms: instrumental, doppler, electric fields, magnetic fields, and 'natural' broadening. In the case of the $H\alpha$ line, broadening due to electric fields(stark broadening) and magnetic fields was negligible. At the electron densities involved the expected stark broadening would be less that .01$\AA$. [47]. If Stark broadening were present in the line,

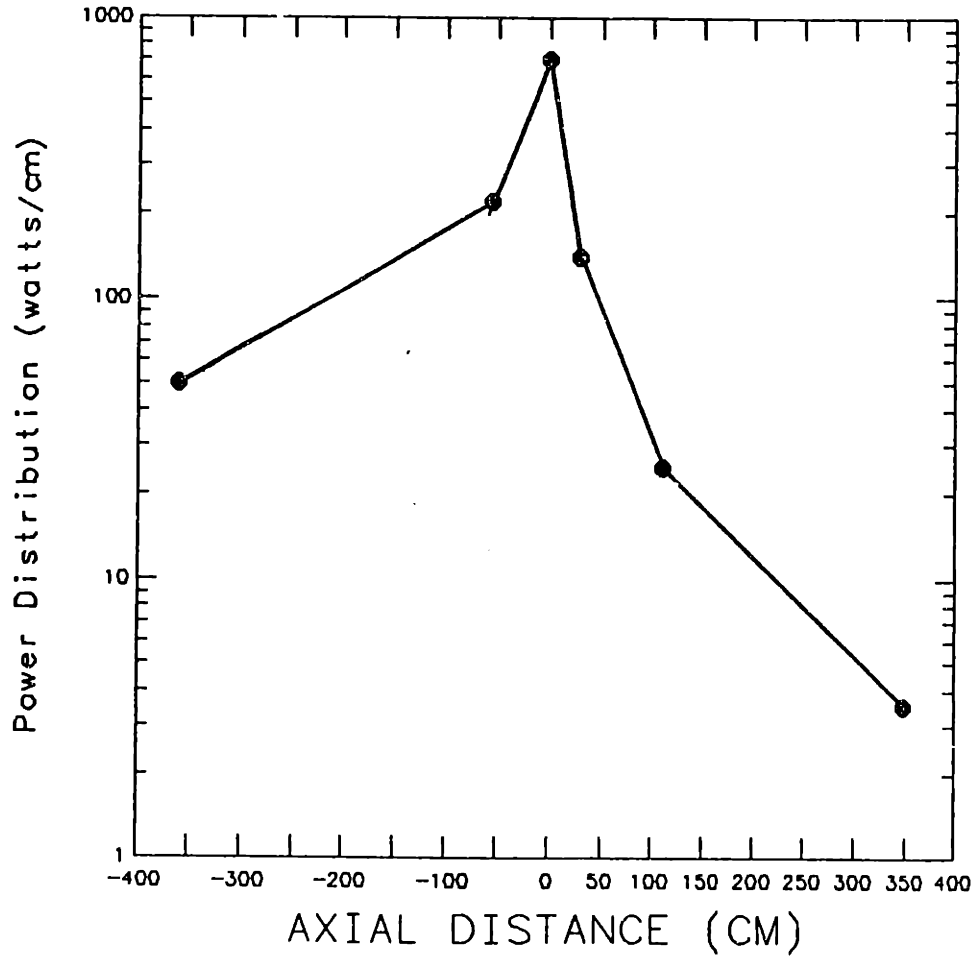

Figure 6.6: Charge-exchange power loss versus axial distance.

the higher n Balmer lines would show the effect of greater broadening. The broadening is proportional to the square of the difference in the quantum numbers of the transition. [48] The line profile of the $n = 8$ to $n = 2$ transition was recorded with the oma. It should show 36 times the stark broadening of the Hα transition. Its measured width is narrower than the measured Hα line width and the instrumental width is greater at the lower wavelength. Broadening due to magnetic fields, Zeeman broadening, is less than .04$\AA$ at a field strength of 2100 gauss [49]. The instrumental and doppler broadening in profiles measured with the Fabry-Perot interferometer and the oma spectrometer were greater (by a factor of 10 at least)than these values.

The major types of broadening important here are 'fine structure', instrumental, and doppler. The largest source of broadening other than instrumental and

doppler is 'fine structure broadening'. The Hα 'line' is a set of lines ,each with a different set of upper and lower j states. The major lines are two lines of approximately equal strength separated by .1$\mathring{A}$. [50] The effective instrumental width was .13$\mathring{A}$. The effective non-doppler broadening is the square root of the sum of the squares of the instrumental and fine structure broadening and equals .16$\mathring{A}$. The doppler broadening is a factor of 4.5 greater than the effective non-doppler broadening.

Analysis of doppler-broadened profiles is usually confined to fitting Maxwellian functions to the profile and inferring a temperature from the width. In this work, the integral equation relating the wavelength distribution $I(\Delta\lambda)$ to the particle energy distribution is used to obtain the energy distribution function. The equation in solved in appendix A. The energy distribution may be obtained from the wavelength distribution as follows:

$$F(E) \propto \frac{dI(\Delta\lambda)}{d\Delta\lambda} \tag{6.9}$$

where $F(E)$ is the particle energy distribution and wavelength is converted to energy through the equation.

$$E = 10.9 \times (\Delta\lambda)^2(ev) \tag{6.10}$$

where $\Delta\lambda$ is expressed in angstroms.

The inversion is applied to the wavelength distribution to obtain the energy distribution of the radiating particles. Figure 6.7 shows the energy distributions obtained from applying the inversion to the profiles in figures 4.11a and 4.12a. The distribution shows particles with energies up to 12 ev. Both distributions show a peak at 1.6 ev. Under typical plasma conditions, ninety percent of the cold component particles have energies less than 3 ev.

The wavelength distribution measured is inconsistent with the Hα profiles measured from atoms arising from the dissociative excitation of molecular hydrogen. If the Hα radiation was emitted by atoms which are products of reactions in which the molecule dissociates into one or two excited atoms, the profile would consist of two distinct components, one with a width of .3$\mathring{A}$ and one with a width of $.9 - 1.5\mathring{A}$. [51,52,53,54,55] These profiles correspond to atomic energy distributions which consist of two components, one with an average energy of $.3 - .4ev$, and one with an average energy of $2 - 6ev$. The wavelength and energy distributions measured in these experiments did not show two distinct components,

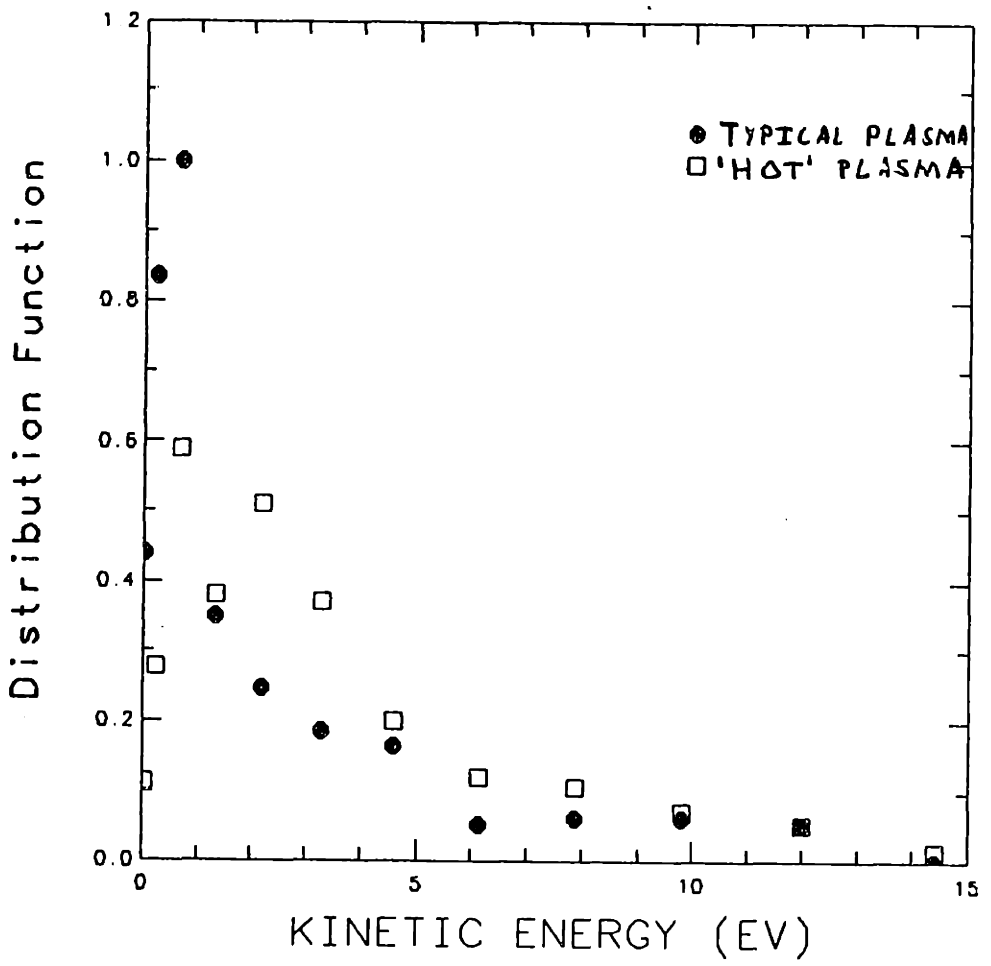

Figure 6.7: Plots of the energy distributions determined from the Hα line profiles.

rather it showed two components blended together. This is consistent with the finding that only 5% of the measured $H\alpha$ results from dissociative excitation. It is also consistent with the brightness profile measurements. The $H\alpha$ are chordal brightness profiles are peaked in the center while the H_2 emissivity profiles are peaked on the plasma edge and are attenuated by a factor of two in the center. If the $H\alpha$ emission is due to dissociative excitation, the $H\alpha$ profile and the H_2 band profile should have the same radial distribution.

The comparison of H_2 continuum intensity to the $G \rightarrow B$ band intensity indicates that molecular ionization dominates over neutral atom dissociation. Molecular ion will most likely dissociate into a proton and a ground state atom through electron collision. This is two-step ionization. There are several other dissociation mechanisms. In addition to molecular ionization and continuum dissociation, the

Process	Rate	$E_0(ev)$
Singlet State Diss.	2×10^{-9}	$.4ev$
Continuum Diss.	3×10^{-9}	$3ev$
Diss. Excitation	5×10^{-9}	$.9ev$
2-step Ionization	5×10^{-8}	$4ev$
Direct Ionization	3×10^{-9}	$6ev$

Table 6.2: Molecular Ionization/Dissociation Rates. From ref.[6].

molecule can dissociate by being excited to the singlet states B, C and then decaying to unbound vibrational states of the ground state. It can also dissociate by excitation to states which dissociate into one or two excited atoms, and it can dissociate into a proton and a ground state atom directly(dissociative ionization). A list of these processes, their rate coefficients and the average energies of the atoms produced, E_0, is given in table 6.3 [6]. Two-step molecular ionization is expected to be the dominant process. The breakup of the molecular ion yields a distribution peaked at 4 ev in energy with a width of 3 ev. This process is illustrated in Figure 6.8, which is plot of the molecular ground state, and molecular ion ground state potentials and the molecular ion $2p\sigma$ state potential [38]. The molecule is first ionized, then excited to the unbound ionic state $2p\sigma$ which then dissociates into an atom and a proton. The particles divide the residual energy equally.

Atoms with energies higher than 7 ev can only come from direct dissociation into a proton and an atom. Figure 6.8 shows this process [38]. The molecule is excited directly from its ground state to the unbound $2p\sigma$ ionic state. In addition, the molecule may be excited to resonance states from which the molecule decays to the unbound $2p\sigma$ state and then dissociate into a proton and a atom(autoionization). Figure 6.9 shows a plot of the energy distribution of protons produced by electron bombardment of molecules [56]. The highest energy component arises from direct breakup, and the other components arise from breakup through intermediate states. Thus, it seems that dissociative ionization may be responsible for the higher energy dissociation products.

The atoms with energies less than 2 ev may arise from either continuum dissociation, dissociative excitation, or may be particles created at higher energies which have lost energy through collisions with the chamber wall. The sum of the rates of the processes producing atoms of these energies is one fifth the rate of

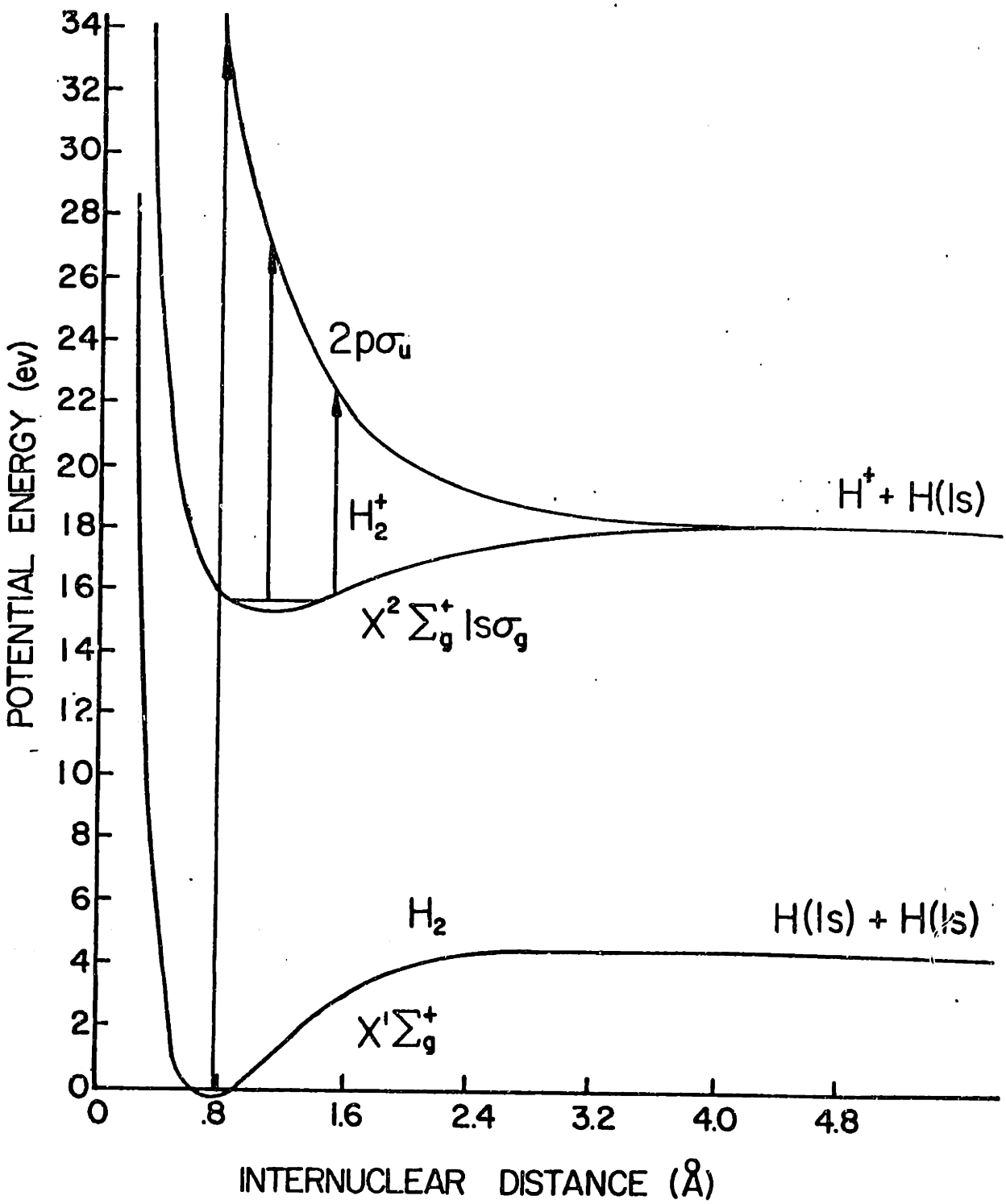

Figure 6.8: H_2 potential energy plots showing ionization and dissociation processes. From ref.[38].

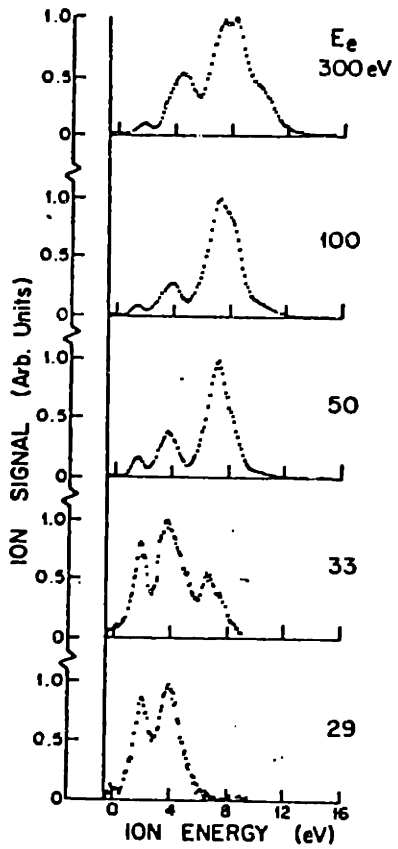

Figure 6.9: Kinetic energy distributions of protons produced by electron collision with H_2. From ref.[56]

ionization. Thus, these processes may explain some of the lower energy particles.

The complete line profile, as measured by the oma spectrometer at 350 cm shows light radiated from particles with energies above 15 ev. The oma profile shows two features: the central cold component, which was investigated with the Fabry-Perot interferometer, and a hot component, which has a half-width of approximately $3\mathring{A}$. The profiles were fitted with a five parameter function. The fitting function is a sum of a 'cold particle' function, F_c, and a 'hot particle' function, which is a Maxwellian. The cold particle function is a convolution of the wavelength distribution measured with the Fabry-Perot interferometer, $E_F(\lambda)$,

and the oma instrumental function $F_{oma}(\lambda)$:

$$F_c(\lambda) = \int F_{oma}(\lambda - \lambda')E_F(\lambda')d\lambda' \tag{6.11}$$

The oma instrumental function is determined by illuminating the oma spectrometer with a hydrogen lamp. The width of the lamp $H\alpha$ line is .18Å. $F_{fit}(\lambda)$ is given by:

$$F_{fit}(\lambda) = A_1 \times F_c(\lambda - A_2) + A_3 \times e^{(\frac{\lambda - A_4}{A_5})^2} \tag{6.12}$$

where A_1 is the amplitude of the cold particle function, A_2 is the central wavelength of the cold particle function,A_3 is the amplitude of the Maxwellian, A_4 is the central wavelength of the Maxwellian, and A_5 is proportional to the width of the Maxwellian. The fitting routine used a gradient-least-squares technique [57]. The fitting function fit the data fairly well at all chordal radii. The central wavelength of both functions differed by less than .03Å, and did not vary with chordal radius. A temperature was obtained from the Maxwellian width of each profile. In addition the areas under both the cold particle function and the Maxwellian were integrated. Figure 6.10 shows a plot of the atomic temperature and the area ratio versus chordal radius. The variations in temperature and ratio are less than the uncertainties, which are mainly statistical in nature.

The hot atomic temperatures obtained are higher than the maximum energies given to atoms in molecular dissociation. The maximum observed atomic dissociation energy is 12 ev. The only mechanism for atoms to achieve higher energies in the Tara plasma is charge-exchange with plasma protons:

$$H_0 + H^+ \rightarrow H^+ + H_0 \tag{6.13}$$

The proton captures the electron and the new atom has the energy of the former proton.

The hot atomic temperatures are 45% ± 10% of the ion temperature at the mean emitting radius, as determined by impurity line doppler widths. This suggests that these hot atoms originated in charge-exchange reactions, obtained the proton energies, and lost energy in reflection on the chamber walls. This may also explain the similarity of the cold atomic profile to the hot atomic profile. If the radial distributions are determined mainly by the wall reflection, then the two components may have similar radial profiles even though they have quite different energies.

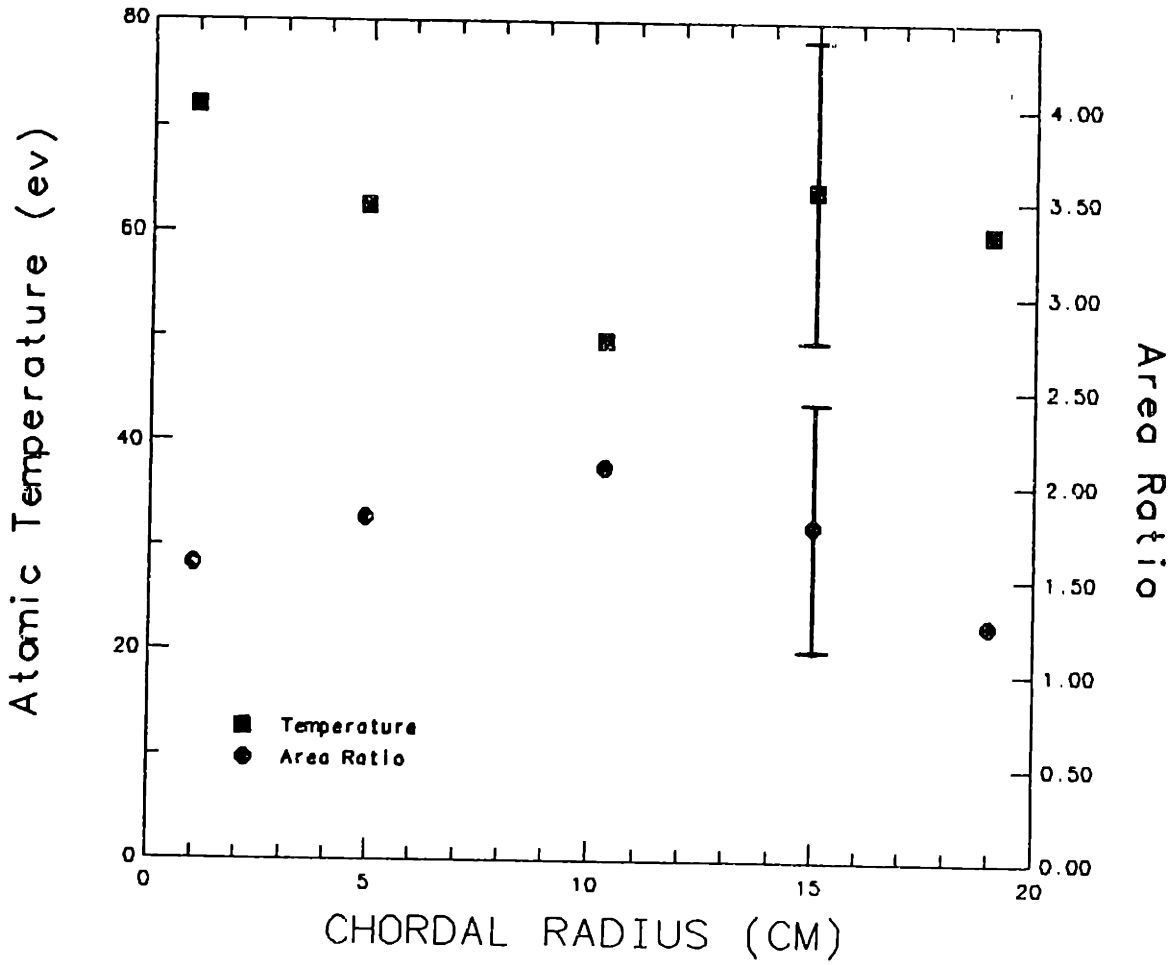

Figure 6.10: Plot of the neutral temperature and area ratio as a function of chordal radius obtained by fitting the Hα profiles with the five-parameter function.

A zero-dimensional model was used to calculate the expected approximate hot/cold component ratio following the treatment in ref. [23]. The following equation relates the time derivative of the hot component to its sources and sinks.

$$\frac{dn_{hot}}{dt} = n_p < \sigma v >_{cx} n_{cold} - n_e < \sigma v >_{ion} n_{hot} - n_{hot}\frac{v}{l} + Rn_{hot}\frac{v}{l} \qquad (6.14)$$

where $< \sigma v >_{cx}$ is the rate of charge exchange, $< \sigma v >_{ion}$ is the rate of ionization, v is the average speed of the hot atoms, l is the average distance traveled to the plasma edge, and R is the reflection probability. In the steady state,

$$\frac{n_{hot}}{n_{cold}} = \frac{n_e < \sigma v >_{cx}}{n_e < \sigma v >_{ion} + (1-R)v/l} \qquad (6.15)$$

Using the average densities and rates for the regions involved, the average speed of the hot atoms, $1.1 \times 10^7 cm/sec$, and the measured ratio of hot to cold atoms

of .62, one obtains:

$$\frac{1-R}{l} = 7.4 \times 10^{-3} cm^{-1} \tag{6.16}$$

The plasma diameter was 40 cm. If the average length traveled to the plasma edge was 50 cm, an R of .63 is obtained. This is within the range of reflection coefficients presented in ref. [58] for reflection of hydrogen atoms on titanium.

The fact that the hot atom component was present only in the profiles measured at 350 cm is consistent with the impurity ion temperature profiles. The mean radius of charge-exchange was 12.5 cm. The impurity temperatures at a radius of 12.5 cm at the 0 cm, 30 cm, and 110 cm axial locations were factors of 3-7 lower than the temperatures at the same radius at 350 cm. If the ion temperature at 12.5 cm was 40 ev at the locations closer to the gas port, and the reflected atoms had a 20 ev temperature, the resulting hot atom component would not be distinguishable from the cold atom component. In addition, the charge-exchange rate is 60% lower at the lower ion temperatures, which would make the hot atom component smaller.

6.4 Atomic and Molecular Density Distribution and Comparison with Models

The atomic and molecular radial density profiles are related to the absolute emissivity profiles. The local atomic or molecular density is obtained by dividing the local Hα and 4205.1$\AA$ emissivities by the product of the local electron density, rate coefficient and branching ratio, if it applies:

$$N_n = \frac{E_n}{n_e Q_{ex} R_B} \tag{6.17}$$

where N_n is the local neutral density, E_n is the local emissivity, n_e is the local electron density, R_B is the branching ratio, and Q_{ex} is the local excitation coefficient. The excitation coefficient is assumed to be constant in radius. The electron temperature varies from 80 ev on axis to 100 ev at the plasma edge. The excitation coefficient for a temperature of 90 degrees is used, and the error introduced is less then 5% [6].

The atomic and molecular density profiles obtained are shown in figure 6.11. Atomic density is concentrated at the edge of the plasma and is down by a factor

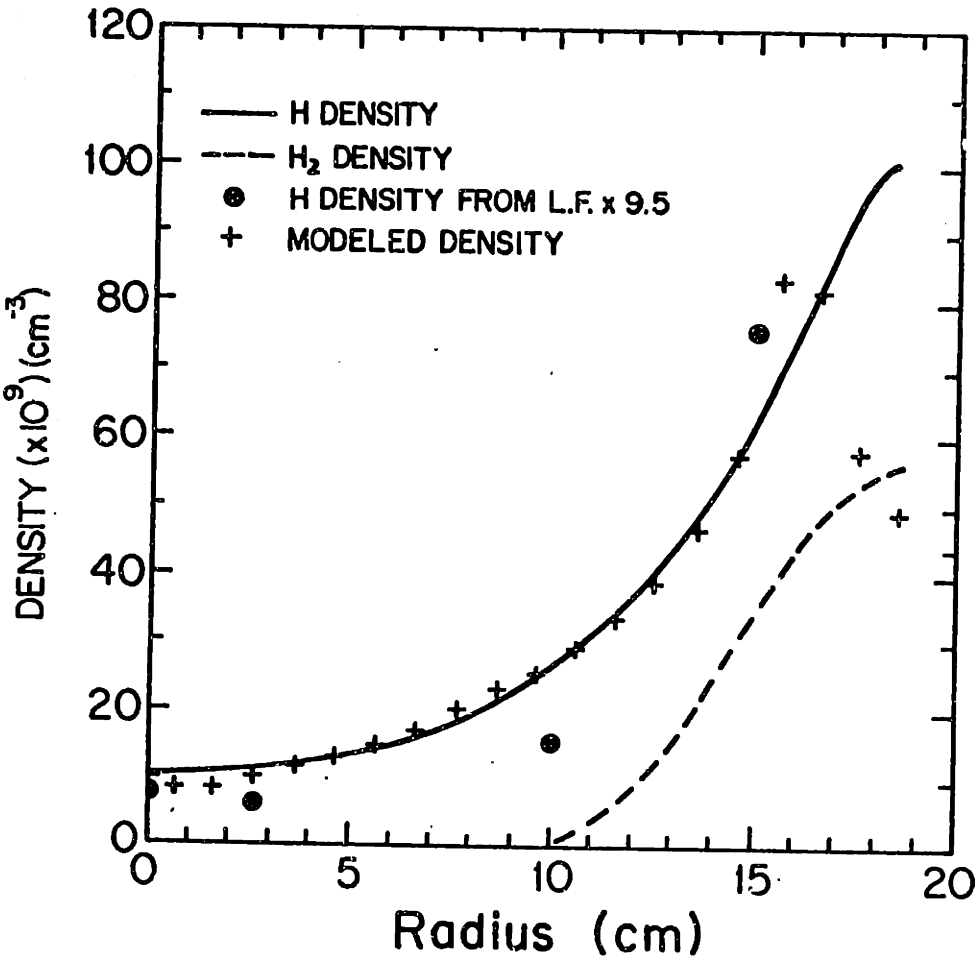

Figure 6.11: Atomic and molecular radial profiles and modeled profile.

of ten on axis. Plotted along with the profile are atomic density values measured by laser fluorescence which have been multiplied by 9.5 [59]. The pressure during the fluorescence measurement was a factor of 2 higher than the gauge pressure during these measurements, which accounts for some of the discrepancy, but the remaining difference cannot be explained. Within the uncertainties in both measurements, both profiles show the same radial distribution, except for the factor of 9.5.

The inferred molecular density profile is similar to the atomic profile at radii beyond 13 cm, but falls to zero at 10 cm. This is explained by the fact that molecules originate on the chamber wall at room temperature, while atoms originate in dissociation reactions, which give the atoms .3-12 ev of kinetic energy. The pressure at 110 cm is obtained by interpolation. The pressure was 2.7×10^{-6} torr.

If the gauge was measuring only molecules the pressure reading would indicate a density of $9.5 \times 10^{10} molecules/cm^3$and if it was measuring only atoms, it would indicate a density of $1.6 \times 10^{11} atoms/cm^3$. Both these numbers are within a factor of 2 of the inferred densities, which is within the uncertainties.

This measurement might not be simply related to either the atomic or molecular density. Since molecules originate on the wall at positions away from the gas port, and have a mean free path of less than 4 cm, they cannot enter the gauges. Atoms, on the other hand, can traverse the plasma and enter the gauges, so it is likely that the gauge reading is a function of the local atomic density. The atoms may recombine inside the gauge so that in general there will be a mixture of atoms and molecules in the gauge. The densities in the gauge will depend on the flux of atoms into the gauge, the recombination, and the rate that atoms and molecules leave the gauge. Thus, the gauge only gives a relative indication of atomic density.

The proportion of atoms and molecules in the device depends upon the balance between atomic creation through molecular ionization(ignoring the smaller contribution from dissociation), and atomic loss through ionization, charge-exchange, and wall absorbtion. In a zero-dimensional model,

$$\frac{dn_H}{dt} = n_e < \sigma v >_{H_2,ion} n_{H_2} - n_e[< \sigma v >_{H,ion} + < \sigma v >_{H,cx}]n_H - (1-R)\frac{v}{l}n_H \tag{6.18}$$

where the $< \sigma v >_{H_2,ion}$ is the rate of molecular ionization, $< \sigma v >_{H,ion}$ is the rate of atomic ionization, $< \sigma v >_{H,cx}$ is the rate of charge exchange, R is the reflection coefficient, v is the average atomic speed, l is the average distance to the edge of the plasma, and n_s is the density of species s.

In the steady state:

$$\frac{n_H}{n_{H_2}} = \frac{n_e < \sigma v >_{H_2,ion}}{n_e(< \sigma v >_{H,ion} + < \sigma v >_{H,cx}) + (1-R)v/l} \tag{6.19}$$

Using the average electron densities and rates in the regions involved, and using a reflection coefficient of 1, one obtains a ratio of atomic to molecular density of .6, while the experimental result was 1.8. A lower reflection coefficient would decrease the atomic to molecular ratio obtained from the model. If the molecular ionization rate were higher than the rate used in the model it would explain some of the discrepancy.

In order to model the neutral transport, a Monte-Carlo code was developed. In the model, the Tara central cell chamber is an infinitely long cylinder with a

radius of 25 cm. Particles are created at a point at a specified radius and random in azimuthal angle. The particles have a specified initial energy and are given a random initial direction. In one time step a particle travels a distance $v\Delta t$ where v is the particle speed and Δt is the time step. After each time step the code tests whether the atom has been ionized or charged-exchanged. In modeling the cold atom transport, the rates of ionization and charge-exchange are summed to give the total loss rate, since either an ionization or charge exchange event removes the cold atom. In modeling the hot atom transport, only the ionization rate is included, since charge-exchange of a hot atom with an ion does not change its energy more than twenty percent on average. The probability P_a of annihilation after a time interval Δt is given by:

$$P_a = Q\Delta t \tag{6.20}$$

where Q is the rate for annihilation. The code models the wall as a partially reflecting locally-flat surface with a reflection probability which depends on the angle of the incident particle. The code determines the angle of incidence and uses the corresponding reflection coefficient, whose value is taken from ref. [58] The greater the angle of incidence, as measured from normal, the greater the reflection probability. The fraction of energy lost on reflection is specified in the code and is also taken from ref. [58].

The cold atom source radius is determined by finding the mean radius of the azimuthally-integrated radial molecular line emissivity distribution, since the molecular emissivity is proportional to the molecular ionization rate. The hot atom source radius is determined by finding the mean radius of the azimuthally-integrated Hα emissivity profile, since the Hα emissivity is roughly proportional to the charge-exchange rate, ignoring ion temperature effects. The cold atom and hot atom source radii are 16 cm and 12.5 cm respectively. The cold atom source energy used is 4 ev, the dissociation energy of the molecular ion. The hot atom source energy used is 150 ev, the ion temperature measured at a radius of 12.5 cm and a z-location of 350 cm, where the hot atom profiles were measured.

The routine also obtains the particle energy distribution. The energies present E_n are equal to:

$$E_n = nfE_i \tag{6.21}$$

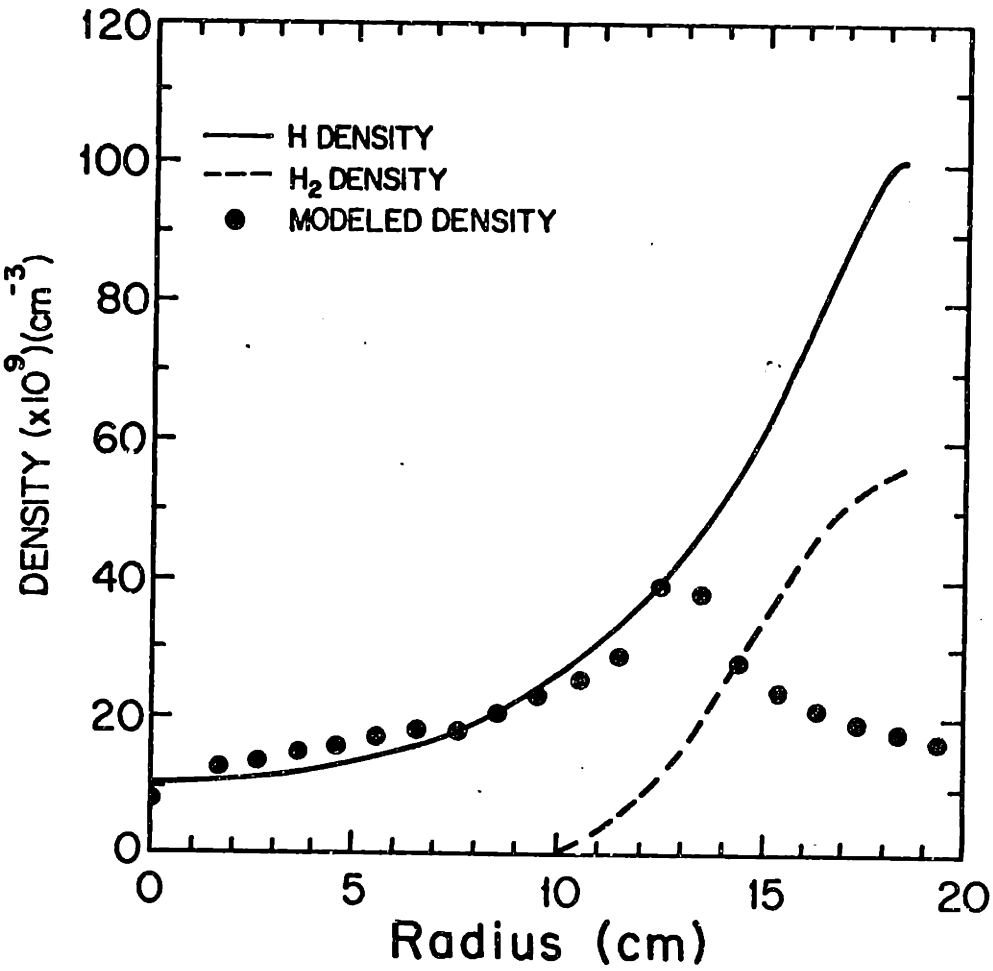

Figure 6.12: Atomic and molecular density profiles along with a modeled profile.

where n is an integer, f is the fraction of energy lost on reflection, and E_i is the initial energy.

Figure 6.11 shows a plot of the radial atomic density profile obtained from the model using an initial energy of 4 ev plotted along with the atomic density profile obtained from the emissivity profile. A profile obtained from a simulation using an initial energy of 150 ev is shown in Figure 6.12. In both cases the specified energy fraction lost on the wall was .5.

Both simulated profiles show a peak at the source radius. The cold atom simulation matches the data profile inside 15 cm. Due to the localization of the source used in the model, the modeled density does not match the inferred density profile for larger radii. The density obtained from the hot atom simulation has much less variation in radius and matches the data profile only inside 12 cm

in radius. Simulations were also run for both energy populations in which the reflection coefficient was independent of angle and set to .5. Those profiles had a lower ratio of edge density to central density and were a poorer match to the data. The edge density to central density ratio for the 4 ev atoms was 10.6 for the angel-variable reflection case and 6.1 for the angle-independent reflection case. The edge-to-center density ratio for the 150 ev case was 3.3 for the angle-variable reflection case and 2 for the angle-independent reflection case. A previous Monte-Carlo atomic density simulation performed for the Tara central cell plasma obtained an edge-to-center attenuation factor of 5 [60]. This previous model assumed an angle-independent reflection coefficient, a reflection probability of .3, and an atomic energy of 2.5 ev. It differs from the angle-independent simulation performed here by 18 %.

Plots of the energy distributions obtained with the model are shown in Figure 6.13. The cold atom case shows 32% of the atoms with energies one half of the initial energy or less. The energy distribution obtained from the high-resolution line profile shows that more than 50% of the cold atoms had energies less than 2 ev. Thus, the code does not accurately predict the cold atom energy distribution. If the lower energy dissociation mechanisms were included in the code, there would be closer agreement between the inferred and modeled distributions. The hot atom model shows 70% of the atoms with energies one half of the initial energy or less. The oma measurement of the hot atom profile showed that 90 % of the hot atoms had energies at one half the ion temperature or less. Therefore, the model does not accurately predict the observed hot atom energy distribution.

One reason the model does not predict the measured energy distributions may be that it models the wall interaction incorrectly. The reflectivity probability used is independent of particle energy. If the reflectivity decreased with increasing energy, the average energy of atoms in the plasma would decrease, since the higher energy particles would have a greater chance of being lost to the wall. The discrepancy in the hot atom density profile may be due to a mistake in the angular dependence of the reflection coefficient used. If the actual reflection probability is a stronger function of angle, a more hollow hot atom profile may be obtained.

Axial transport may be investigated by studying the axial brightness profiles. The z-dependence of the emission indicates the presence of sources away from the gas port. With no sources present a population of atoms or molecules with

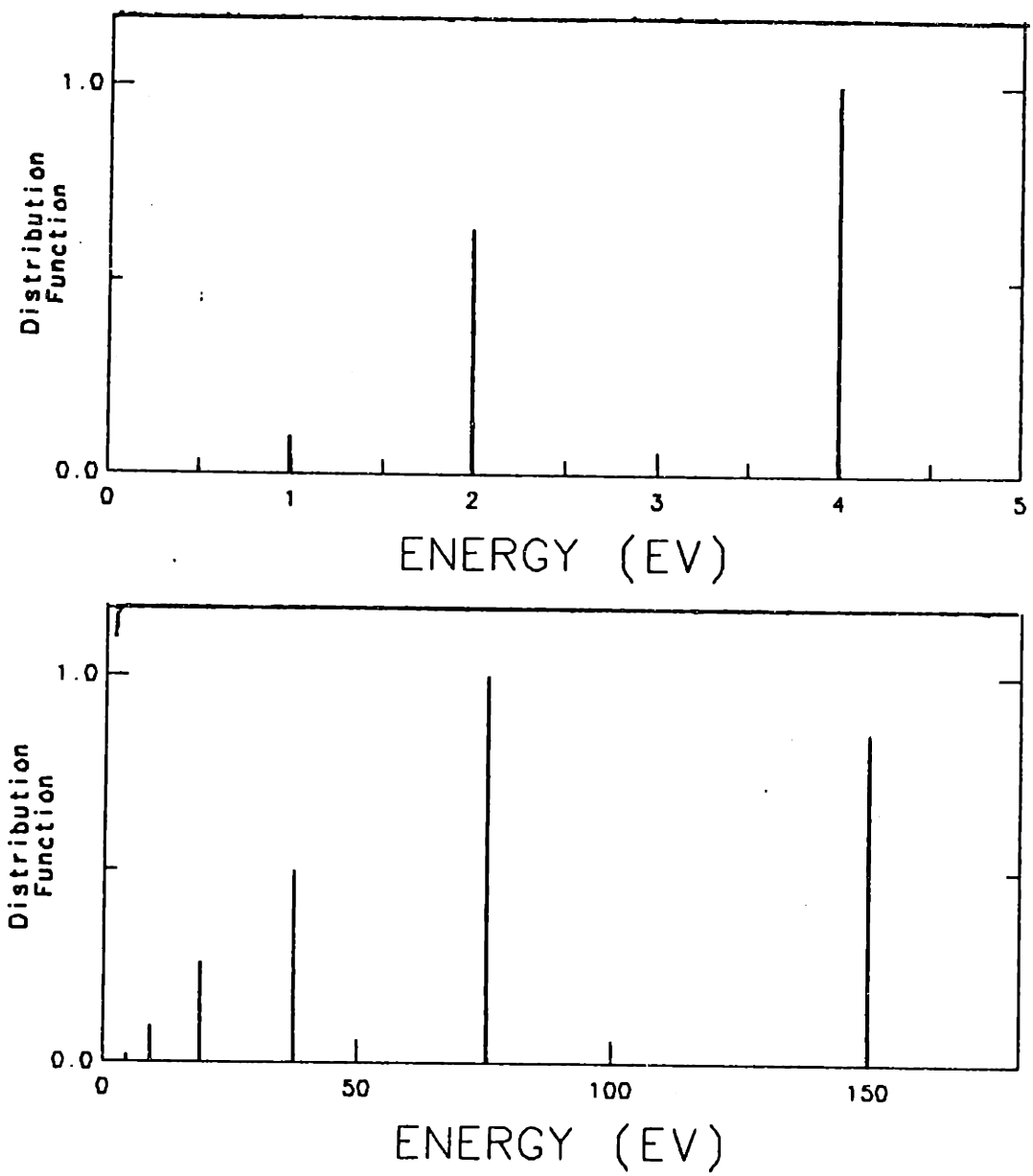

Figure 6.13: (a)Energy distribution obtained from model for 4 ev atoms, and (b), for 150 ev atoms.

z-directed velocities would decay exponentially in distance from the gas port, with the e-folding length l_e being:

$$l_e = \frac{v_p}{n_e Q} \tag{6.22}$$

where v_p is the particle velocity, n_e is the electron density, and Q is the rate coefficient for particle annihilation. If particles are emitted isotropically, the e-folding length would decrease, since the average z-component of velocity would decrease. In addition, wall collisions may cause loss of particles or particle energy which cause the decay in z to be greater than exponential.

Instead, the observed e-folding length for atomic density over most of the plasma length was greater than the length given by equation 6.22 for 4 ev atoms. The e-folding length for 4 ev atoms with z-directed velocities was 20 cm between the gas port and the location 30 cm north of it. Because of the above mentioned effects the e-folding length should have been less that 20 cm if the gas port were the only source. The e-folding length was observed to be 19 cm between 0 cm and 30 cm, 40 cm between 30 cm and 110 cm, and 86 cm between 110 cm and 350 cm. Thus, there must have been be sources of atoms outside the gas box. The e-folding length for 300 Kelvin molecules with z-directed velocities was 1.6 cm. The e-folding length observed was 13 cm between 0 cm and 30 cm and 61 cm between 30 cm and 110 cm. Thus, there must have been sources of molecules away from the gas port. The likely source of molecules is the vessel wall. Bombardment by high energy atoms can liberate molecules from the wall. The south half of the machine showed higher gauge readings. This might have been due to a higher rate of molecule influx due to higher energy atoms striking the wall. The molecules desorbed from the wall could then ionize and dissociate to supply atoms.

6.5 Summary and Discussion

Local atomic hydrogen and molecular hydrogen ionization rates were inferred from measurements of Hα and H_2 band emissivity profiles. H_2 band emission measurements were used to determine the percentage of Hα emitted by atoms excited through molecular dissociation (5%). Thus, the Hα light was emitted mainly from atoms excited from their ground states, and a measurement of Hα emission could be used to determine the atomic ionization rate with a 95 % accuracy, ignoring other uncertainties. H_2 band emission was used to determine molecular

ionization rates for the first time. Using assumptions made about the molecular density distribution in the gas box, the local rates were integrated over the plasma volume to estimate the total ionization source, 462 amps. 208 amps were due to atomic ionization and 254 amps were due to molecular ionization. 100 amps of molecules were injected and 154 amps of molecules were recyled. The recycling occurred within 110 cm of the gas port. The power lost in charge-exchange, and neutral ionization and radiation was 90 kilowatts.

Analysis of the Hα line wavelength distribution shows the presence of two energy components: a central cold component radiated by atoms with an energy distribution maximized at 1 ev and extending to 12 ev, and a hot component which is roughly Maxwellian and has a temperature of 70 ev. Since molecular ionization is the dominant molecular break-up process, the majority of the cold atoms probably arise from the dissociation of molecular ions. The hot atoms probably arise from charge-exchange collisions in which a cold atom acquires the energy of a plasma proton, and then reflects off the wall, losing approximately 55% of its energy. The radial distributions of both components are identical within the accuracy of measurement, perhaps because both profiles are determined by wall interactions and not plasma interactions. The ratio of hot atoms to cold atoms observed is consistent with the result of a zero-dimensional model, using a reflection coefficient of .63. The absence of hot atoms at z = 0 cm, 30 cm, and 110 cm, indicates a lower outer plasma ion temperature at those axial locations, which is consistent with impurity ion temperature measurements.

Atomic and molecular densities inferred from emission measurements show the neutral densities were concentrated on the outer portion of the plasma. Molecules have a short mean free path for ionization in the edge plasma, 1.6 cm, and do not penetrate to the plasma core. Atoms have a longer mean free path for charge-exchange or ionization, 13 cm, and a fraction does penetrate to the core. The atomic density is down on the axis by a factor of 10. Results of a three-dimensional atomic transport model are consistent with the profile of cold atomic density computed from emission measurements and inconsistent with the hot atomic density profile computed from measurements. The discrepancy may be due to inaccurate energy loss and reflection coefficients used in the hot atom modeling. Axial profiles indicate the major source of neutrals (90%)is the gas box, with a smaller source being the vessel walls (10%) outside the gas box. The wall source decreases

with distance from the gas port.

Chapter 7

Thesis Summary and Suggestions for Continued Work

The atomic hydrogen and molecular hydrogen emission from the Tara central cell plasma has been investigated using several spectrometers. Particle densities and ionization rates were inferred from absolute intensity measurements. The plasma fueling is radially concentrated at the plasma edge and is a factor of 2 lower at the plasma center. The fueling is concentrated at the gas port and is attenuated a factor of 610 at a distance of 350 cm north of the gas port. The total fueling rate is estimated at 462 amps. The power lost in neutral particle radiation, ionization and charge- exchange is estimated at 90 kilowatts.

High resolution measurements of the Hα line show two components in the profile measured at z = 350 cm and one component in the profiles measured at z = 0 cm, 30 cm, and 110 cm. These components represent a 'cold' atom component with an average energy of 1.5 ev and at a 'hot' atom component with a temperature of 70 ev. The cold atoms most likely originate in molecular ion dissociation reactions and the hot atoms most likely originate in charge-exchange reactions. The energy distributions of the radiating atoms are independent of plasma radius. The hot component was observed only at z = 350 cm, which is consistent with the higher edge ion temperature there.

Emission from hydrogen molecules in the plasma was observed in the form of line emission and continuum emission. Individual lines in several visible bands were resolved. The most intense visible molecular lines were in the $G \rightarrow B$ bands. The band emission intensity measurements were used to determine spatial molecular density and ionization profiles and to determine the fraction of the Hα light

emitted by atoms excited through molecular dissociative processes, which was 5%. The molecular dissociative continuum was identified in a wavelength scan of the ultraviolet emission in the gas box. The observed wavelength distribution approximately matches the H_2 continuum distribution calculated for certain conditions. The ratio of continuum emission to $G \rightarrow B$ line emission was used to determine the ratio of molecular ionization to continuum dissociation, which was 40.

A three-dimensional model was developed to simulate atomic transport. Using an angle-variable reflection probability and an energy reflection loss fraction of .5, the density profile generated by the model for the cold atom case matches the cold atom density profile determined from measurements, but the profile generated for the hot atom case does not match the hot atom density profile determined from measurements. The energy distributions obtained by the model show a significant fraction of both hot and cold atoms are at energies below their creation energies, but the fraction is lower than the measured fraction in both cases. These discrepancies may be due to inaccuracies in the model.

Future research in the area of visible molecular hydrogen spectroscopy would benefit from a knowledge of the Franck-Condon factors of the observed bands, which would allow a calculation of the vibrational state distribution from a measurement of the relative band intensities. In addition to studying the bands observed in this work, other bands of the same systems may also be investigated for this purpose. Excitation, ionization, and dissociation rates may depend upon the vibrational level distribution. This effect could be studied to obtain more accurate rates. In the case of plasmas with lower electron temperatures,$T_e < 15$ ev, the excitation rates for the bands studied in this work will be much lower and the Fulcher bands will be the most intense visible bands. In that case a measurement of the Fulcher band intensities together with a knowledge of the excitation cross sections could be used to infer molecular densities and ionization/dissociation rates. The ratio of Fulcher band intensities to the $G \rightarrow B$ band intensities is a function of electron temperature and if the cross sections are measured to sufficient accuracy, this ratio may be used to determine the electron temperature in plasmas which emit enough light in those bands.

Appendix A

Line Shape Inversion Calculation

In this appendix, the equation relating the wavelength distribution of a doppler-broadened line to the energy distribution of the radiating particles is derived. This derivation follows the method in ref. [61]. This derivation is only applicable where the broadening is essentially only doppler and where the radiating particles are isotropic in velocity space.

A photon radiated by a non-relativistic atom moving with velocity v and radiating into a direction which makes an angle θ with respect to its velocity will be doppler-shifted by an amount $\Delta\lambda$ where

$$\Delta\lambda = \frac{\lambda v}{c} cos\theta \tag{A.1}$$

where λ is the wavelength radiated by the atom at rest and c is the speed of light. If photons are observed from only one direction, z, and v_z is the component of velocity in that direction, then $\Delta\lambda = \lambda v_z/c$. Then, if $f(v_z)dv_z$ is the number of radiating atoms in the emitting volume with z-components of velocity between v_z and $v_z + dv_z$,

$$f(v_z)dv_z = I(\Delta\lambda)d(\Delta\lambda) \tag{A.2}$$

where $I(\Delta\lambda)d(\Delta\lambda)$ is the number of radiated particles with wavelength shifts between $\Delta\lambda$ and $\Delta\lambda + d(\Delta\lambda)$. Since $\Delta\lambda = \lambda v_z/c$, $d(\Delta\lambda) = \lambda/c\ dv_z$ and

$$f(v_z) = I(\Delta\lambda)\lambda/c \tag{A.3}$$

So, a measurement of $I(\Delta\lambda)$ gives $f(v_z)$. $f(v_z)$ is related to the three dimensional velocity distribution function $F(v_x, v_y, v_z)$ by the equation:

$$f(v_z) = \int\int F(v_x, v_y, v_z)dv_x dv_y \tag{A.4}$$

where $F(v_x, v_y, v_z)dv_x, dv_y, dv_z$ is the number of particles with velocities between v_x and $v_x + dv_x$, v_y and $v_y + dv_y$,and v_z and $v_z + dv_z$, and the integration is over all v_x and v_y for which $F(v_x, v_y, v_z)$ is non-zero. If the distribution is isotropic in velocity space, then $F(v_x, v_y, v_z) = F(v)$ where $v^2 = v_x^2 + v_y^2 + v_z^2$. The distribution is then spherically symmetric in velocity space with a probability density which depends only on the magnitude v.

Let $v_\perp^2 = v_x^2 + v_y^2$ and let v_m denote the maximum speed for which the distribution function is non-zero. Then

$$f(v_z) = \int_0^{v_m^2 - v_z^2} F(v) 2\pi v_\perp dv_\perp \tag{A.5}$$

Since $v^2 = v_\perp^2 + v_z^2$, $vdv = v_\perp dv_\perp$ for fixed v_z. Then ,

$$f(v_z) = 2\pi \int_{v_z}^{v_m} F(v) v dv \tag{A.6}$$

Define a function $g(v)$ where $g(v)dv$ equals the number of particles with speeds between v and $v + dv$. Then

$$g(v)dv = 4\pi v^2 F(v) dv \tag{A.7}$$

and

$$F(v) = \frac{g(v)}{4\pi v^2} \tag{A.8}$$

So that

$$f(v_z) = 1/2 \int_{v_z}^{v_m} \frac{g(v)}{v} dv \tag{A.9}$$

It follows from this equation that $f(v_z)$ will be a monotonically decreasing function for any $g(v)$.

Differentiating equation A.9 and evaluating at $v_z = v$ gives

$$\frac{df(v)}{dv} = -1/2 \frac{g(v)}{v} \tag{A.10}$$

from which follows:

$$g(v) = -2v \frac{df(v)}{dv} \tag{A.11}$$

Using equation A.3,

$$g(v) = -\frac{2\lambda \Delta\lambda}{c} \frac{dI(\Delta\lambda)}{d(\Delta\lambda)} \tag{A.12}$$

The kinetic energy distribution function $G(E)$ where $G(E)dE$ is the number of radiating particles with energies between E and $E + dE$ is given by :

$$G(E)dE = g(v)dv \tag{A.13}$$

Therefore,

$$G(E) = -\frac{2\lambda^2}{mc^2}\frac{dI(\Delta\lambda)}{d(\Delta\lambda)} \tag{A.14}$$

where m is the mass of the radiating particle.

Thus, a measurement of $I(\Delta\lambda)$ can be differentiated to obtain $G(E)$, the kinetic energy distribution.

Bibliography

[1] B.I.Cohen. *Status of Mirror Fusion Research 1980.* Technical Report UCAR 10049-80-Rev.1, Lawrence Livermore National Laboratory, 1980.

[2] J.Kesner etal. *Introduction to Tandem Mirror Physics.* Technical Report PFC/RR-83-35, MIT, 1983.

[3] T.C.Simonen. *Summary of Results from the Tandem Mirror Experiment.* Technical Report UCRL-53120, LLNL, 1981.

[4] J.Kesner etal. A tandem mirror with axisymmetric central-cell ion confinement. *Nuclear Fusion*, 22, 1982.

[5] R.S.Post etal. Improved plasma startup in the Tara central cell. *Nuclear Fusion*, 27, 1987.

[6] R.K.Janev etal. *Atomic and Molecular Processes in Hydrogen-Helium Plasma.* Technical Report PPPL-TM-368, PPPL, June 1985.

[7] L.C. Johnson and E. Hinnov. *Ionization, Recombination, and Population of Excited Levels in Hydrogen Plasmas.* Technical Report MATT-909, PPPL, August 1972.

[8] K.Behringer etal. *Reprints of JET Posters at the 27th Annual Meeting of the Division of Plasma Physics of the American Physical Society.* Technical Report JET-P(85)31, JET, November 1985.

[9] F.W.Hofman etal. *Behavior of Neutral Hydrogen and Helium in C Stellarator Discharges.* Technical Report Matt-305, PPPL, September 1964.

[10] E.Hinnov etal. *Interpretation of Atomic Hydrogen Light in the C Stellarator.* Technical Report Matt-270, PPPL, May 1964.

[11] A.R.Striganov and N.S.Sventitskii. *Tables of Spectral Lines of Neutral and Ionized Atoms.* IFI/Plenum, New York, 1968.

[12] O.T.Strand. *A Study of Impurities in the Tandem Mirror Experiment Using Extreme Ultraviolet Spectroscopy.* Technical Report UCRL-53295, LLNL, May 1982.

[13] M.E.Foord. *Visible Continuum Measurements on the Alcator C Tokamak: Changes in Particle Transport During Pellet Fuelled Discharges.* Technical Report PFC/RR-87-2, MIT, December 1987.

[14] D.E.Post etal. Steady-state radiative cooling rates for low density, high-temperature plasma. *Atomic Data and Nuclear Tables*, 20(5), Nov. 1978.

[15] C.Breton etal. Ionization equilibrium and radiative cooling of a high temperature plasma. *J. Quant. Spectrosc. Radiat. Transfer*, 19, 1978.

[16] D.L.Book. *NRL Plasma Formulary.* Technical Report 0084-4040, Naval Research Laboratory, 1987.

[17] F.Chen. *Introduction to Plasma Physics.* Plenum Press, New York, 1974.

[18] S.L. Allen etal. *Impurity Characteristics of TMX-U.* Technical Report UCID-20026, LLNL, May 1984.

[19] T.L. Yu. *Spectroscopic Study of Sources and Control of Impurities in TMX-U.* Technical Report, LLNL, November 1984.

[20] D.H.McNeill. Power balance in Elmo Bumpy Torus: bulk electrons and ions in a 37 kw discharge. *Plasma Physics and Controlled Fusion*, 28(4), 1986.

[21] D.H.McNeill. Edge region hydrogen line emission in the PDX Tokamak. *J. Vac. Sci. Technol.*, 2, Feb. 1984.

[22] D.H.McNeill. Balmer-alpha emission and hydrogen-atom energy in ion-source discharges. *Physical Review A*, 25(4), May 1982.

[23] D.H.McNeill. *Spectral Line Shapes.* Volume 2, Walter deGruyter and C0., New York, 1983.

[24] D.H.McNeill. Power balance in EBT: bulk electrons and ions in a 37 kw discharge. *Plasma Physics and Controlled Fusion*, 28(4), 1986.

[25] J.L.Terry. The far uv spectrum of H_2. *J.Vac.Sci.Technol. A*, 1(2), April 1983.

[26] D.H.McNeill. *Molecular Origin of Background Light in Thomson Scattering Measurements.* Technical Report PPPL-2351, PPPL, June 1986.

[27] G. Herzberg. *Spectra of Diatomic Molecules.* Van Nostrand Reinhold Company Inc., New York, 1950.

[28] M. Karplus and R. Porter. *Atoms and Molecules.* W.A.Benjamin, Inc., Menlo Park, California, 1970.

[29] A.L.Hughes and P.Lowe. Intensities in the hydrogen spectrum. *Physical Review*, 21(3), March 1923.

[30] R.J.Anderson etal. Electron impact excitation of the $G^1\Sigma_g^+$ state of H_2. *J.Opt.Soc.Am.*, 67(12), December 1977.

[31] R.L.Day etal. Electron impact excitation of the singlet-g states of H_2. *J.Chem.Phys.*, 71(9), Nov. 1979.

[32] G.H.Dieke. The molecular spectrum of hydrogen and its isotopes. *Journal of Molecular Spectroscopy*, 2, 1958.

[33] M.Pealat etal. Rovibrational molecular populations, atoms, and negative ions in H2 and D2 magnetic multicusp discharges. *J.Chem.Phys.*, (82):4943, June 1985.

[34] *Exploration of a Hydrogen Discharge Using Resonant Multiphoton Ionization*, Brookhaven National Laboratory, October 1986. Presented at the Fourth International Symposium on the Production and Neutralization of Negative Ions and Beams.

[35] H.M.James and A.S.Coolidge. Continuous spectra of H2 and D2. *Physical Review*, 55, January 1939.

[36] A.S.Coolidge. Experimental verification of the theory of the continuous spectra of H2 and D2. *Physical Review*, 65, April 1944.

[37] H.W.Drawin and H.Henning. *Mesures Optique sur Deca II.* Technical Report EUR-CEA-FC-384, Association-Euratom-CEA, March 1966.

[38] T.E.Sharp. Potential energy curves for molecular hydrogen and its ions. *Atomic Data*, 2, 1971.

[39] T.L.Kwok etal. Dipole moments and transition probabilities of the $a^3\Sigma_g^+$ - $b^3\Sigma_u^+$ system of molecular hydrogen. *Physical Review A*, 34, 1986.

[40] C.R.Lishawa etal. Excitation of continuum radiation in collisions of electrons and metastable argon atoms with H2 and D2. *J.Chem.Phys.*, 83, July 1985.

[41] A.Dalgarno etal. A new continuous emission spectrum of the hydrogen molecule. *The Astrophysical Journal*, 162, October 1970.

[42] T.L.Stephens and A.Dalgarno. Spontaneous radiative dissociation in molecular hydrogen. *J.Quant.Spectrosc.Radiant.Transfer.*, 12, 1972.

[43] J.A.Samson. *Techniques of Vacuum Ultraviolet Spectroscopy.* McMillan, 1967.

[44] J.H.Irby etal. Comparison of Tara fueling rate measurments with a 3d Monte Carlo simulation. In *Bulliten of the American Physical Society*, American Physical Society, 1987.

[45] K.Brau. Camera fueling measurements. 1987. unpublished.

[46] R.L.Freeman and E.M.Jones. *Atomic Collision Processes in Plasma Physics Experiments.* Technical Report CLM-R 137, UKAEA, 1974.

[47] H.Griem. *Plasma Spectroscopy.* McGraw-Hill, New York, 1964.

[48] H.A. Bethe and E.E.Saltpeter. *Quantum Mechanics of One- and Two-Electron Atoms.* Plenum Publishing Corp., New York, 1977.

[49] A.C. Mitchell and M.W. Zemansky. *Resonance Radiation and Excited Atoms.* Cambridge University Press, Cambridge, 1961.

[50] R.C.Williams. The fine structures of Hα and Dα under varying discharge conditions. *Physical Review*, 54, October 1938.

[51] B.L.Carnahan and E.C.Zipf. Dissociative excitation of H_2,HD_2, and D_2 by electron impact. *Physical Review A*, 16(3), Sept. 1977.

[52] C.Karolis and E.Harting. Electron impact dissociation cross sections in hydrogen and deuterium, leading to Balmer alpha and beta emission. *J.Phys.B:Atom.Molec.Phys.*, 11(2), 1978.

[53] G.A.Khayrallah. Electron impact dissociation of molecular hydrogen and deuterium: production of atomic hydrogen and deuterium α , β, and γ lines. *Physical Review A*, 13(6), June 1976.

[54] R.S.Freund etal. Dissocative excitation of H_2: spectral line shapes and electron impact cross sections of the balmer lines. *J.Chem.Phys.*, 64(3), Feb. 1976.

[55] M.Higo and S.Kamata. Electron impact dissociation of molecular hydrogen and deuterium: isotope effect on the emission cross section of H^* and D^* (n = 3,4,5). *Chemical Physics*, 73, 1982.

[56] A.Crowe and J.W.McConkey. Experimental evidence for new dissociation channels in electron-impact ionization of H_2. *Phys.Rev.Lett.*, 31(4), July 1973.

[57] P.R.Bevington. *Data Reduction and Error Analysis for the Physical Sciences.* McGraw-Hill, New York, 1969.

[58] O.S.Oen and M.T.Robinson. Computer simulation of the reflection of hydrogen and the sputtering of hydrogen from metal hydrides. *Journal of Nuclear Materials*, 76, 1978.

[59] W.C.Guss etal. Atomic hydrogen density measurements in the Tara Tandem Mirror Experiment. 1988. Submitted for publication.

[60] P. Goodrich. *Neutral Particle Transport in the Tara Tandem Mirror Experiment.* Master's thesis, MIT, 1986.

[61] T.G.Moran. *Techniques for Obtaining Velocity Distributions of Atoms or Ions from Doppler-broadened Spectral Line Profiles.* Technical Report PFC/RR-86-24, MIT, 1986.